

T-2647

A TIME-DOMAIN ELECTROMAGNETIC SURVEY  
OF COCHETOPA HILLS AND ALKALI SPRINGS,  
SAGAUCHE COUNTY, SOUTH-CENTRAL COLORADO

CLOSED RESERVE

ARTHUR LAKES LIBRARY  
COLORADO SCHOOL of MINES  
GOLDEN, COLORADO 80401

by

Kamil E. Ibrahim

ProQuest Number: 10782386

All rights reserved

INFORMATION TO ALL USERS

The quality of this reproduction is dependent upon the quality of the copy submitted.

In the unlikely event that the author did not send a complete manuscript and there are missing pages, these will be noted. Also, if material had to be removed, a note will indicate the deletion.



ProQuest 10782386

Published by ProQuest LLC (2018). Copyright of the Dissertation is held by the Author.

All rights reserved.

This work is protected against unauthorized copying under Title 17, United States Code  
Microform Edition © ProQuest LLC.

ProQuest LLC.  
789 East Eisenhower Parkway  
P.O. Box 1346  
Ann Arbor, MI 48106 – 1346


T-2647

A thesis submitted to the Faculty and the Board of Trustees of the Colorado School of Mines in partial fulfillment of the requirements for the degree of Master of Science (Geophysics).

Golden, Colorado

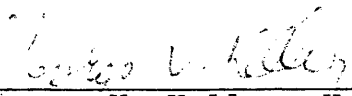
Date Dec 6, 1982

Signed: Kamil E. Ibrahim  
Kamil E. Ibrahim

Approved:   
C.H. Stoyer  
Thesis Advisor

Golden, Colorado

Date 6 Dec 82

  
George V. Keller, Head  
Department of Geophysics

ABSTRACT

A controlled source Time-Domain Electromagnetic (TDEM) survey was conducted in the Cochetopa Hills and Alkali Springs of south-central Colorado, during the summer of 1981. The survey was initiated and supported by the Geophysics Department at Colorado School of Mines as part of its educational goals.

A grounded wire source varying in length between 200 meters and 1,400 meters was used with N-S and E-W orientations. A vertical-axis induction loop was employed to measure the time rate of change of the magnetic field at 89 receiver sites, covering an area of about 150 square km. Signals from receivers as far as 8 km from the source were obtained, and transients that lasted from 250 msec to 1.5 sec were recorded.

Data acquisition and preliminary interpretation were made on site by a MINC-11 mini-computer. Final interpretations were achieved through layered models derived from the data via non-linear inversions.

The results of the survey indicate a three-layer earth model. A combined thickness of up to 1,500 meters was obtained for the first two layers. The resistivity of the third layer is high, and its exact value is not determined. The results

also indicate an increasing trend in the total thickness of the volcanic ash-flows and tuffs, westward. Moreover, the TDEM method has also been able to confirm the presence of a moderately shallow basement (80-100 meters) near Alkali Springs, with resistivities greater than 50 ohm-meters. In addition, the results correlate well with the known geology of the area and its structural features, such as the Sheep Creek fault zone, Sheep Creek syncline, and the outcrops of Precambrian basement near Alkali Springs.

TABLE OF CONTENTS

	<u>Page</u>
ABSTRACT . . . . .	iii
LIST OF FIGURES . . . . .	viii
ACKNOWLEDGEMENTS . . . . .	xiii
INTRODUCTION . . . . .	1
TECTONIC HISTORY OF THE STUDY AREA . . . . .	4
GENERAL GEOLOGY AND HISTORY OF THE STUDY AREA . .	9
Introduction . . . . .	9
Precambrian and Paleozoic Rocks . . . . .	9
Tertiary Volcanic Rocks . . . . .	13
Structure of the Tertiary Rocks . . . . .	16
PREVIOUS GEOPHYSICAL STUDIES . . . . .	17
THEORY . . . . .	20
Expressions for Apparent Resistivity . . . . .	29
All-Time Apparent Resistivity . . . . .	31
Calibration Factor . . . . .	35
THE SURVEY . . . . .	37
Current Source (Figure 11) . . . . .	38
Receiver (Figure 12) . . . . .	38
Data Processing . . . . .	41
INTERPRETATION OF RESULTS . . . . .	51
General . . . . .	51

	<u>Page</u>
Qualitative Interpretation . . . . .	54
Maximum Voltage Apparent Resistivity (MVAR) Method . . . . .	54
Total Longitudinal Conductance (S) . . . . .	56
Total Longitudinal Conductance (S) from Apparent Resistivity Curves . . . . .	60
Quantitative Interpretation . . . . .	69
Interpreted Depth-Resistivity Maps . . . . .	74
Total Longitudinal Conductance (S) from Inversions . . . . .	77
Cross-Section Along Profile 1 . . . . .	79
Cross-Section Along Profile 2 . . . . .	79
Cross-Section Along Profile 3 . . . . .	81
Cross-Section Along Profile 4 . . . . .	81
Cross-Section Along Profile 5 . . . . .	83
Cross-Section Along Profile 6 . . . . .	85
Cross-Section Along Profile 7 . . . . .	85
The Evaluation of TDEM Results . . . . .	88
CONCLUSIONS . . . . .	90
REFERENCES . . . . .	93
APPENDICES . . . . .	98
Appendix A - Plots of apparent resistivity- time curves for early- and late- time asymptotes . . . . .	99
Appendix B - A table containing calculated parameters for earth models used in the inversion, for all receiver locations . . . . .	185

	<u>Page</u>
Appendix C - Explanation of the meaning of the symbols used in the inversion of apparent resistivity curves, using the computer program SATI . . . . .	190

LIST OF FIGURES

<u>Figure</u>		<u>Page</u>
1	Physiographic setting showing the location of the study area (after Bruns, et al., 1971) . . . . .	5
2	Map of San Luis Valley (after Gaca, 1965) .	6
3	Geologic map of the study area, showing the N-S trending Sheep Creek fault zone and the sedimentary outcrops near Alkali Springs (after Bruns, et al., 1971). For description of map units, please see Figure 3a . . . . .	10
3a	Explanation of the rock units and geologic symbols of the geologic map of Figure 3 . . . . .	11
4	A composite stratigraphic column of the study area (after Knepper, 1974) . . . . .	12
5	Structural map showing the location of faults (solid lines) mapped by Mamah (1979) near Villa Grove village and Mineral Hot Springs. The hatched lines indicate the location of the same faults as depicted from the geology (after Mamah, 1979) . . . . .	19
6	Set of apparent resistivity-time curves for TDEM coupling between grounded wire and vertical-axis loop, for a uniform earth, variable resistivity . . . . .	27
7	Set of apparent resistivity-time curves for TDEM sounding over a uniform earth using a wire-loop geometry, variable offset . . . . .	28
8	Line-source, loop receiver configuration (modified from Bond, 1981) . . . . .	30

<u>Figure</u>	<u>Page</u>
9	Apparent resistivity-time curve showing the early- and late-time asymptotes for a uniform half-space . . . . . 32
10	A curve of normalized emf vs. normalized time with the early, intermediate and late stages indicated. The model shows a resistive medium overlying a conductive medium (after Bond, 1981) . . . . . 33
11	Schematic diagram for the source used in the survey (after Ibrahim and Stoyer, 1981) . . . . . 39
12	Schematic diagram for the receiver used in the survey (after Ibrahim and Stoyer, 1981) . . . . . 40
13	Raw stacked transient recorded at Station 4, using Source A, showing the general amplitude and shape of a transient curve. This transient was recorded close to the source, hence it has a low noise level . . . . . 42
14	Raw stacked transient from Station 74, using Source C, showing a very high level of noise . . . . . 43
15	A raw stacked transient recorded at Station 61, using Source C, showing a resistive medium over a conductive one . . . . . 44
16	Raw stacked transient recorded at Station 46, using Source B, showing a very clean signal . . . . . 45
17	Source-receiver layout used in the survey. Sources A, B and C are practically equivalent in length (1,300 m). Source D is the longest (1,400 m). Numbers indicate the station locations . . . . . 46

<u>Figure</u>	<u>Page</u>	
18	Early- and late-time apparent resistivity curve for Station 42, using Source B. The reversal at the late stage could probably be explained as due to low-level noise . . . . .	50
19	TDEM curves for a sequence of layers in which the second layer is more resistive than the first. The parameter on each curve is the separation between source and receiver in meters . . . . .	52
20	TDEM curves for a sequence of layers in which the second layer is more conductive than the first. The parameter on the curves is the separation between the source and receiver in meters . . . . .	53
21	Raw stacked transient from Station 51, using Source C. The total window is 3.33 seconds. The curve shows a resistive near surface layer over a conductive layer. At late stage the curve shows insulating basement . . . . .	55
22	A maximum voltage apparent resistivity (MVAR) map of the study area, showing the trend of the subsurface resistivity. Contour interval in ohm-meters . . . . .	57
23	A map showing the location of the profiles	58
24	Plots of maximum voltage apparent resistivity (MVAR) value for the stations along profile 5, indicating the resistivity trend . . . . .	59
25	A total longitudinal conductance (S) map of the study area, as calculated from the early- and late-time apparent resistivity curves, showing the trend of increase in the total thickness of the volcanics westward. Contour values in mhos . . . . .	61

<u>Figure</u>	<u>Page</u>
26 All-time apparent resistivity contour map of profile 4. Contour values in ohm-meters . . . . .	62
27 All-time apparent resistivity contour map of profile 5. Contour values in ohm-meters . . . . .	64
28 All-time apparent resistivity contour map of profile 6. Contour values in ohm-meters . . . . .	65
29 All-time apparent resistivity map at 0.1 second. Values denote apparent resistivity in ohm-meters . . . . .	67
30 All-time apparent resistivity map at 0.03 second. Values indicate apparent resistivity in ohm-meters . . . . .	68
31 Example of inversion of the early- and late-time apparent resistivity curves, using a two-layer earth model . . . . .	71
32 Example of inversion of the early- and late-time apparent resistivity curves, using a three-layer earth model . . . . .	72
33 Plot of calibration factor for the stations along profile 5 . . . . .	73
34 An interpreted resistivity map at a depth of 100 meters. Contour interval is 10 ohm-meters . . . . .	75
35 An interpreted resistivity map at a depth of 500 meters. Contour interval is 10 ohm-meters . . . . .	76
36 A total longitudinal conductance (S) map of the study area, constructed from the inversion results. The map shows the trend of increase in the total thickness of the volcanics westward. Contours are in mhos . . . . .	78

<u>Figure</u>	<u>Page</u>	
37a,b	Interpreted cross-sections extrapolated from the data along profiles 1 and 2, respectively. Numbers designate resistivities in ohm-meters . . . . .	80
38a,b	Interpreted cross-sections obtained from the data along profiles 3 and 4, respectively. Values indicate resistivities in ohm-meters . . . . .	82
39	An interpreted W-E trending cross-section along profile 5. Values indicate resistivities in ohm-meters . . . . .	84
40	A N-S trending, interpreted cross-section from the data of profile 6. Values indicate resistivities in ohm-meters . . . . .	86
41	An interpreted W-E trending cross-section obtained from the data along profile 7. Values indicate resistivities in ohm-meters . . . . .	87
42 - 126	Plots of apparent resistivity-time curves for the early- and late-time asymptotes, calculated from equations 10 and 11 respectively. Apparent resistivities are in ohm-meters, and times are in seconds. (These figures are part of Appendix A.) . . .	100

ACKNOWLEDGEMENTS

I wish to express my gratitude to my parents, who have been proudly carrying the moral and financial burden of my life for so many years.

Of all the people who have assisted me during the course of this work, I would like to thank my advisor, Dr. C.H. Stoyer, who has contributed generously during all stages of this research. He has always been available for discussions, and his numerous suggestions and comments have been instrumental to the completion of this work, as was his careful and patient reading of the manuscript.

I am highly grateful to Professor G.V. Keller, from whom I learned a great deal about electrical methods. His comments on the draft were gratefully received and carefully used in the preparation of the final draft.

Thanks are also due to Dr. A.W. Ibrahim for the many valuable discussions which he has provided.

Financial support during the course of my study at the Colorado School of Mines was partially furnished by the Geophysics Department and partially by a scholarship from the African American Institute.

Special thanks go to Ms. Gail Baker and Mrs. Alice Robinson. I am also indebted to Mrs. Marilyn Scobey for typing this manuscript.

## INTRODUCTION

Electromagnetic (EM) methods have found their earliest applications in mining geophysics as a tool for locating conductive ore bodies (Mamah, 1979). It seems that the first practical application of the method dates back to 1913 in Germany, as revealed by the patent 322-040 (King, 1971; Mamah, 1979). The 1920s marked a period of achievement in Europe, as many ore bodies were discovered. In the United States, the method first found its application as early as 1917, when H. Conklin obtained U.S. patent 1,211,197 on an induction method that deployed a loop source energized by an alternating current (Kaufman and Keller, 1981, 1982).

The earliest application of EM sounding methods seemed to be in 1933, when the "ELTRAN method" was first introduced. This method used a dipole-dipole configuration and square current pulses. However, the method proved futile in the 1950s for oil exploration in sedimentary basins (Patra and Mallick, 1980). Very little success accompanied its application until the 1960s, when the method was revived by Baringer Research Ltd. through their airborne system, which they had flown with great success over several countries (Boniwell, 1967). A parallel development of EM sounding methods took place in the Soviet Union, and many papers were

published dealing with the theoretical developments. The Russian scholars, however, were acknowledged for their efforts to reduce the theoretical developments to forms that can be used in exploration (Kaufman and Keller, 1981, 1982).

The EM methods manifest themselves into two major techniques characterized by different types of excitation. The frequency-domain uses a harmonic source of excitation, whereas the time-domain commonly uses a square wave as its method of excitation. The frequency domain methods have found their application in profiling and, to a lesser extent, in EM sounding. The other technique has been widely used in EM sounding, as described by many articles in Russian literature.

Two methods of time-domain have come into being as a result of extensive research, namely, the short-offset (Keller, 1969; and others) and the long-offset. In Russia, the short-offset sounding method appears to have been favored over the long-offset method that was extensively used over the past decade in the United States in geothermal exploration (Keller, 1971; Jackson and Keller, 1972; and others). In the United States, the short-offset sounding method found its application only in experimental surveys related to oil exploration (Souto, 1980).

The time-domain methods have found many applications over the last decade in the search for geothermal resources, especially after the energy crisis became a real menace (Keller, 1970; Skokan, 1974).

Moreover, the method is a useful tool for mineral exploration (Spies, 1976a,b), and for groundwater exploration in arid and semi-arid regions and coastal areas (Collet, 1967). So far, a major advantage of the method has been in solving the conducting overburden problem (Spies, 1976a).

Time-domain sounding field surveys have been carried out by Keller, Crewdson, Daniels (1978), Skokan (1974), Mamah (1979), Tulinius (1980), and others.

During the summer of 1981, a time-domain electromagnetic survey was conducted by the students of the Colorado School of Mines in south-central Colorado. The survey was initiated and supported by the Geophysics Department of Colorado School of Mines to achieve a two-fold purpose:

- 1) to familiarize the students with the basic aspects of the method;  
and
- 2) to determine the structure of the region and guide future studies.

### TECTONIC HISTORY OF THE STUDY AREA

The surveyed area (Figure 1) lies in the northern San Juan Mountains, just outside the San Luis Valley, and includes the Cochetopa Hills to the west and Alkali Springs and Trickle Mountain to the east.

This area, which covers approximately 150 square kilometers, lies between latitudes  $38^{\circ} 06'$  and  $38^{\circ} 15'$  north and between longitudes  $106^{\circ} 22'$  and  $106^{\circ} 37'$  west, in Sagauche County, south-central Colorado. The area is mainly accessed by U.S. Highway 285, Colorado State Highway 114, and local paved and dirt roads within the study area.

The San Luis Valley (Figure 2) is a complex hinged graben having an eastward tilt. The valley began subsiding in Miocene time. It extends for more than 240 kilometers in a N-S direction, from Poncha Pass, Colorado, to about 26 kilometers south into New Mexico. Flanking the valley on the east is the Sangre Cristo Range of Precambrian and Paleozoic age, and on the west, the eastern portion of San Juan volcanic field mountains. The average altitude of the valley is about 2,350 meters above sea level.

The valley constitutes a major unit of the Rio Grande Rift system, which began at least 18 million years ago, as evidenced by fossils and K-Ar dates on interbedded volcanic

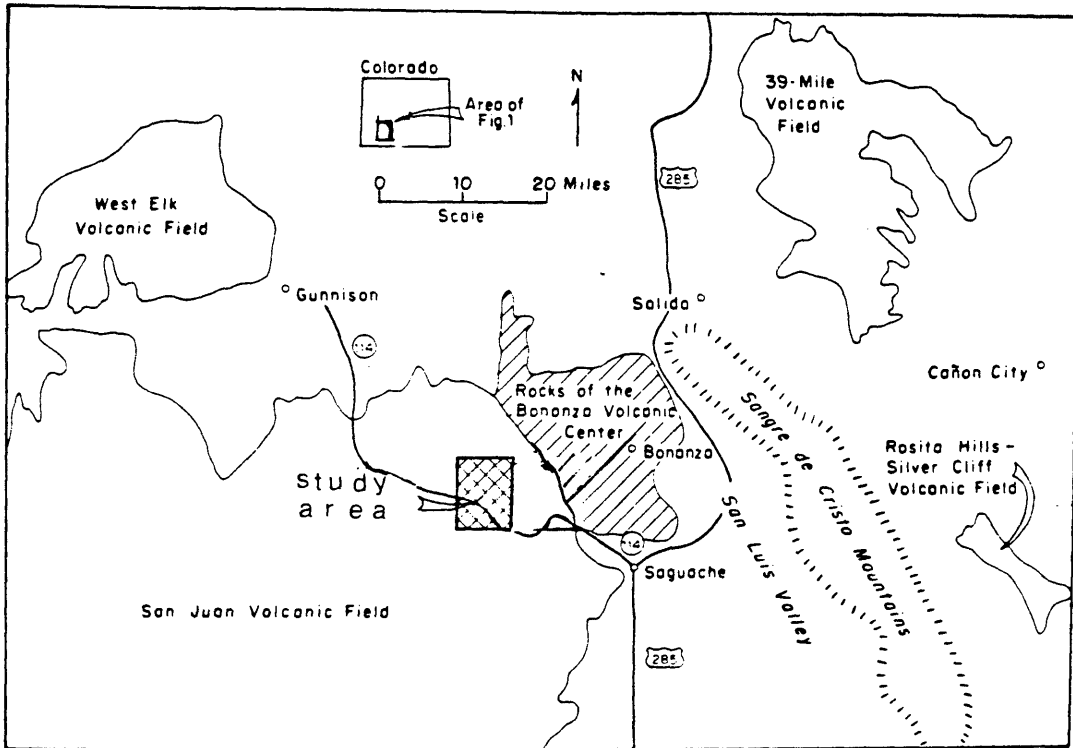


Figure 1 . Physiographic setting showing the location of the study area (after Bruns, et al., 1971).

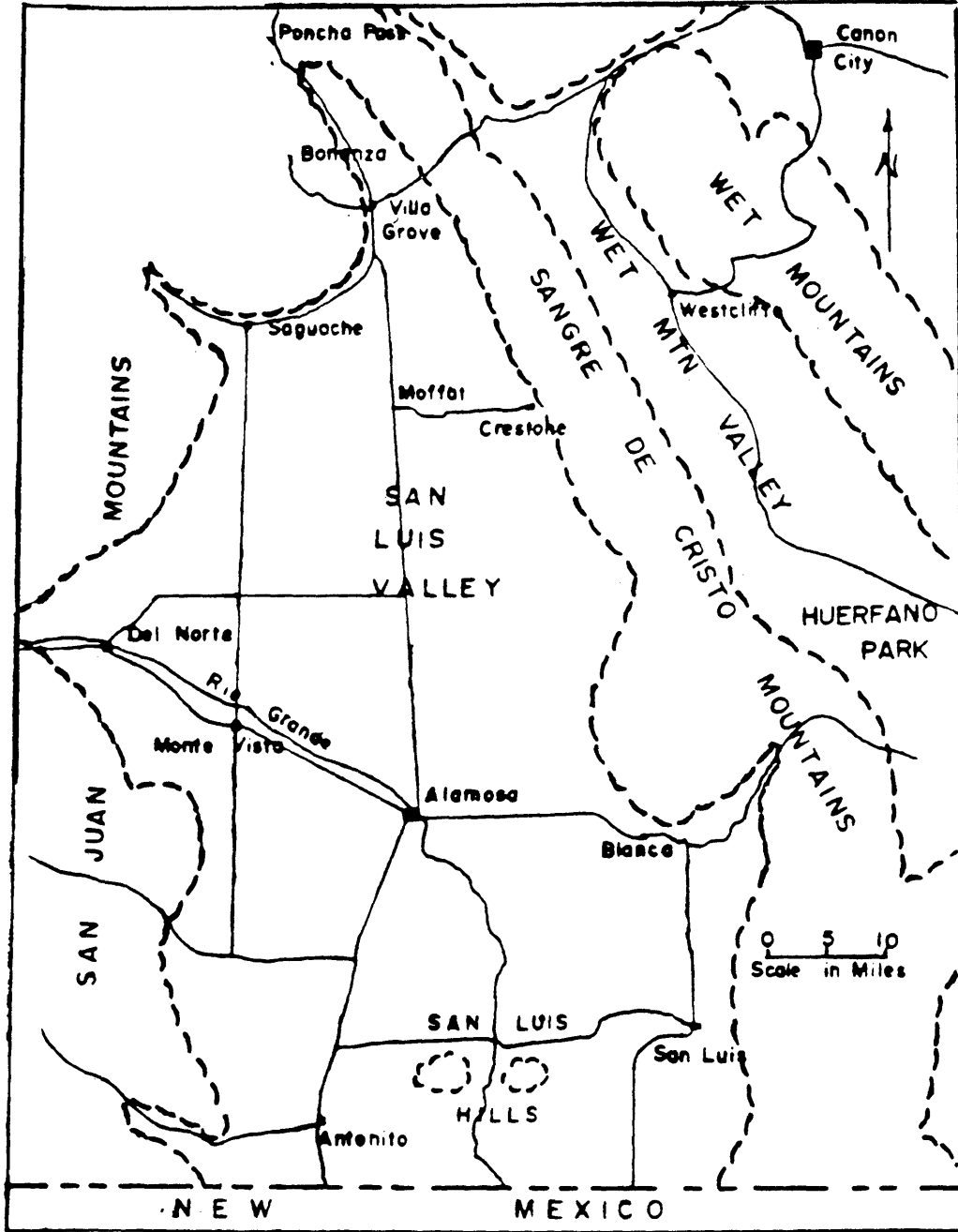


Figure 2. Map of San Luis Valley (after Gaca, 1965).

rocks (Chapin, 1971). The Rio Grande is a complex series of horsts and grabens, with a northerly trend extending from southern New Mexico into central Colorado, probably Middle- to Late Miocene in age (10-30 m.y.). The rift system is characterized by structural features such as normal faulting, filled grabens, and volcanism (Gaca, 1965). Origin of the rift system is associated with the reactivation of the north-trending southern Rocky Mountains by regional extension (Chapin, 1978). From the gravity evidence, Gaca (1965) indicated that the San Luis Valley is probably a very large rift depression, internally broken by block-faulting.

The geological development of the area started probably during the early Pre-Cambrian time by the deposition of unknown thickness of silicious clastic sediments (Knepper and Marrs, 1971). These sediments were then subjected to a phase of metamorphism and intense deformation, followed by a phase of igneous activity in the form of plutons, sills, and dikes.

The Paleozoic era was considered a period of tectonic dormancy, except for occasional uplifts.

During the Late Cretaceous period and until Late Eocene, the Laramide Orogeny was active in central Colorado. Rejuvenation of pre-existing structures was a major event that occurred during this period (Knepper, 1974). Structures associated with this Orogeny include folds, high-angle reverse

faults, and normal faults. Among these faults, Knepper (1974) listed Villa Grove fault, Sheep Creek fault, and the Kerber Creek fault.

## GENERAL GEOLOGY AND HISTORY OF THE STUDY AREA

### Introduction:

Over the years, the region has been visited by many geologists in an effort to study its history and stratigraphy. The earliest work was compiled and summarized by Larsen and Cross (1956). Recent work by the graduate students of Colorado School of Mines (Geology) has contributed immeasurably in understanding the geology of the region (Mayhew, 1969; Bruns, 1971; Knepper, 1974).

The geology of the study area (Figure 3) has been described in a number of publications, with a summary being provided by Bruns, et al. (1971), and Knepper (1974). The stratigraphic section which is applicable to the area is shown in Figure 4.

### Precambrian and Paleozoic Rocks:

Precambrian igneous and metamorphic rocks are exposed in several erosional windows, with the largest exposure being reported east of Alkali Springs (not shown on the geologic map). In the area described in this thesis, these rocks are predominantly medium- to coarse-grained quartz-biotite-microcline schist, fine-grained hornblende and biotite gneisses, intruded with subordinate amounts of granites and pegmatites.

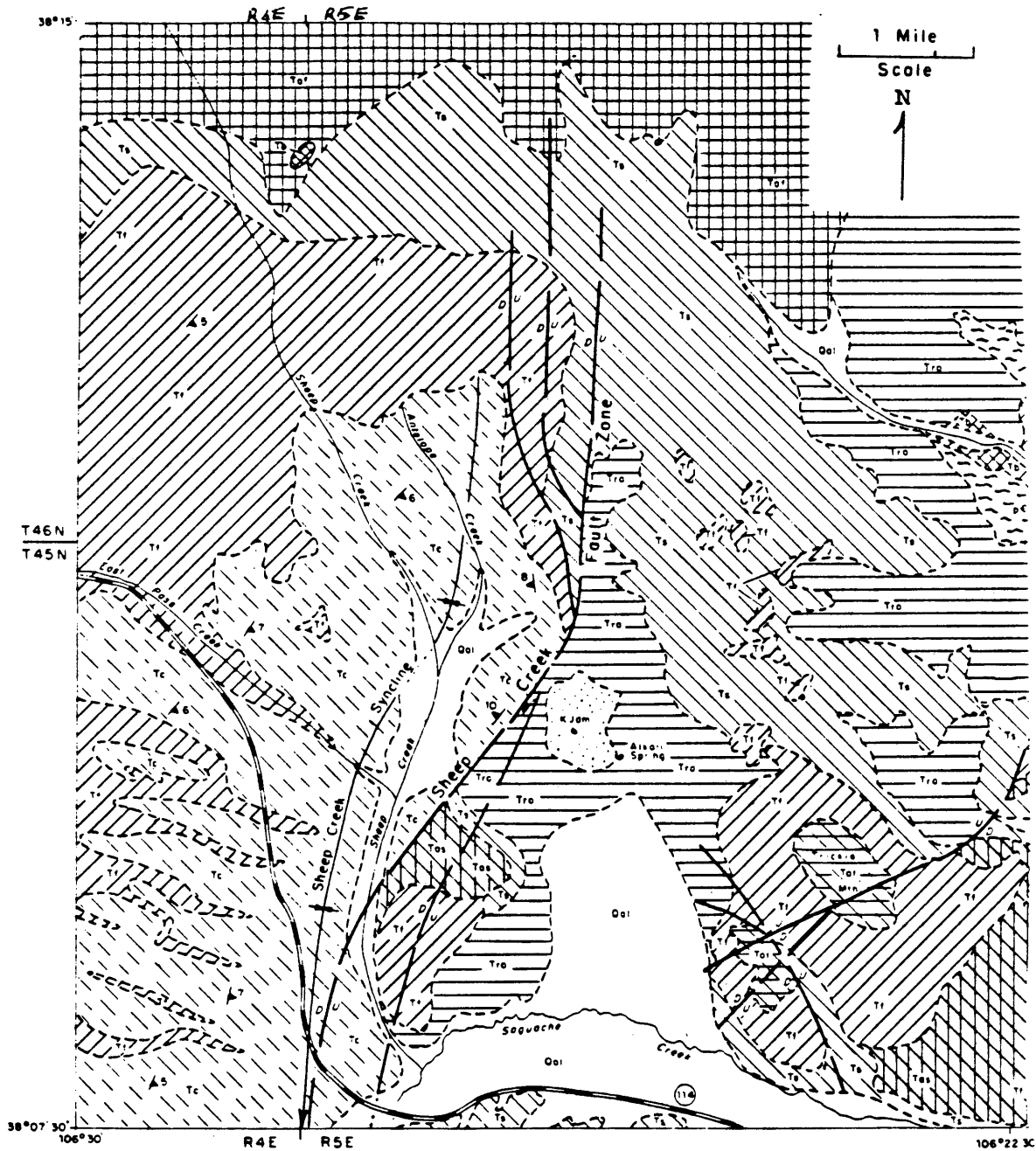


Figure 3. Geologic map of the study area, showing the N-S trending Sheep Creek fault zone and the sedimentary outcrops near Alkali Springs (after Bruns, et al., 1971). For description of map units, please see Figure 3a.

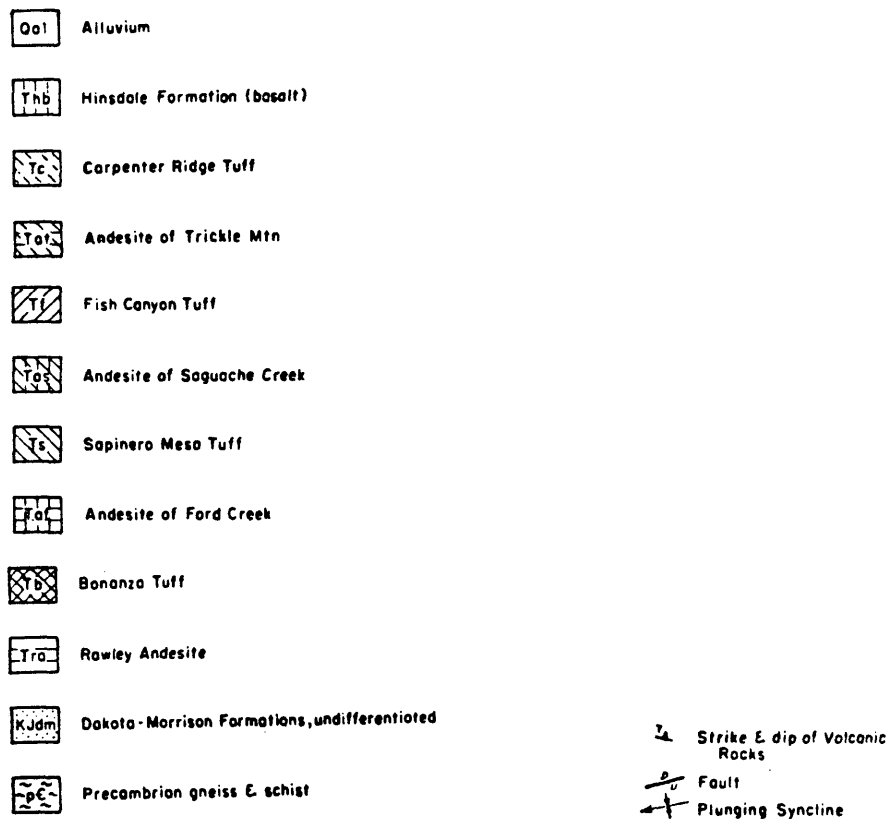


Figure 3a. Explanation of the rock units and geologic symbols of the geologic map of Figure 3.

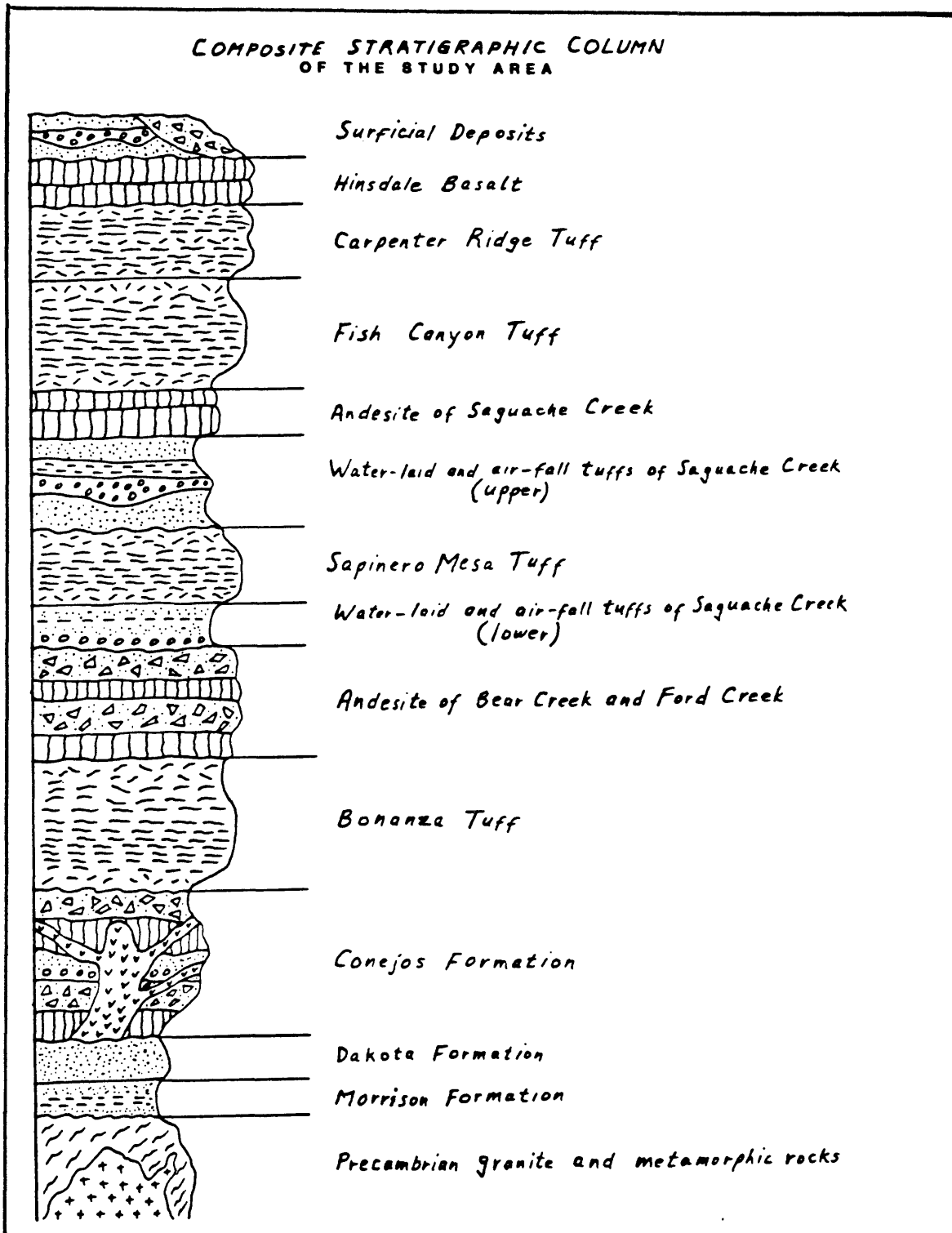


Figure 4. A composite stratigraphic column of the study area (after Knepper, 1974).

By Late Cambrian time, these rocks were intensively eroded to a smooth surface, on which sedimentary rocks of Paleozoic and Mesozoic age were unconformably deposited. These sediments comprise the Morrison Formation and the Dakota Sandstone which are preserved in synclines northwest of Alkali Springs (Figure 3). Here, the Morrison Formation is as much as 15 meters thick and composed mainly of mudstones, siltstones, and shales. The environment of deposition was determined to be both Continental and Lacustrine.

The Morrison Formation is overlain conformably by about 15-23 meters of fine- to medium-grained ferruginous orthoquartzite of the Dakota Sandstone. The variation in thickness was mainly due to differential erosion. The formation is divided into three distinct lithological units. The basal unit consists predominantly of conglomerate and sandstone, whereas the middle unit and the upper unit primarily consist of texturally variable sandstones. The environment of deposition was believed to vary from fluvial environment for the basal unit to fluvial and shallow marine environment for the middle unit. The upper unit was deposited in a variety of near-shore littoral environment.

#### Tertiary Volcanic Rocks:

Tertiary rocks within the area shown on the accompanying geology map (Figure 3) are believed to be the largest ero-

sional remnant of an originally continuous composite San Juan volcanic field, largely of Oligocene age, now fragmented by post-volcanic faulting and erosion (Steven and Epis, 1968). The sequence consists of lavas of intermediate composition and breccias, followed closely in time by ash-flow of silicic composition, and ending with a bimodal association of basalt and rhyolite. They rest with marked unconformity on the Pre-Cambrian rocks.

The Conejos Formation (Larsen and Cross, 1956) constitutes the oldest unit of the volcanic sequence, and comprises most of the "early intermediate lavas and breccias" which were said to be erupted from a number of local volcanics in the region. The age of the formation, as determined by the potassium argon method, is between 31 and 35 million years, or largely Early and Middle Oligocene (Lipman, Steven and Mehnert, 1970). In the typical locality (not shown on the map of Figure 1), a maximum thickness of 1,700 meters was reported. Bruns (1971) subdivides the formation into five distinct units based on mode of occurrence.

Subsequent depositions of tuffs and ash-flows had followed the eruption of Conejos lavas on the existing erosional surfaces.

The Rawley flows are conglomerations of units originating from different sources (Knepper, et al., 1971). These predominantly consist of heterogeneous assemblage of andesite

flows, breccias, and agglomerates. They have a variable thickness of 60-790 meters due to the pre-volcanic topography present during the time of extrusion. The earliest flows accumulate in the topographic lows, although the Rawley flow's presence on hilltops is not uncommon. Lipman, Steven and Mehnert (1970) report ages of 33 and 34 million years for the Rawley.

However, the most extensive Tertiary volcanic unit in the area is the Fish Canyon, a distinctive, moderately welded, tuffaceous ash-flow which was believed to be erupted from the LaGarita Caldera during the Early Oligocene time nearly 28 million years ago. It consists of crystal-rich quartz latite tuffs, commonly containing phenocrysts of andesite, sanidine, and biotite. Pumice lapilli, however, are also common. A maximum thickness of about 170 meters has been reported.

The youngest ash-flow sheets present in the study area are crystal-poor quartz latites with subordinate amounts of andesite, sand, and biotite as phenocrysts. These flows are collectively called Carpenter Ridge Tuff. They form extensive grass-covered dip slopes between Sheep Creek and the western edge of the area, especially above Colorado State Highway 114. A maximum thickness of about 120 meters has been reported for these flows.

The Hinsdale Formation, which is a bimodal association of rhyolites and basalts, represents the last volcanic activity in the San Juan volcanic field. Lipman, Steven and Mehnert (1970) have shown that this association ranges widely in age between 5 and 23.5 million years, and occurs in numerous isolated outcrops.

Holecene, undifferentiated, surficial deposits overlie locally the volcanic flows. They include moderate stream gravels and sands, older terrace deposits, and alluvial fans.

#### Structure of the Tertiary Rocks:

The Tertiary rocks of the area are mildly deformed by an eastward tilt, and all the units older than the Hinsdale basalt seem to have been affected by faulting and folding. The most significant block-faulting is displayed along the Sheep Creek fault zone (Figure 3). Other structural features include the north-northeast-trending Sheep Creek syncline and small compactional folds that are commonplace in the ash-flows.

### PREVIOUS GEOPHYSICAL STUDIES

Although practically all the geophysical work done in the San Luis Valley area did not include the present study area, I found it worthwhile to mention here some of the surveys that were carried out in the region and believed to be of some help in guiding this research.

Holmer (1954), in a study of the regional gravity of Colorado, concluded that the residual gravity minima associated with the San Juan volcanic field was due to the uplift of basin areas under the flows. His interpretation was supported by the geologic postulation that the undulations in the topography in the vicinity of Cochetopa Hills might be a result of inhomogeneity in the topography underlying the volcanics.

Gaca (1965) observed a low Bouguer anomaly west of the town of Sagauche. His interpretation showed a depth of about 1,200-2,400 meters to the basement in the vicinity. He also reported a gravity low near Villa Grove, northeast of Sagauche, with a minimum depth of 4,880 meters to the basement over this low.

Electrical surveys have also been carried out by Jordan (1974), Arestad (1977), and Mamah (1979), who conducted a time-domain survey near Villa Grove village and Mineral Hot

Springs. He reported apparent resistivity values of 10-30 ohm-meters near the hot springs. He was also able to ascertain the presence of graben structures south of Villa Grove and south of Mineral Hot Springs, based on criteria of transient reversals and low apparent resistivity values (Figure 5).

Other geophysical studies include seismic reflection studies by Uitti (1980), Bellatti (1981), and others.

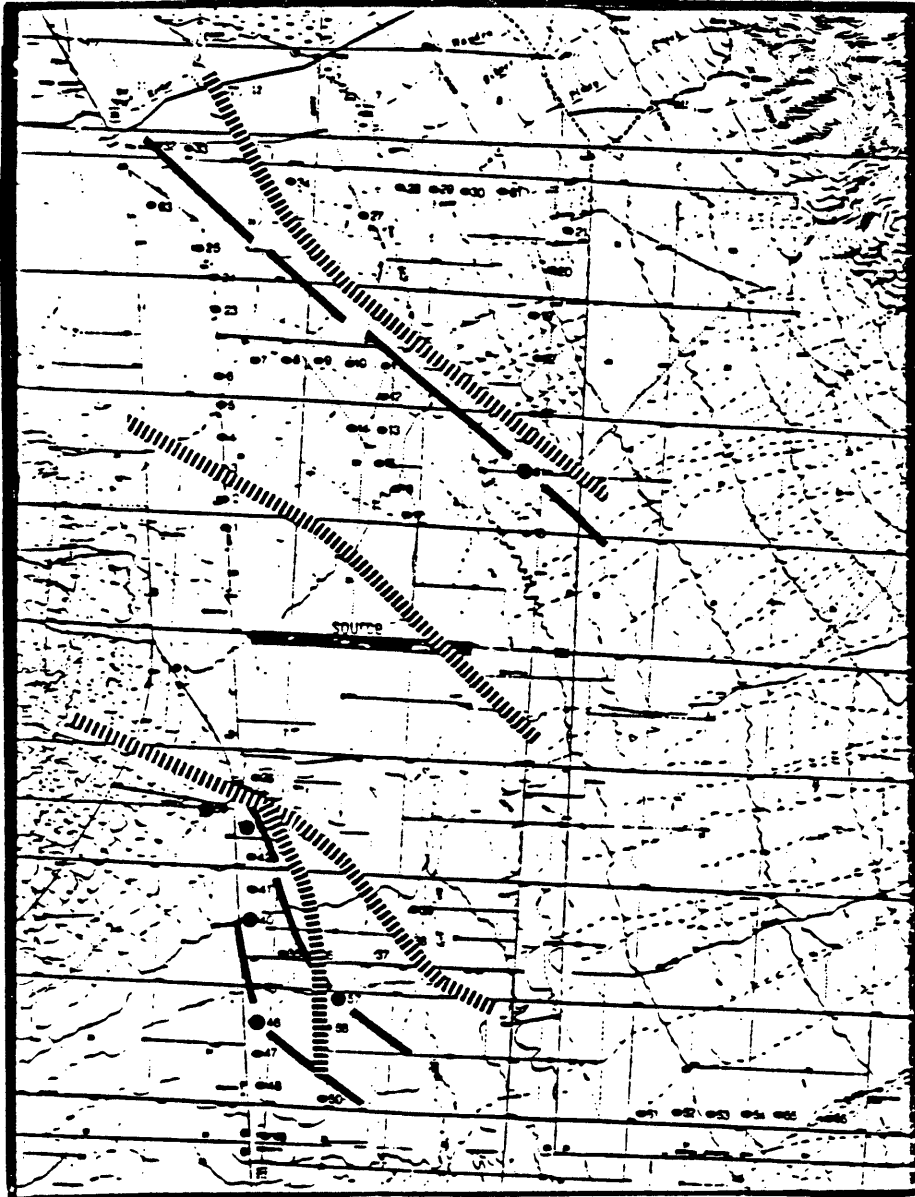


Figure 5. Structural map showing the location of faults (solid lines) mapped by Mamah (1979), near Villa Grove village and Mineral Hot Springs. The hatched lines indicate the location of the same faults as depicted from the geology (after Mamah, 1979).

### THEORY

Transient electromagnetic methods, in principle, are based on generating a time-varying magnetic field by passing a changing current through a length of grounded wire or an ungrounded coil (Mamah, 1979; Tulinus, 1980). This in turn induces electric fields and resultant eddy currents if there are nearby conductors (Mamah, 1979). The direction of the induced current flow in the subsurface is such as to produce a secondary magnetic field that decays within a relatively short time, depending on the physical properties of the medium (Bond, 1981). The decay, however, generates a transient response that can last 20 seconds or more (Stoyer, 1980).

In spite of the fact that the transient curve contains a broad band of frequencies, the response at early times contains both low and high frequency groups, while only the low frequency part of the spectrum prevails at the late times (Morrison, et al., 1969). Therefore, it is well accepted that at early times only shallow depth can be reached, while deeper zones can be reached at late times.

The theory of electromagnetic (EM) methods is based on the solution of Maxwell's equations governing the behavior of EM fields:

$$\nabla \times \bar{H} = \frac{\bar{E}}{\rho} + \epsilon\mu \frac{\partial \bar{E}}{\partial t} \quad (1)$$

$$\nabla \times \bar{E} = - \frac{\partial \bar{B}}{\partial t} \quad (2)$$

$$\text{div } \bar{B} = 0 \quad \text{or} \quad \bar{B} = \nabla \times \bar{A} \quad (3)$$

$$\text{div } \bar{E} = 0 \quad (4)$$

where:

$\bar{H}$  = the magnetic field vector (A/M),

$\bar{E}$  = the electric field vector (v/m),

$\rho$  = the resistivity (ohm-meters),

$\epsilon$  = the permittivity (F/M),

$\mu$  = the magnetic permeability,

$\bar{B}$  = the magnetic induction field vector,  
Weber/m<sup>2</sup>,

$t$  = time in seconds, and

$\bar{A}$  = vector potential.

The assumptions made to solve these equations for the layered earth problem include:

- 1)  $\mu$  is constant for the medium =  $4\pi \times 10^{-7}$  (H/M);
- 2) Displacement current  $\epsilon\mu \frac{\partial \bar{E}}{\partial t}$  is ignored;
- 3) The conductivity of the layer above the medium (air) is assumed to be zero;

- 4) Cylindrical symmetry is assumed;
- 5) The depth of penetration is inversely proportional to frequency (or proportional to time).

The frequency domain solution of the electromagnetic diffusion equation for  $B_z$ , due to a grounded wire source on a plane-layered earth, is a Hankel transform (Wait, 1962; and others):

$$B_z = \frac{-IdL\mu_0}{2\pi} \frac{\partial}{\partial y} \int_0^{\infty} \frac{\lambda}{\eta_0 + \frac{\eta_1}{R_{11}}} J_0(\lambda r) d\lambda \quad (5)$$

where the moment of a grounded wire source is the product of current,  $I$ , and length,  $dL$ ; and

$r$  = the separation between the midpoints of the transmitter and the receiver,

$\eta_0$  = a modified wave number for the upper half-space:

$$\eta_0 = \sqrt{\omega\mu_0\epsilon} \quad ,$$

$\eta_1$  = a modified wave number for the first layer in the lower half-space:

$$\eta_1 = \sqrt{j\omega\mu_0\sigma_1} \quad ,$$

where:

$\omega$  = the angular frequency,

$\sigma_1$  = the conductivity of the first layer in the lower half-space (mohs per meter),

$\lambda$  = the transform variable in the Hankel integral;  
it has the units of inverse distance,

$R_{11}$  = Kernel function represents the effects of the layers beyond the first in the lower half-space, and can be presented in a recursive form as follows (Wait, 1962; Keller, et al., 1982; and others):

$$R_{11} = \frac{1 - ke^{-2n_1h_1}}{1 + ke^{-2n_1h_1}} \quad (5a)$$

$$k = \frac{n_2 - n_1Q}{n_2 + n_1Q} \quad (5b)$$

$$Q = \frac{1 - ke^{-2n_2h_2}}{1 + ke^{-2n_2h_2}} \quad (5c)$$

.  
.  
.  
.

$$Q = \frac{1 - ke^{-2n_{N-1}h_{N-1}}}{1 + ke^{-2n_{N-1}h_{N-1}}} \quad (5d)$$

$$k = \frac{n_N - n_{N-1}}{n_N + n_{N-1}} \quad (5e)$$

where:

$h_i$  = the thickness of each layer,

$N$  = the total number of layers,

$n$  = the number of layers counted down from the surface.

The kernel function ( $R_{11}$ ) of equation (5a) becomes unity for a uniform half-space, and so an expression for the field behavior over a uniform earth in the frequency domain (Wait, 1961; Vanyan, 1967; Keller, 1968) can be obtained from equation (5):

$$B_Z(\omega) = \frac{IdL}{2\pi\sigma} \frac{1}{r^4} [3 - e^{-\gamma r} \{(3 + 3\gamma r + \gamma r^2)^2\}] \quad (5f)$$

where:

$$\gamma = (j \mu \sigma \omega)^{\frac{1}{2}} \text{ is the propagation constant.}$$

The expression for the induction field ( $B_Z$ ), due to an impulse function current excitation, can be obtained in the time-domain by performing the inverse cosine Fourier transform of the real part, on the above expression. The result is:

$$B_Z(t) = \frac{2}{\pi} \int_0^{\infty} \text{Re } B_Z(\omega) \cos \omega t \, d\omega. \quad (6)$$

In actual field operation, a step current excitation is normally used, and a measurement of  $\frac{\partial B_Z}{\partial t}$  is obtained at the receiver site. This situation is mathematically equivalent to measuring  $B_Z$  at the receiver due to an impulse input, since the latter is derived from a step by differentiation.

The induced voltage at the receiver is given by:

$$V(t) = -A \frac{\partial \bar{B}}{\partial t} \quad (7)$$

where A is the effective area of the receiver (actual area x number of turns). Making the appropriate substitutions, an expression for the total voltage (Wait, 1951) can be derived:

$$V(t) = \frac{3 A I y \rho}{2 \pi r^5} \left[ \operatorname{erf}(u) \frac{-2}{\sqrt{\pi}} (u + 2/3 u^3) e^{-u^2} \right], \quad (8)$$

where:

$$u = \left( \frac{\mu_0 r^2}{4 \rho t} \right)^{\frac{1}{2}}$$

$$\operatorname{erf}(u) = \frac{2}{\sqrt{\pi}} \int_0^u e^{-t^2} dt \quad \text{is the error function.}$$

The above expression is limited to cases where the earth is homogeneous. If the earth does not change laterally, then numerical techniques should be sought to evaluate the Hankel integral of equation (5). Anderson (1979) developed an inexpensive and rapid convolution algorithm to evaluate the Hankel transform integrals of orders 0 and 1, using the adaptive digital filtering technique. The algorithm avoids the evaluation of Bessel's functions, which is required with numerical integration techniques. The adaptive feature allows general use of the filters for a large class

of kernels. The accuracy of these filters compares very well with those of numerical quadrature methods for well-behaved kernels. It is perfectly adequate for matching any transients which can be recorded from the earth's surface.

A set of transient apparent resistivities vs. time for a wire-loop system, using step function excitation for a uniform earth, is shown in Figure 6.

The curves were calculated for a range of resistivities (between 1.0 and 50.0 ohm-meters) and an arbitrary offset of 5.0 kilometers. These curves show a rollover time which separates the early-time behavior from the late-time behavior (Kaufman and Keller, 1981, 1982). The position of this rollover time is a function of the conductivity of the medium. It occurs later in time over a conductive earth, and the resulting transient magnetic field has a lower amplitude. This behavior is reversed when a resistive medium is encountered.

The influence of the separation between the source and the receiver is illustrated in the curves of Figure 7. They show an increase in the position of the rollover with increasing source-receiver distance ( $r$ ).

An expression for this rollover time is given by:

$$t = 0.15 \mu_0 \sigma r^2. \quad (9)$$

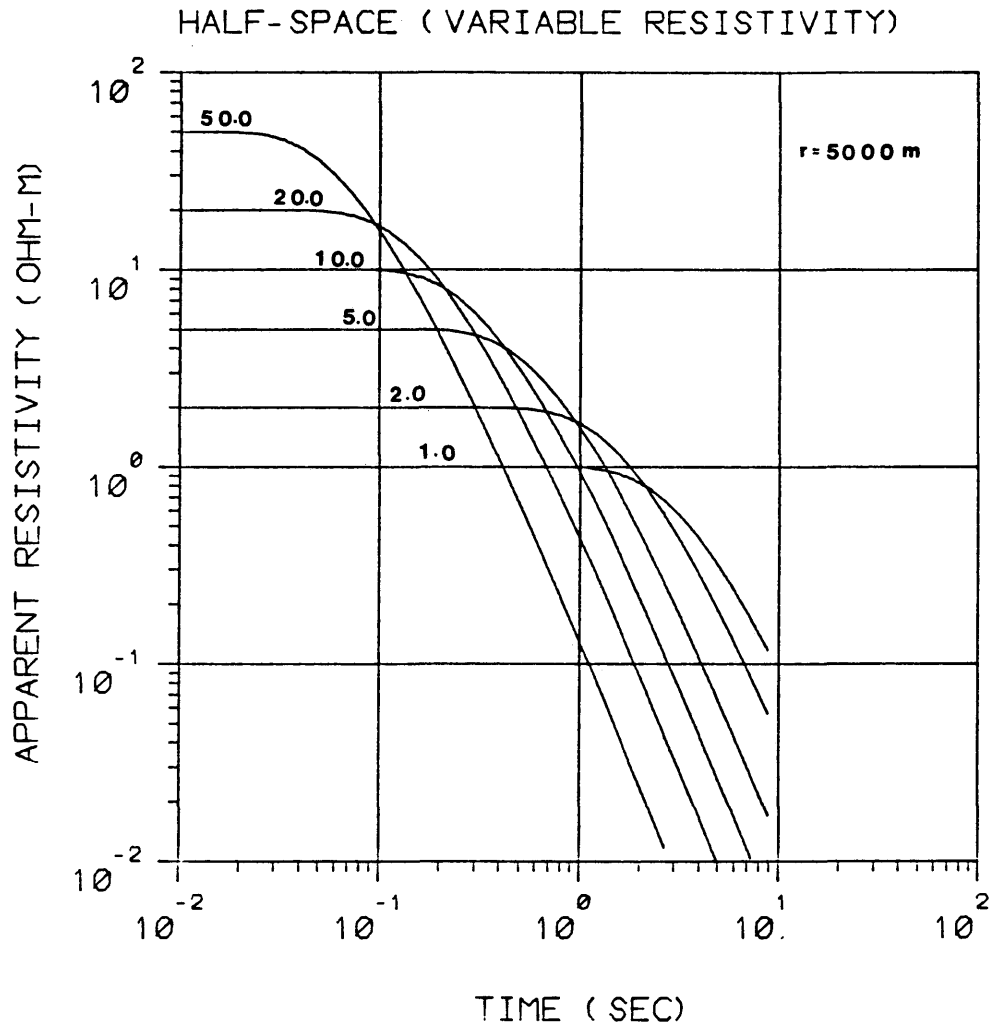


Figure 6. Set of apparent resistivity-time curves for TDEM coupling between grounded wire and vertical-axis loop, for a uniform earth, variable resistivity.

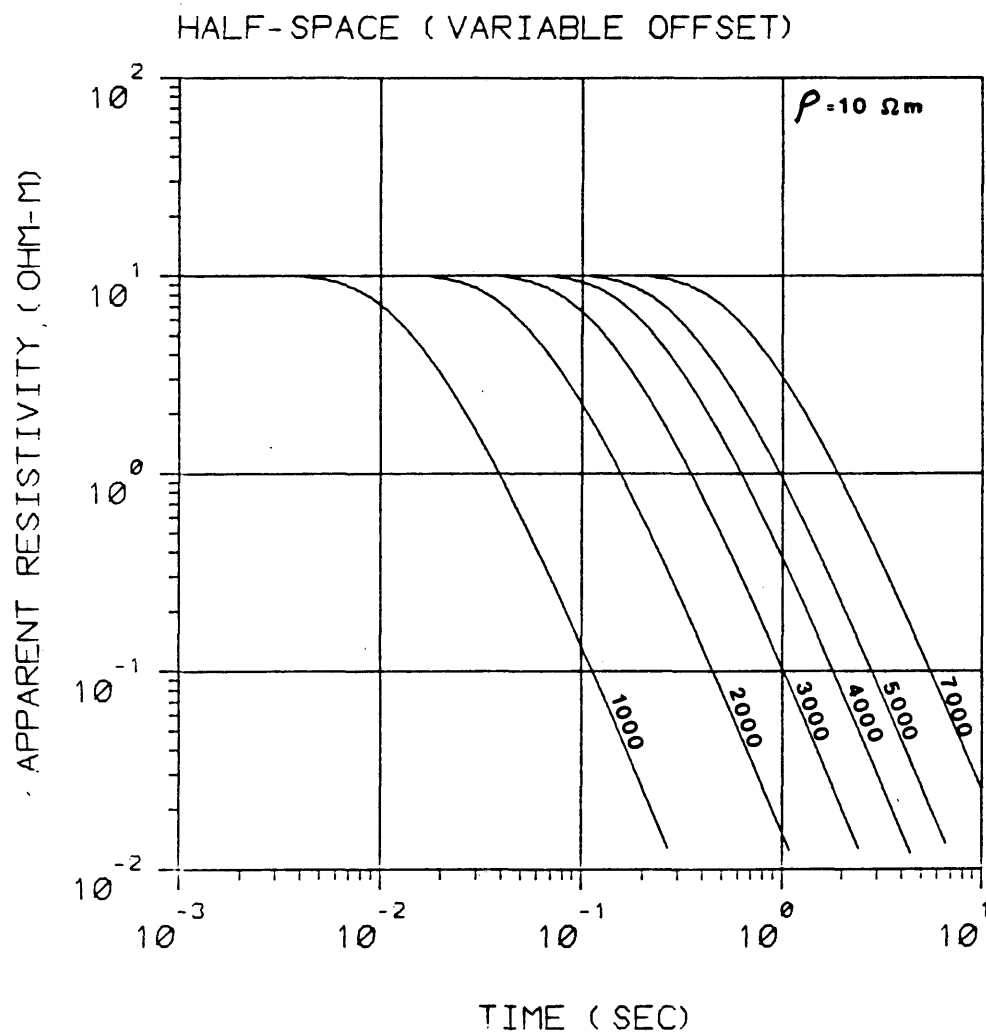


Figure 7. Set of apparent resistivity-time curves for TDEM sounding over a uniform earth using a wire-loop geometry, variable offset.

Expressions for Apparent Resistivity:

The early-time asymptote can be derived from equation (8) by letting  $t$  approach zero. Inversion of this very early-time expression will give the equation of apparent resistivity at early time:

$$\rho_a = \frac{2\pi r^5 V(t)}{3 M A y} \quad (\text{early}) \quad (10)$$

where:

$\rho_a$  = early-time apparent resistivity,

$V(t)$  = recorded voltage,

$M$  = source moment (length x current), directed along the x-axis,

$y$  = the y-component of  $r$  (source receiver distance); see Figure 8.

The above expression is valid when:

$$\tau/r = 2\pi\sqrt{2t/\mu\sigma r^2} < 2,$$

where  $\tau$  is the normalized time. In the early time, the transient voltage is directly dependent on the resistivity.

Similarly, an expression for apparent resistivity at late time can be obtained by inverting the expression for the late-time (by letting  $t$  approach infinity) asymptote:

$$\rho_a = \left[ \frac{AIL y}{40\pi^{3/2} t^5 V(t)} \right]^{2/3} \quad (\text{late}). \quad (11)$$

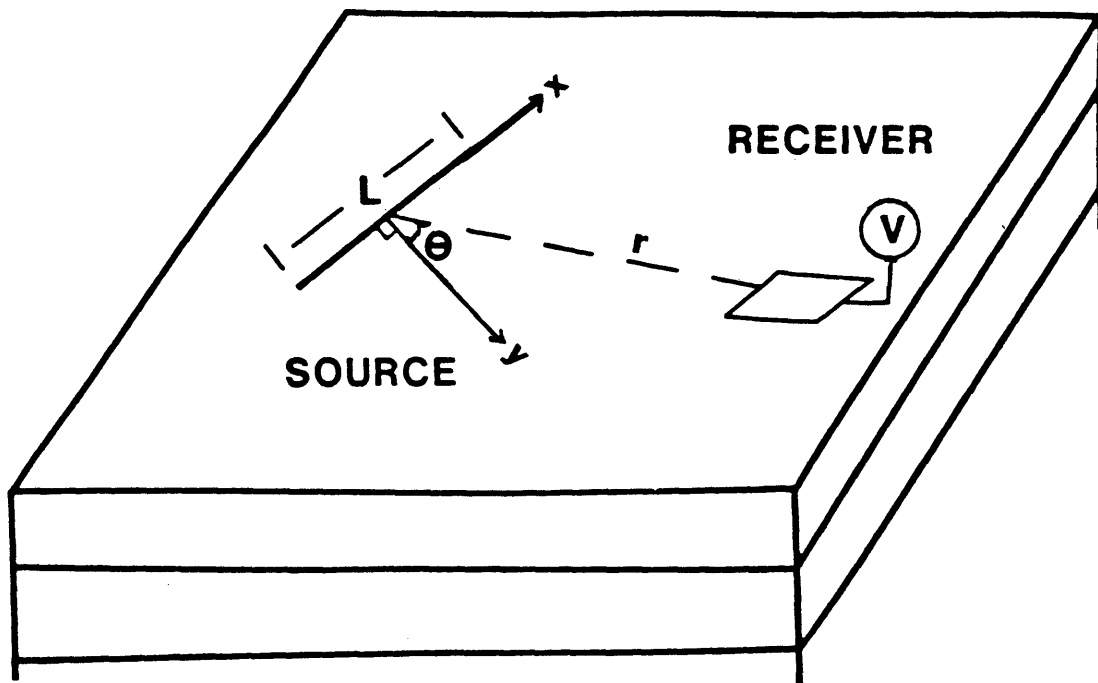


Figure 8. Line-source, loop receiver configuration (after Bond, 1981).

The late stage can only be reached when  $\tau/R > 12$ . Unlike the case of early time, where the recorded voltage rises to a certain value and remains constant, the late stage voltage decays logarithmically with a slope that equals the inverse of the time constant. For these reasons, transients over resistive earth maintain high amplitudes and live for short times, whereas those recorded over conductive media decay slowly with lower amplitudes. At late time, the received voltage is proportional to the conductivity to the 3/2 power.

Figure 9 is a bilogarithmic plot of apparent resistivity curves as calculated from the early- and late-time asymptotes. The curves show, in addition to early- and late-time apparent resistivities, an intermediate stage in which neither of the formulas for early- and late-time apparent resistivities holds (Figure 10).

#### All-Time Apparent Resistivity:

The all-time apparent resistivity is a technique in which the point of closest approach between the early- and late-time asymptotes is used to define half-space curves (Stoyer, 1982, personal communication).

The all-time apparent resistivity is defined as:

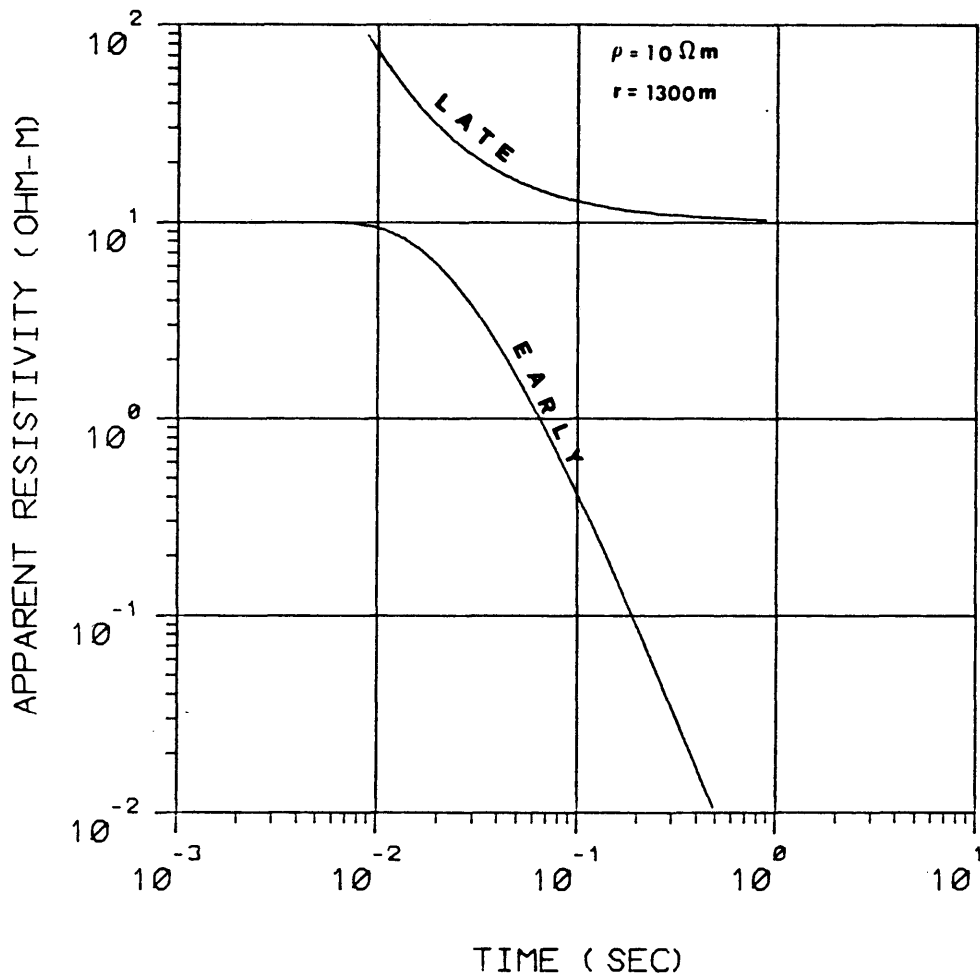


Figure 9. Apparent resistivity-time curve showing the early- and late-time asymptotes for a uniform half-space.

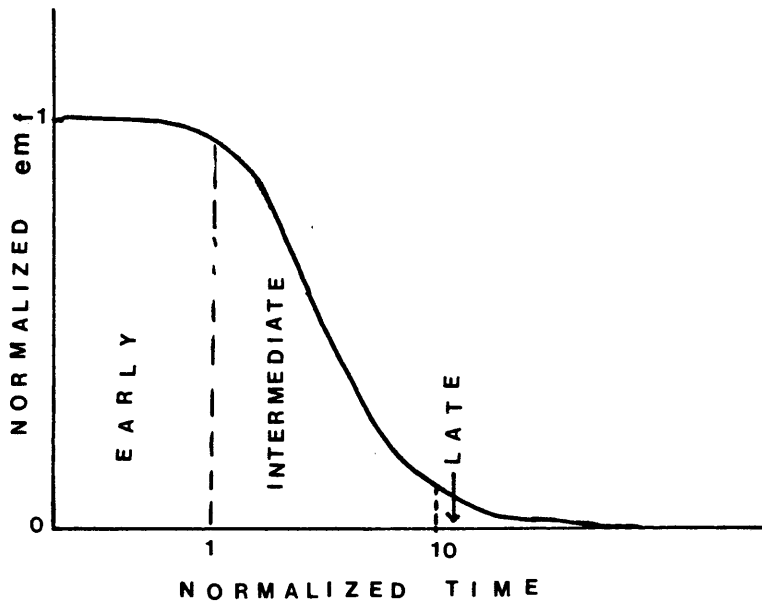


Figure 10. A curve of normalized emf vs. normalized time with the early, intermediate and late stages indicated. The model shows a resistive medium overlying a conductive medium, (after Bond, 1981).

$$\rho_a = \frac{\rho_H f(V_F)}{f(V_{HS})} \Big|_{\rho = \rho_H} \quad (12)$$

where:

$\rho_a$  = all-time apparent resistivity,

$V_F$  = the voltage observed on the surface of a horizontally stratified medium,

$V_{HS}$  = the voltage that would have been measured at the same instant,  $t$ , on the surface of a uniform half-space with resistivity  $\rho_H$ ,

$f(V_f)$  = an interpolation function between early- and late-time asymptotic values of  $\rho_a$ .

From the time of closest approach ( $t_c$ ), the half-space resistivity ( $\rho_H$ ) can be determined, and hence an expression for all-time apparent resistivity as a function of early and late times can be obtained:

$$\rho_a = \rho_H \frac{F(\rho_{a,E}, \rho_{a,L})}{F(\rho_{a,E}, \rho_{a,L})} \Big|_{\rho = \rho_H} \quad (13)$$

where:

$\rho_H$  = half-space resistivity,

$\rho_{a,E}$  = early-time apparent resistivity,

$\rho_{a,L}$  = late-time apparent resistivity.

The function  $F$  can be defined as:

$$F(\rho_{a,E}, \rho_{a,L}) = \rho_{a,E} \cdot \frac{t^2}{t^2 + t_c^2} + \rho_{a,L} \frac{t_c^2}{t^2 + t_c^2} \quad (14)$$

where  $t_c$  is the time of close approach.

During the very early part of the transient coupling the apparent resistivity approaches that of the first layer, while at the late stage it approaches the resistivity of the basement.

An expression for half-space response can be obtained by substituting equation (14) into equation (13). This response becomes a straight line in the logarithmic domain.

#### Calibration Factor:

The amplitude of the transient signal is distorted by lateral inhomogeneities and errors in field parameters such as area of the receiving loop, source current, and source length. These errors can be removed by a calibration procedure which yields amplitudes free of magnetometric resistivity (MMR) effects. These amplitudes can only then be inverted to horizontal layered earth, which has no MMR anomaly (Edwards, et al., 1978).

The following discussion presents a procedure to determine the calibration factor. The induction field,  $B(\omega)$ , for a grounded wire in the presence of plane homogeneous earth, is given by:

$$B(\omega) \Big|_{\omega \rightarrow 0} = \frac{\mu A I dx \cos \theta}{4\pi r^2} . \quad (15)$$

From the above expression, it is noted that over plane earth the magnetic induction is independent of the conductivity of the earth, and only depends on the source receiver separation. This relationship is equivalently true for a loop source, which has no MMR effects.

Apparent resistivity can be given by:

$$\rho_a(\omega) \Big|_{\omega \rightarrow 0} = \frac{2\pi r^4}{3 A I dx \cos \theta} \cdot B(\omega)$$

or

$$\rho_a(\omega) \Big|_{\omega \rightarrow 0} = \frac{2\pi r^4}{3 A I dx \cos \theta} \cdot \frac{\mu A I dx \cos \theta}{4\pi r^2} = \frac{\mu r^2}{6}. \quad (16)$$

The calculation of apparent resistivity completely removes the distortions in the amplitude of the signal caused by the field parameters.

Equation (16) is related to time-domain through the inverse Fourier transform:

$$\rho_a(\omega) \Big|_{\omega=0} = \int_0^{\infty} \rho_{aE}(t) e^{-j\omega t} dt \Big|_{\omega \rightarrow 0} = \int_0^{\infty} \rho_{aE}(t) dt$$

or

$$\int_0^{\infty} \rho_{aE}(t) dt = \frac{\mu r^2}{6}. \quad (17)$$

If the two sides of equation (17) are not equal, then the difference determines the amplitude of the calibration factor.

### THE SURVEY

In the survey which was conducted during the summer of 1981, the time-domain electromagnetic method was chosen over other electrical methods because of its ability to penetrate to greater depths. The method demonstrates a superiority over the frequency-domain method, because the signal is sampled in the absence of the primary field.

A time-varying magnetic field was generated by introducing an electric current through a grounded length of wire. Electrodes were used at the ends of the wire to maintain the proper contact with the ground. The source was continuously pulsed with a 20-60 amperes peak-to-peak current in the form of a square wave obtained by suddenly reversing the direction in which the current was flowing in the source.

Four sources were used in the survey to provide signals for all the stations in the study area. They ranged in length from 200 meters to 1,400 meters. Soundings were made at numerous locations, some distance from the source. The range was largely dependent upon the source strength and the average resistivity of the earth.

Current Source (Figure 11):

The sources were energized with three-phase, 60-cycle currents provided by a 27KVA maximum capacity gasoline ONAN generator. A three-phase transformer was used to step up the 220-volt output to 440VAC. Direct current output (square wave) was obtained by means of two sets of six-diode rectifiers. Each set was responsible for directing the current flow in one direction. Reversal of the current direction was accomplished by mechanical switches at approximately ten-second intervals.

Receiver (Figure 12):

A vertical-axis induction loop was used to measure the time rate of change of the magnetic field ( $\frac{\partial H}{\partial t}$ ) at each receiver site. About 300 meter-length of 26 conductors was laid in the form of a square on a reasonably flat ground. The effective area of such a coil was about 150,000 square meters. The voltage output generated in the loop was low level. In order to enhance the signal from the loop, pre-amplifiers with gains of several thousand were used. The signal would then be filtered, recorded on a MINC-11 mini-computer, and finally stored on a floppy disc. Examples of typical transient waveforms recorded in the field are shown

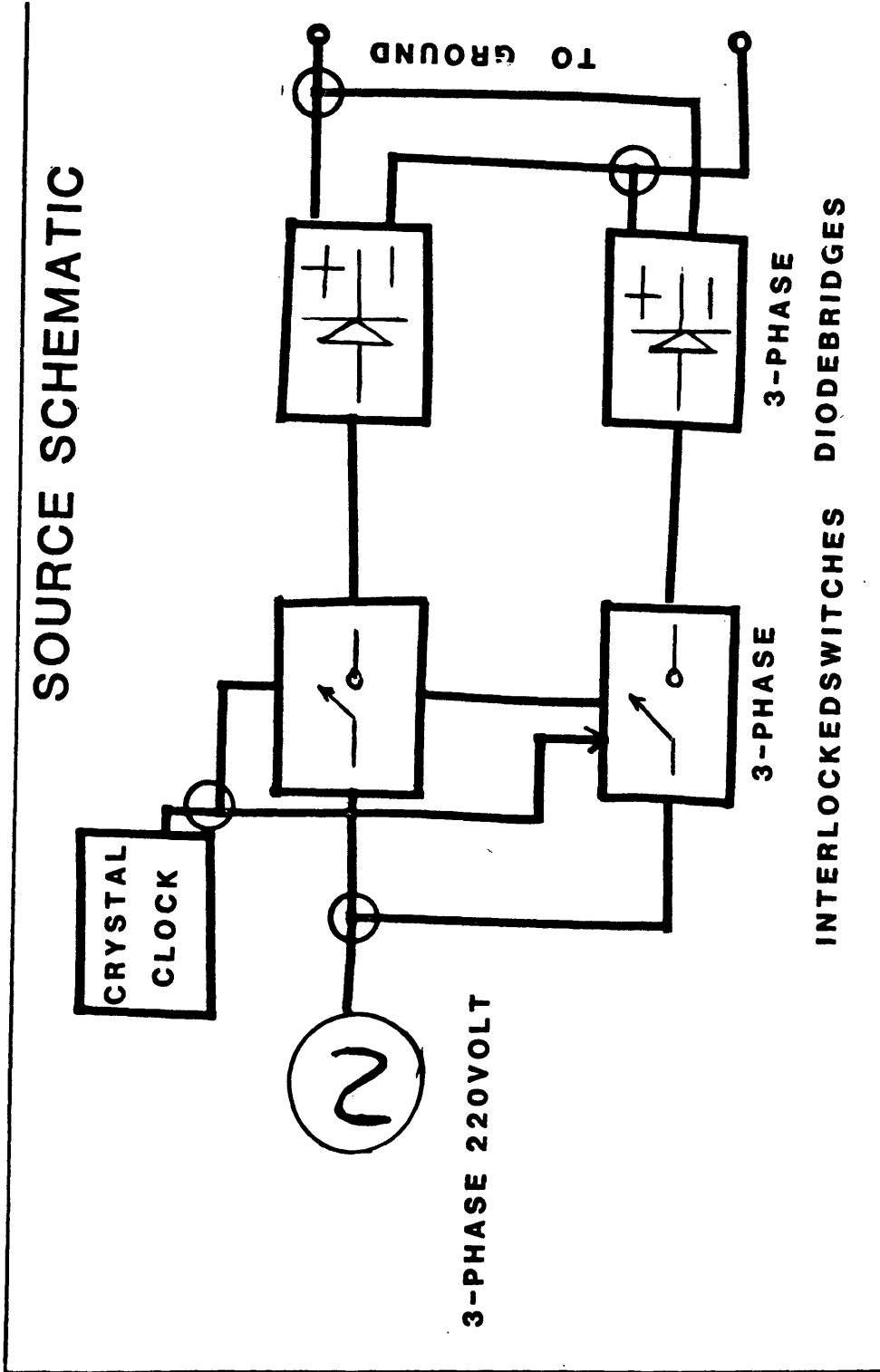


Figure 11. Schematic diagram for the source used in the survey (after Ibrahim and Stoyer, 1981).

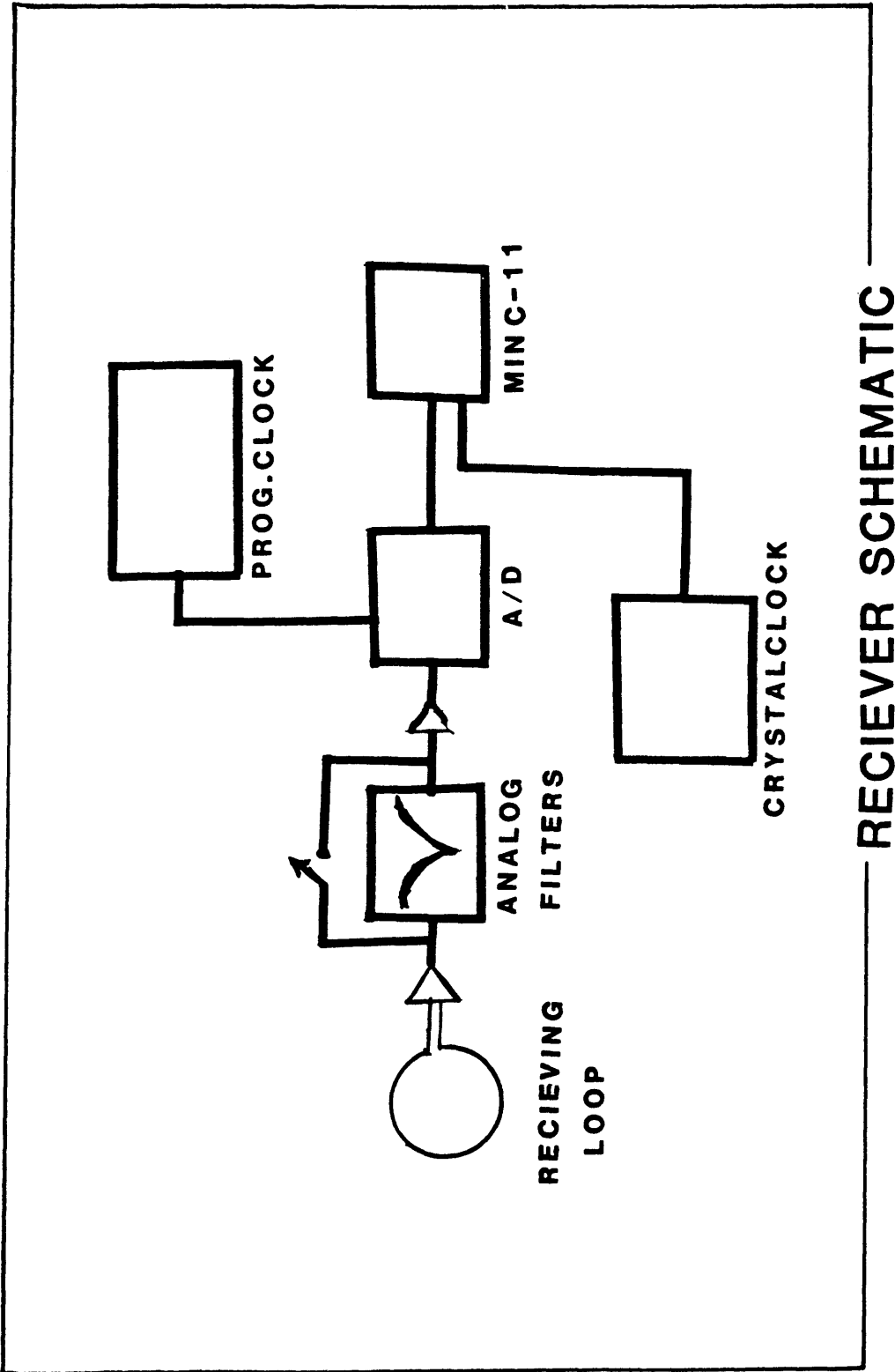


Figure 12. Schematic diagram for the receiver used in the survey (after Ibrahim and Stoyer, 1981).

in Figures 13, 14, 15, and 16.

At an offset distance of 1-8 km from the source, 91 receiver sites were visited. Transients from 89 stations were obtained. Figure 17 is a location map showing the stations layout. While some of the stations were visited more than once before good quality data were collected, Stations 59 and 60 were unsuccessfully visited. The location of the stations within the study area was largely governed by the accessibility of roads. However, separation of half-a-mile between stations proved adequate for this survey.

#### Data Processing:

The observed voltage was subjected to extensive data reduction prior to interpretation. The first stage in the reduction of the field data consisted of the following steps:

- 1) Digitizing and stacking of transients at each station;
- 2) Deconvolution to minimize the distortions introduced by the recording equipment;

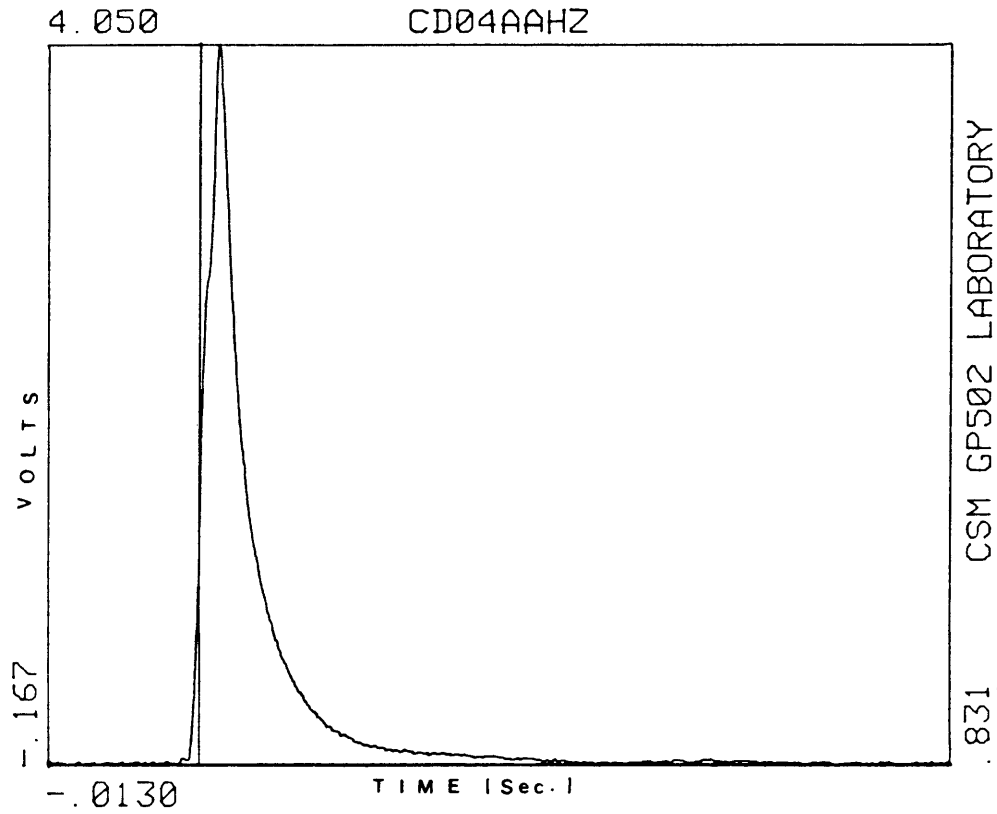


Figure 13. Raw stacked transient recorded at Station 4, using Source A, showing the general amplitude and shape of a transient curve. This transient was recorded close to the source, hence it has a low noise level.

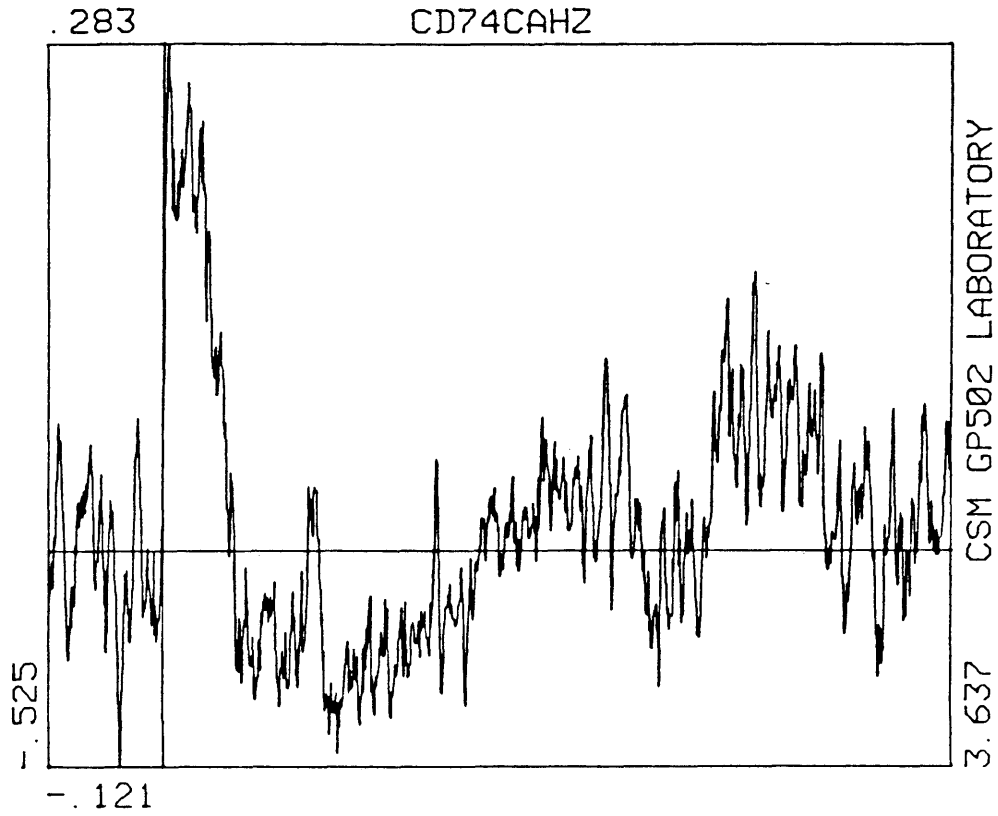


Figure 14. Raw stacked transient from Station 74, using Source C, showing a very high level of noise.

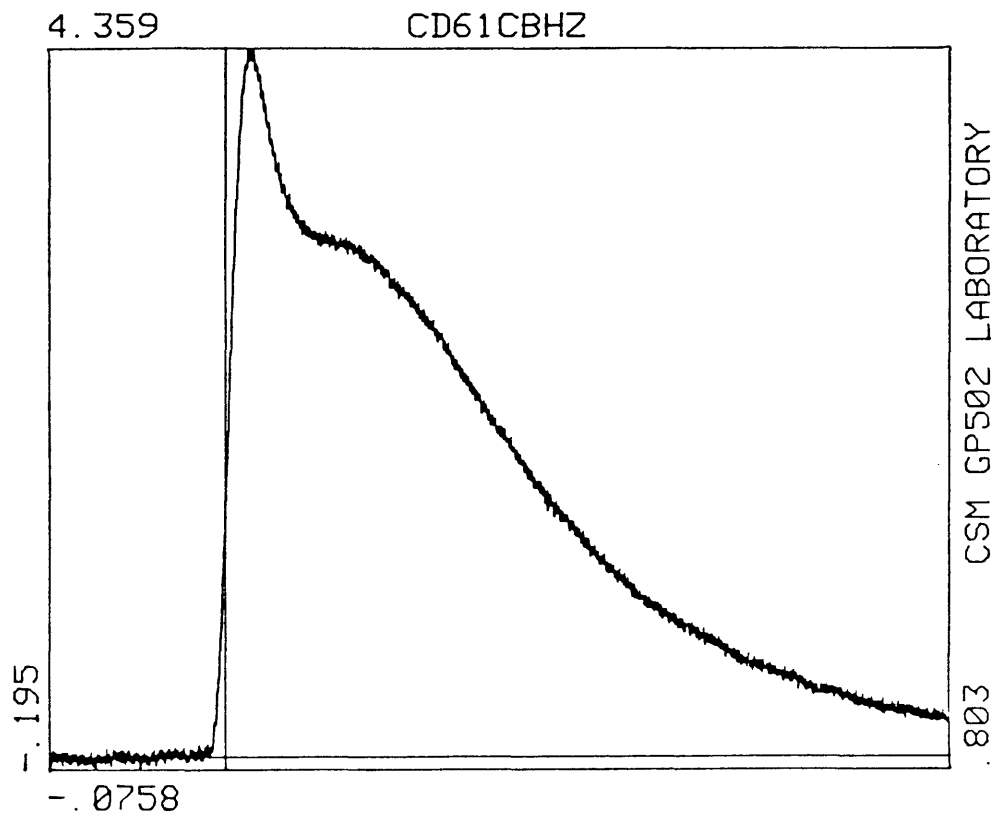


Figure 15. A raw stacked transient recorded at station 61, using source C, showing a resistive medium over a conductive one.

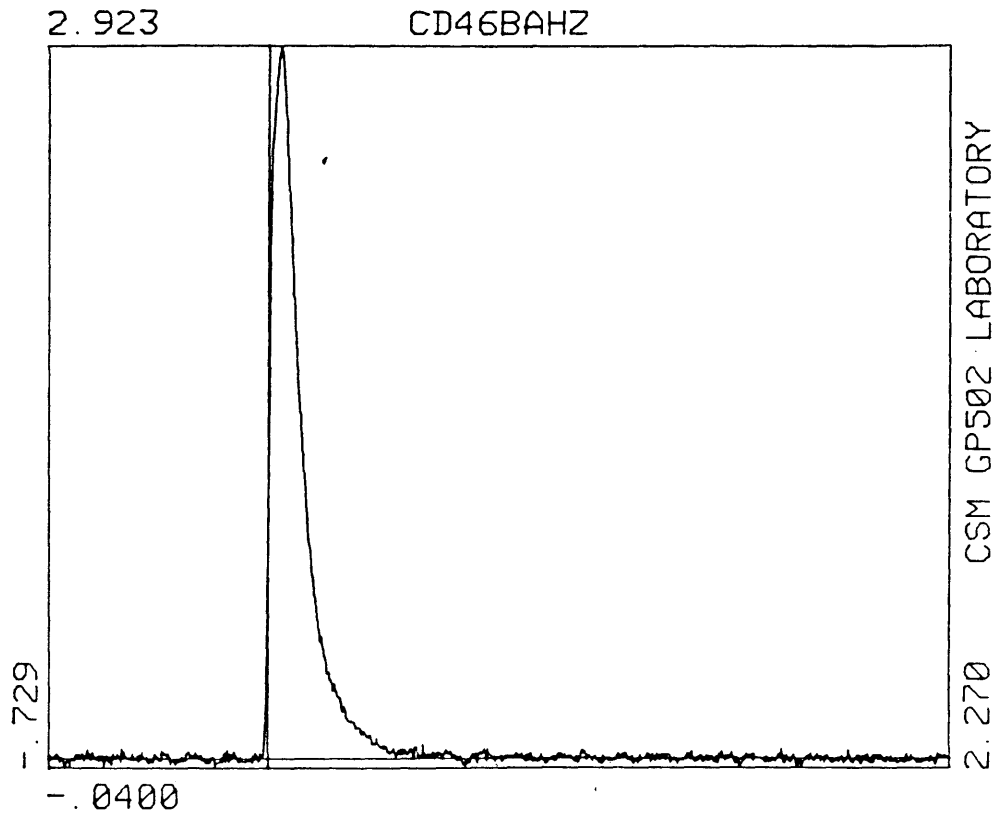


Figure 16. Raw stacked transient recorded at Station 46, using Source B, showing a very clean signal.

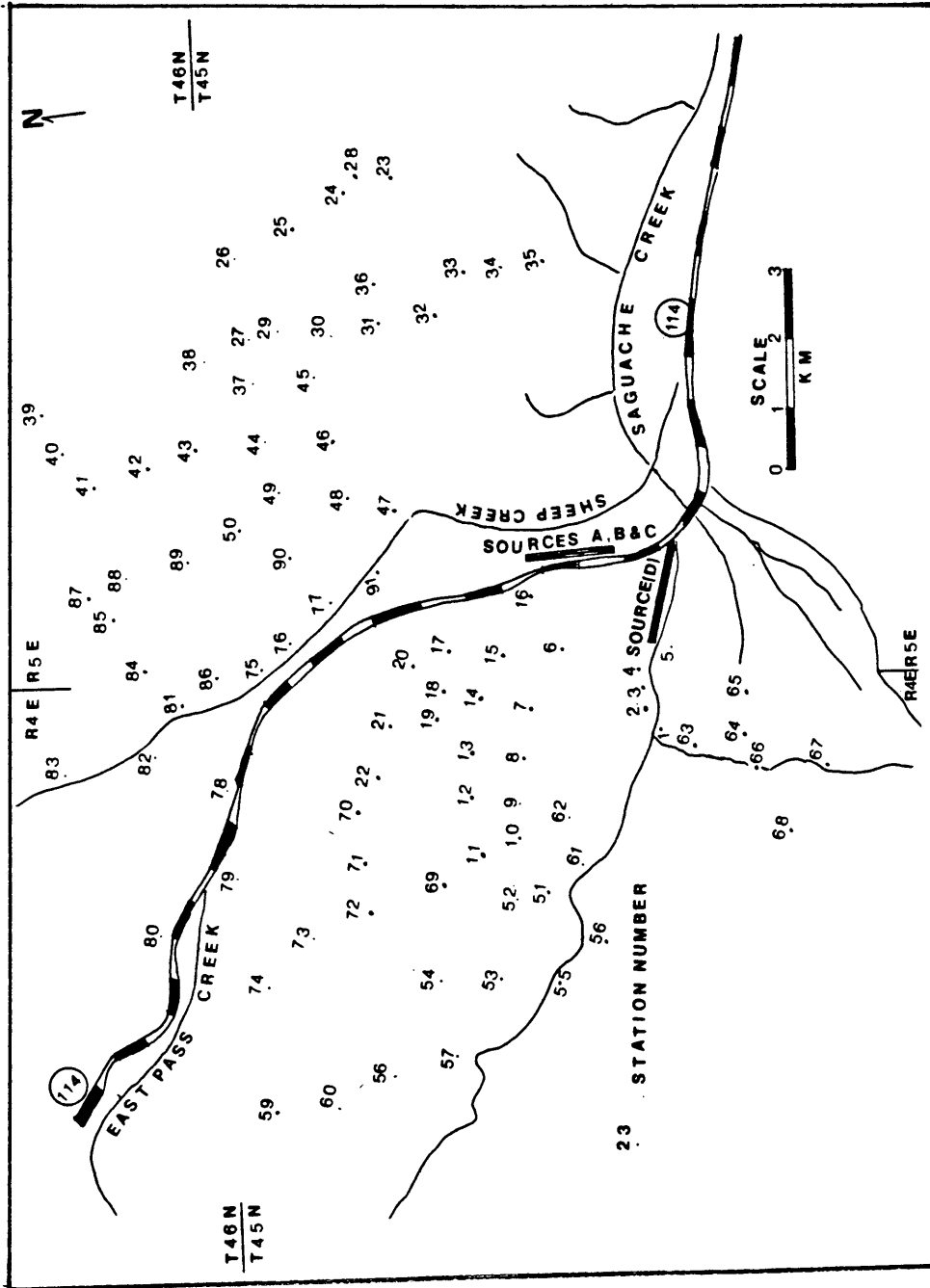


Figure 17. Source-receiver layout used in the survey. Sources A, B and C are practically equivalent in length (1,300 m). Source D is the longest (1,400 m). Numbers indicate the station locations.

- 3) Smoothing with an exponentially time-varying filter to reduce high frequency noise in the late times;
- 4) Conversion of measured voltages to early- and late-time apparent resistivities for comparison with theoretical models.

The signal received from a single transmission was digitized at a rate of one sample every few milliseconds. The first few transients were displayed on an oscilloscope to select and stack the good quality ones. A coherence test was then performed to reject the distorted transients and add the good ones to the cumulative stack. About 32-64 stacks were recorded at each receiver location. The primary purpose of stacking, however, was to improve the signal-to-noise ratio by a factor of  $(N-1)^{\frac{1}{2}}$  for a large number,  $N$ , of signals.

The system response poses a serious problem in the time-domain surveys, because the transient curves are used directly in the interpretation. Changes in the shape of the transient curve, due to the distortions introduced by the filters, should be accounted for. For this reason, it is appropriate to remove the distortions introduced by the system via deconvolution.

A new deconvolution approach in time-domain was used to remove the system response (Stoyer, 1981, personal communication). The recorded signal was the convolution of the input current with the earth and system responses, i.e.:

$$r(t) = s(t) * v(t)$$

where:

$r(t)$  = recorded signal;

$s(t)$  = system response;

$v(t)$  = earth response.

Basically, the following steps were carried out to obtain the earth response:

- 1) The system response was cross-correlated with the recorded signal in order to remove the effect of the phase angle response. The resulting deconvolved function was then a zero phase.
- 2) The amplitude distortions at the early part of the signal were alleviated by convolving the system response  $s(t)$  with the earth response, assuming that the earth response and the output function of step 1 were equal. The outputs from

step 1 and step 2 were then compared in order to obtain the earth response. If the comparison was good enough, then  $v(t)$  should be the earth response; otherwise, a correction should be added to  $v(t)$  to bring it closer to the earth response.

The variation of signal-to-noise ratio at early and late times provides a basis for separating the signal from the noise during the late part of the signal, without affecting the deconvolution on the early part. This is accomplished by applying a linear smoothing filter in the logarithmic domain.

Finally, the measured voltages were converted into early- and late-time apparent resistivities as calculated from equations (10) and (11). Figure 18 is a bilogarithmic plot of the early- and late-time apparent resistivities with time. The early time occurs as late as  $t = 15$  msec, while the late time happens as early as  $t = 550$  msec. The distortions of the curve at the early time are mainly ascribed to the untimely receiving of the signal, caused by the drifting in the clocks. The curve also exhibits reversal at the late time, which could be attributed to low-level noise which eventually becomes greater than the transient signal as we progress to later times.

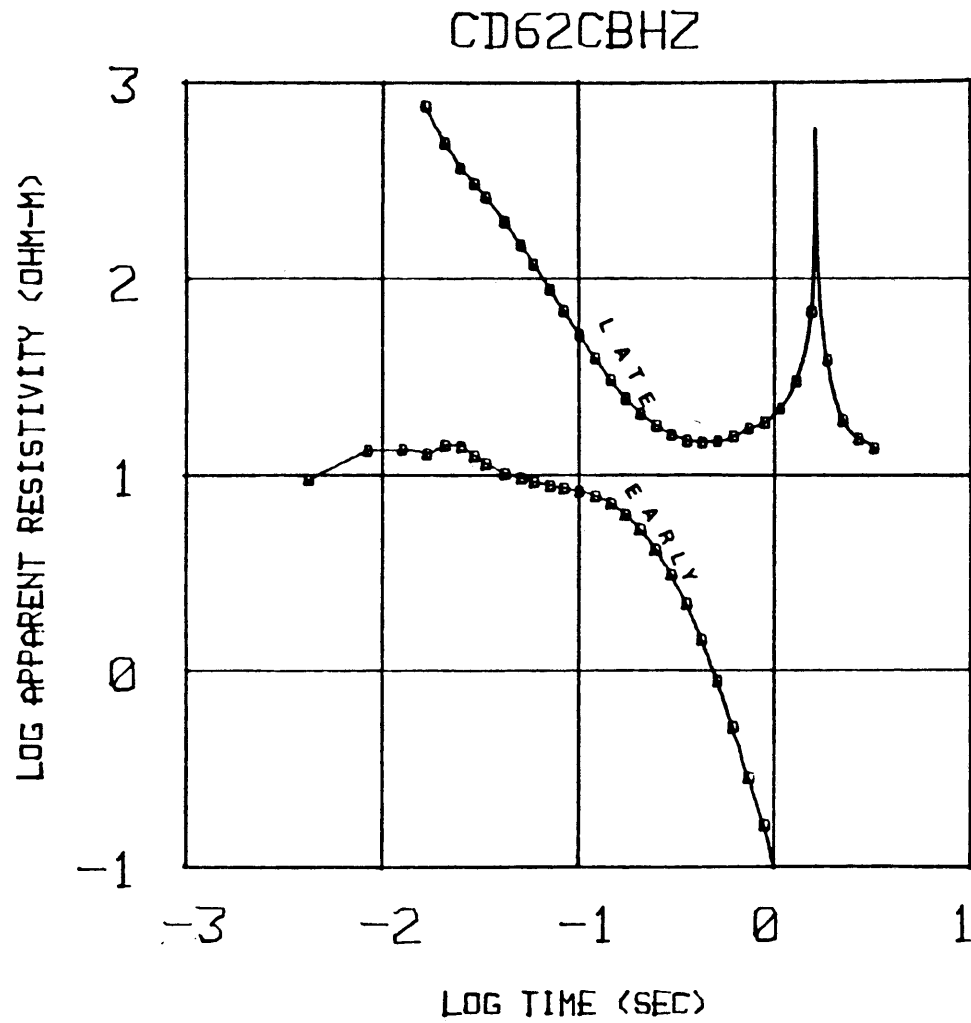


Figure 18. Apparent resistivity-time curve for Station 62 showing early and late time asymptotes.

## INTERPRETATION OF RESULTS

### General:

The interpretation of transient electromagnetic sounding data over stratified earth is sometimes complicated by the principle of equivalence. The essential feature of equivalence is that for certain relationships among the layers parameters of two different sequences, the sounding curves cannot be differentiated in a practical sense (Patra and Mallick, 1980). Measures to resolve this problem will not be discussed in this thesis.

Interpretation of time-domain electromagnetic data is achieved either by curve-matching or the inverse technique.

Theoretical curves can be computed for a horizontally uniform earth composed of a sequence of layers (Silva, 1969; Vanyan (1967); Anderson (1979)). Earth models composed of three and four layers, however, are adequate for practical purposes. A set of early-time theoretical curves for a two-layer earth model in which the surface layer is more conductive than the subsurface is shown in Figure 19. Another situation where the converse is true is shown in Figure 20. A remarkable difference between the two families of curves is the presence of a maximum in the family of the first set.

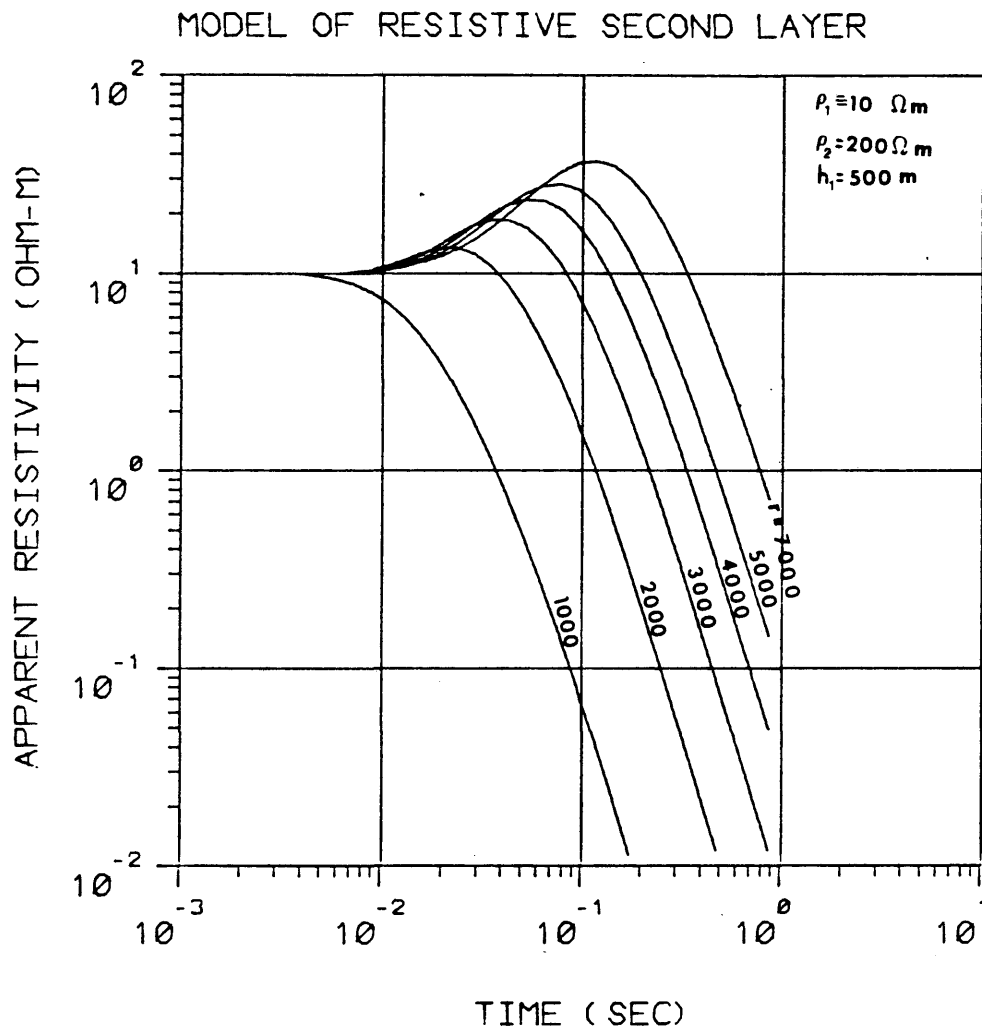


Figure 19. TDEM curves for a sequence of layers in which the second layer is more resistive than the first. The parameter on each curve is the separation between source and receiver in meters

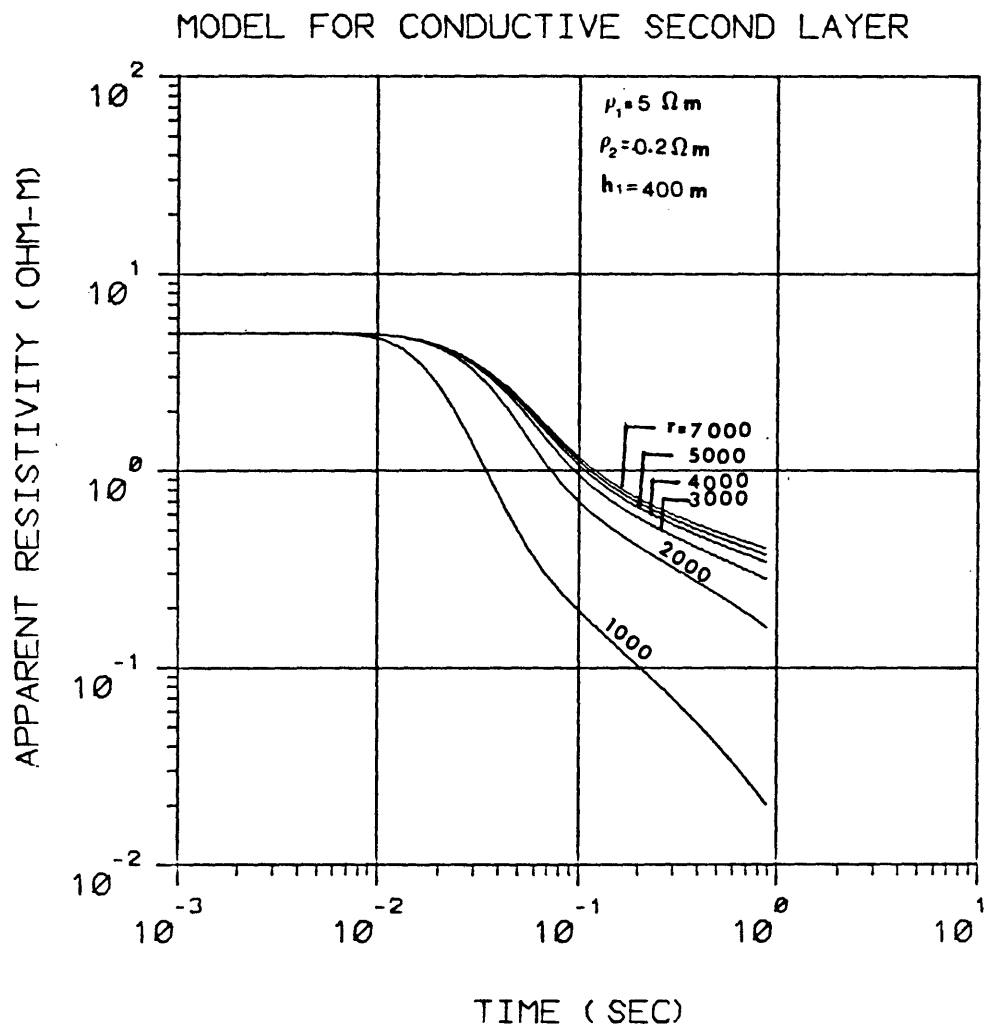


Figure 20. TDEM curves for a sequence of layers in which the second layer is more conductive than the first. The parameter on the curves is the separation between the source and receiver in meters.

Kaufman (1972) has explained this for the case of a conductive second layer, as due to the high intensity current associated with the early time, the result of which is a high intensity induced magnetic field. He also explained that at late time the behavior is a function of conductivity.

Qualitative Interpretation:

The voltage transient curves from the study area exhibit a wide range of characteristics. Figure 21 is a superposition of two transients recorded at Station 51. The first part corresponds to a resistive near-surface ground, whereas the second portion reflects the behavior over a conductive, relatively deeper structure. The total time window is 3.33 seconds. From the shape of the transient response, it is evident that responses over resistive media are usually of high amplitude and short life, while they decay very slowly with low amplitude over conductive media.

Maximum Voltage Apparent Resistivity (MVAR) Method:

Maximum voltage apparent resistivity (MVAR) maps can be constructed to determine the distribution of the subsurface resistivities. The MVAR approaches the resistivity of the first layer, when the substratum is more conductive, due

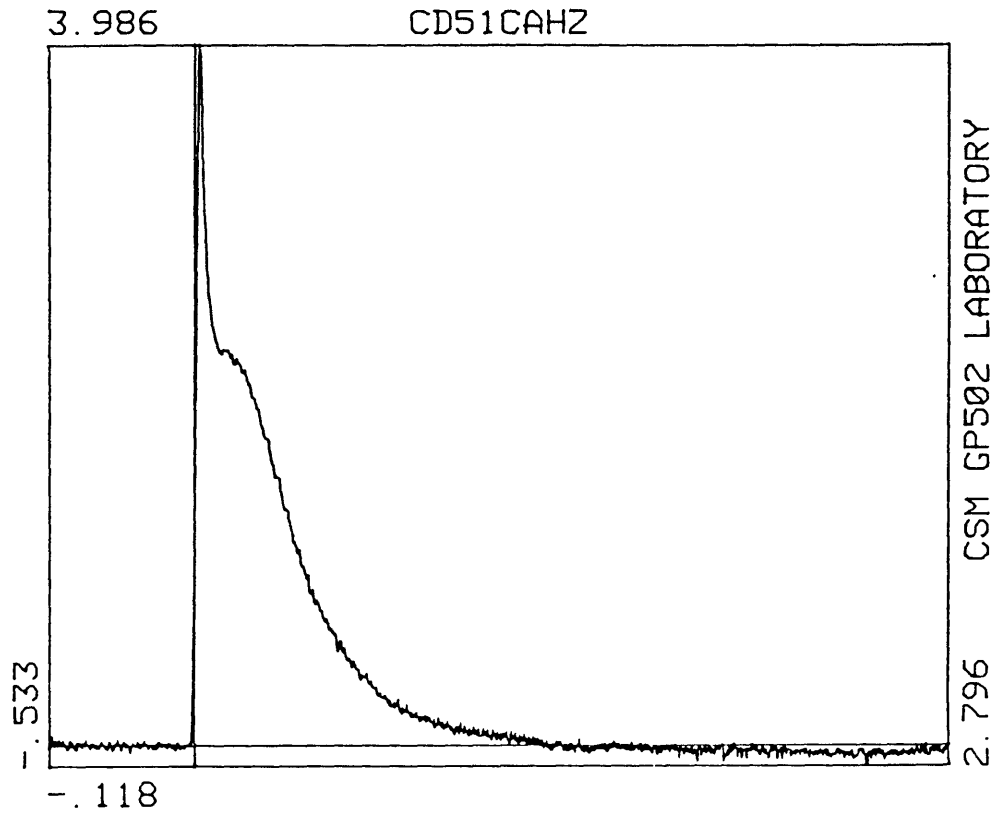


Figure 21. Raw stacked transient from station 51, using source C. The total window is 3.33 seconds. The curve shows a resistive near surface layer over a conductive layer. At late stage the curve shows insulating basement.

to the fact that a big portion of the current will diffuse through the upper layer and the surface of the second layer. However, the converse is true when the substratum is more resistive. Much of the current will diffuse through the second layer, and hence the MVAR will approach the second layer resistivity. The influence of the separation between the source and the receiver ( $r$ ) on the MVAR maps is noticeable. High values of MVAR are always associated with larger offset distances.

A map of MVAR for the study area, Figure 22, clearly indicates a definite trend of increase in the values of the MVAR, both northward and eastward. The map also shows a steep gradient to the east, which is partially coinciding with the Sheep Creek fault zone. The low resistivity anomaly that characterizes the western part of the map is an indicative of a conductive volcanic material. A plot of MVAR values along profile 5 (see Figure 23) indicates the presence of an anomalous low under Stations 19 and 17. The MVAR values generally tend to increase eastward (Figure 24).

#### Total Longitudinal Conductance (S):

The total longitudinal conductance is an approach often used to determine the minimum depth to the basement, provided that the change in resistivity of the overlying conductors is insignificant. The basement has a considerably larger value of

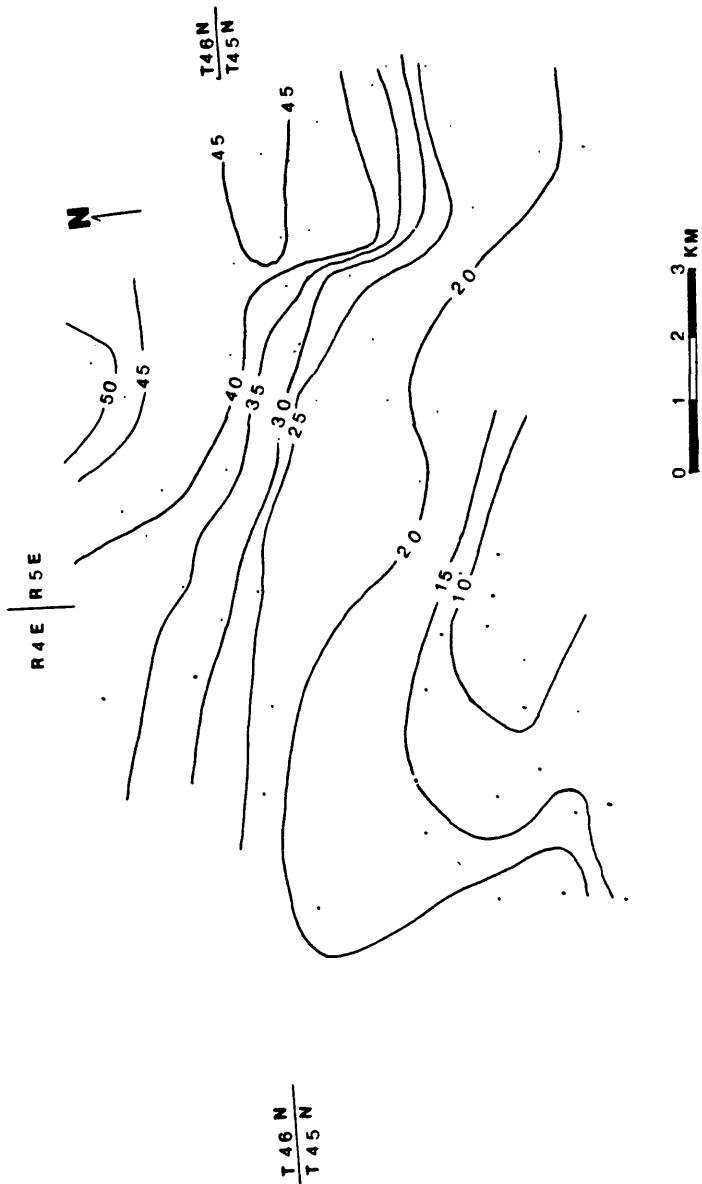


Figure 22. A maximum voltage apparent resistivity (MVAR) map of the study area, showing the trend of the subsurface resistivity. Contour interval in ohm-meters.

R4E | R5E

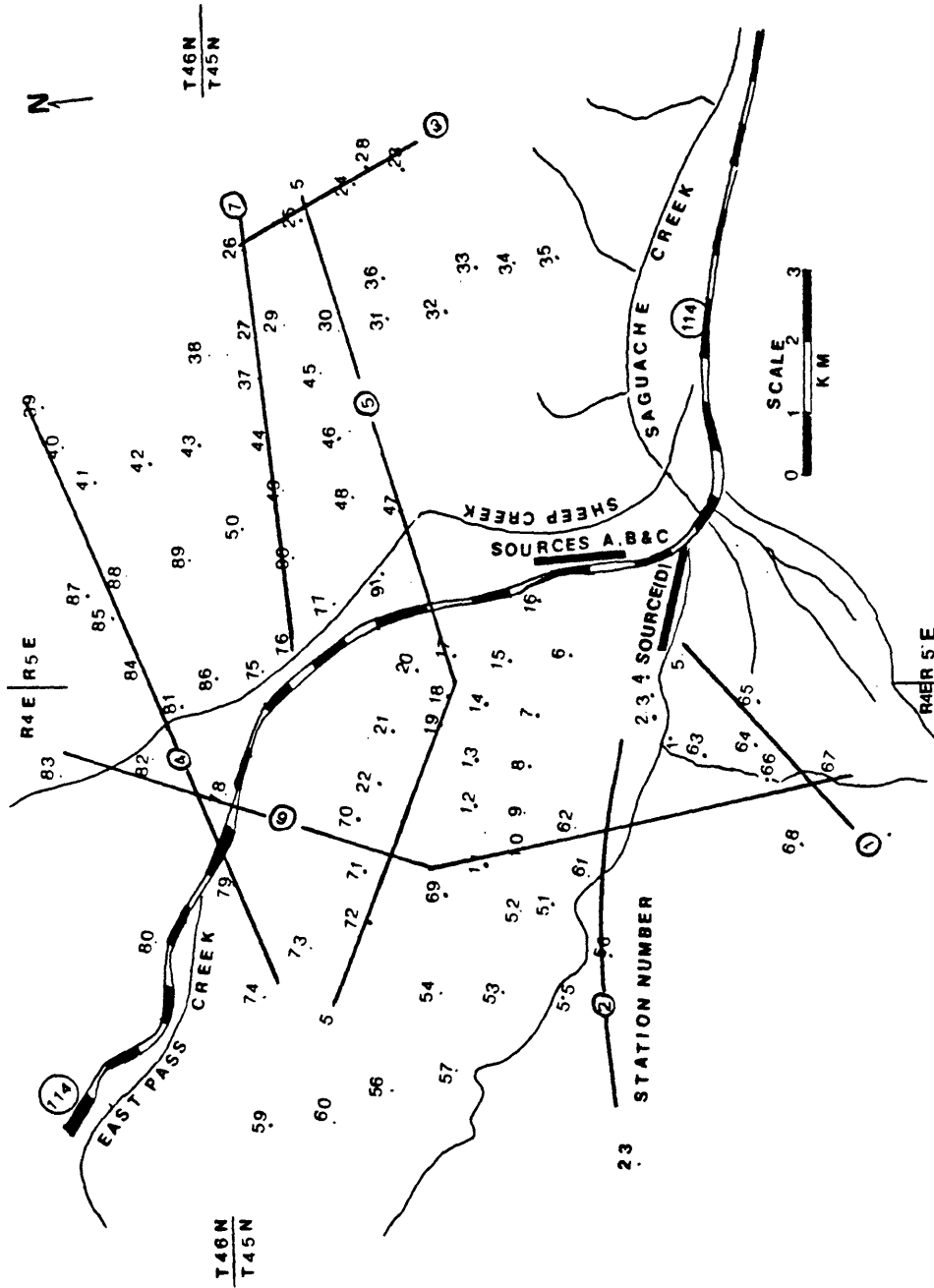


Figure 23. A map showing the location of the profiles.

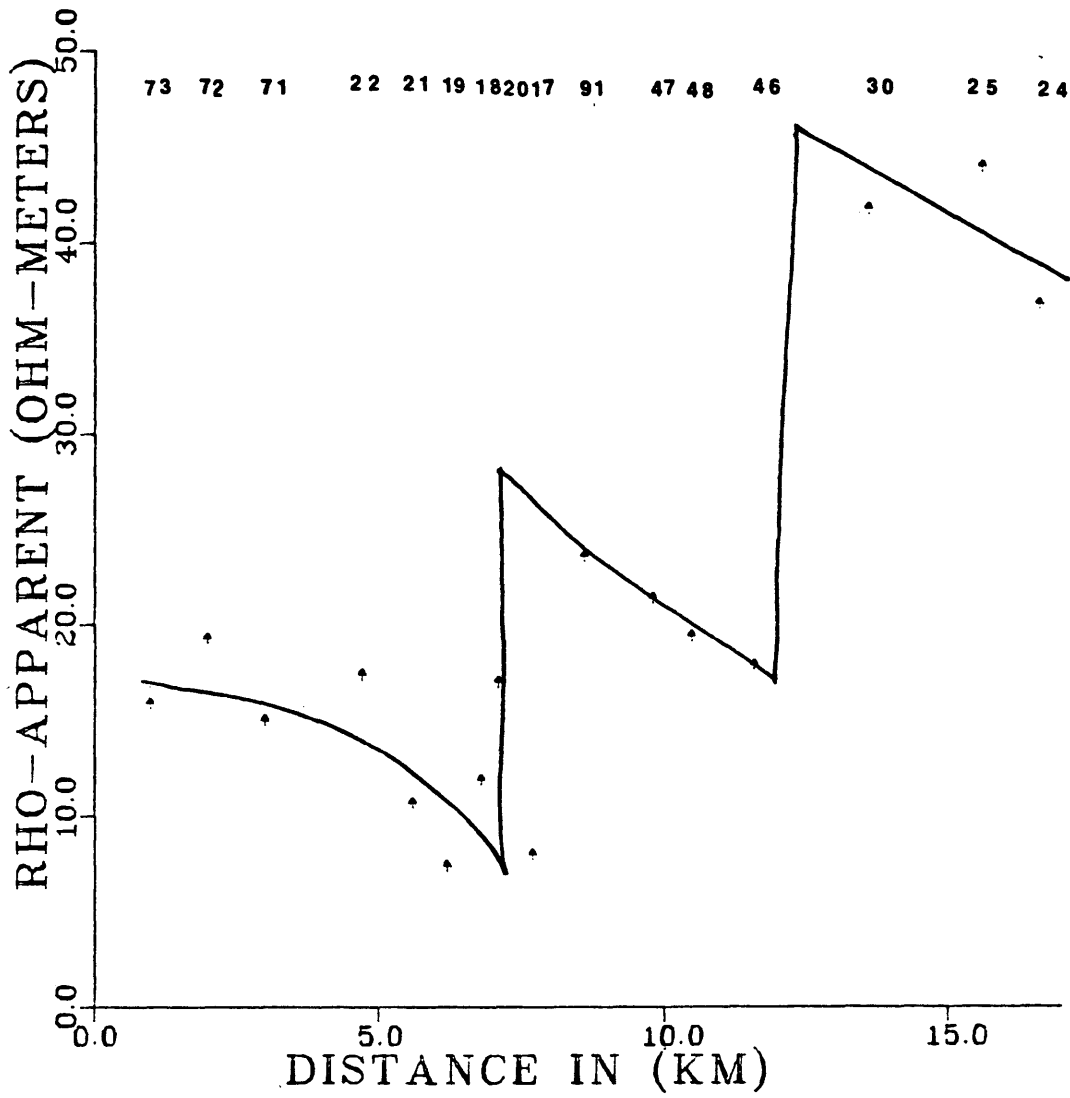


Figure 24. Plots of maximum voltage apparent resistivity (MVAR) value for the stations along profile 5, indicating the resistivity trend.

resistivity than any of the overlying layers. It is determined by adding together the longitudinal conductance of each individual layer above the basement:

Total Longitudinal Conductance (S)  
from Apparent Resistivity Curves:

The total longitudinal conductance values are calculated by using the minimum time on the late-time curve and the first layer resistivity as calculated from the early-time asymptote of the apparent resistivity curve. The map in Figure 25 indicates an increasing trend in the values of S from 100 mhos in the east to 230 mhos in the west. This increase is attributed to the change in the total thickness of the volcanic ash and flows, rather than the change in its resistivity, since the latter changes insignificantly in that direction. The map also indicates the presence of a discontinuity that could be due to faulting within the basement.

Evidently, both MVAR and the total longitudinal conductance maps compare favorably with each other and with the geology of the area. Both methods were able to show features such as the Sheep Creek fault zone and the shallow basement in the east and around Alkali Springs.

Results of this transient survey were also displayed as zones of all-time apparent resistivity maps. Figure 26

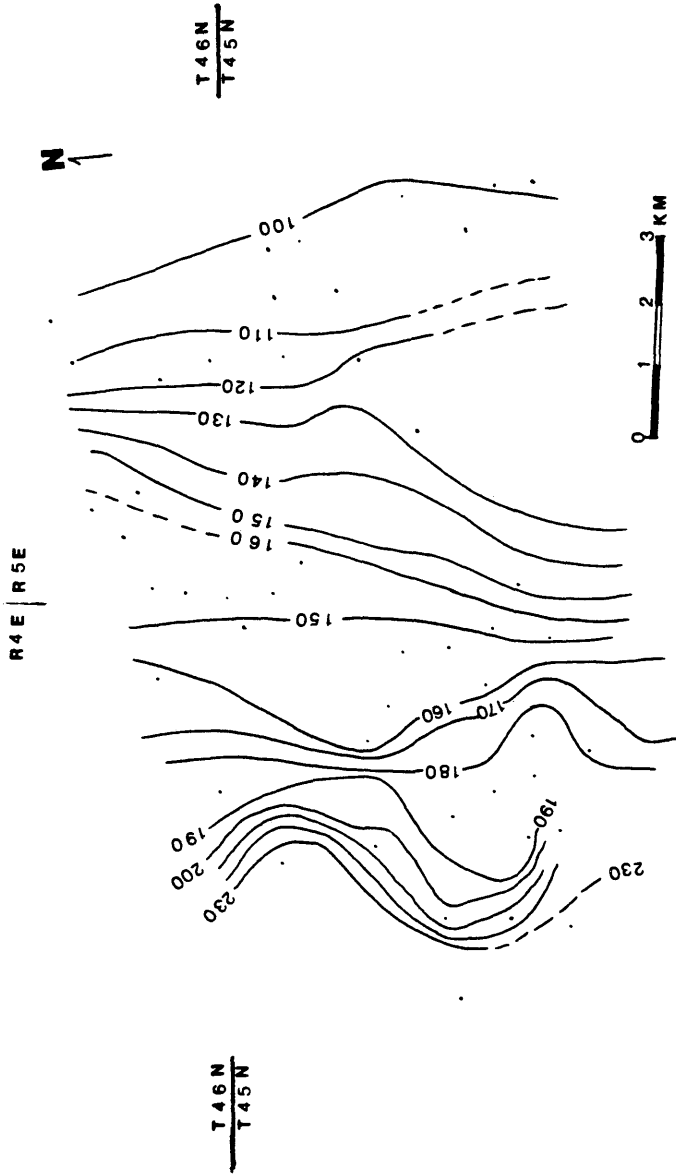


Figure 25. A total longitudinal conductance (S) map of the study area, as calculated from the early- and late-time apparent resistivity curves, showing the trend of increase in the total thickness of the volcanics westward. Contour values in mhos.

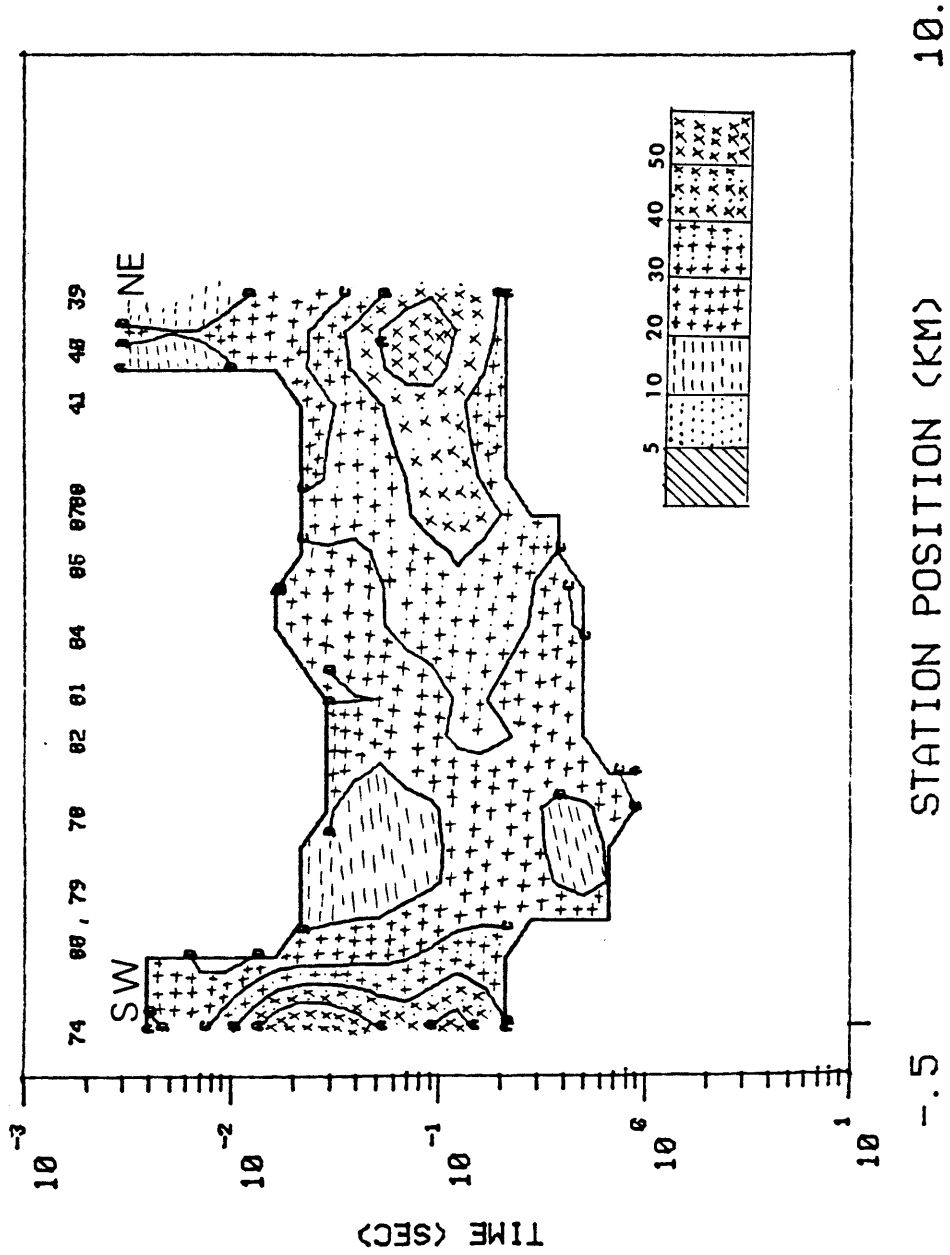


Figure 26. All-time apparent resistivity contour map of profile 4. Contour values in ohm-meters.

shows the distribution of all-time apparent resistivity with time along profile 4 (see Figure 23). The map clearly indicates a high resistivity distribution in the NE and another high in the SW; which might indicate the presence of the basement. Isolated low resistivity anomalies are also seen, which could probably indicate the presence of conductive ash-flows and tuffs.

Figure 27 shows a high resistivity distribution in the east and a relatively homogeneous earth westward beyond Station 46 (see Figure 23). This trend suggests the presence of a fault under Station 46, which partially coincides with the Sheep Creek fault zone. The low resistivity values under Station 36 (Alakali Springs) could possibly be attributed to the presence of sedimentary rocks or conductive volcanic material.

In Figure 28, a relatively homogeneous earth with low resistivity distribution makes up most of the map. The low resistivity values probably indicate the presence of saturated volcanic material. A trend of increase in the resistivity northward is evident from the map. The vertical contact (between Stations 11 and 12) might suggest a possible fault in that location. Maps of all-time apparent resistivity at selective times have also been constructed.



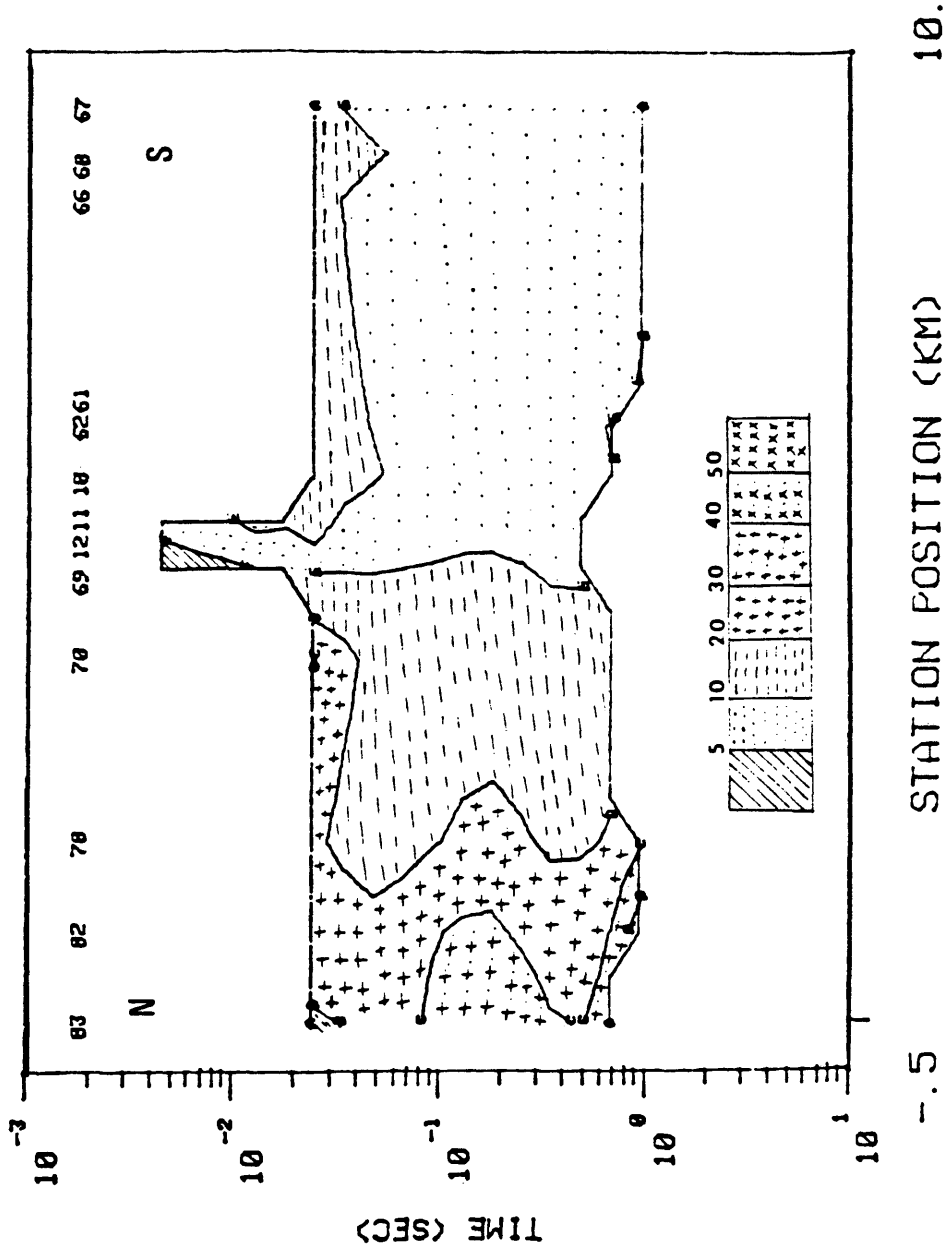


Figure 28. All-time apparent resistivity contour map of profile 6. Contour values in ohm-meters.

Figure 29 shows the distribution of resistivity at 0.1 second. The general trend is an increase of resistivity in an eastward direction. A zone of low resistivity (less than 10 ohm-meters) is clearly shown in the southwestern part of the map, which could probably be associated with conductive volcanic material. From the map, it is also evident that a shallow basement is present in the east. This is compatible, however, with the geology of the area, which indicates the occurrence of a very shallow basement around Alkali Springs (see geologic map, Figure 3).

Figure 30 is another all-time apparent resistivity at 0.03 second. The trend of the increase in resistivity eastward is also evident here. The low resistivity zone is more pronounced in this case, which might suggest the presence of a shallow conductor; probably saturated volcanic tuffs. Few isolated resistivity anomalies are also present, which reflect the near surface topography.

From the above discussions, it is clear that these maps are able to give a notion about the geologic setting of the study area.

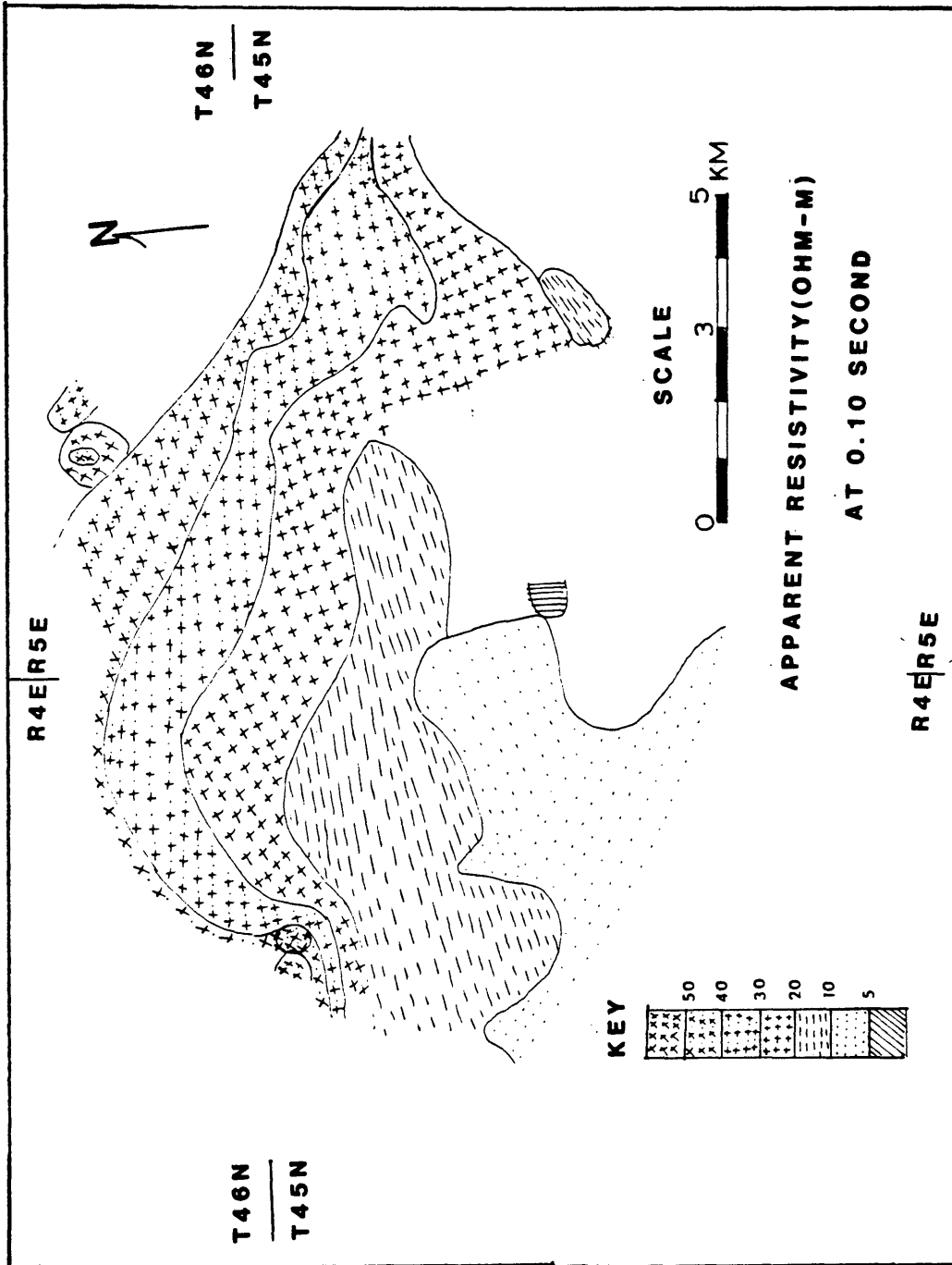


Figure 29. All-time apparent resistivity map at 0.1 second. Values denote apparent resistivity in ohm-meters.

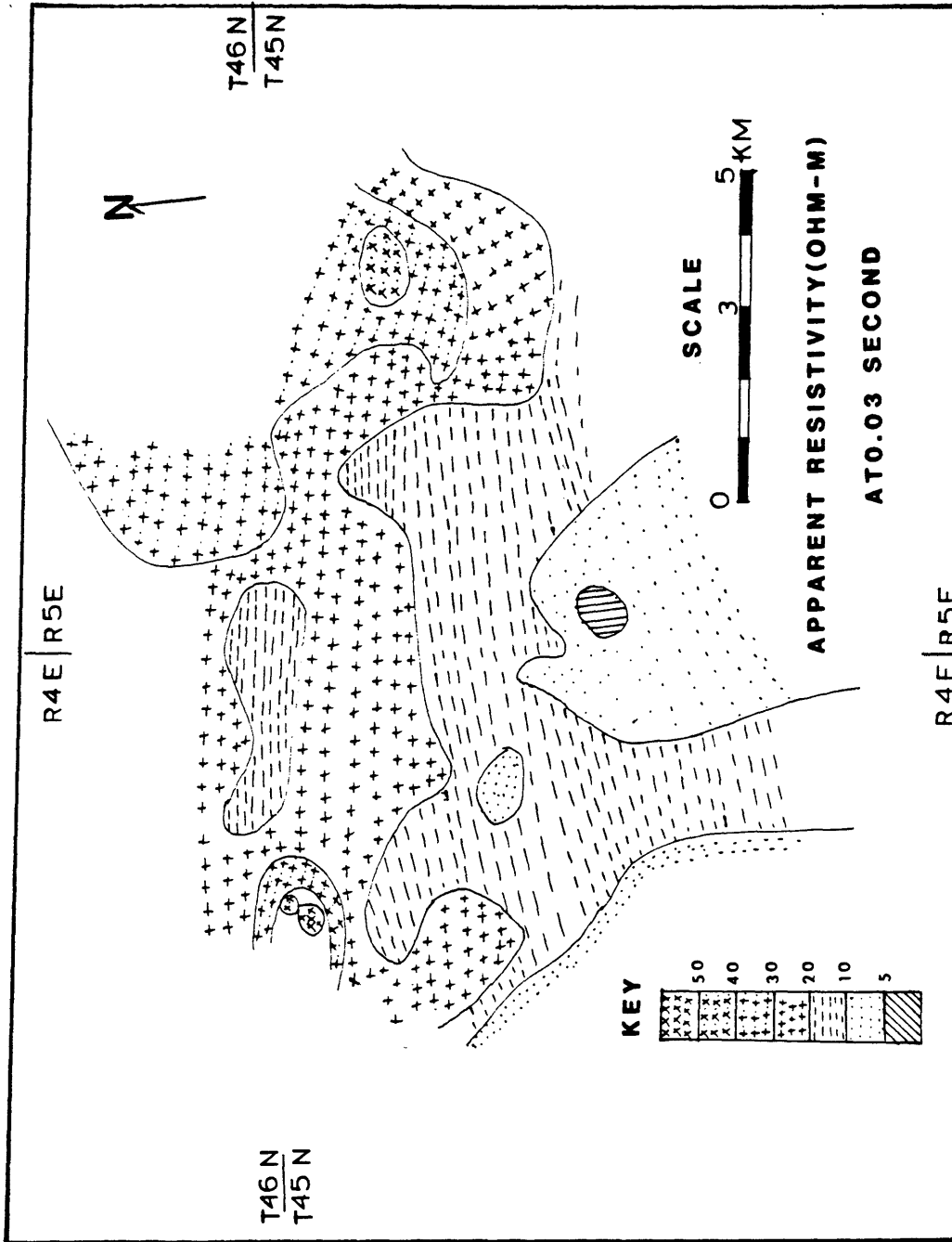


Figure 30. All-time apparent resistivity map at 0.03 second. Values indicate apparent resistivity in ohm-meters.

Quantitative Interpretation:

Machine-assisted interpretations based on comparing field data with a similar curve derived from theoretical calculations have successfully replaced the conventional curve-matching approaches. Unexceptionally, all machine-assisted interpretations require the development of an algorithm for accurate computations of the expected electromagnetic field responses, from a set of parameters that adequately describe a sequence of layers (Forward Problem). The other requirement is the development of a scheme whereby an accurate fit between the field data and a theoretically computed curve can be sought. Generalized linear inversion has been commonly applied to this end. The method employs the least-square error criterion between the observed data and a model curve. This error is given by:

$$E = \frac{1}{N} \sum_{n=1}^{\infty} (\text{Ln } \rho_{f,n} - \text{Ln } \rho_{m,n})^2$$

where:

E = the RMS error,

N = the number of data points,

Ln = the natural logarithm,

$\rho_{f,n}$  = observed apparent resistivity values, and

$\rho_{m,n}$  = theoretical resistivity values.

The purpose of the least-square fitting is to search iteratively for an earth model that can best fit the field data, by adjusting the model parameters (resistivities and thicknesses) until the square-error is minimized or falls below a certain value. Several iterations may be needed before this condition is met.

The Semi-Automatic Transient Inversion (SATI) program (Stoyer, 1979) was used to invert the field data to a two- and three-layered earth. The program employs a least-square ridge-regression inversion approach to generate transient curves. The field data values were input to the program and an educated initial guess of the model parameters, based on the analysis of the early- and late-time resistivities was made. Figures 31 and 32 show examples of the fit in terms of two- and three-layered earth, respectively (Appendix C). Appendix B contains the results obtained from the inversion process.

The mismatching between the field curve and the calculated curve could be further reduced if the calculated curve was multiplied by the calibration factor. A plot of this factor for the stations along profile 5, Figure 33, shows a similarity with the plot of MVAR for the same profile (see Figure 24). The plot clearly shows the same discontinuity under Stations 19 and 17 as inferred from the plot

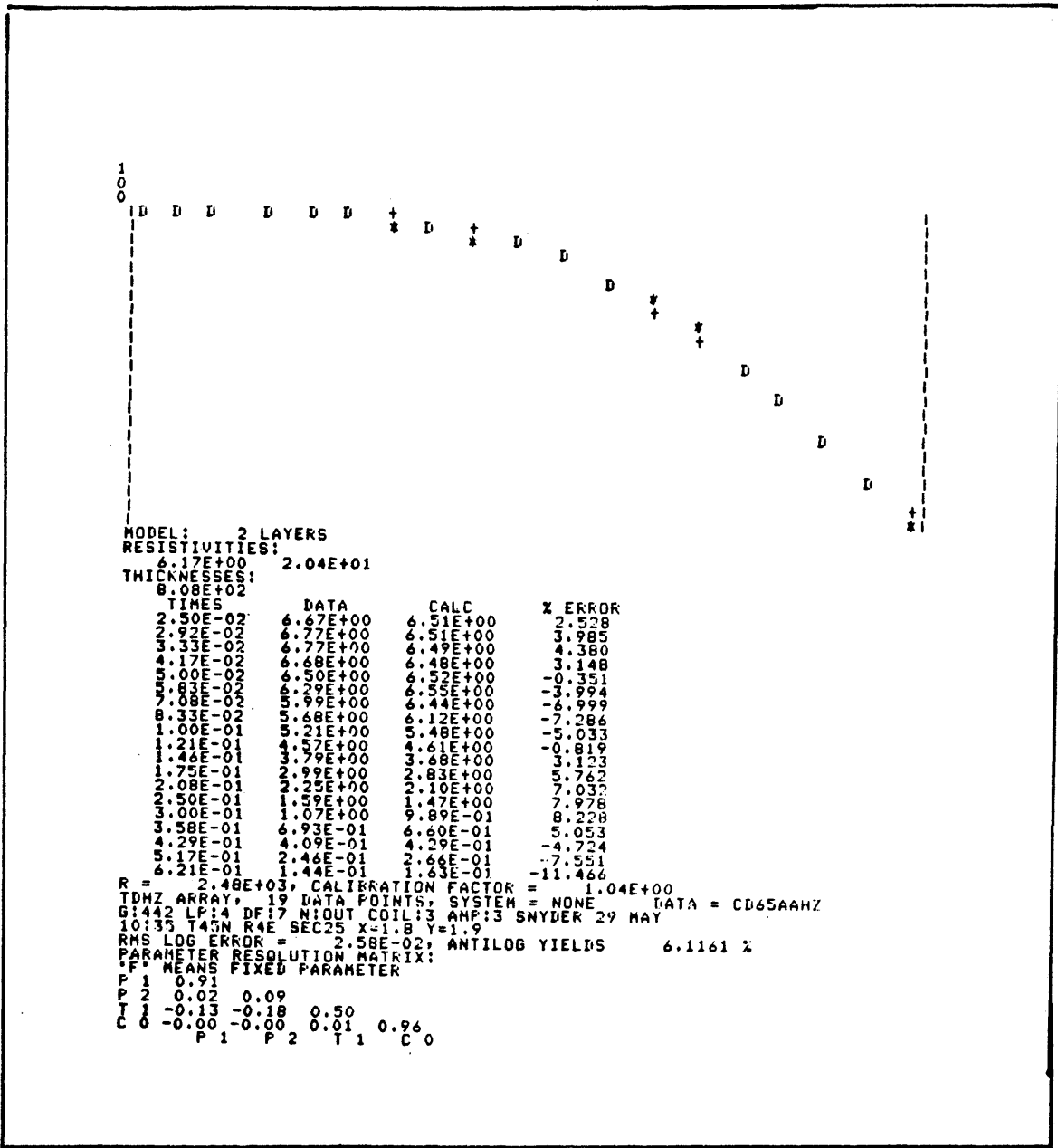


Figure 31. Example of inversion of the early- and late-time apparent resistivity curves, using a two-layer earth model.

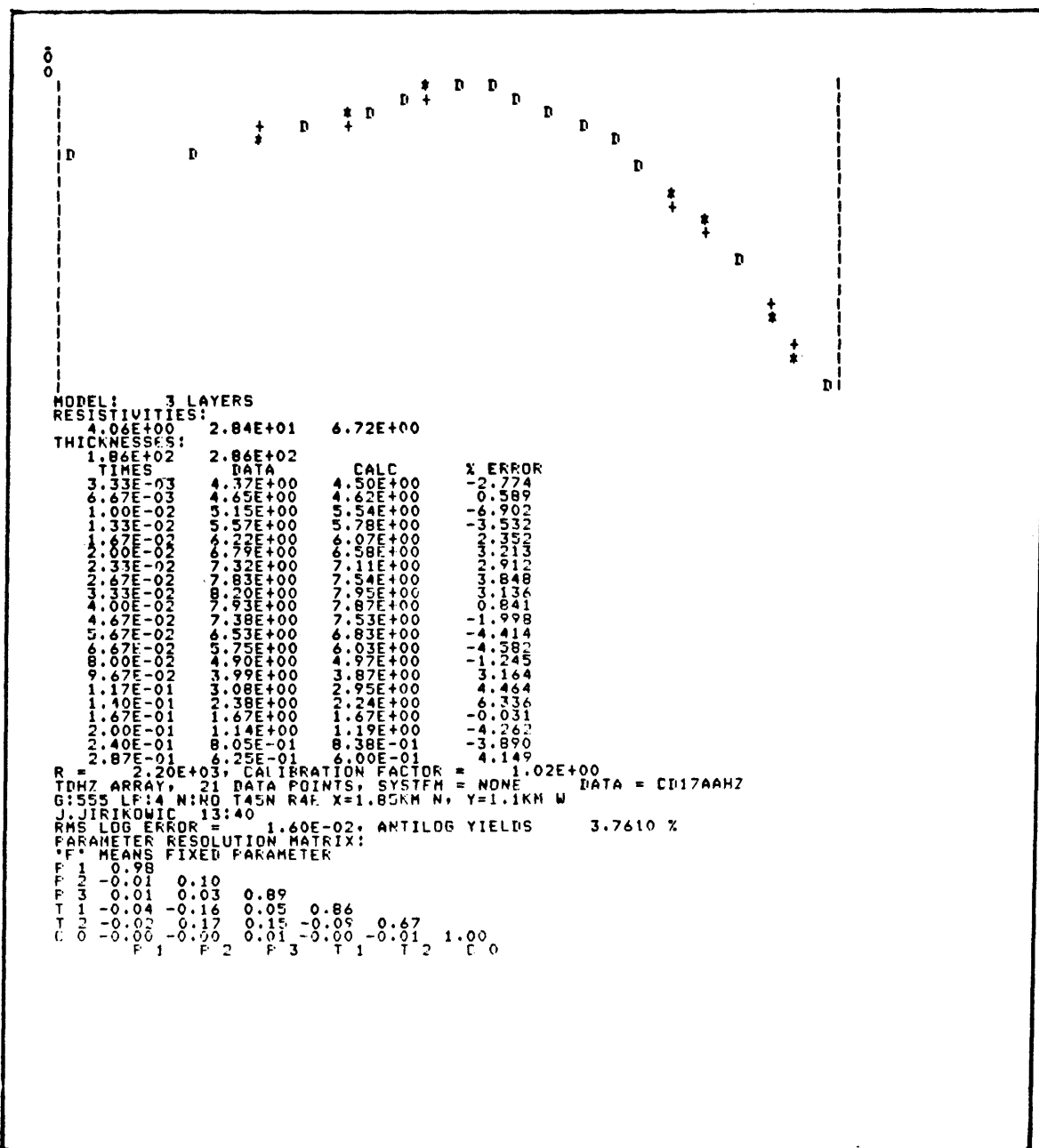


Figure 32. Example of inversion of the early-and late-time apparent resistivity curves, using a three-layer earth model.

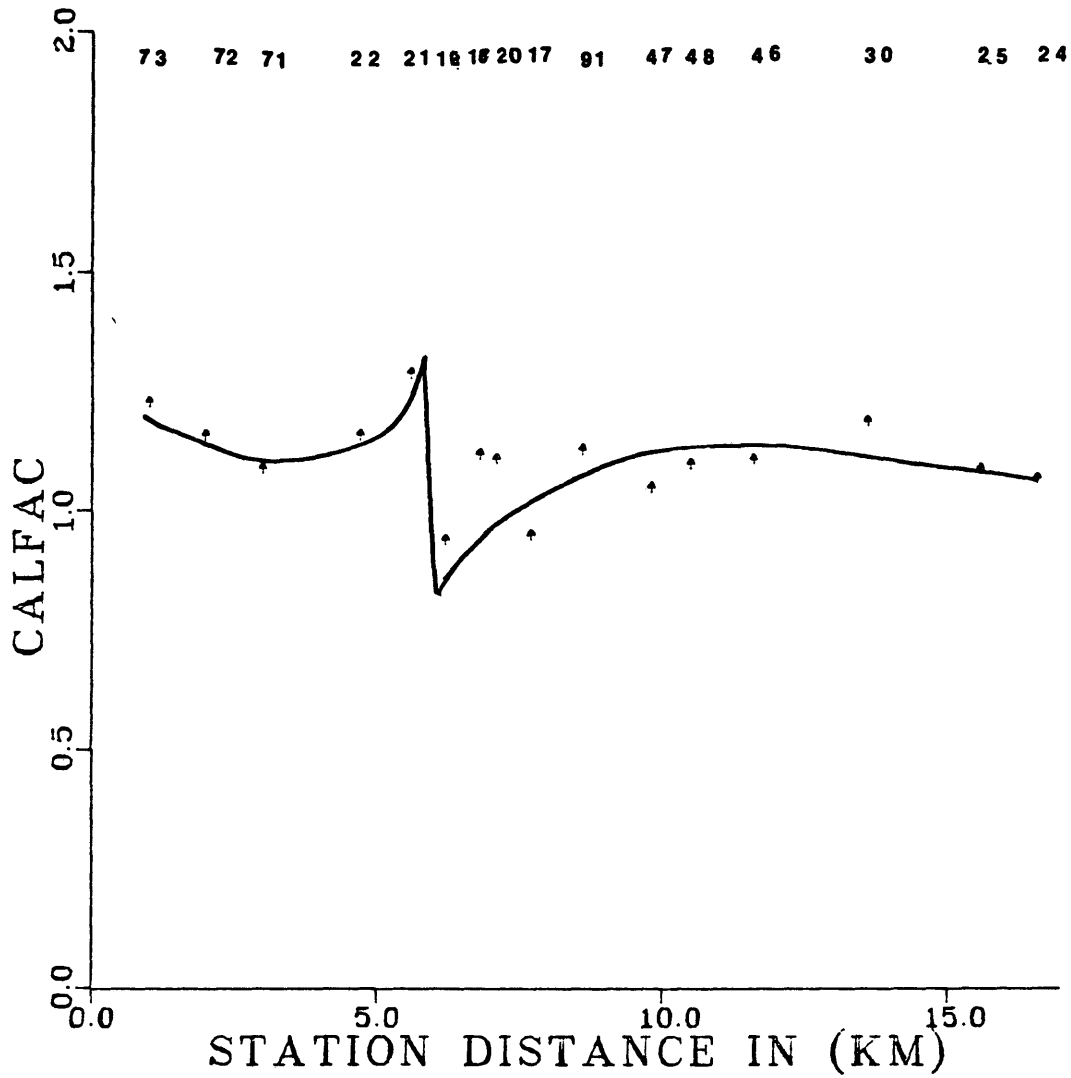


Figure 33. Plot of calibration factor for the stations along profile 5.

of maximum voltage apparent resistivity. A linear behavior is noticed over the rest of the curve, which might indicate an earth with fairly constant properties.

Interpreted Depth-Resistivity Maps:

Figure 34 is an interpreted resistivity map at a depth of 100 meters. At this depth, the map indicates a high resistivity distribution in the west, which probably reflects the inhomogeneous volcanic topography in the vicinity of the Cochetopa Hills (Steven and Epis, 1968). A low resistivity distribution exists at the far east part of the map, which might be due to the Paleozoic sediments and shallow conductive volcanic material. A local high also shows immediately to the west of this low distribution. The low resistivity values in the central part of the map could have been associated with the ash-flows which are predominant in that part (see geologic map, Figure 3). The trend depicted in this map clearly indicates the presence of a fault zone, which coincides with the Sheep Creek fault zone. Evidence of Sheep Creek syncline can also be inferred from the distribution of resistivities on this map.

A similar map at a depth of 500 meters (Figure 35) also indicates the high resistivity distribution in the western part of the map. This, however, gives a clue about

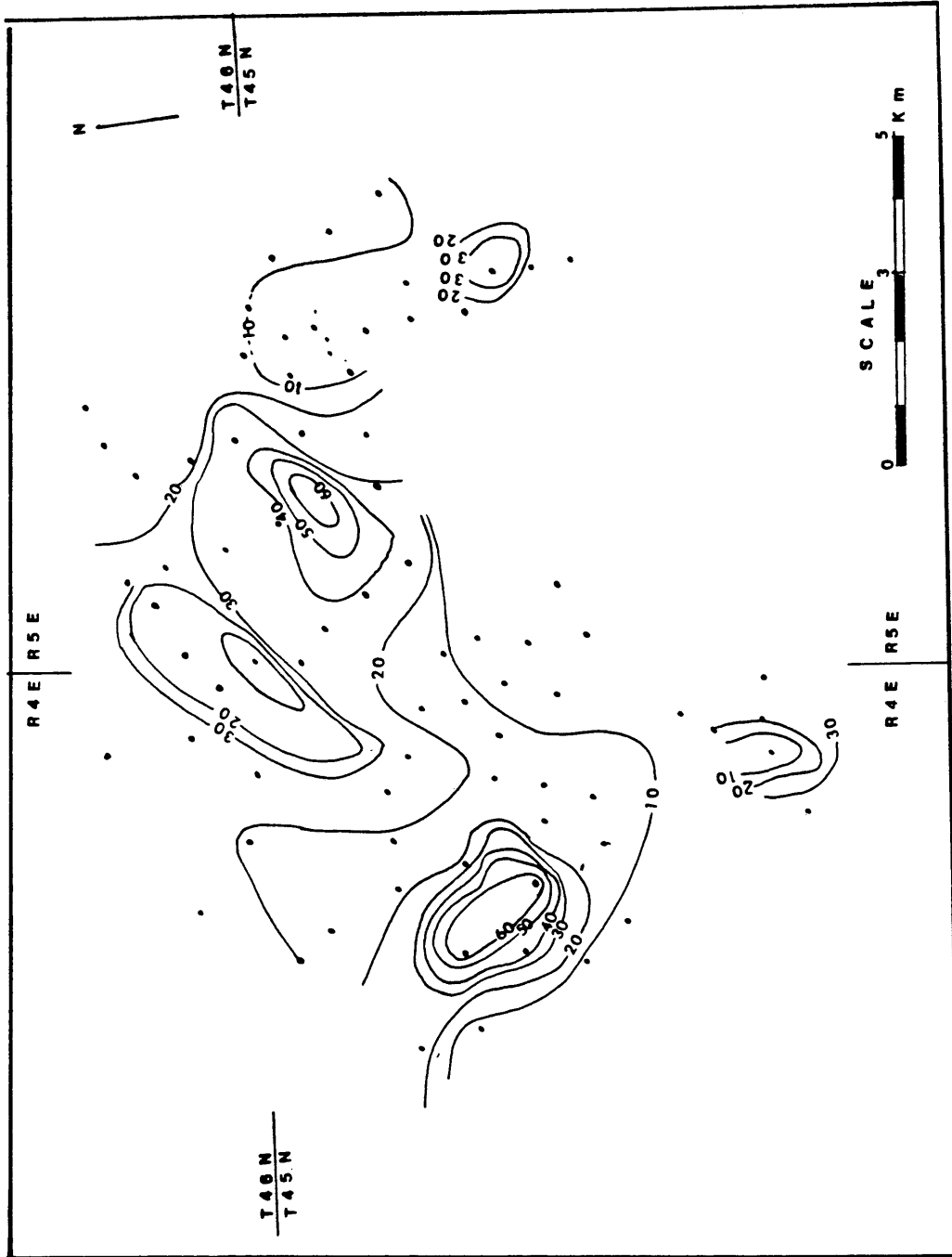


Figure 34. An interpreted resistivity map at a depth of 100 meters. Contour interval is 10 ohm-meters.

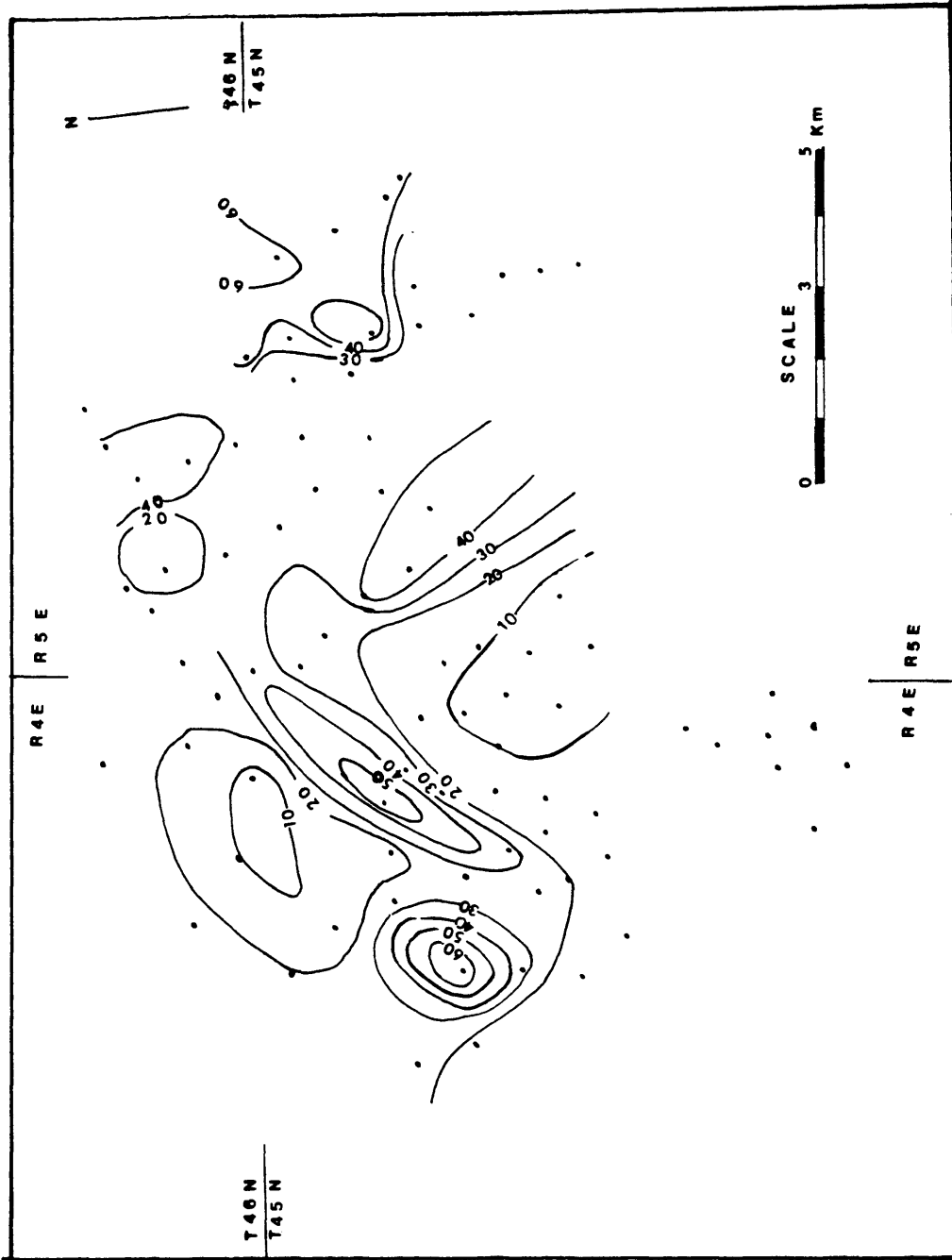


Figure 35. An interpreted resistivity map at a depth of 500 meters. Contour interval is 10 ohm-meters.

the complexity of the geology at that part. Other than this, very little structure can be extracted from this map due to the lack of resolution with depth.

Total Longitudinal Conductance (S) from Inversions:

The map of S (Figure 36) indicates an increase in total longitudinal conductance from 20 mhos at the east to a value of 160 mhos in the west. This increase in the value of S indicates an increase in the total thickness of the volcanic material in that direction. The change in the resistivity in that direction, however, is insignificant. The map also indicates the presence of a discontinuity that could be interpreted as due to faulting within the basement. In addition to that, a structural trough, which coincides with the Sheep Creek syncline, is also evident (see Figure 3).

It is clear from the above discussions that the total longitudinal conductance map discussed earlier compares very well with the S map obtained from inversion results. It is also evident from the results that both approaches correlate favorably with the geology of the area.

Quantitative interpretation was also achieved by constructing cross-sections from the inversion results. For the locations of these cross-sections, see Figure 23.

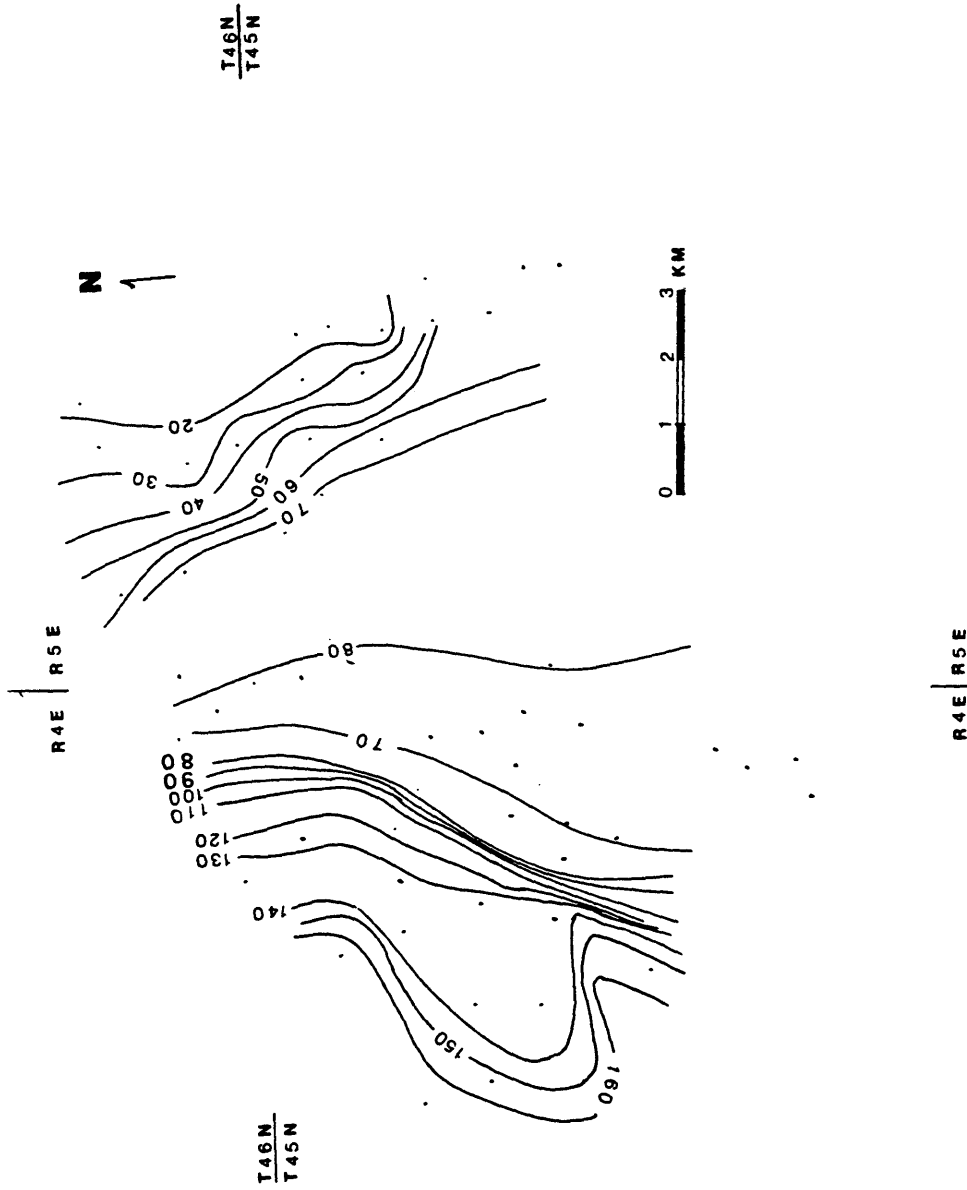


Figure 36. A total longitudinal conductance (S) map of the study area, constructed from the inversion results. The map shows the trend of increase in the total thickness of the volcanics westward. Contours are in mhos.

### Cross-Section Along Profile 1:

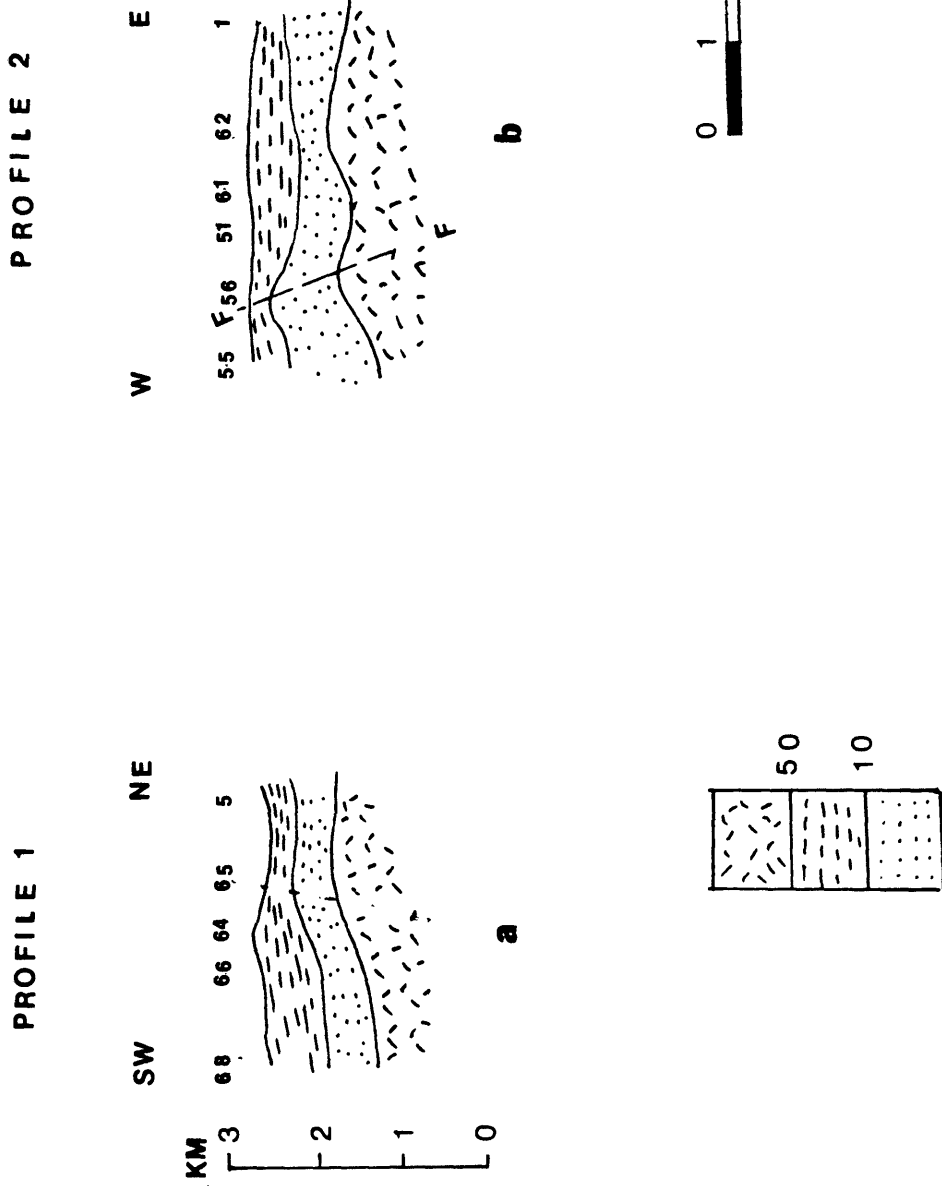
A cross-section trending SW-NE (Figure 37a) shows a conductive layer (less than 10 ohm-meters) in between two resistive layers. The top layer, with a resistivity of 10-50 ohm-meters, appears to correspond to the Carpenter Ridge ash-flow (see geologic map, Figure 3). Apparently, the conductive intermediate layer is saturated tuff, probably the Sapinero Mesa tuff. This conclusion is supported by the apparent low resistivity of the surface layer of profile 3. The geologic map suggests the existence of faulting across this profile. This small displacement faulting (the Sheep Creek fault) is not indicated in the resistivity profile.

From this model it is possible to suggest the existence of the water table at a depth range from 350-600 meters, as marked by the presence of the low resistivity intermediate layer.

### Cross-Section Along Profile 2:

The succession of rock units that characterizes the cross-section of profile 1 is also observed on the W-E trending cross-section along profile 2 (Figure 37b), north of profile 1.

The model suggests a possible faulting parallel to



Figures 37a, b. Interpreted cross-sections extrapolated from the data along profiles 1 and 2, respectively. Numbers designate resistivities in ohm-meters.

Sheep Creek fault zone, as indicated by the thinning of the layers westward. The geologic map, however, does not indicate the presence of such fault. A maximum thickness of about 650 meters is obtained for the intermediate layer.

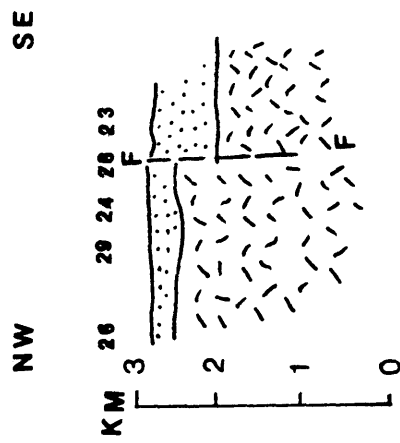
#### Cross-Section Along Profile 3:

This model suggests a two-layer earth (Figure 38a) with a top layer that thins northwest. This layer is probably the Sapinero Mesa tuff, which has a moderately high resistivity (10-50 ohm-meters) due to the fact that it is a dry surface layer. It is underlain by a resistive layer (more than 50 ohm-meters), probably the basement. The top layer and the basement are traversed by a vertical fault with a displacement of about 530 meters. The location of this fault indicates a possible coincidence with an unnamed fault which traverses Trickle Mountain (geologic map, Figure 3), in a SW-NE direction.

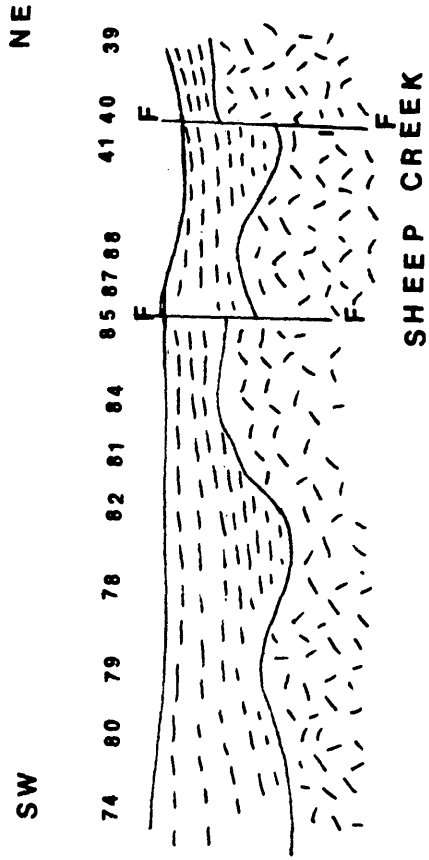
#### Cross-Section Along Profile 4:

This cross-section (Figure 38b) runs SW-NE across the Sheep Creek fault zone, and consists of a moderately resistive top layer (10-50 ohm-meters) composed of an assemblage of rock units with a variable thickness that reflects the

PROFILE 3



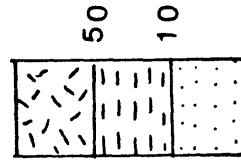
PROFILE 4



SHEEP CREEK

FAULT

b



a



Figures 38a, b. Interpreted cross-sections obtained from the data along profiles 3 and 4, respectively. Values indicate resistivities in ohm-meters.

pre-existing topography. The top layer rests unconformably on a resistive substratum with resistivity greater than 50 ohm-meters. The model indicates a system of faults which is coincident with the location of the Sheep Creek fault zone, as shown in the geology map (Figure 3). The model also indicates an estimated displacement of approximately 300 meters.

#### Cross-Section Along Profile 5:

This model indicates a two-layer earth with an outcrop composed of three lithological units, depending on location (Figure 39). The model clearly reflects the complexity of the geology under the profile, especially in the western part. This complexity is also suggested by frequent faulting, as shown in the geologic map. A system of graben and horst structures with variable displacements coincides with the Sheep Creek fault zone. This interpretation, however, is merely suggested by the writer, and is not necessarily the same as that given by the geologic map due to the complexity of the geology and the inability of the method to resolve the structural features associated with this complex pattern.

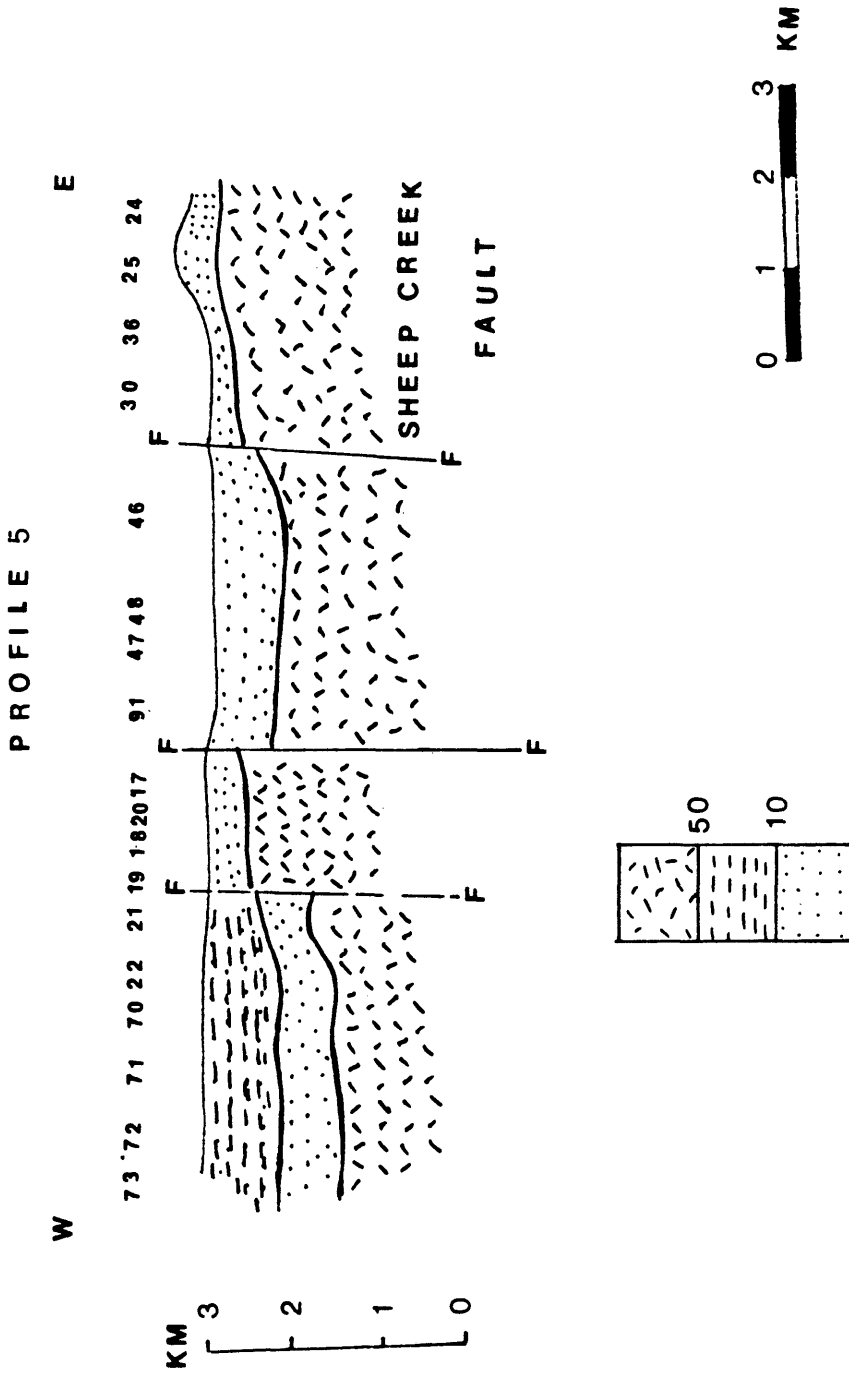


Figure 39. An interpreted W-E trending cross-section along profile 5. Values indicate resistivities in ohm-meters.

Cross-Section Along Profile 6:

A low resistivity zone (less than 10 ohm-meters) characterizes this model (Figure 40), with local occurrences of moderately high resistive rocks, probably Fish Canyon Tuff. This model does not completely show the spatial distribution of the Fish Canyon Tuff as suggested by the geologic map (Figure 3), except where the measurements were made on these tuffs. Although the method did not have enough resolution to isolate the effects of different structures comprising the geology in this particular part of the study area, nevertheless, it was able to resolve some of these complexities.

Cross-Section Along Profile 7:

This cross-section (Figure 41) crosses both the Sheep Creek fault zone and syncline (see location map, Figure 23), and runs in an E-W direction.

The section is mainly composed of two layers. The top layer has a range of resistivity between 10-50 ohm-meters, and rests on a resistive substratum (>50 ohm-meters), probably the basement. The upper layer is composed of a variety of volcanic material, undifferentiated by its resistivity. The thickness of this layer apparently reaches its maximum

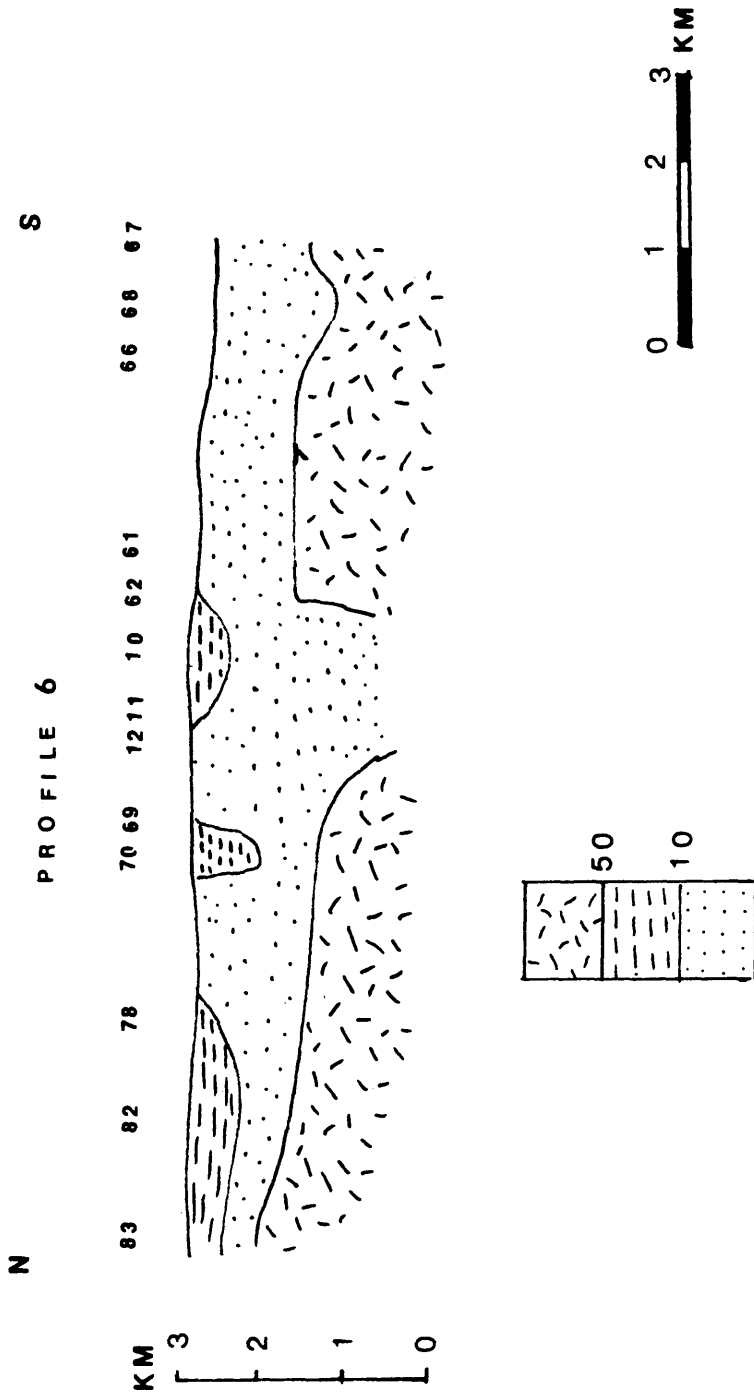


Figure 40. A N-S trending, interpreted cross-section from the data of profile 6. Values indicate resistivities in ohm-meters.

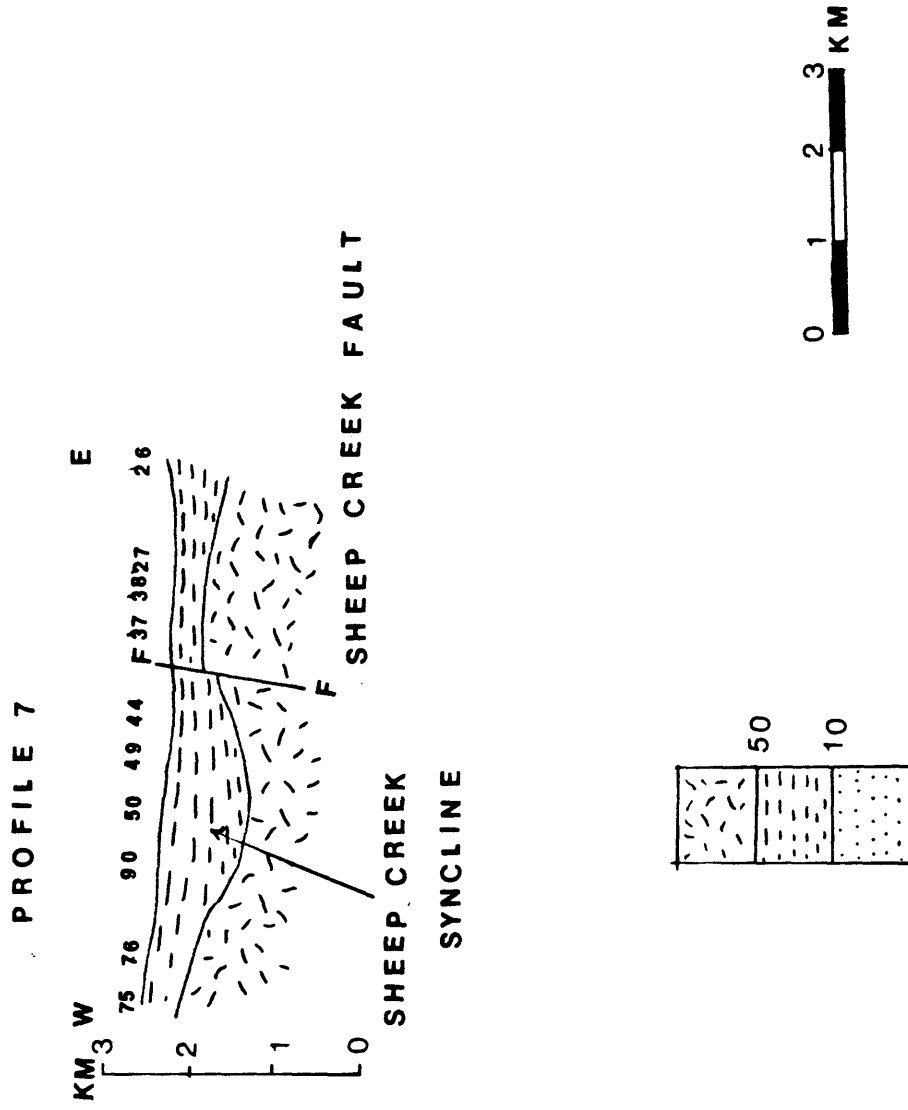


Figure 41. An interpreted W-E trending cross-section obtained from the data along profile 7. Values indicate resistivities in ohm-meters.

at the center of the section and tapers outward. This attitude clearly demonstrates the presence of a structural trough, which happens to coincide with the Sheep Creek syncline (see geologic map, Figure 3). Faulting is also evident, with very small displacement. The location of this fault coincides with the Sheep Creek fault zone.

#### The Evaluation of TDEM Results:

The cross-sections indicated the presence of two- and three-layer earth. In the case of the three-layer earth, the section consists of a moderately dry surface layer with resistivities between 10 and 50 ohm-meters (Figures 37, 39, and 40), underlain by a conductive layer representing moderately saturated volcanic tuffs and flows (less than 10 ohm-meters). The thicknesses of these two layers vary greatly, with a tendency for the high values to be in the western portion of the study area. Thicknesses of up to 1,200 meters were obtained. The third layer appeared to be inhomogeneous, with a wide range of resistivities (>50 ohm-meters), which probably indicates the presence of the basement.

In terms of two-layer earth, the results of the inversions of Stations 34 to 41 inclusively, indicated the presence

of a shallow conductor (probably sediments) near Alkali Springs (see Figure 3), at a depth ranging between 100-500 meters, underlain by a relatively resistive substratum (>50 ohm-meters).

### CONCLUSIONS

The results of this survey demonstrated the ability of the time-domain electromagnetic method in resolving structures as deep as 1,500 meters below the surface with the geometry used. However, it was impossible, in the absence of another control method, to confirm whether the conductor below this depth was real or an effect of field distortions by the lateral changes in resistivity.

In addition, the following conclusions are drawn from this study:

- 1) A low resistivity zone (5-10 ohm-meters) lies under some of the profiles. This zone probably indicates the existence of saturated fractured volcanic flows and tuffs at depth.
- 2) The method succeeded in determining the longitudinal conductance of the layers above the basement and the basement resistivity.
- 3) The time-domain electromagnetic method was also able to determine a thick sequence of volcanic flows and tuffs in

the western part of the study area, which unconformably overlies the electrical basement.

- 4) A shallow basement was shown in the east, around Alkali Springs, at a depth of 80-100 meters, which compares fairly well with the depth inferred from the geologic mapping.
- 5) Structural features, such as the NE-SW trending system of normal, graben, and horst faults which accurately coincide with the Sheep Creek fault zone, were revealed by this study. Also, displacements up to 400 meters were reported associated with these faults. The results, ascertained, as well, the existence of the Sheep Creek syncline.
- 6) Although it is unjustifiable to draw an accurate picture of what the subsurface structure looks like in the absence of another method, nevertheless, the method has proven adequate and

inexpensive to answer some of the structural problems associated with volcanic regions.

- 7) Finally, the results of this survey have shown a good correlation with the known geology of the area.

REFERENCES

- Anderson, W.L., et al., 1967, Methods of calculation and verification of results: Quarterly, Colorado School of Mines, vol. 62, no. 1, pp. 79-81.
- Anderson, W.L., 1979, Numerical integration of related Hankel transforms of order 0 and 1 by adaptive digital filtering: Geophysics, vol. 44, no. 7, pp. 1245-1265.
- Arestad, J.F., 1977, Resistivity studies in the upper Arkansas Valley and Northern San Luis Valley, Colorado: Thesis T-1934, Colorado School of Mines, Golden, CO.
- Bellatti, J.T., 1981, A field investigation comparing conventional compressional-wave, converted wave, and horizontally polarized shear-wave reflections: Thesis T-2491, Colorado School of Mines, Golden, CO.
- Bond, M.A., 1981, An integrated geophysical study of the Shaw Warm Spring area, San Luis Valley, south-central Colorado: M.S. Thesis T-2400, Colorado School of Mines, Golden, CO.
- Boniwell, J.B., 1967, Some recent results with the input airborne EM system: Can. Min. Metall. Bull., vol. 60, pp. 325-332.
- Bruns, D.L., 1971, Geology of the Lake Mountain northeast quadrangle, Sagauche County, Colorado: M.S. Thesis T-1367, Colorado School of Mines, 79 p.
- Bruns, D.L., et al., 1971, Stratigraphic relations between Bonanza Center and adjacent parts of the San Juan volcanic field, south-central Colorado: in H.L. James, editor, Guidebook of the San Luis Basin, Colorado: 22nd Field Conference, New Mexico Geological Society, pp. 183-190.
- Chapin, C.E., 1971, The Rio Grande Rift, part I: Modifications and additions: in H.L. James, editor, Guidebook of the San Luis Basin, Colorado: 22nd Field Conference, New Mexico Geological Society, pp. 191-201.

- Gaca, J.R., 1965, Gravity studies in the San Luis Valley area, Colorado: M.S. Thesis T-1021, Colorado School of Mines, Golden, CO, 73 p.
- Ghosh, D.P., 1971, The application of linear filter theory to the direct interpretation of geoelectrical resistivity sounding measurements: Geophys. Prosp., vol. 19, no. 2, pp. 192-217.
- Holmer, R.C., 1954, A regional gravity survey of Colorado: Ph.D. Thesis T-801, Colorado School of Mines, Golden, CO.
- Ibrahim, K.E., and Stoyer, C.H., 1981, Time-domain electromagnetic survey of the Cochetopa Hills and Alkali Springs area in south-central Colorado: SEG, 51st Annual International Meeting, Los Angeles, CA.
- Jackson, D.B., and Keller, G.V., 1972, An electromagnetic sounding survey of the summit of Kilauea Volcano, Hawaii: Jour. Geophys. Research, vol. 77, no. 26, pp. 4957-4965.
- Jordan, J.M., 1974, Geothermal investigations in the San Luis Valley, south-central Colorado: Thesis T-1478, Colorado School of Mines, Golden, CO, 89 p.
- Kaufman, A.A., 1972, The theoretical basis of the transient soundings in the near-zone: Nauka Siberian Div., Acad. Sci. USSR.
- Kaufman, A.A., and Keller, G.V., 1981, 1982, Frequency and transient electromagnetic soundings, Elsevier (in press).
- Keller, G.V., 1968, Electrical prospecting for oil: Quarterly, Colorado School of Mines, vol. 63, no. 2, pp. 1-268.
- \_\_\_\_\_, 1969, Electromagnetic surveys in the central volcanic region, preliminary report: Rept. 55, Geophys. Div., Dept. of Sci. and Ind. Res., New Zealand, 65 p.
- \_\_\_\_\_, 1970, Induction methods in prospecting for hot water: Geothermics (Special Issue 2), vol. 2, pt. 1, pp. 318-332.

- \_\_\_\_\_, 1971, Natural-field and controlled-source methods in electromagnetic exploration: *Geoexploration*, vol. 9, no. 2, pp. 99-147.
- Keller, G.V., Crewdson, R.A., and Daniels, J.J., 1978, Time-domain electromagnetic survey in Black Rock Desert - HuaLapi Flat area of northwestern Nevada: *Quarterly*, Colorado School of Mines, vol. 73, no. 4, pp. 47-56.
- Keller, G.V., et al., 1982, Electrical exploration for oil and gas: Summary report of investigations carried on by the Dept. of Geophys., Colorado School of Mines, Golden, CO.
- King, C.A., 1971, Time-domain electromagnetic coupling: Thesis T-1427, Colorado School of Mines, Golden, CO, 62 p.
- Knepper, D.H., 1974, Tectonic analysis of the Rio Grande Rift zone, central Colorado: Thesis T-1593, Colorado School of Mines, Golden, CO, 237 p.
- Knepper, D.H., and Marrs, R.W., 1971, Geologic development of the northern San Luis Valley and Bonanza Volcanic Center: in H.L. James, editor, *Guidebook of the San Luis Basin*, Colorado: 22nd Field Conference, New Mexico Geological Society, pp. 249-264.
- Larsen, E.S., Jr., and Cross, W., 1956, Geology and petrology of the San Juan region, southwestern Colorado: U.S. Geol. Surv. Prof. Paper 258, 303 p.
- Lipman, P.W., Steven, T.A., and Mehnert, H.H., 1970, Volcanic history of the San Juan Mountains, Colorado, as indicated by potassium-argon dating: *Bull. Geol. Soc. America*, vol. 81, no. 8, pp. 2329-2352.
- Mamah, Luke, 1979, The influence of finiteness of source on the time-domain electromagnetic sounding: Thesis T-2222, Colorado School of Mines, Golden, CO, 139 p.
- Mayhew, J.D., 1969, Geology of the eastern part of the Bonanza volcanic field, Sagauche County, Colorado: M.S. Thesis T-1226, Colorado School of Mines, Golden, CO, 94 p.

- Meinardus, H.A., 1967, The kernel function in direct-current resistivity interpretation: Ph.D. Thesis T-1103, Colorado School of Mines, Golden, CO.
- Morrison, H.F., et al., 1969, Quantitative interpretation of transient electromagnetic fields over a layered half-space: Geophys. Prosp., vol. 17, pp. 82-101.
- Patra, H.P., and Mallick, K., 1980, Time-varying geoelectric sounding: Elsevier.
- Silva, L.R., 1969, Two-layer master curves for electromagnetic soundings: M.S. Thesis T-1250, Colorado School of Mines, Golden, CO, 117 p.
- Skokan, C.K., 1974, A time-domain electromagnetic survey of the East Rift Zone, Kilauea Volcano, Hawaii: Ph.D. Thesis T-1700, Colorado School of Mines, Golden, CO.
- Souto, J.M., 1980, Test of time-domain electromagnetic exploration for oil and gas: Ph.D. Thesis T-2278, Colorado School of Mines, Golden, CO, 152 p.
- Spies, B.R., 1976a, The transient electromagnetic method in Australia: Bur. Min. Res., J. of Austral. Geol. and Geophys., vol. 1, pp. 23-32.
- \_\_\_\_\_, 1976b, The derivation of absolute units in electromagnetic scale modelling: Geophys., vol. 41, no. 5, pp. 1042-1047.
- Steven, T.A., and Epis, R.C., 1968, Oligocene volcanism in south-central Colorado, pp. 241-258: in R.C. Epis, editor, Cenozoic Volcanism in the Southern Rocky Mountains: Quarterly, Colorado School of Mines, vol. 63, no. 3, 287 p.
- Stoyer, C.H., 1979, Unpublished computer programs, Colorado School of Mines, Golden, CO.
- \_\_\_\_\_, 1980, TDEM modelling experiment: Graduate Geophys. Course 502 class notes, Colorado School of Mines, Golden, CO.
- \_\_\_\_\_, 1980, An analytic comparison of time- and frequency-domain electromagnetic methods: Report to DOE, contract ET-78-S-02-5084, 134 p.

- Tulinius, H., 1980, Time-domain electromagnetic survey in Krafla, Iceland: Thesis T-2325, Colorado School of Mines, Golden, CO.
- Uitti, P.B., 1980, Interpretation of seismic reflection data from the southern San Luis Valley, south-central Colorado: Thesis T-2341, Colorado School of Mines, Golden, CO.
- Vanyan, L.L., 1967, Electromagnetic depth soundings: New York, Consultants Bureau.
- Wait, J.R., 1961, The electromagnetic fields of a horizontal dipole in the presence of a conducting half-space: Can. J. Phys., vol. 39, pp. 1017-1028.
- \_\_\_\_\_, 1962, Electromagnetic waves in stratified media: MacMillan, New York.

APPENDICES

APPENDIX A

Appendix A contains the plots of apparent resistivity-time curves for the early- and late-time asymptotes, calculated from equations 10 and 11 respectively. Apparent resistivities are in ohm-meters, and times are in seconds (Figures

The title is explained as follows:

Example: CD04 AA HZ

CD04 = station number,

A = source used (A),

A = transient sequence,

HZ = vertical component of  
the magnetic field.

CALFAC = Calibration Factor

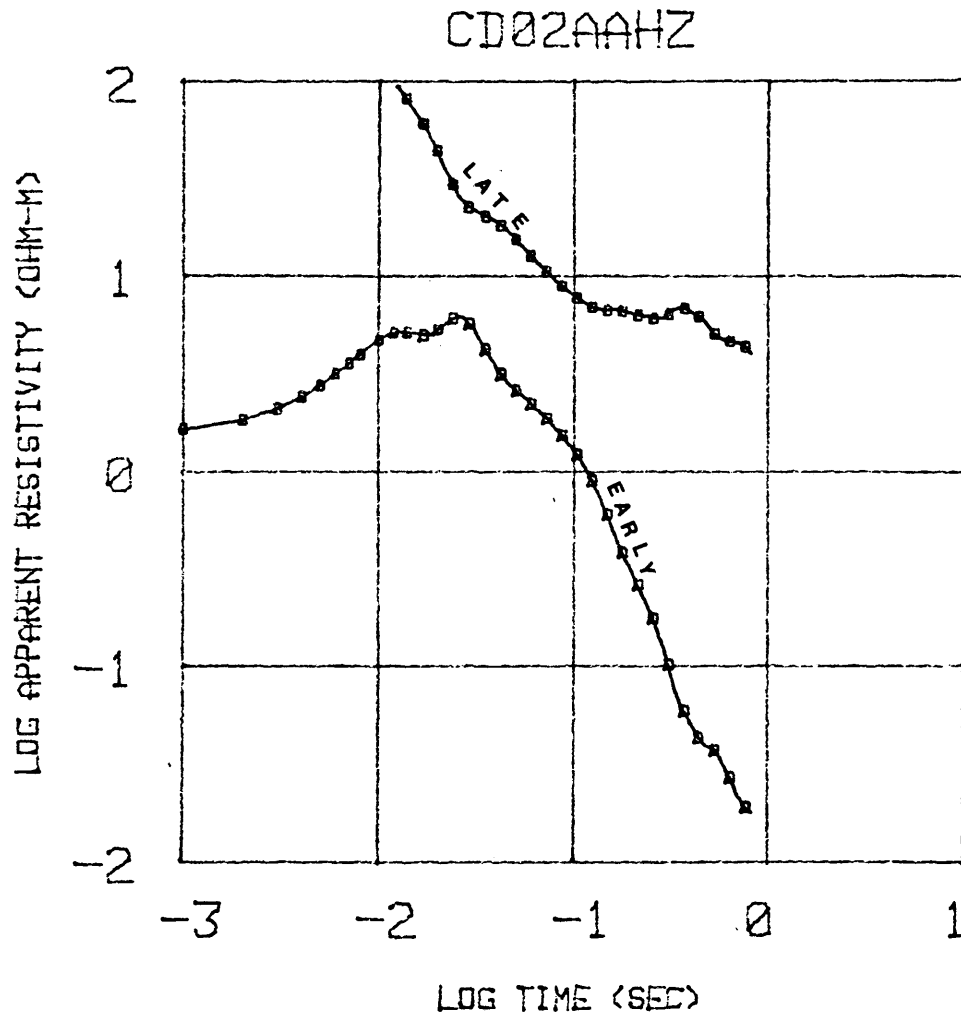


Figure 42

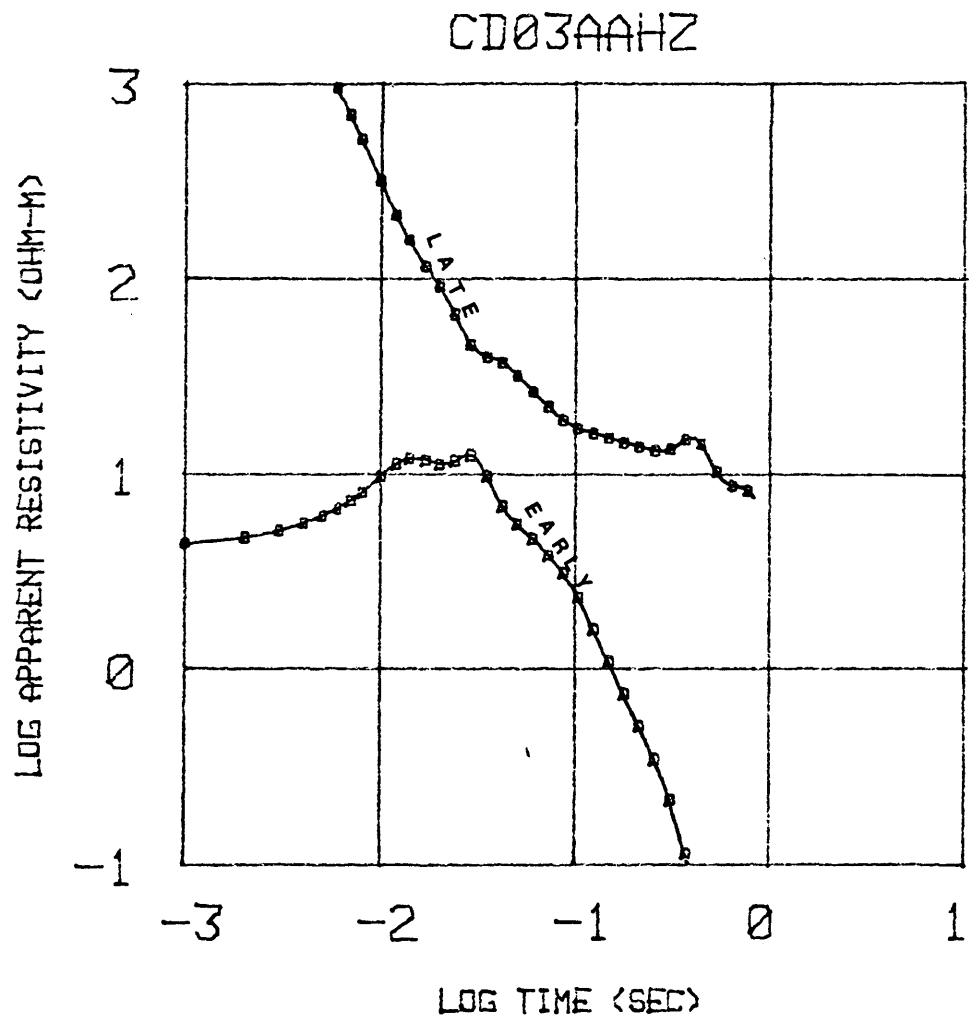


Figure 43

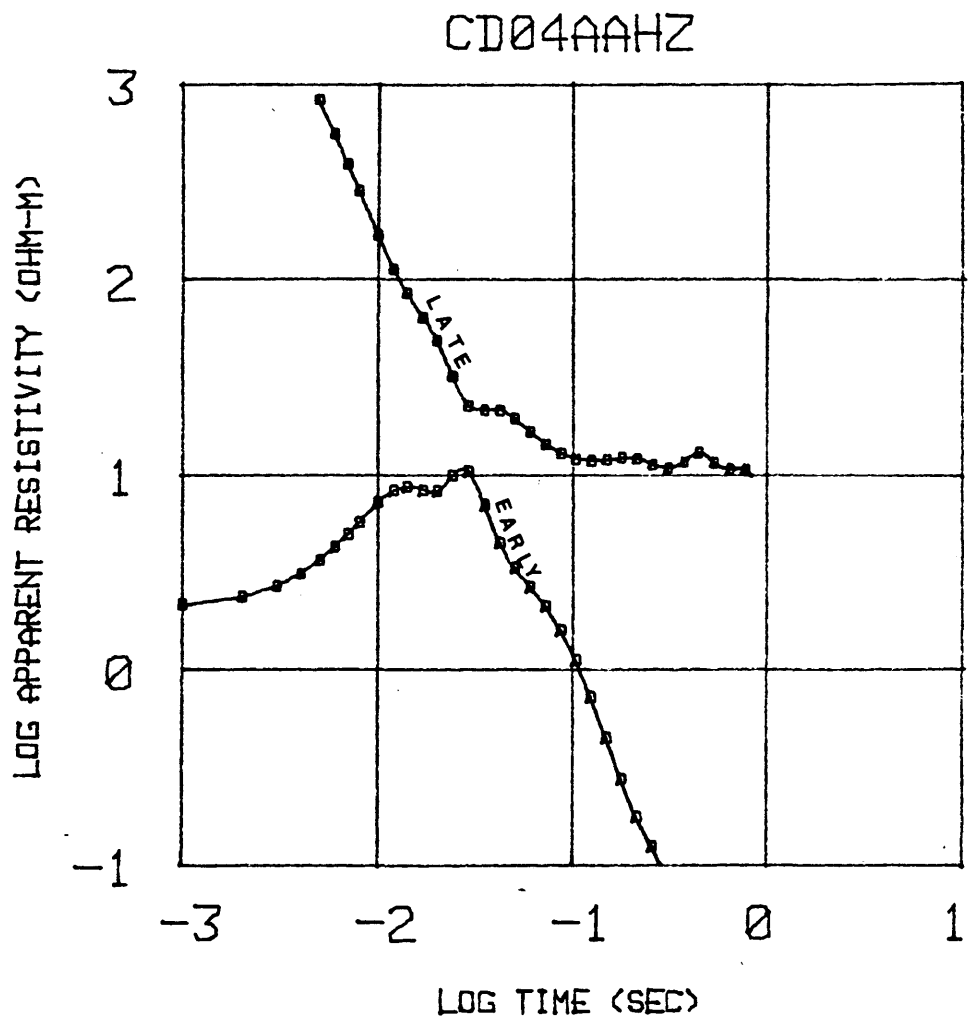


Figure 44

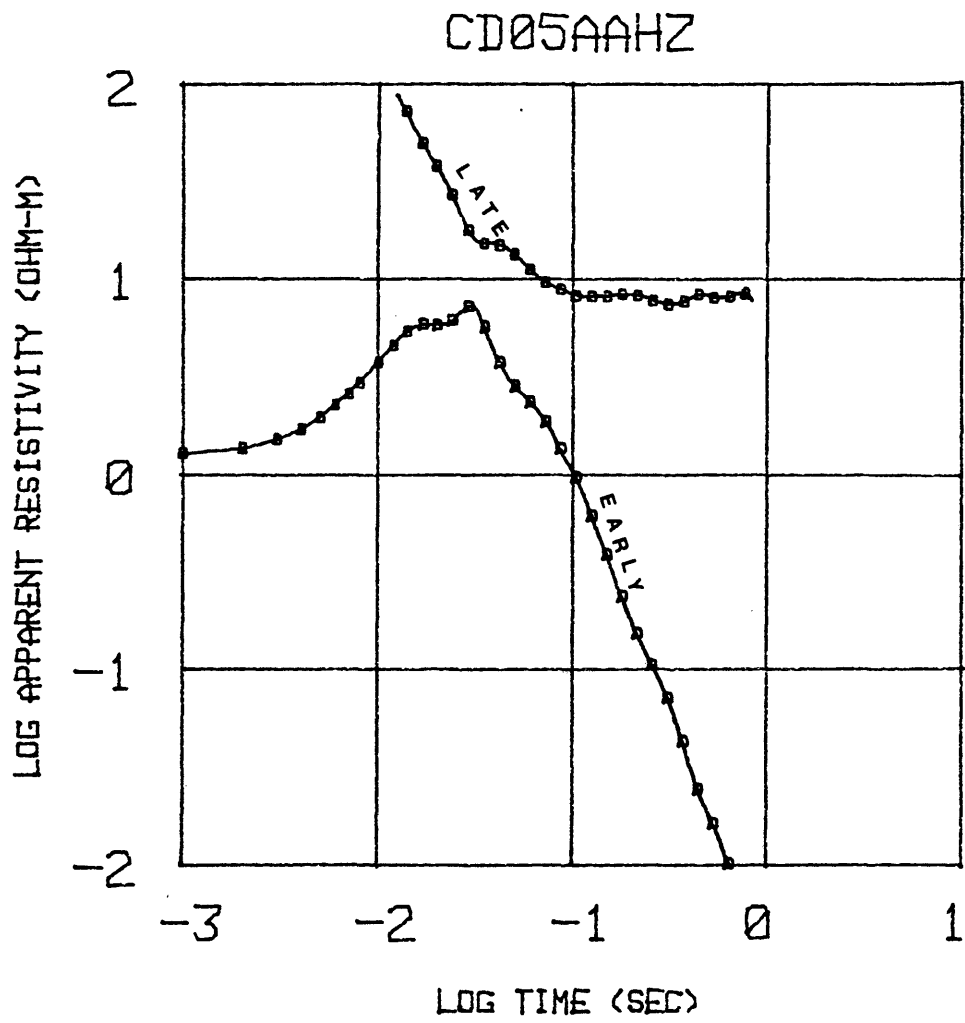


Figure 45

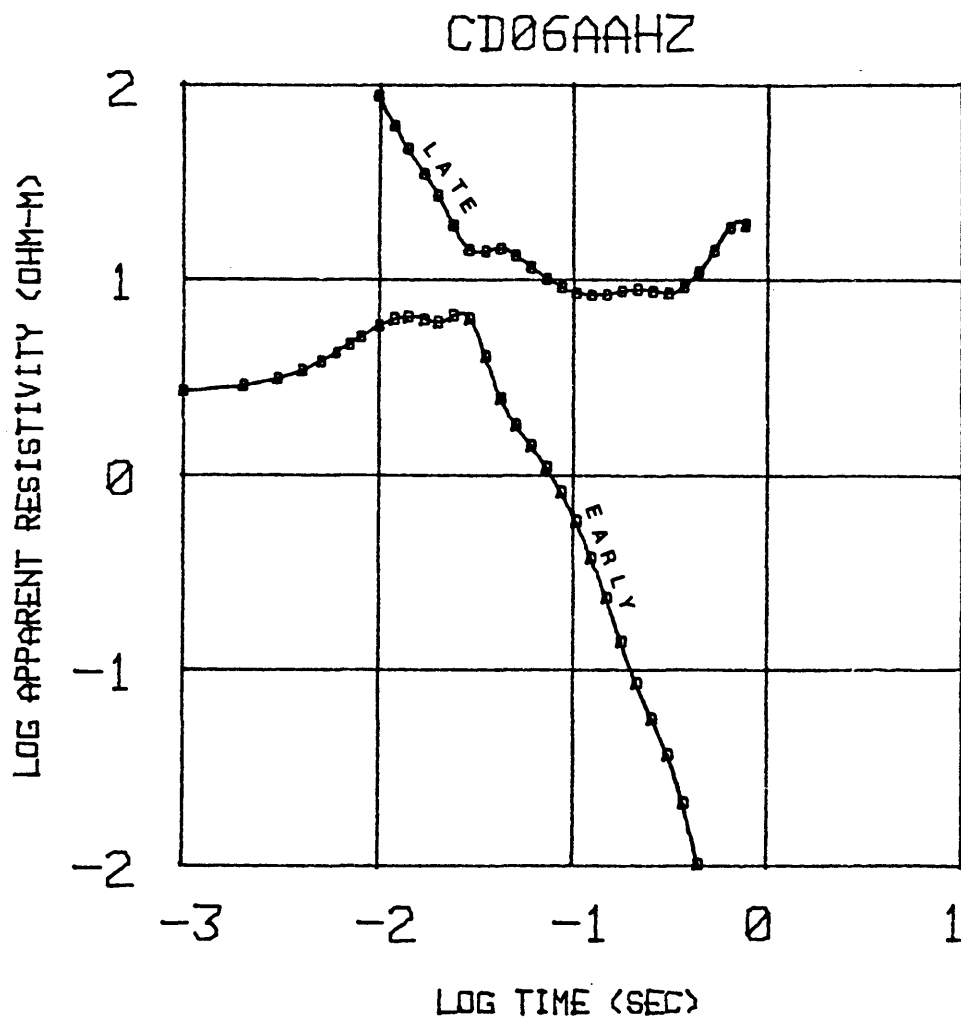


Figure 46

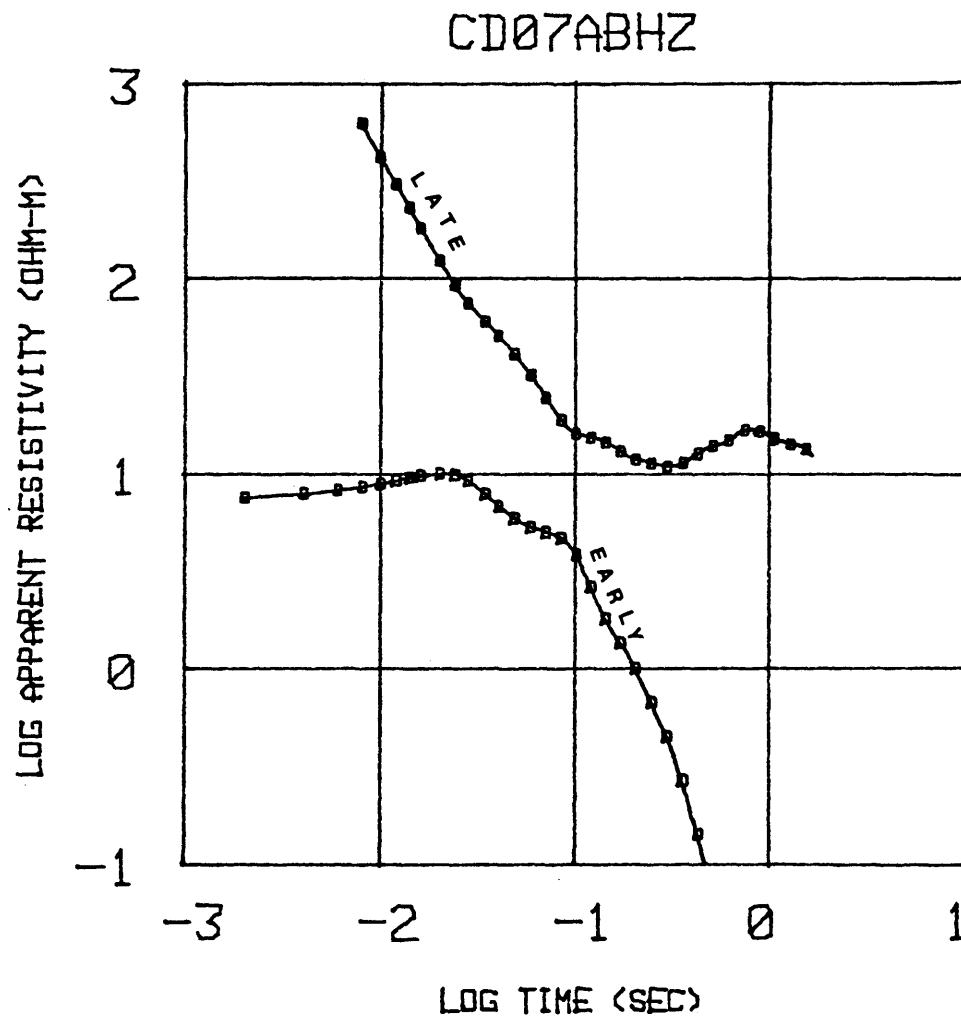


Figure 47

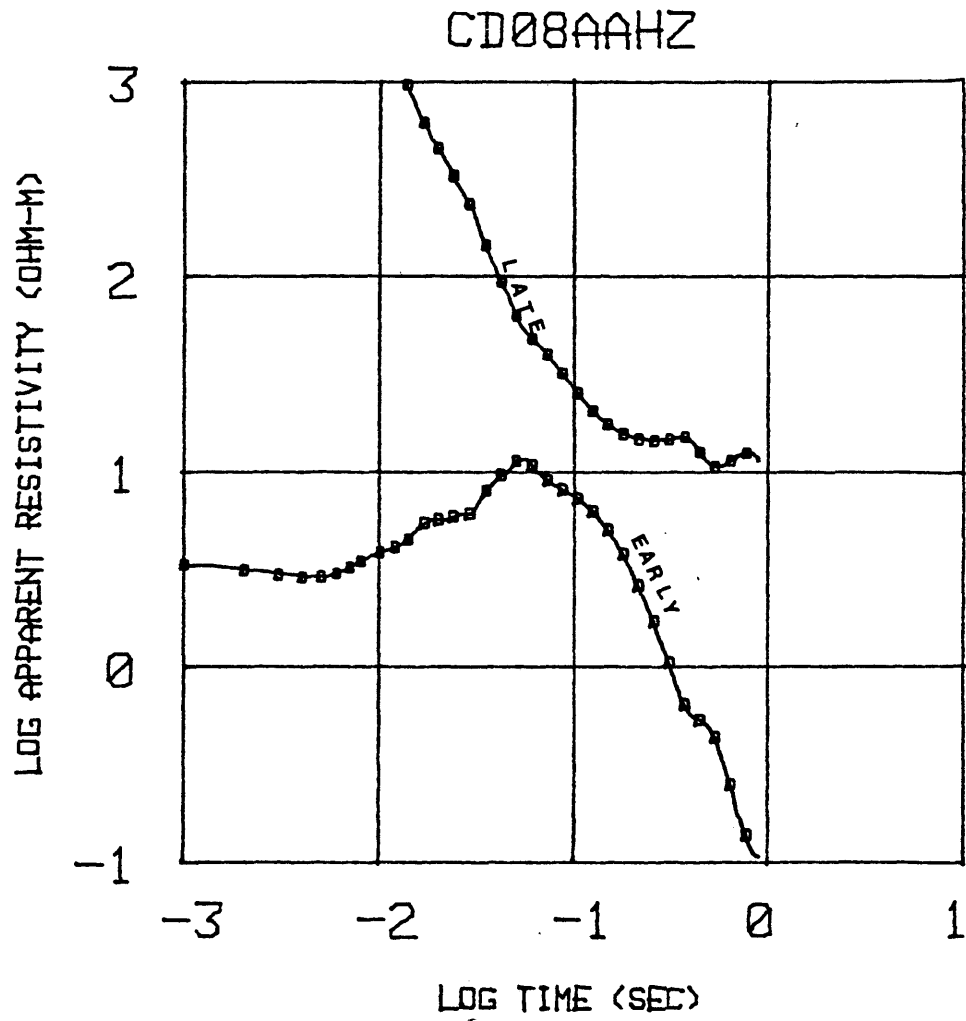


Figure 48

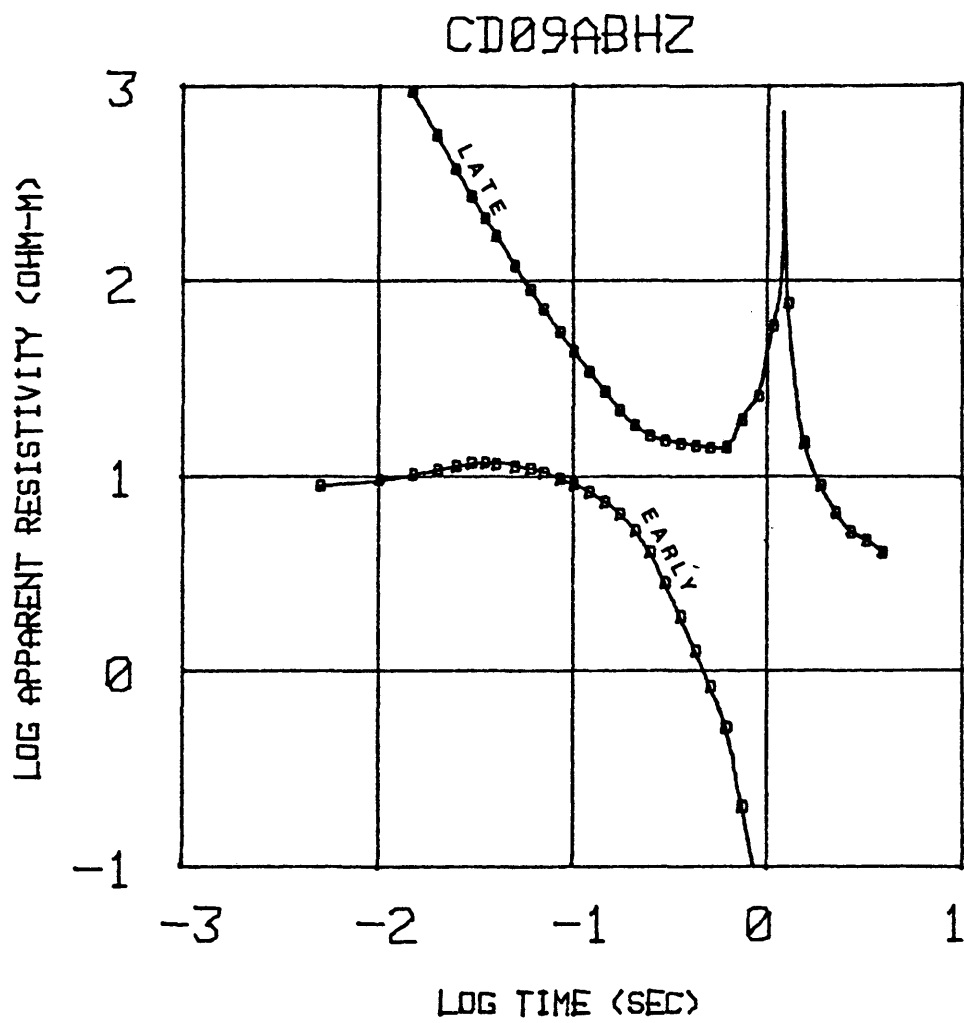


Figure 49

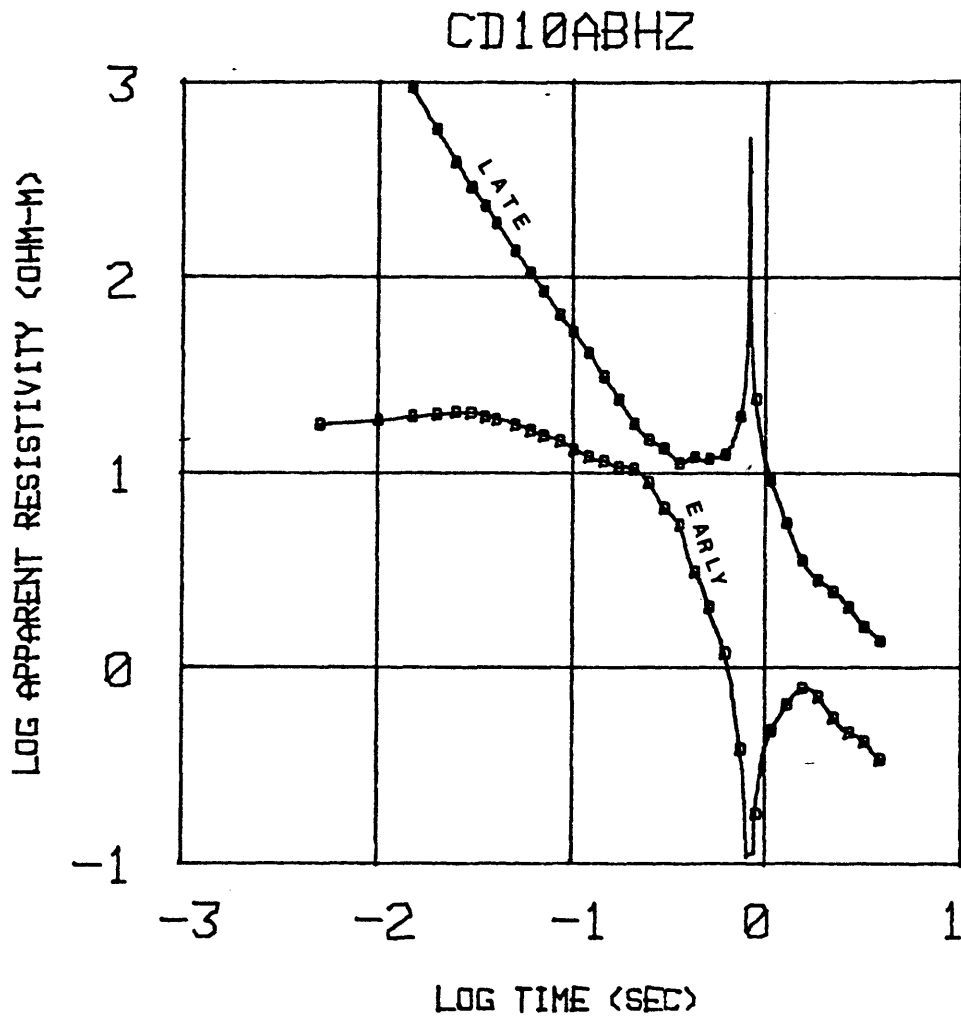


Figure 50

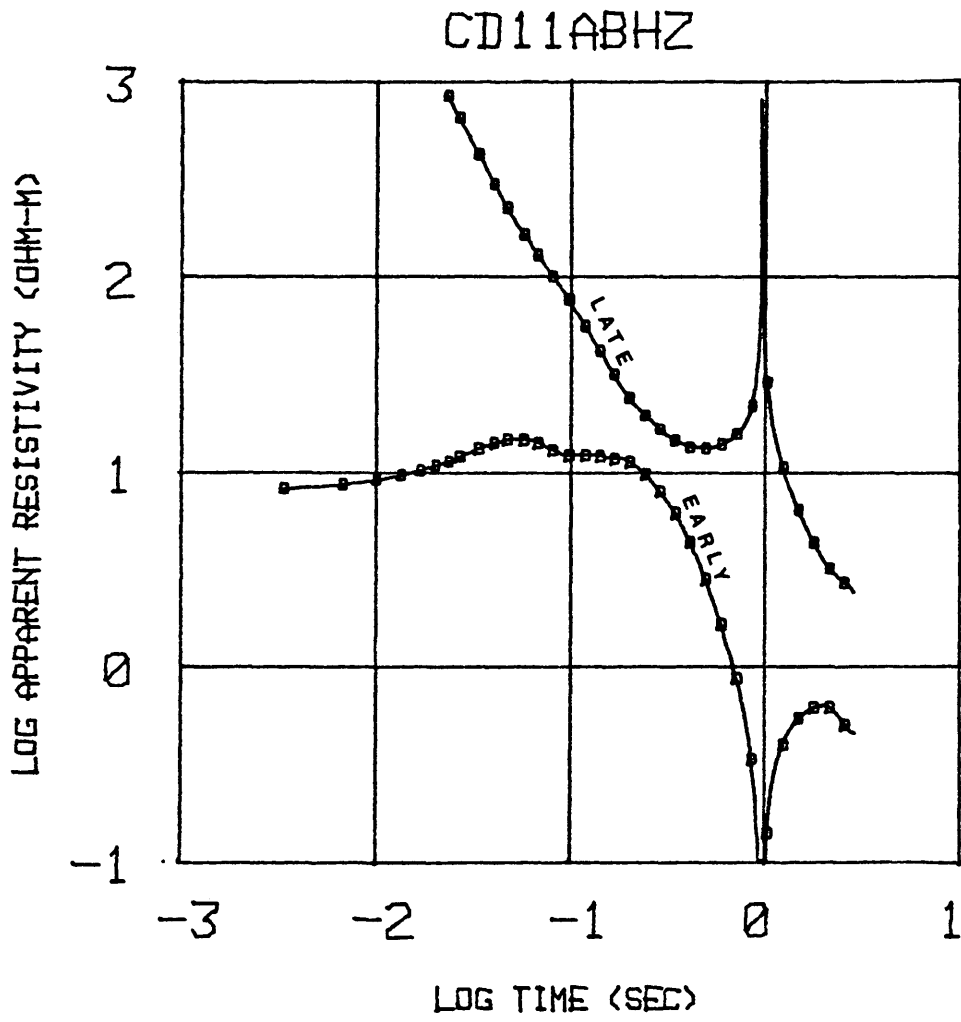


Figure 51

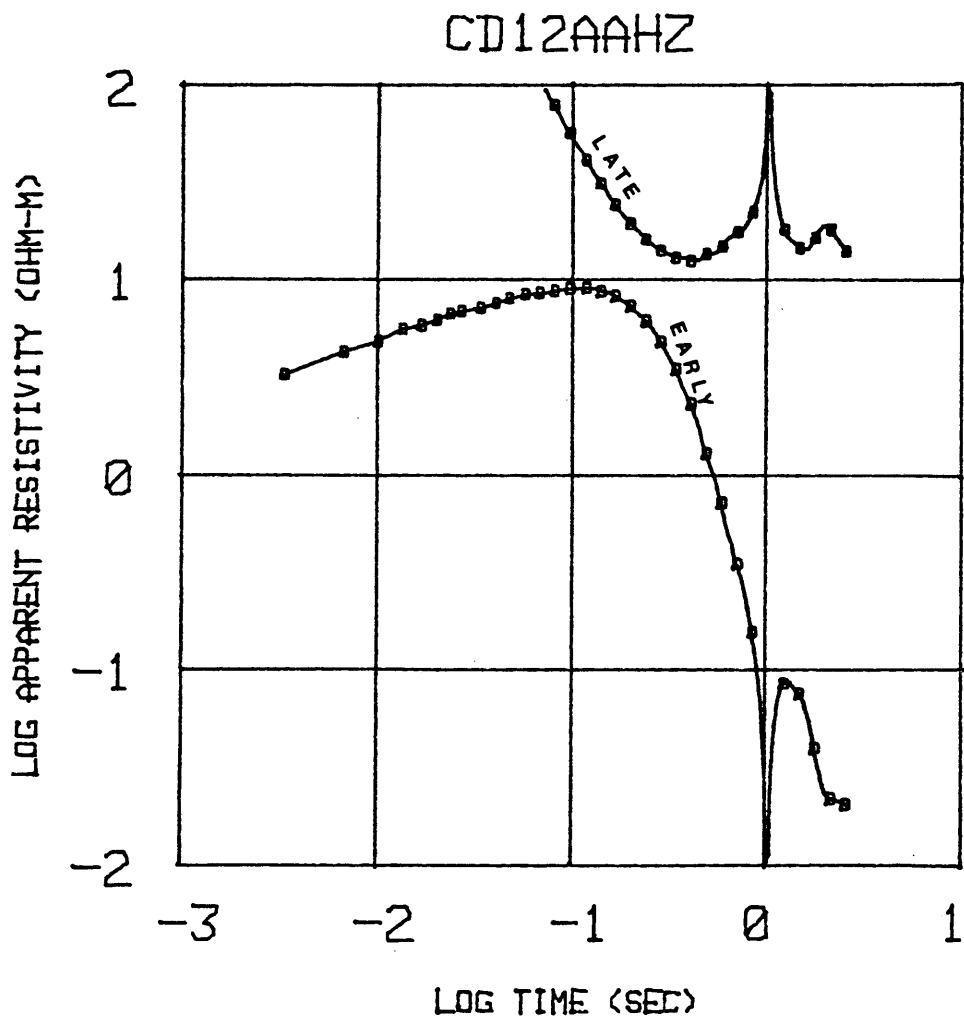


Figure 52

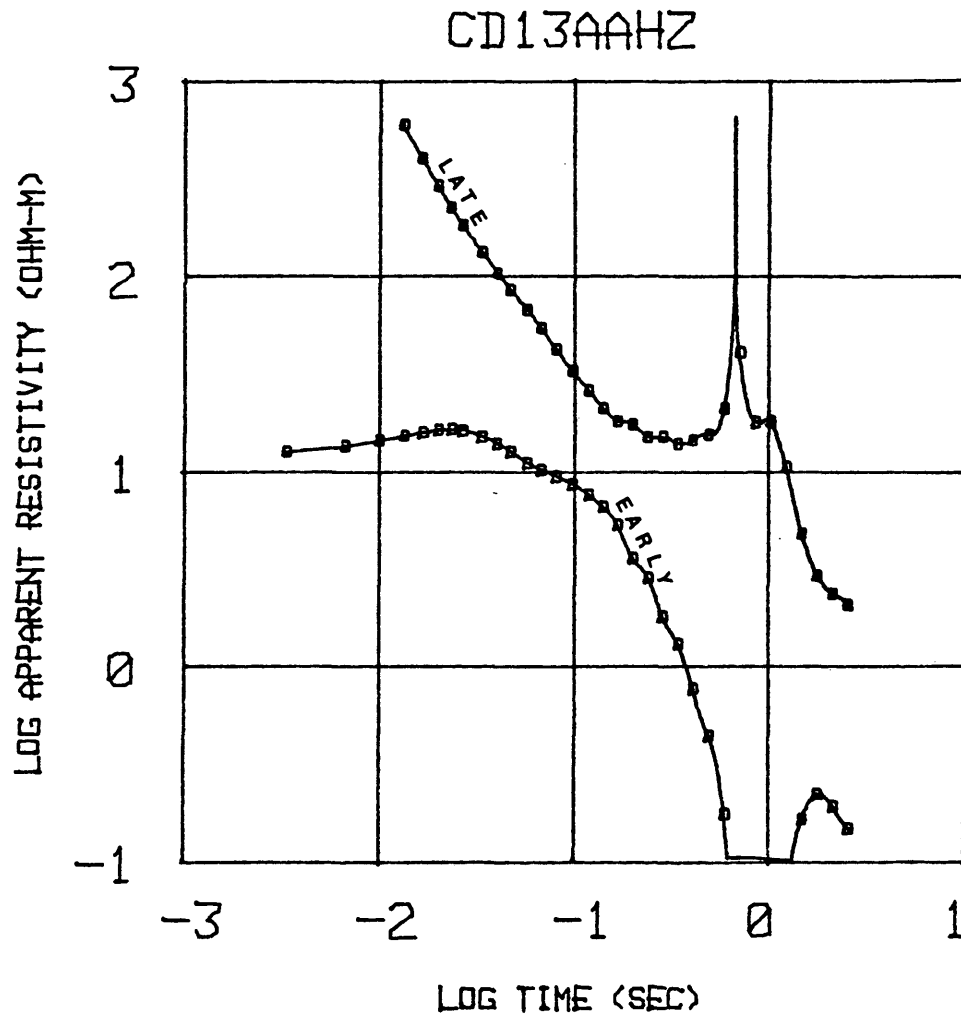


Figure 53

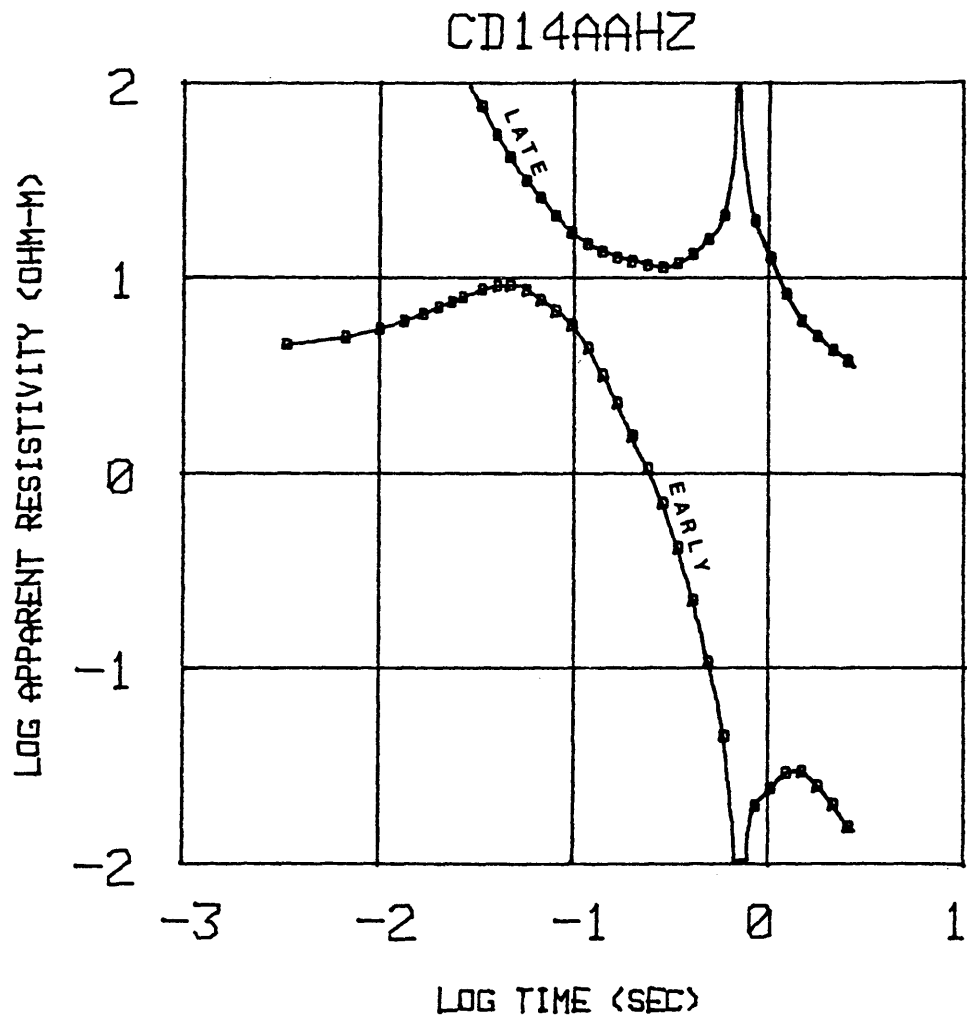


Figure 54

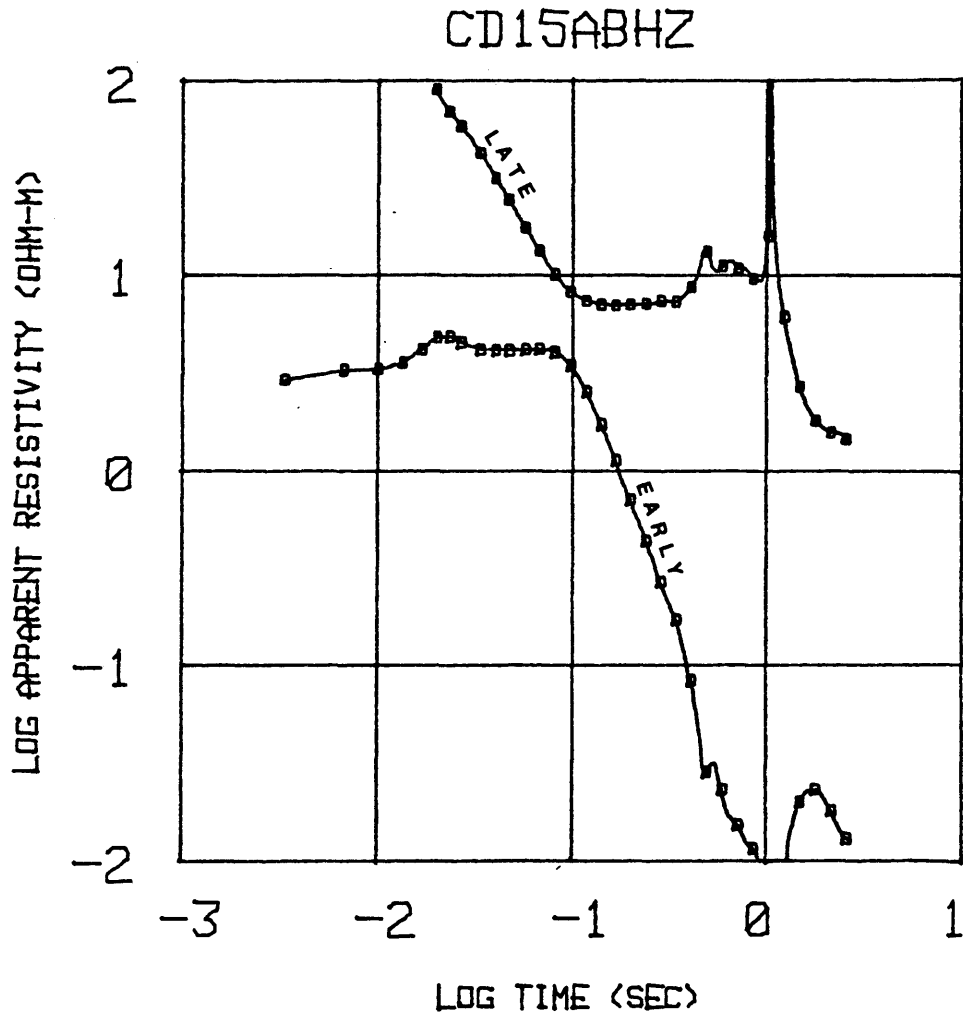


Figure 55

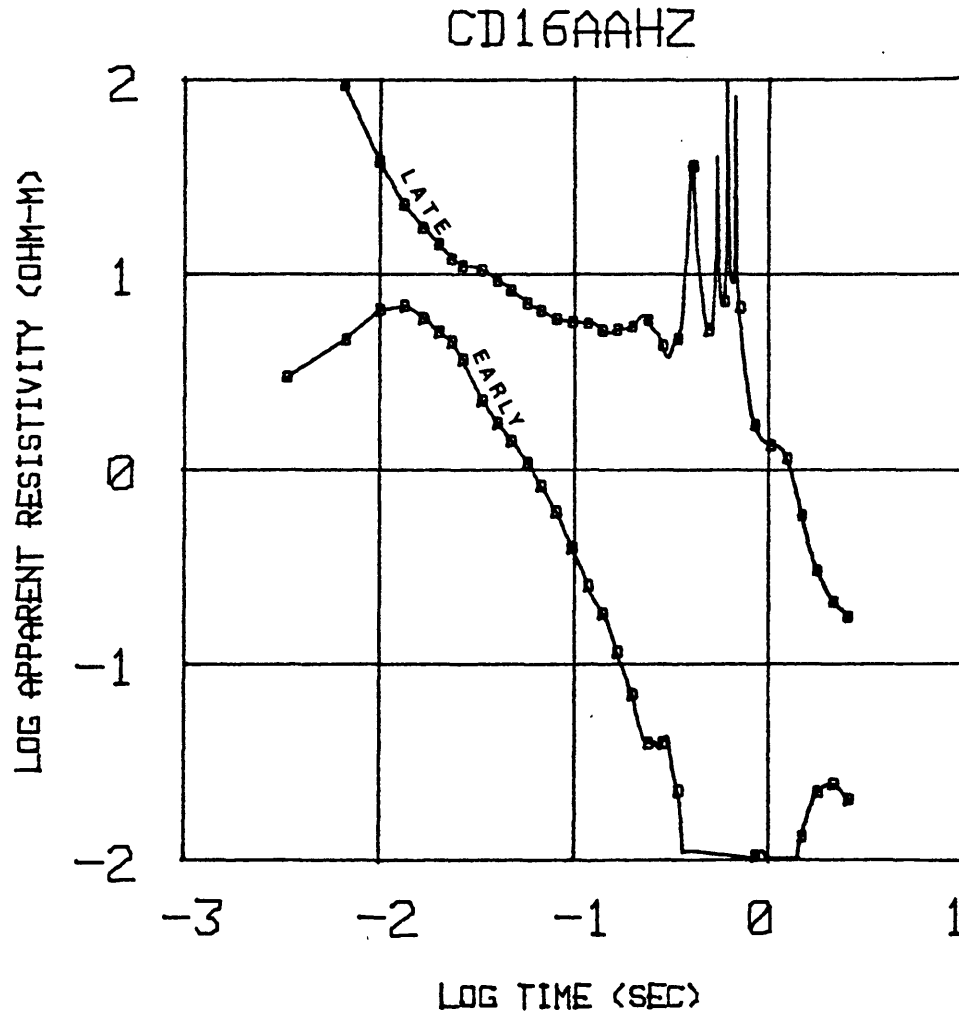


Figure 56

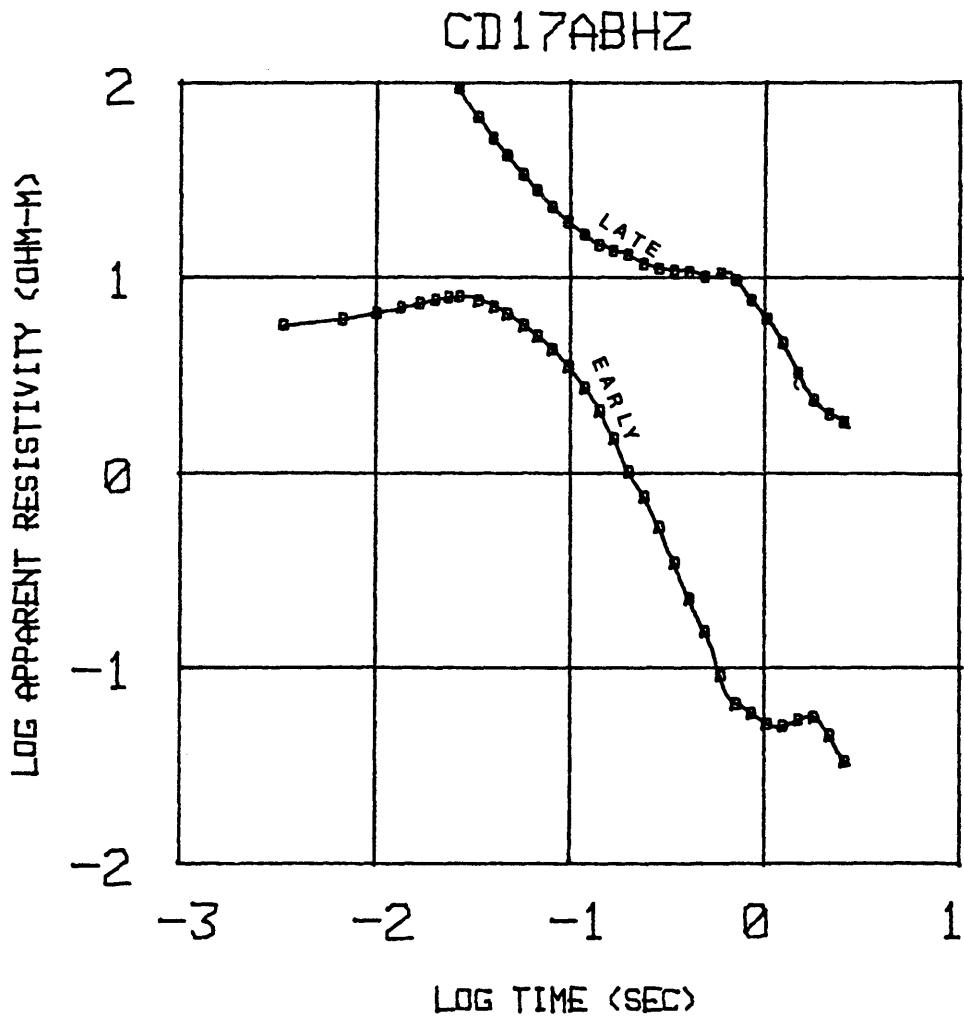


Figure 57

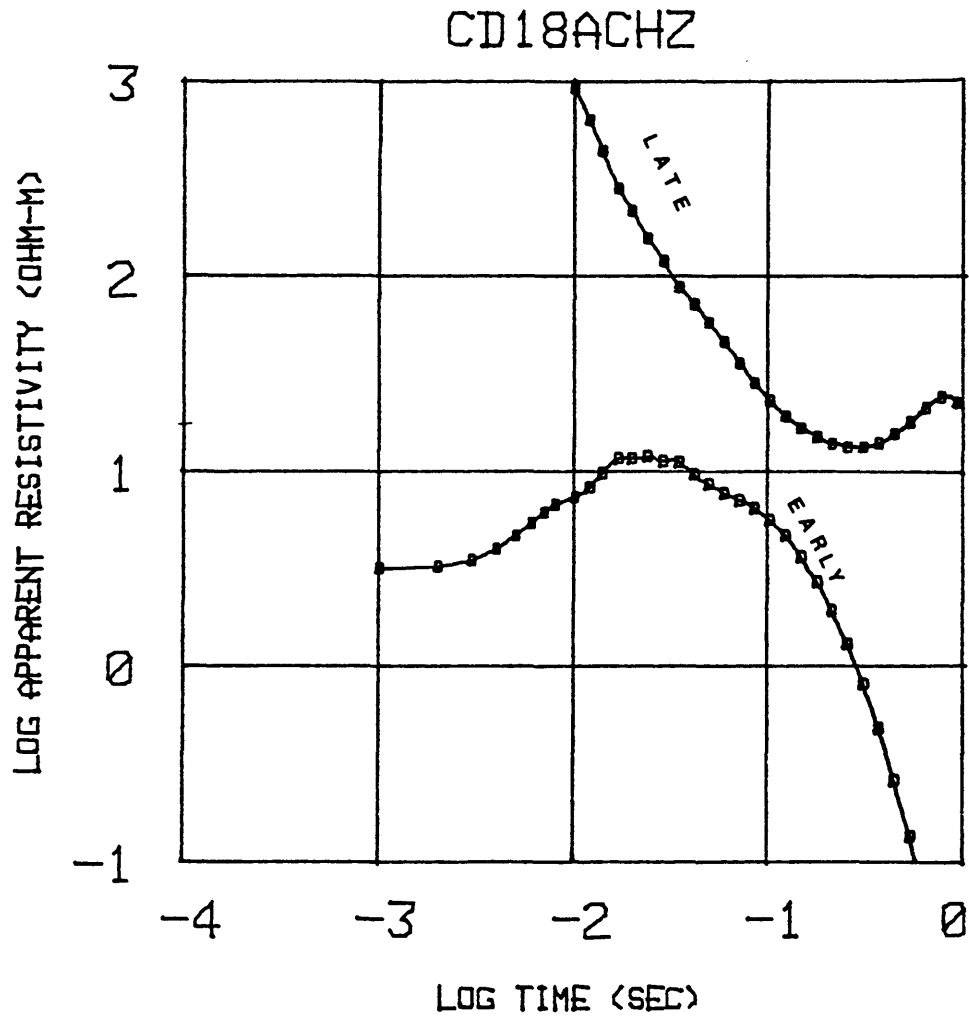


Figure 58

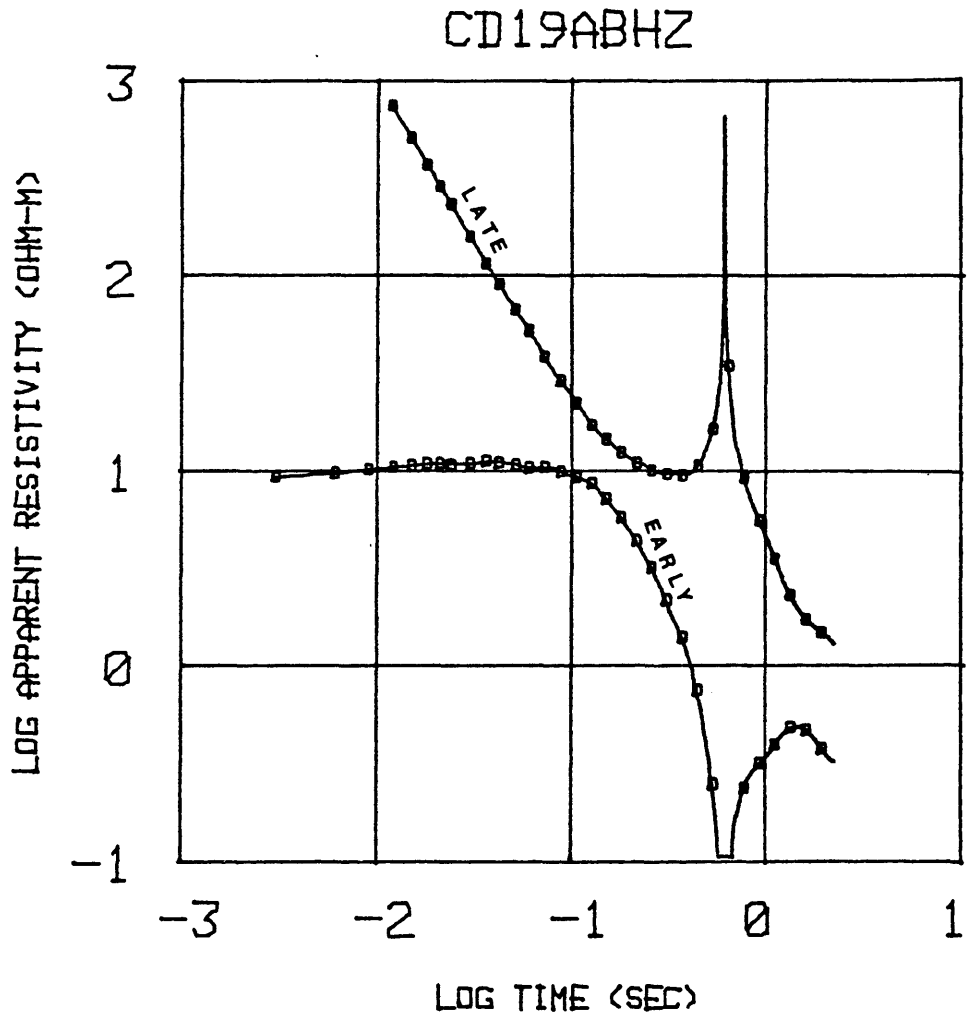


Figure 59

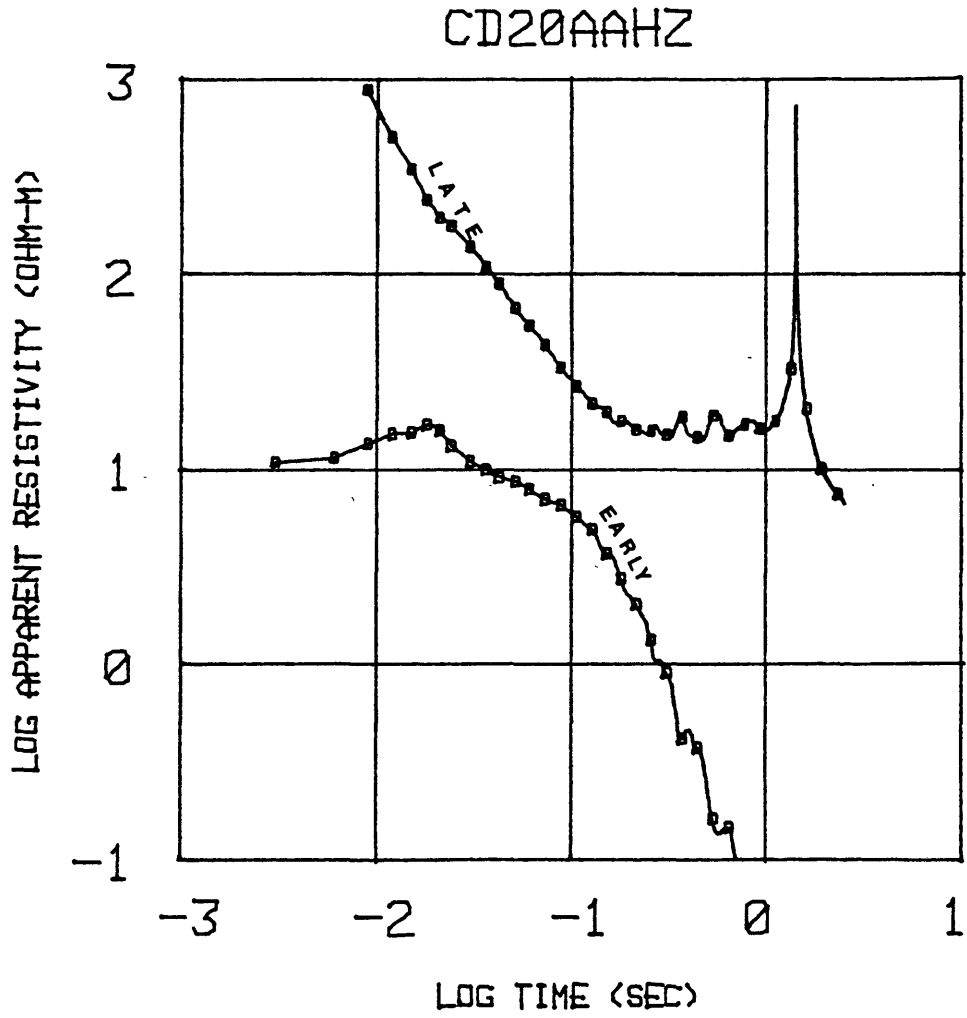


Figure 60

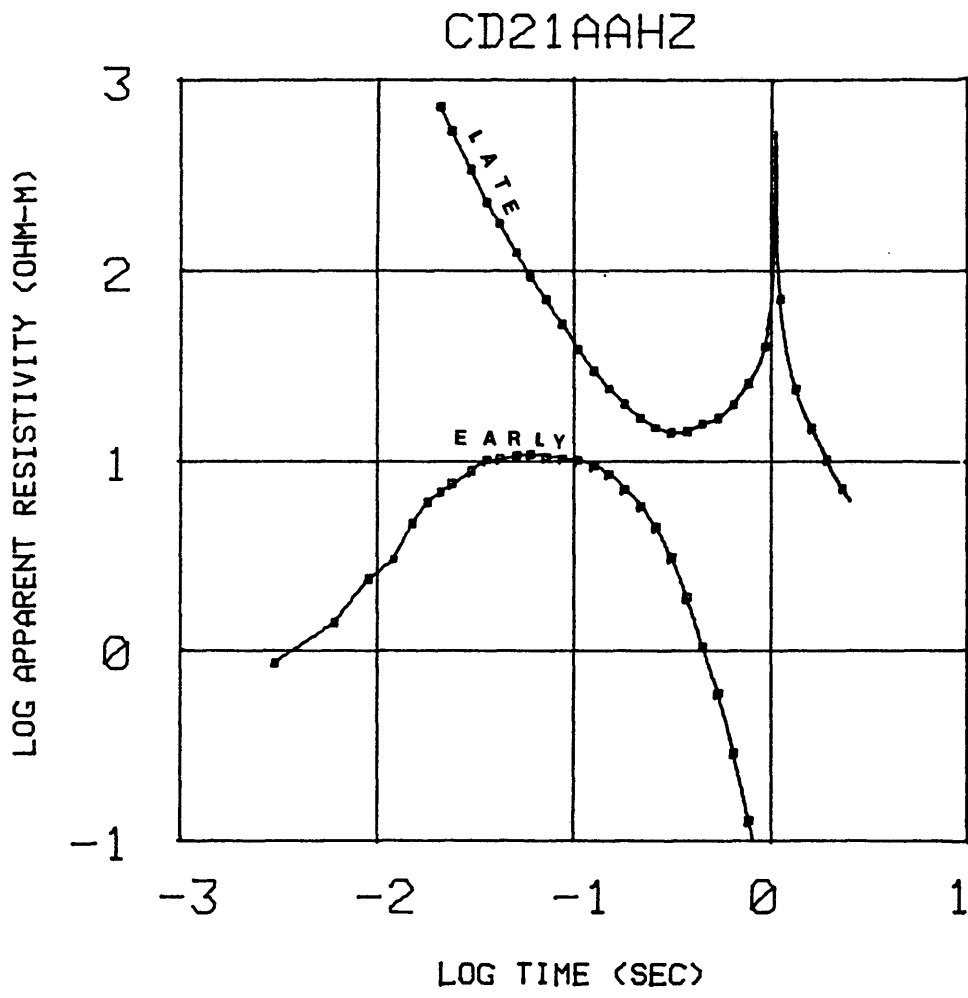


Figure 61

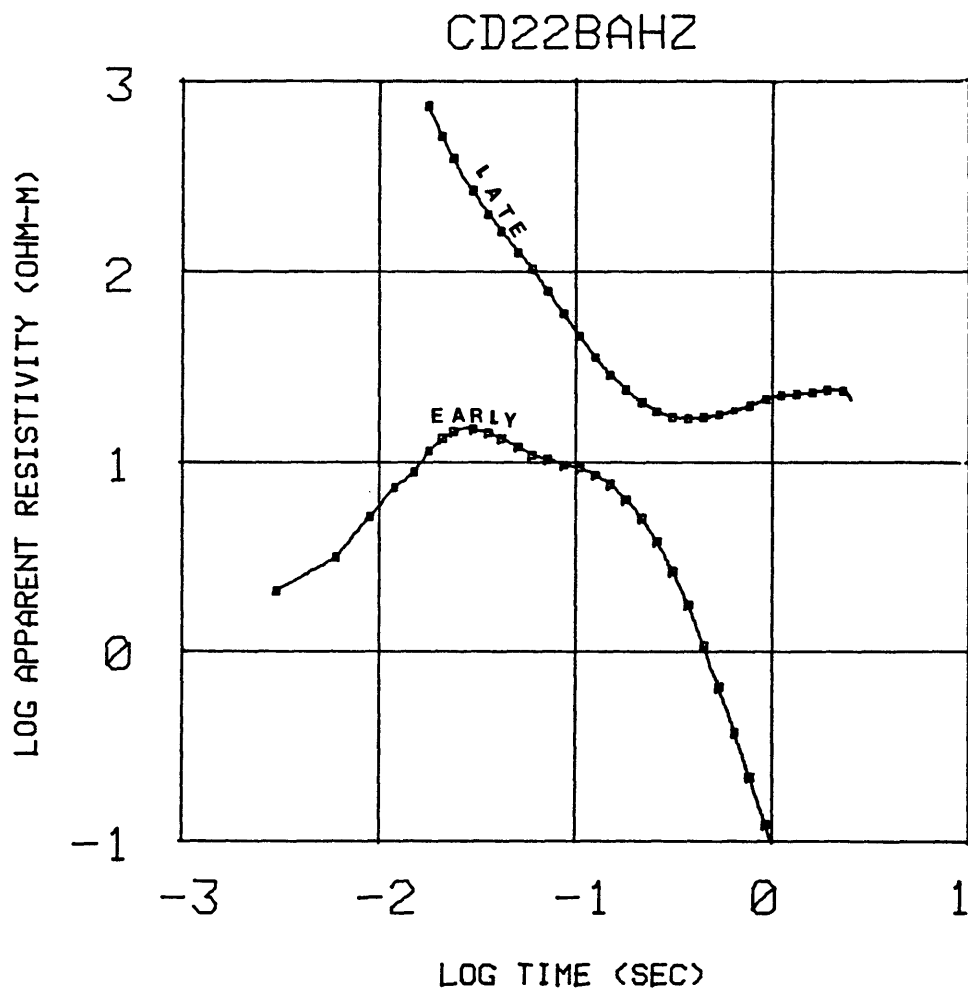


Figure 62

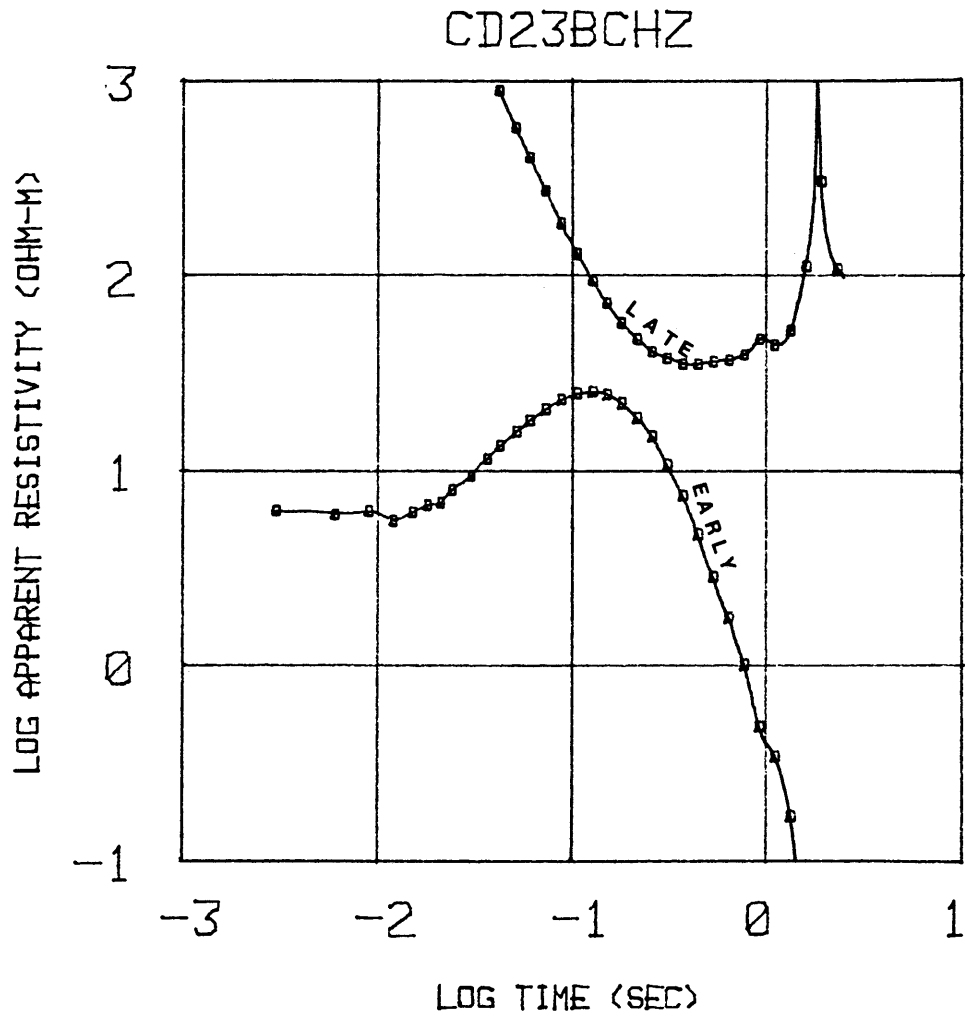


Figure 63

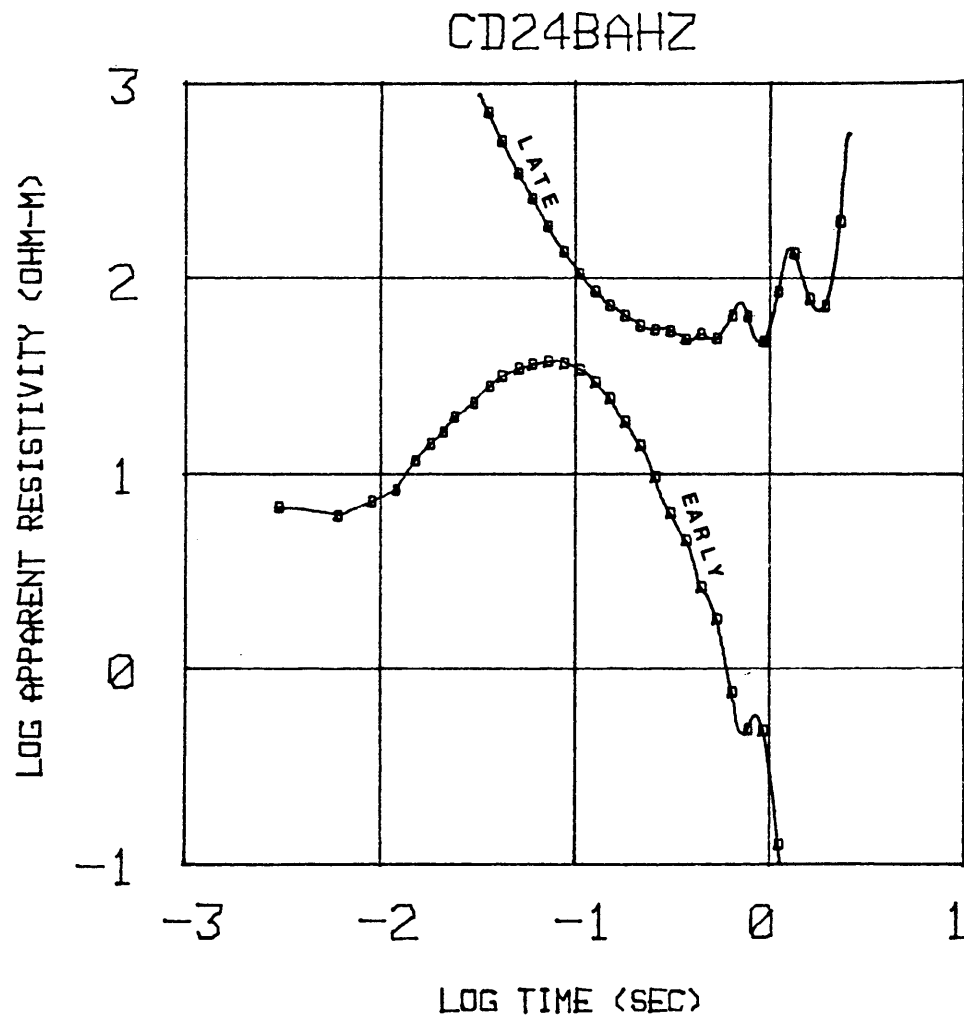


Figure 64

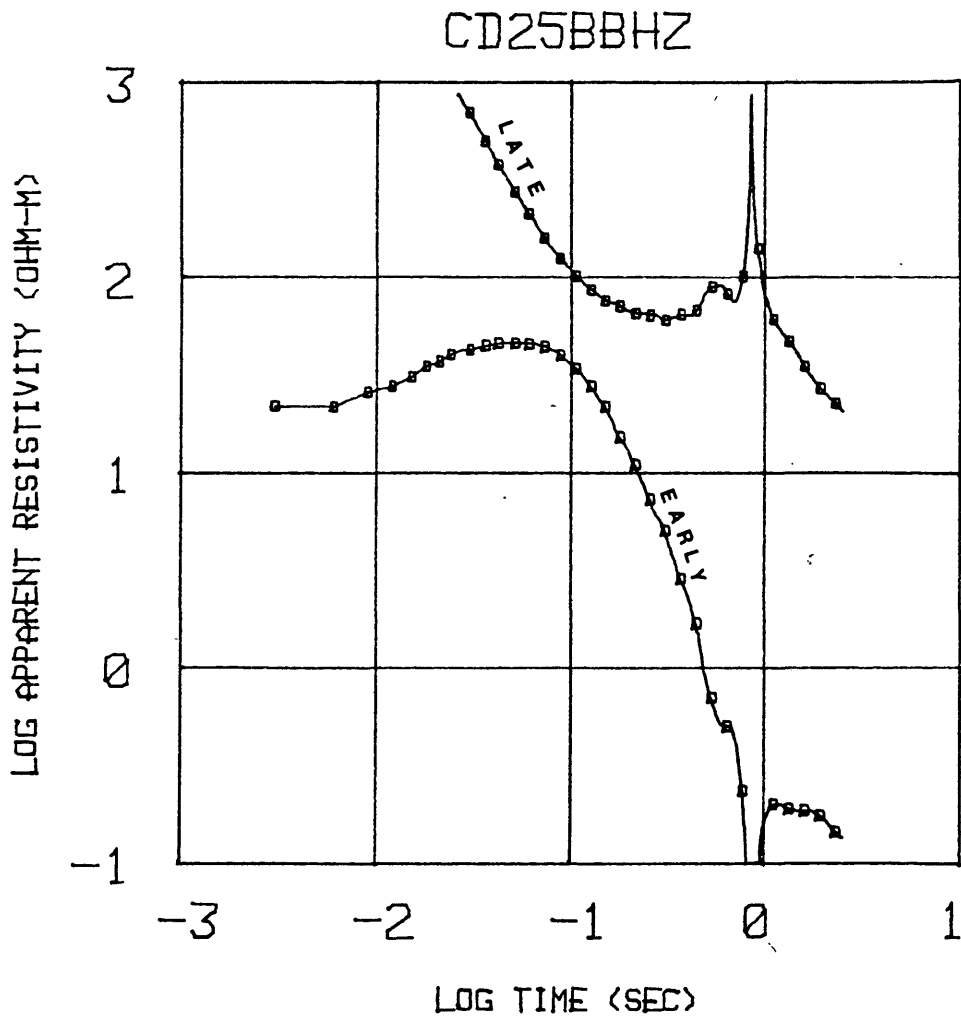


Figure 65

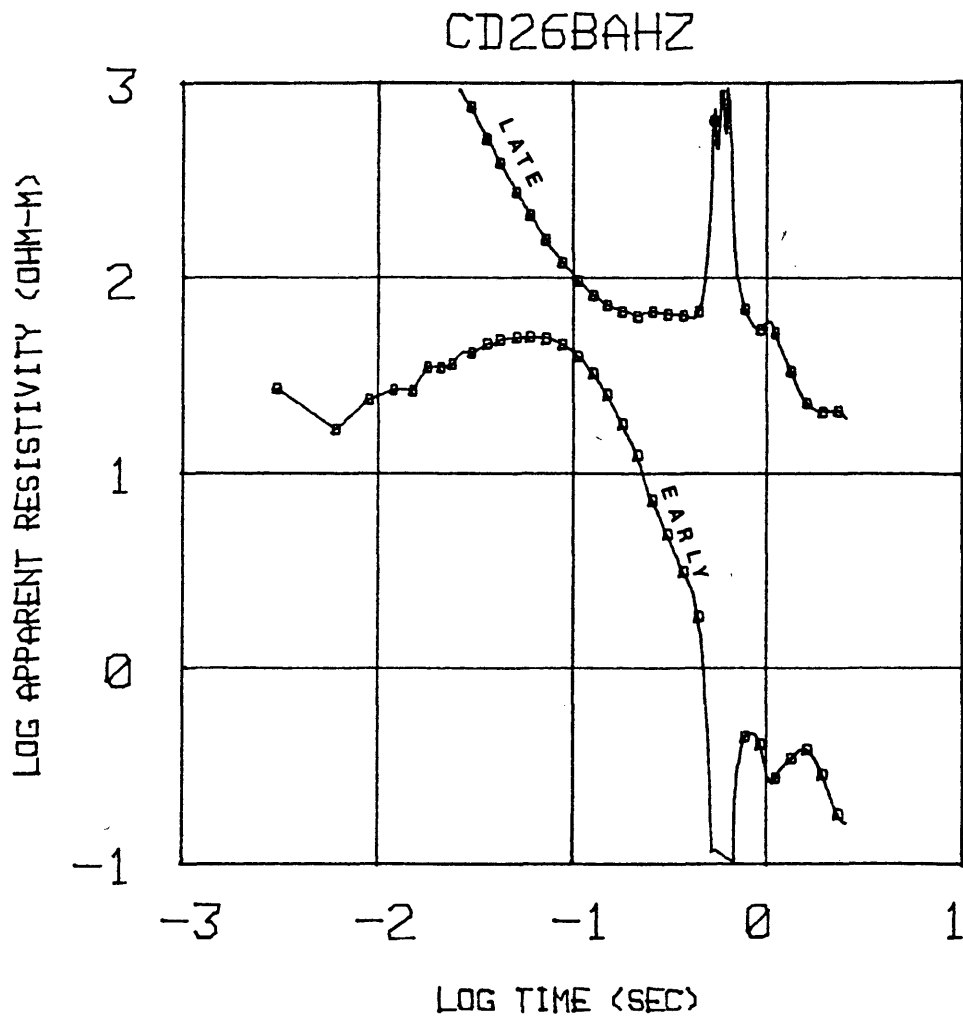


Figure 66

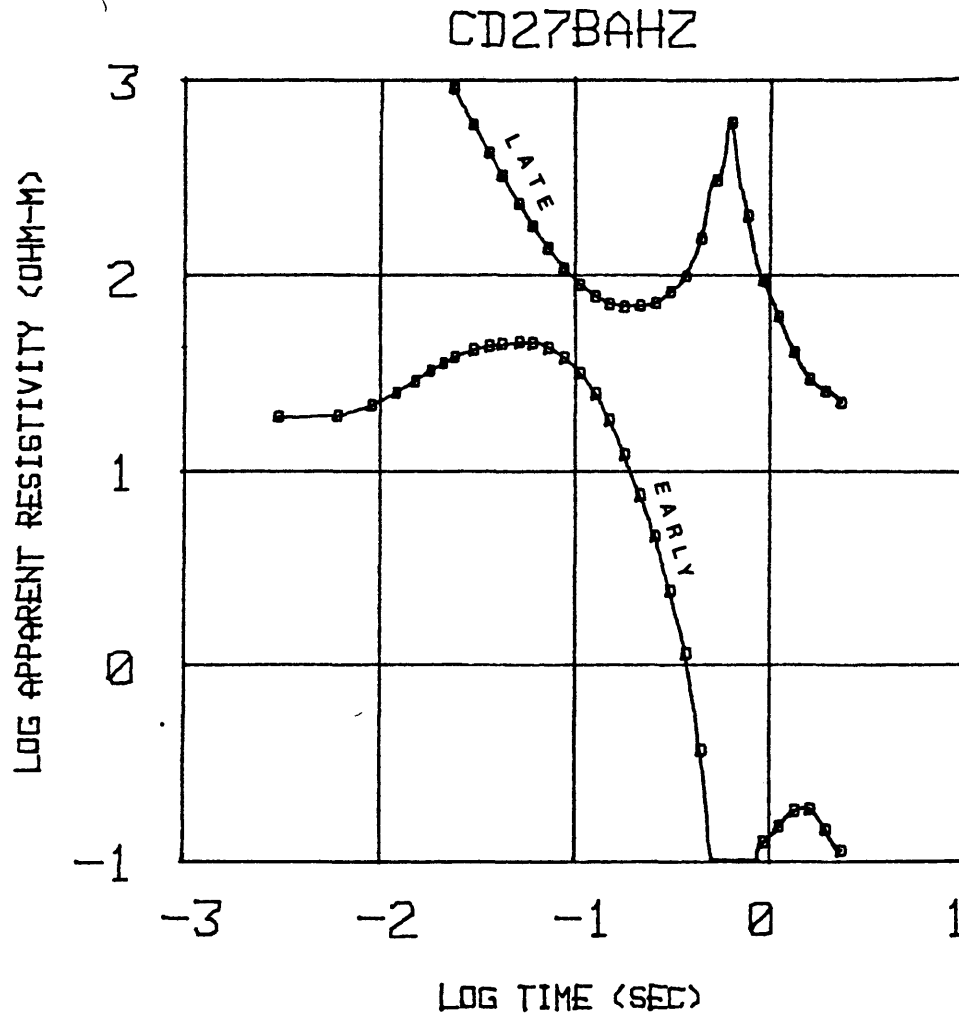


Figure 67

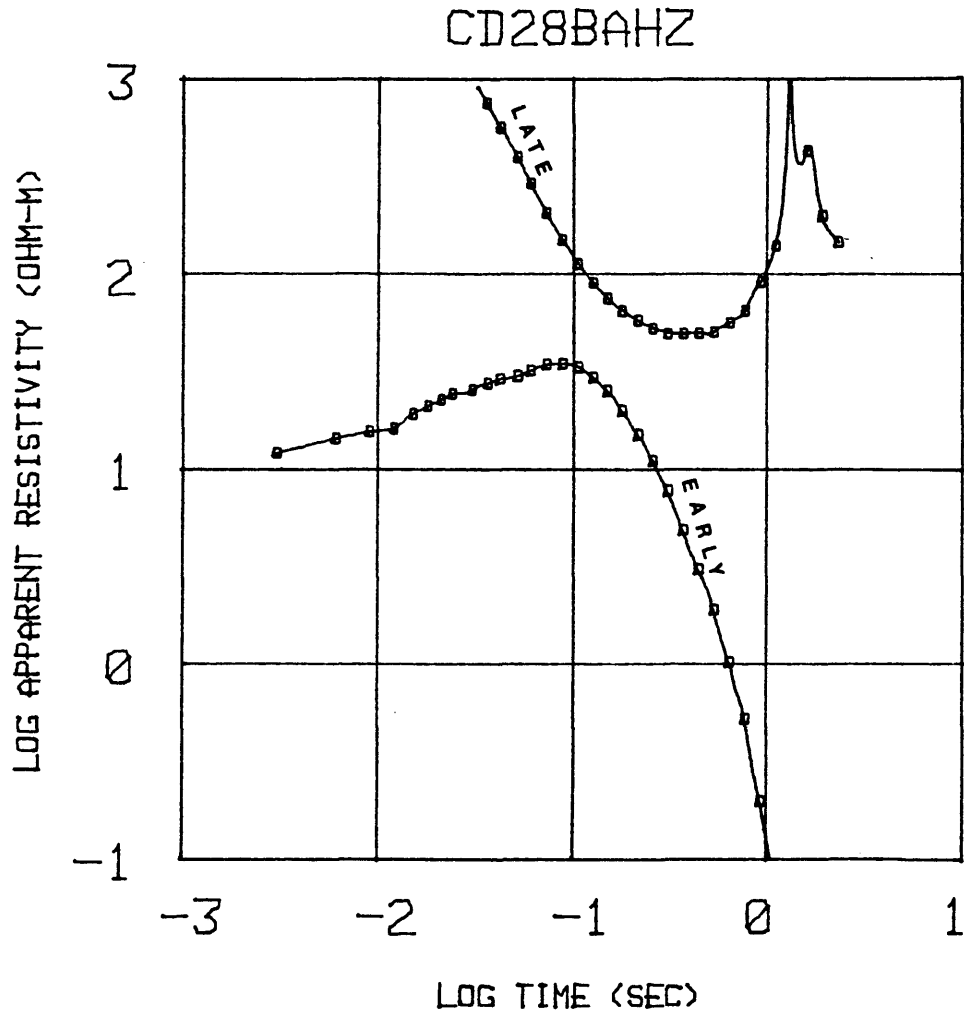


Figure 68

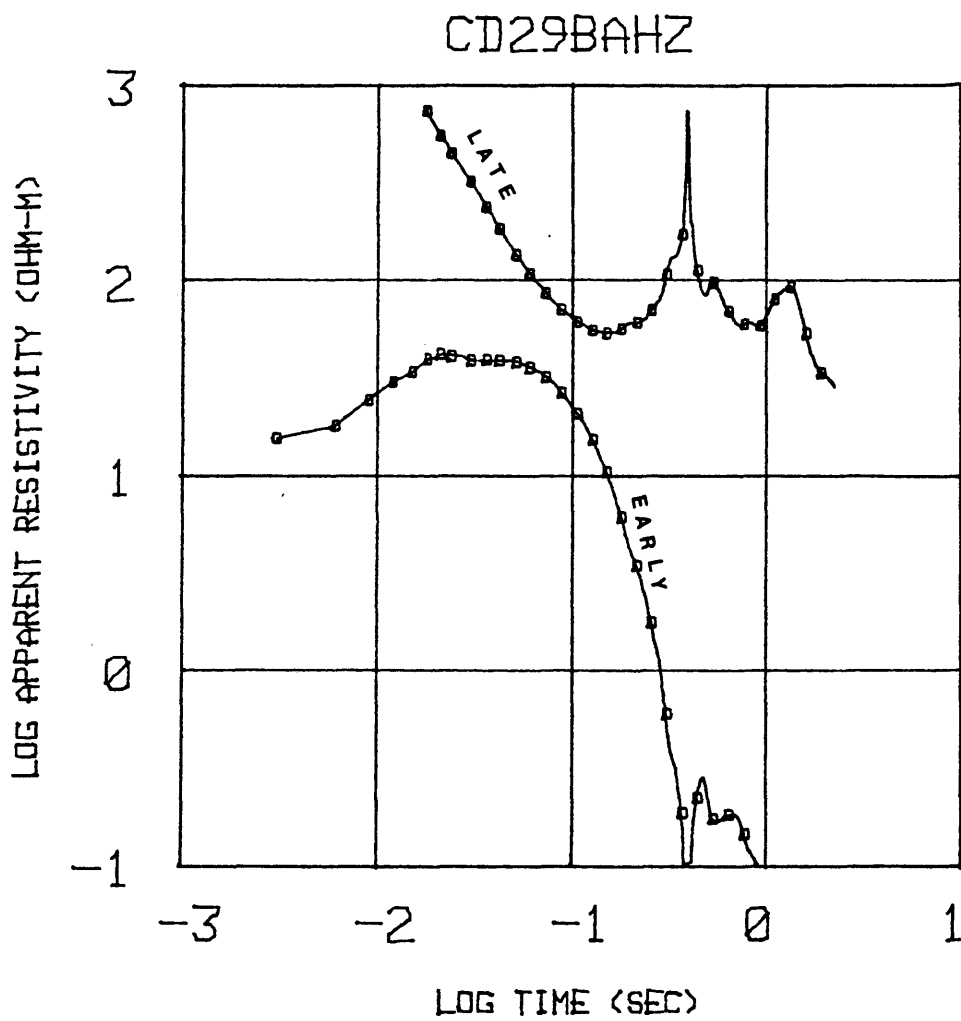


Figure 69

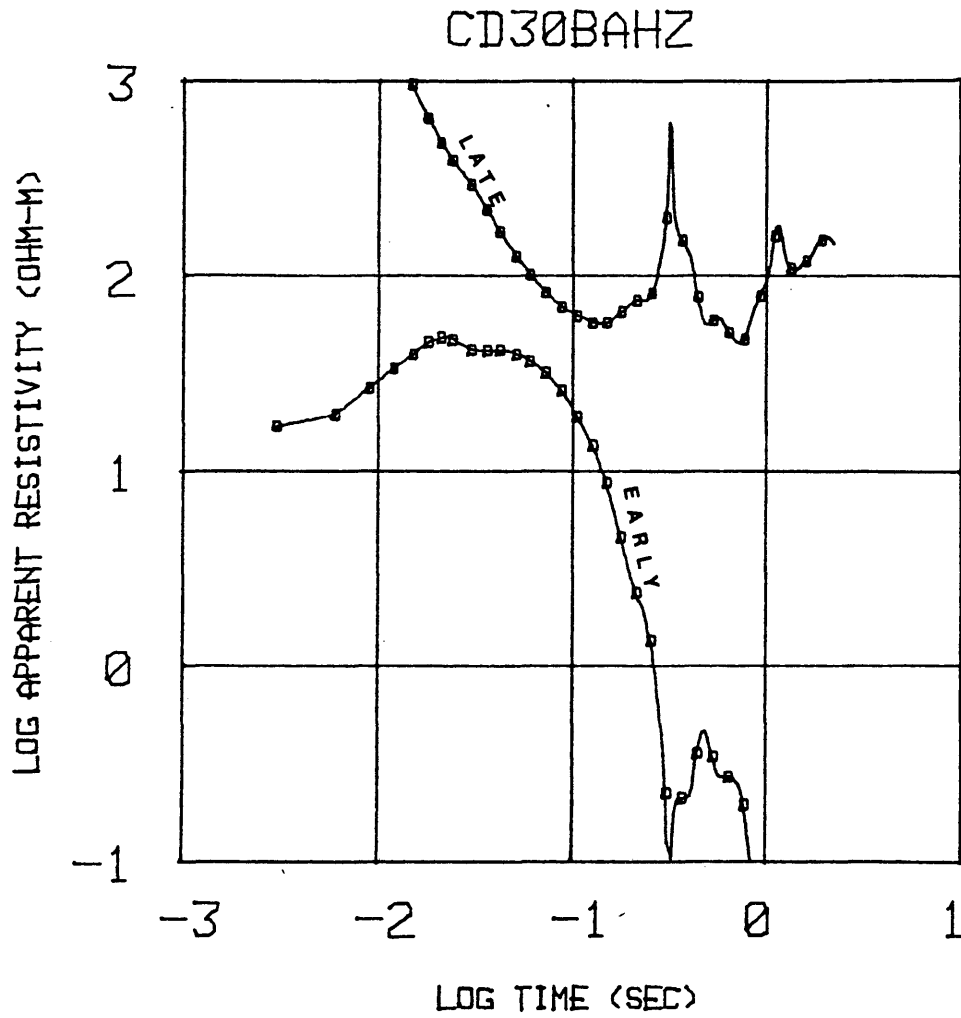


Figure 70

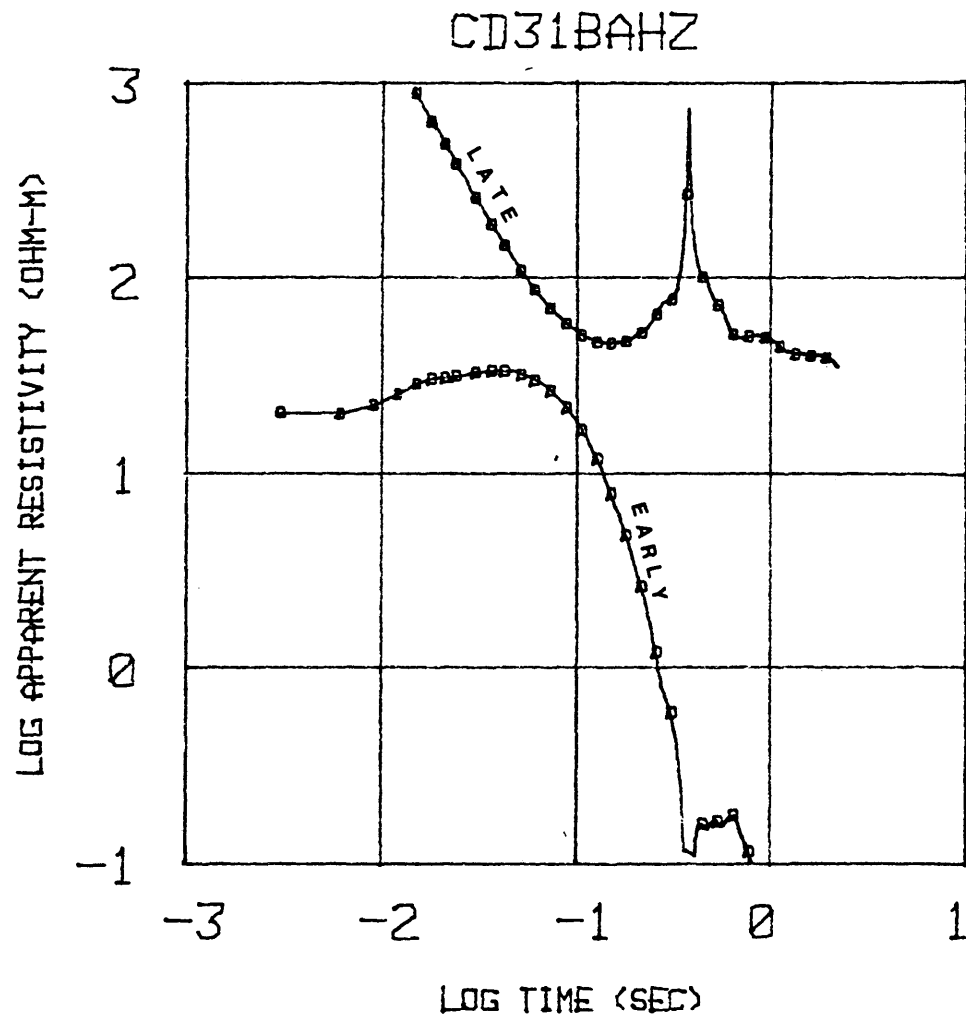


Figure 71

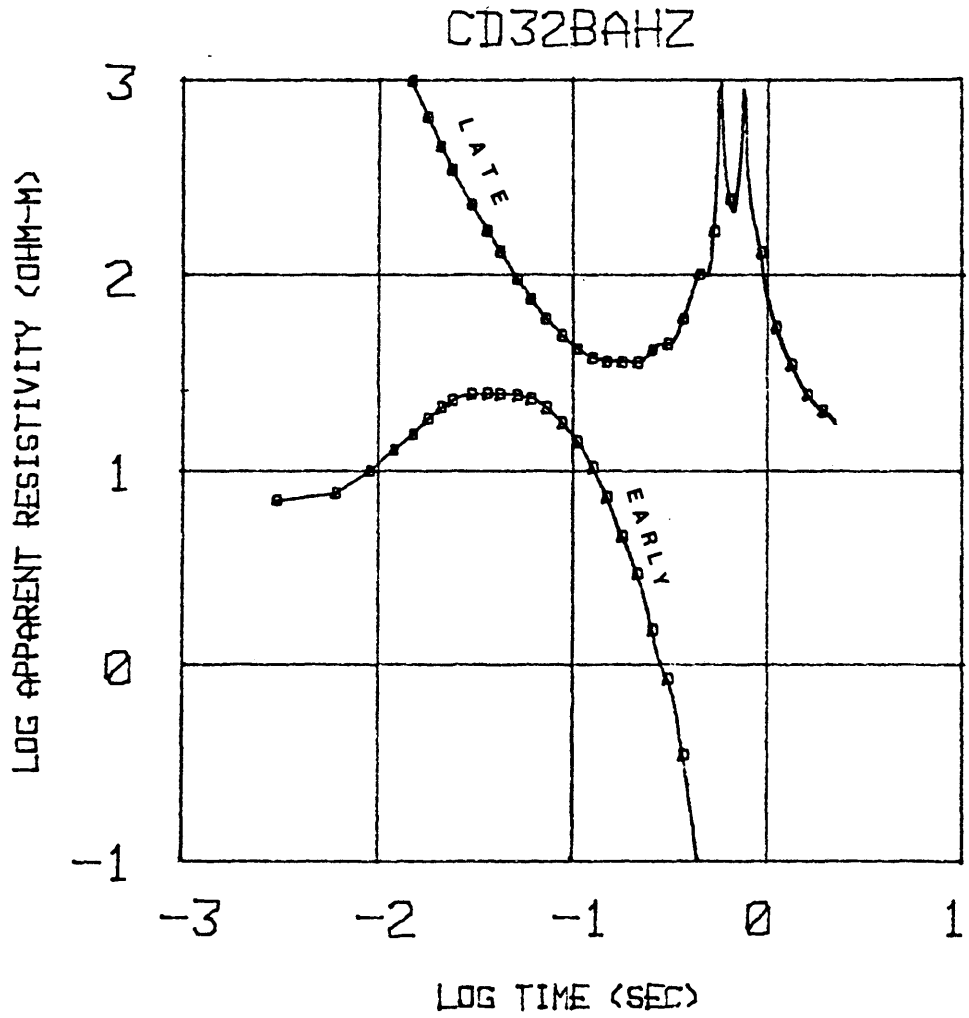


Figure 72

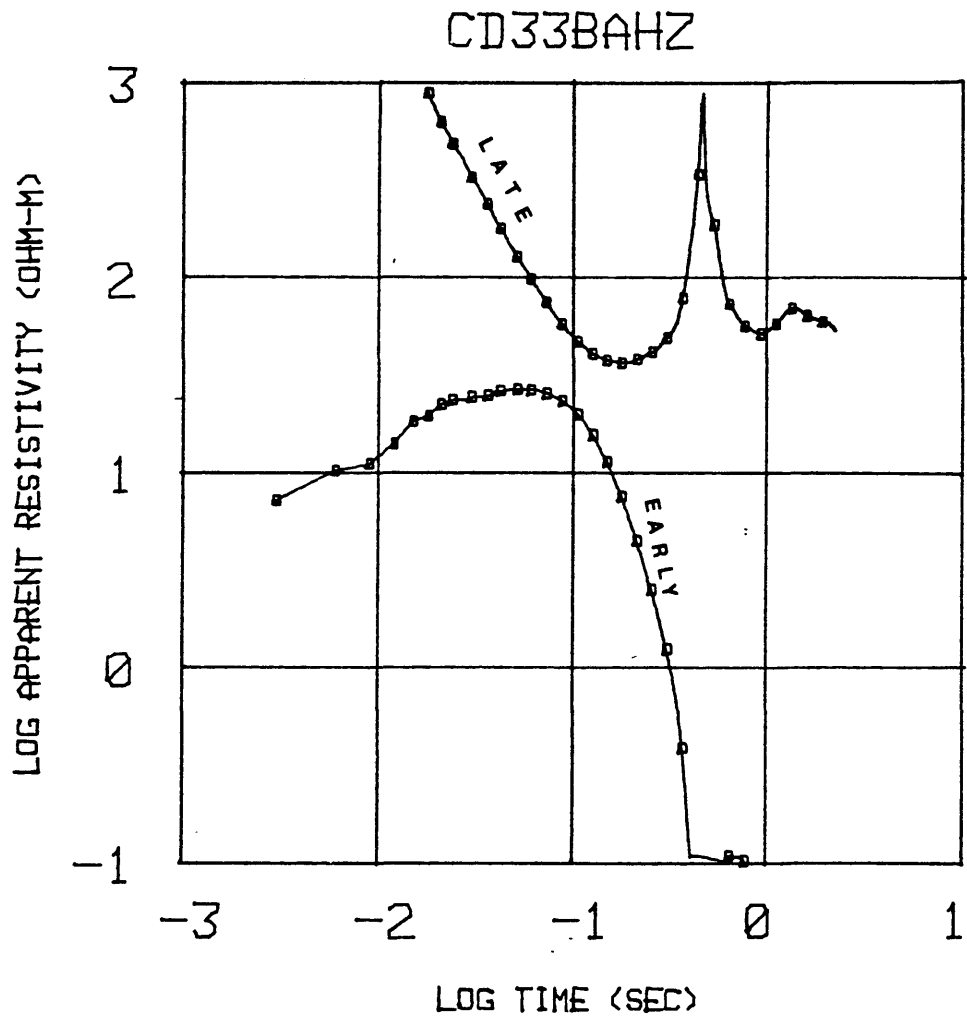


Figure 73

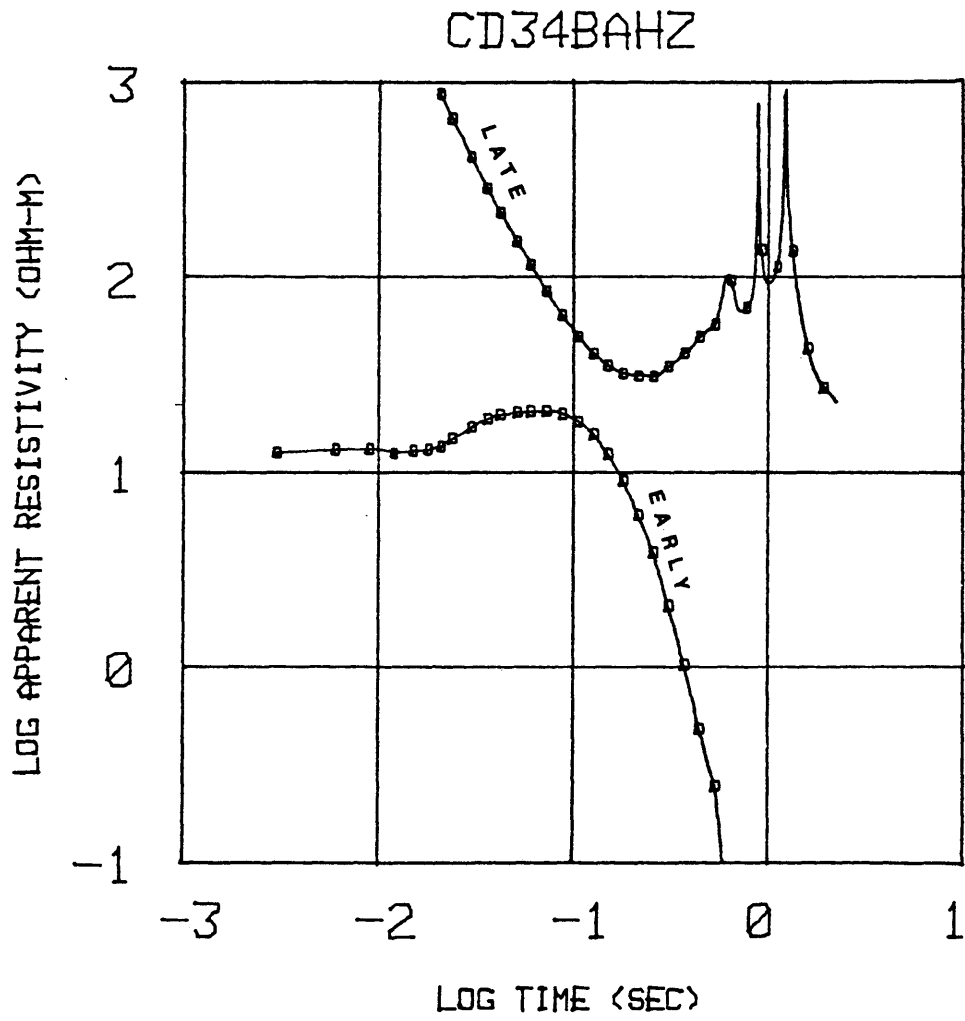


Figure 74

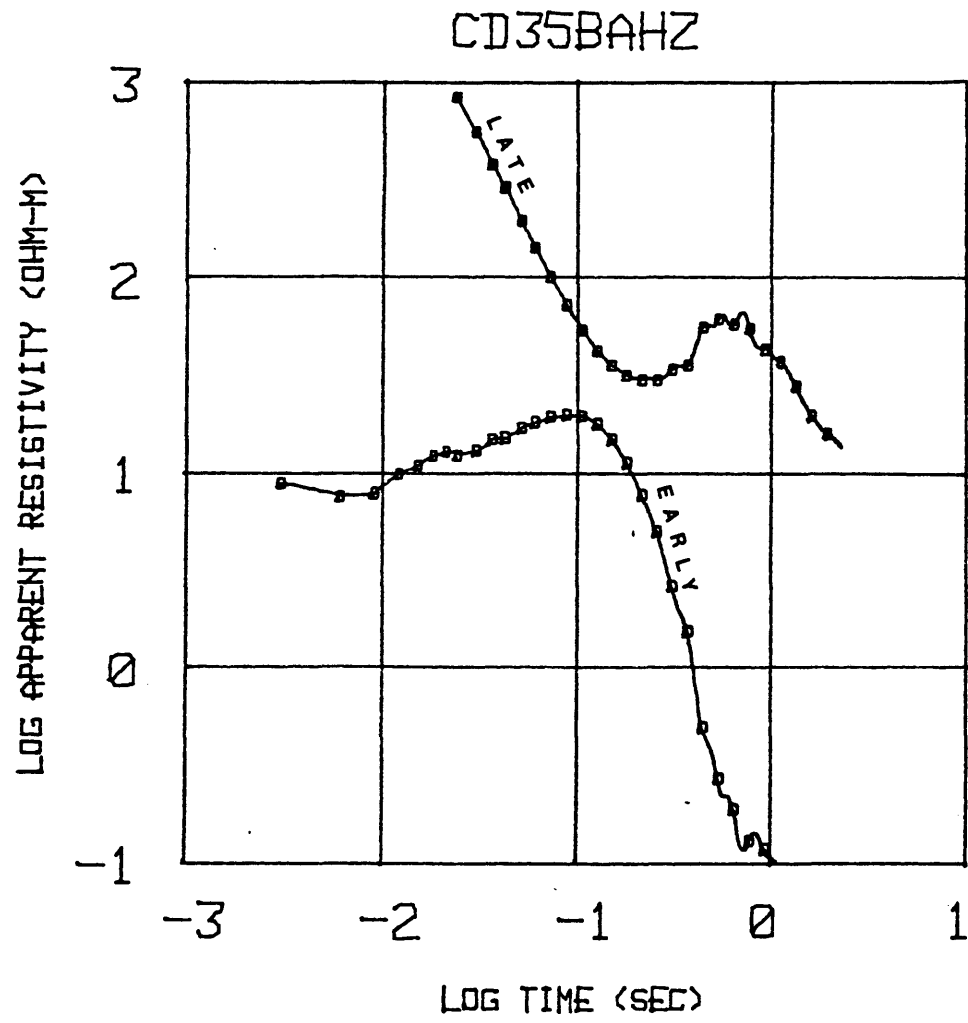


Figure 75

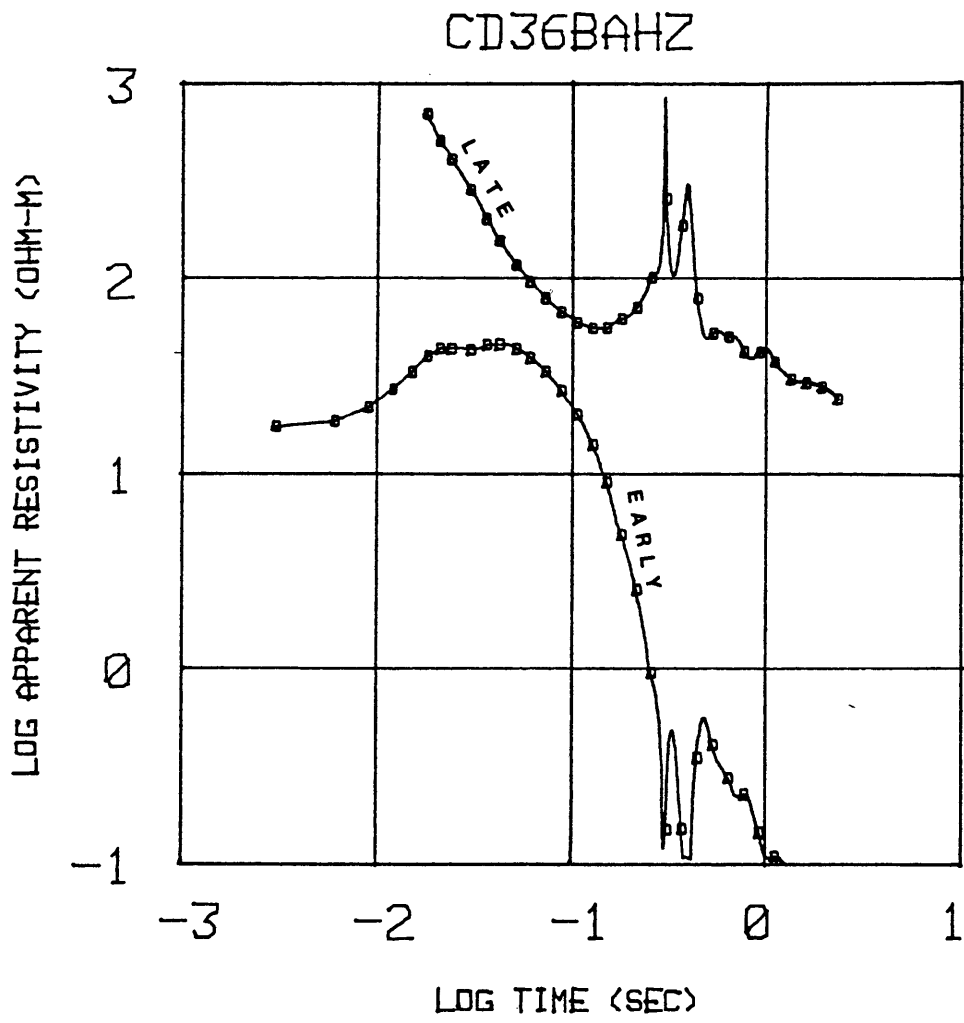


Figure 76

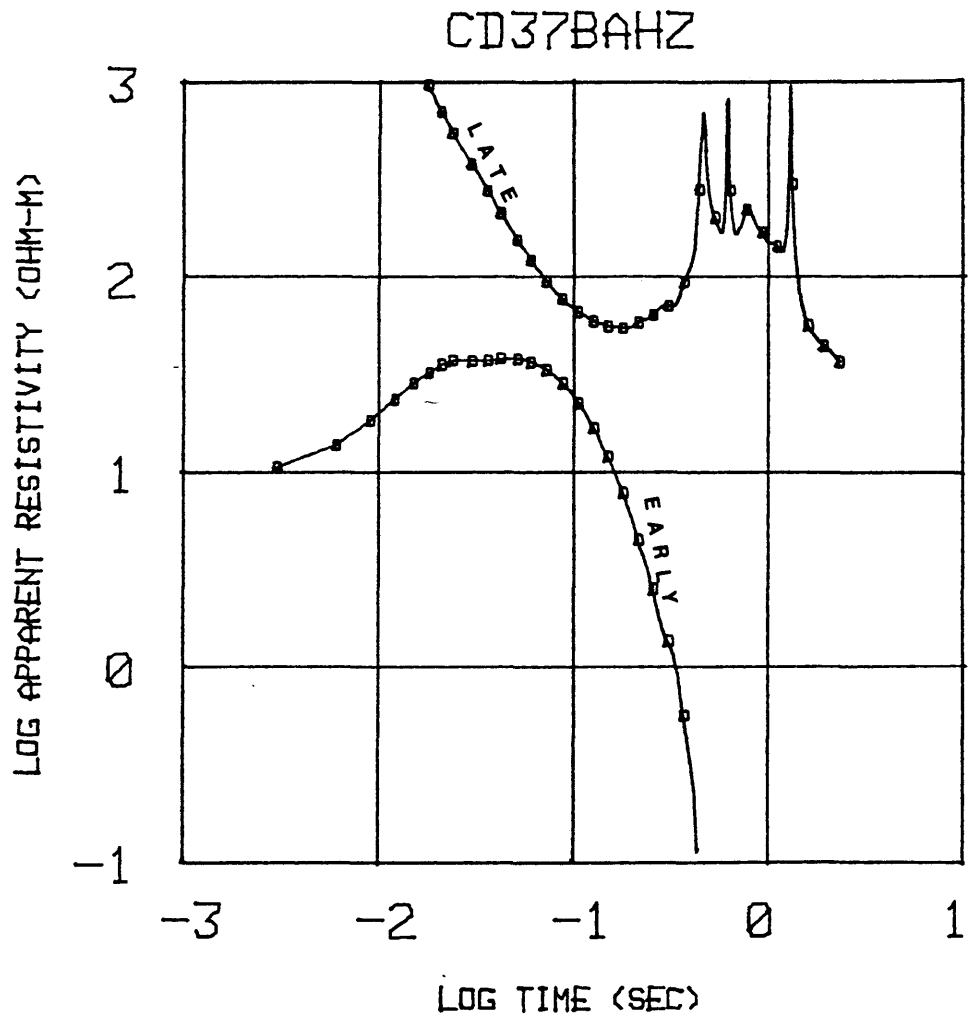


Figure 77

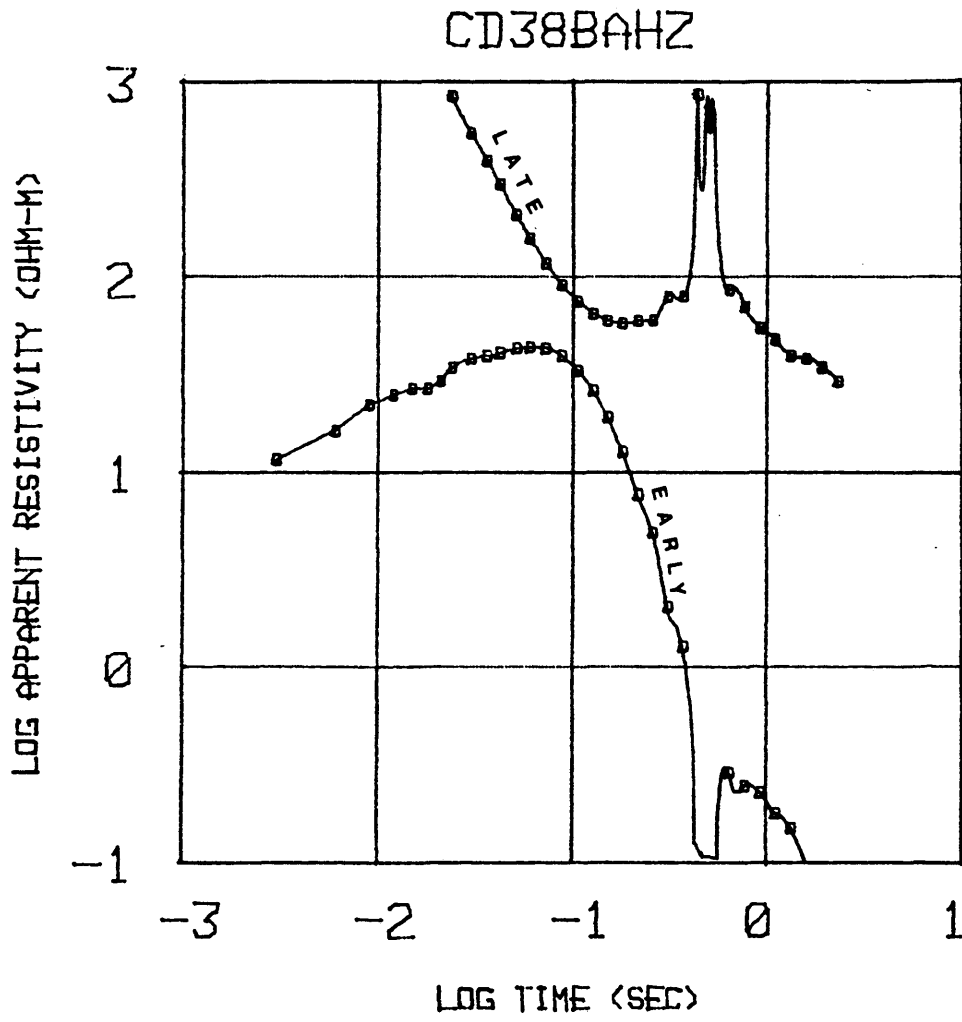


Figure 78

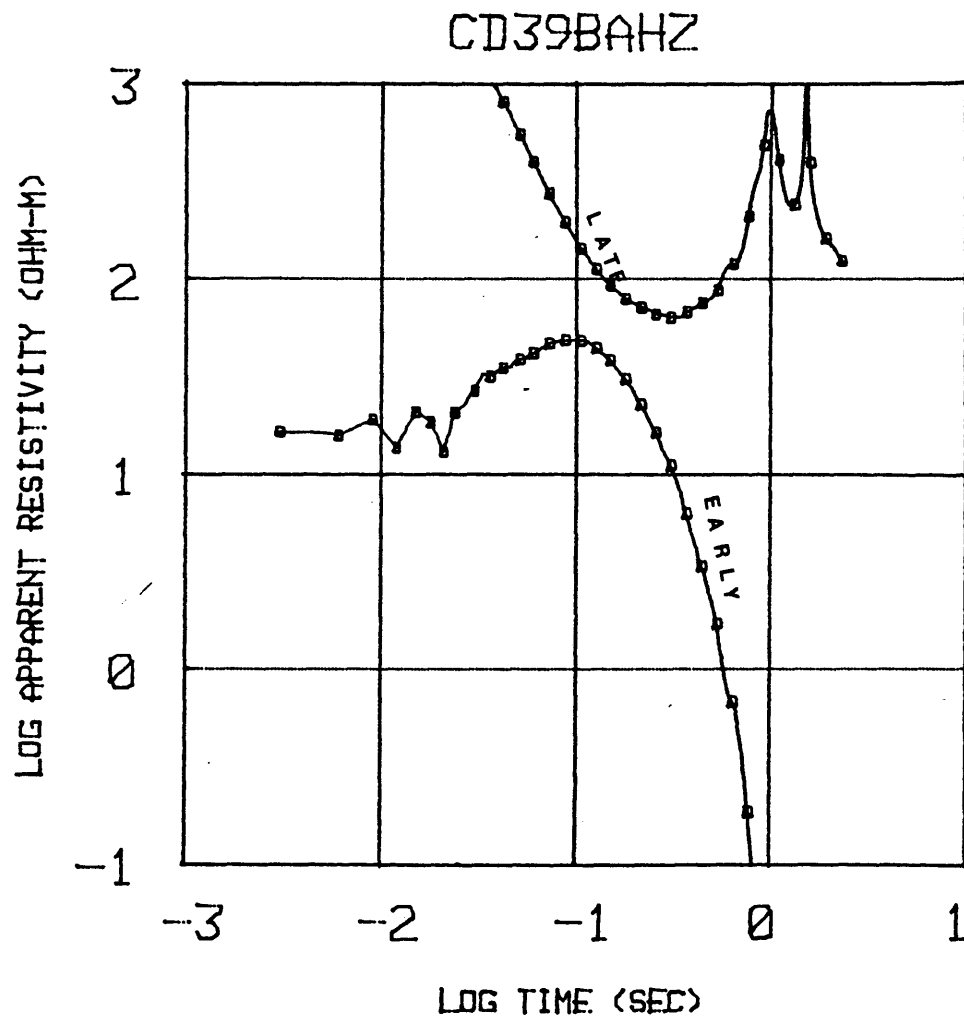


Figure 79

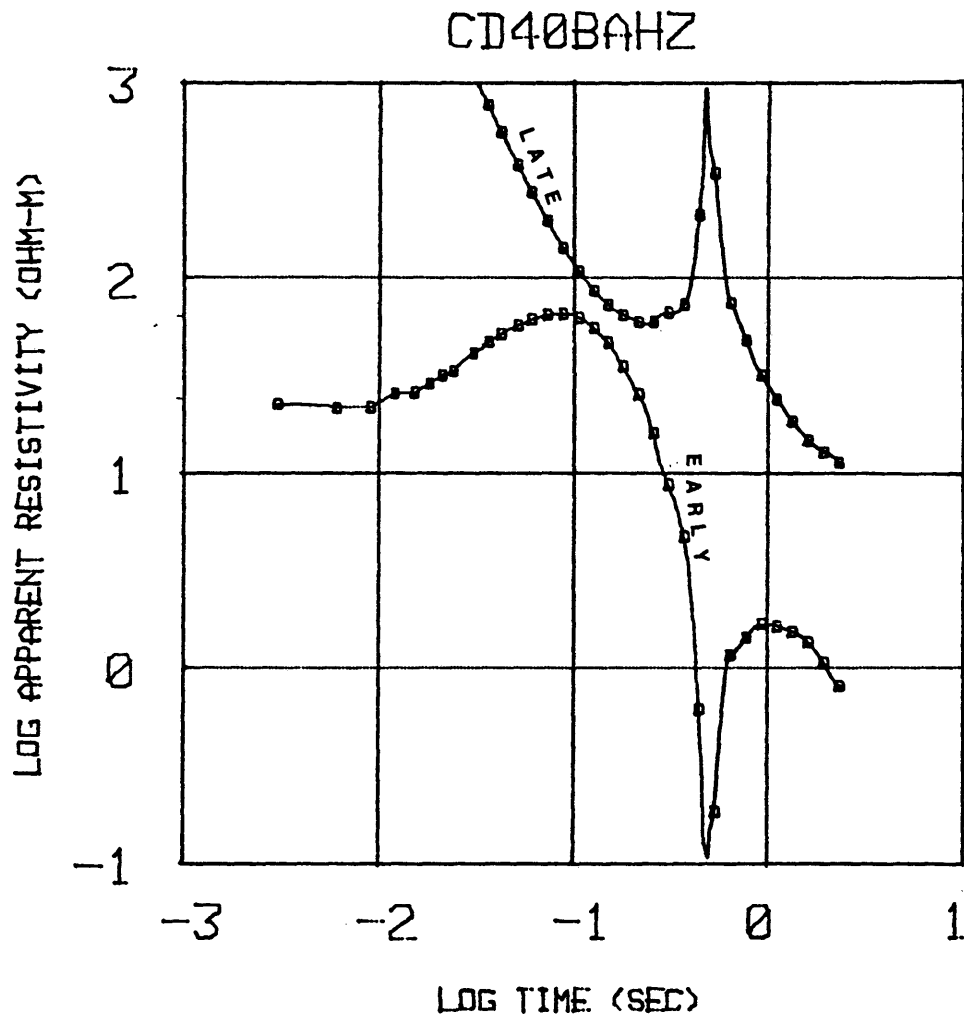


Figure 80

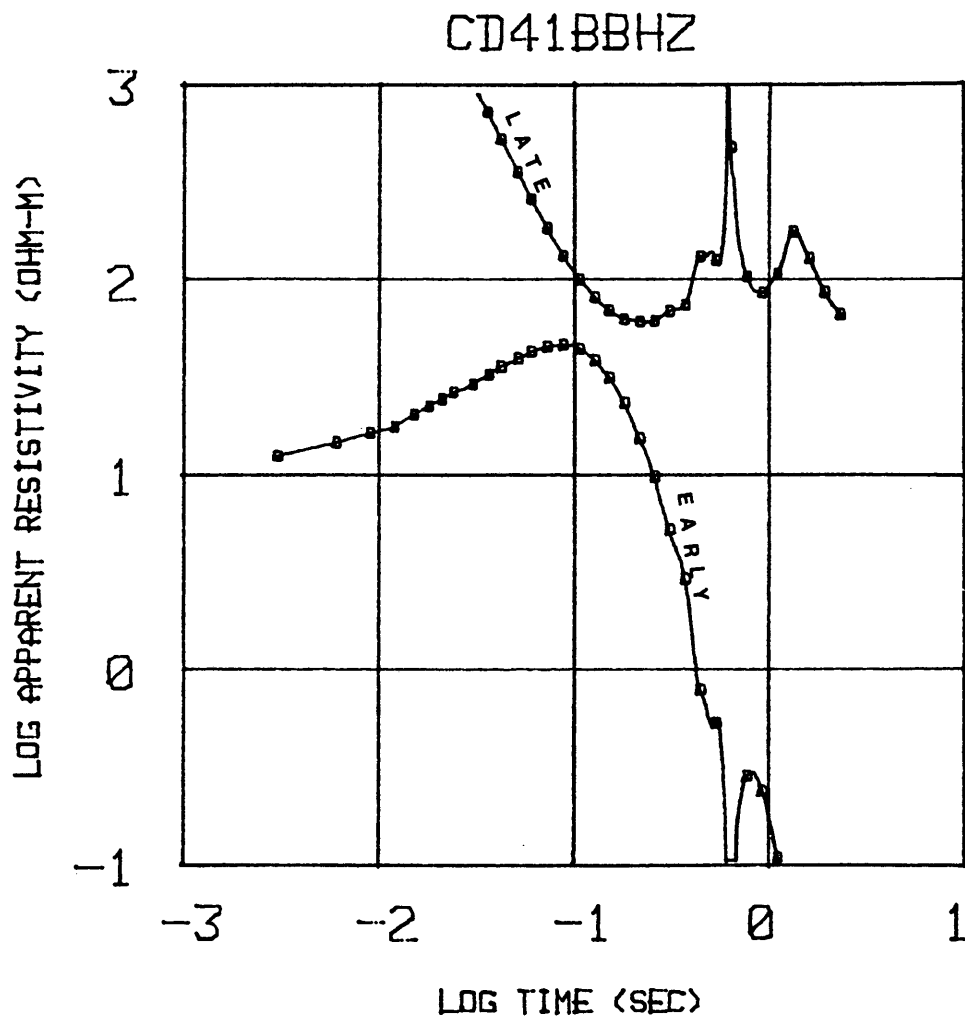


Figure 81

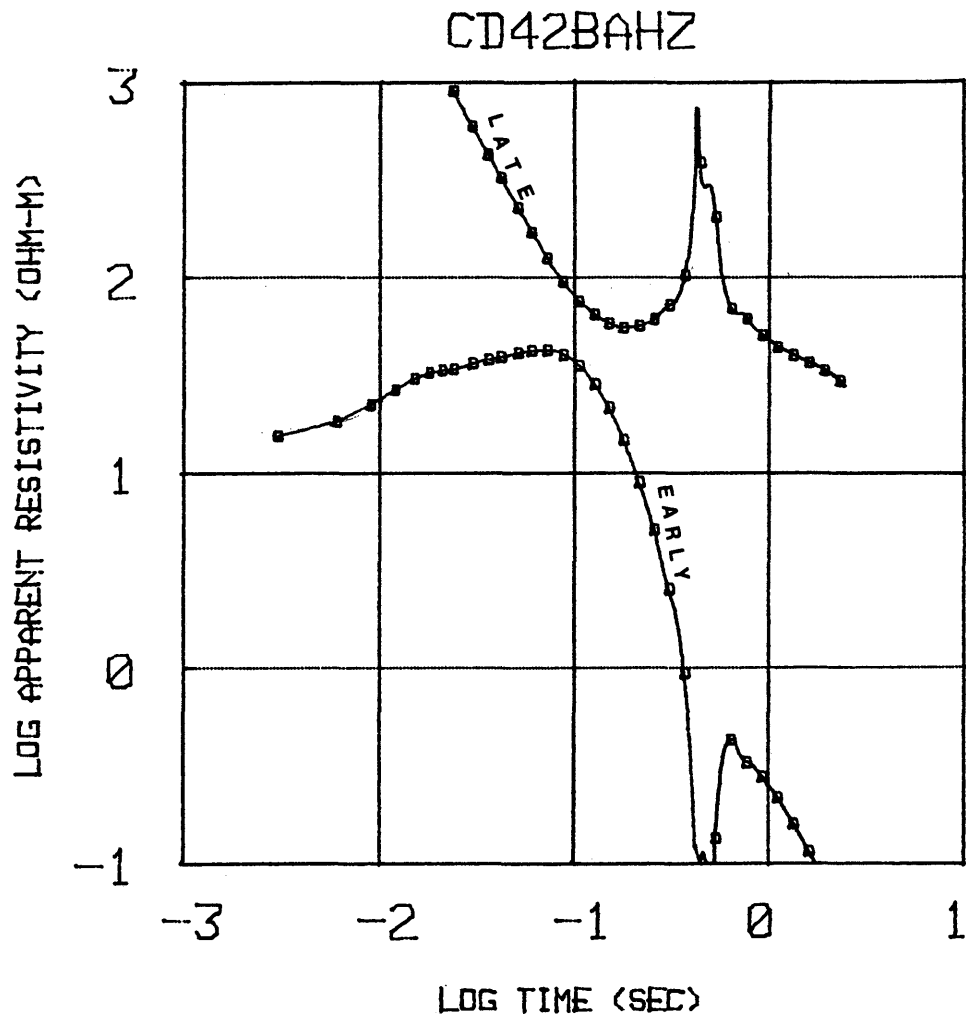


Figure 82

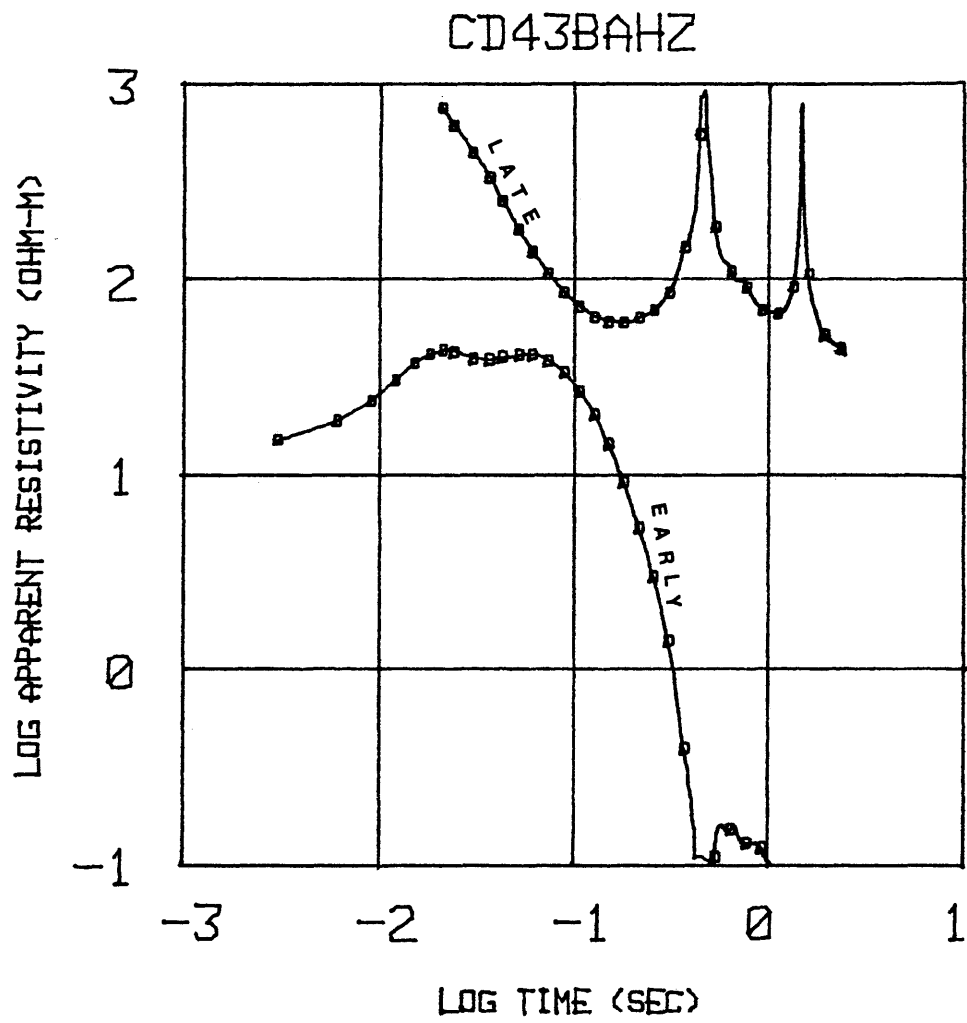


Figure 83

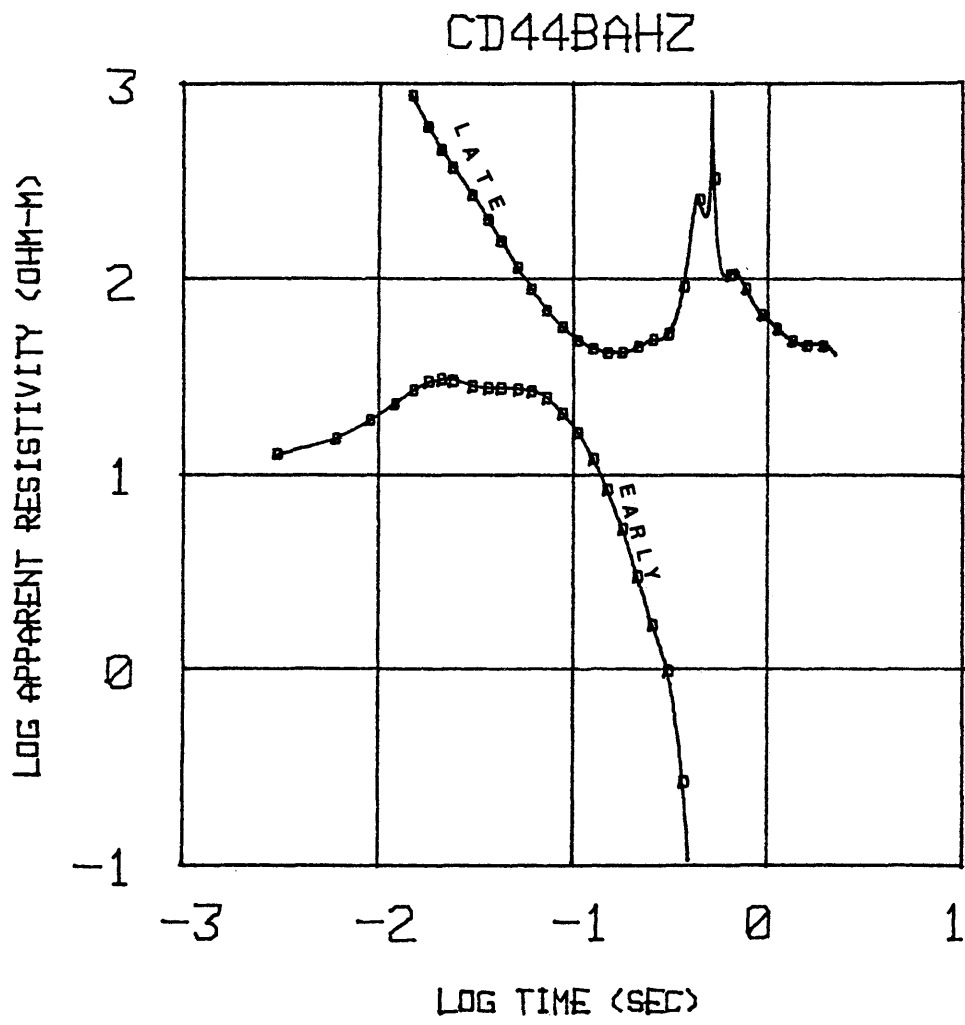


Figure 84

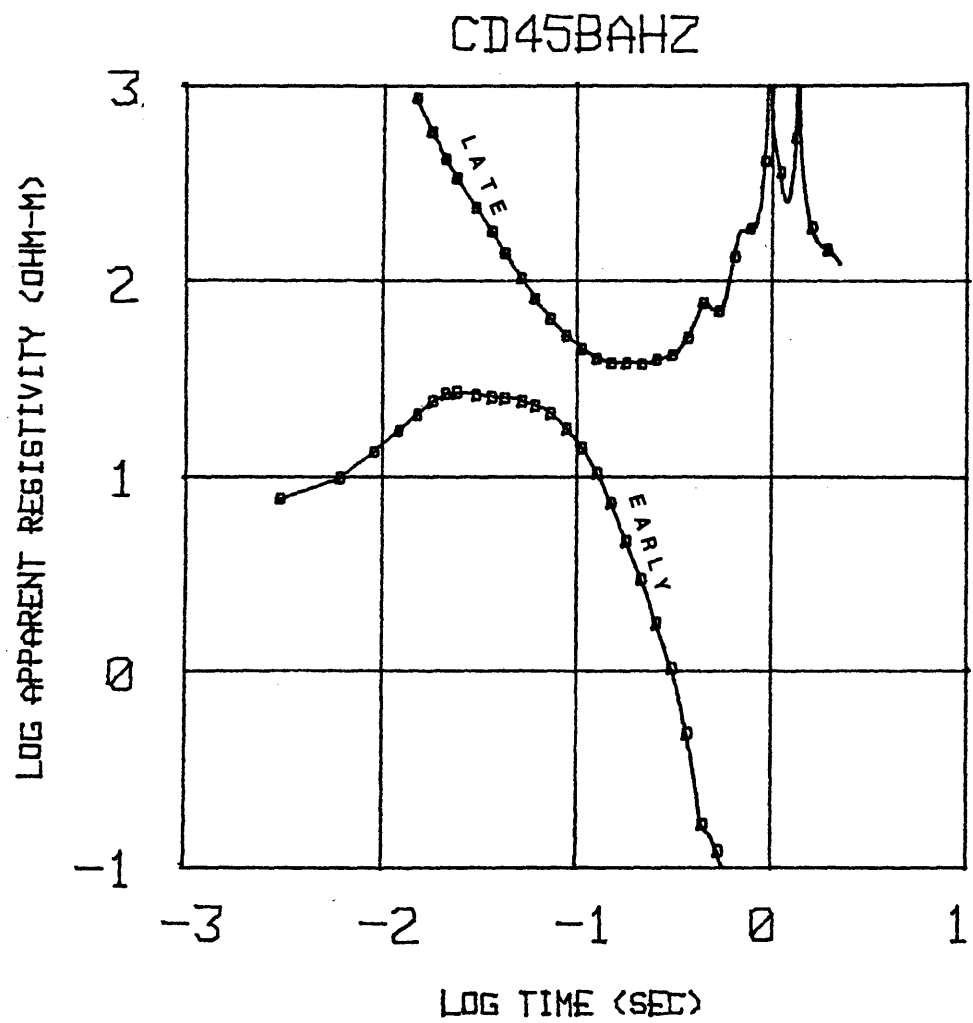


Figure 85

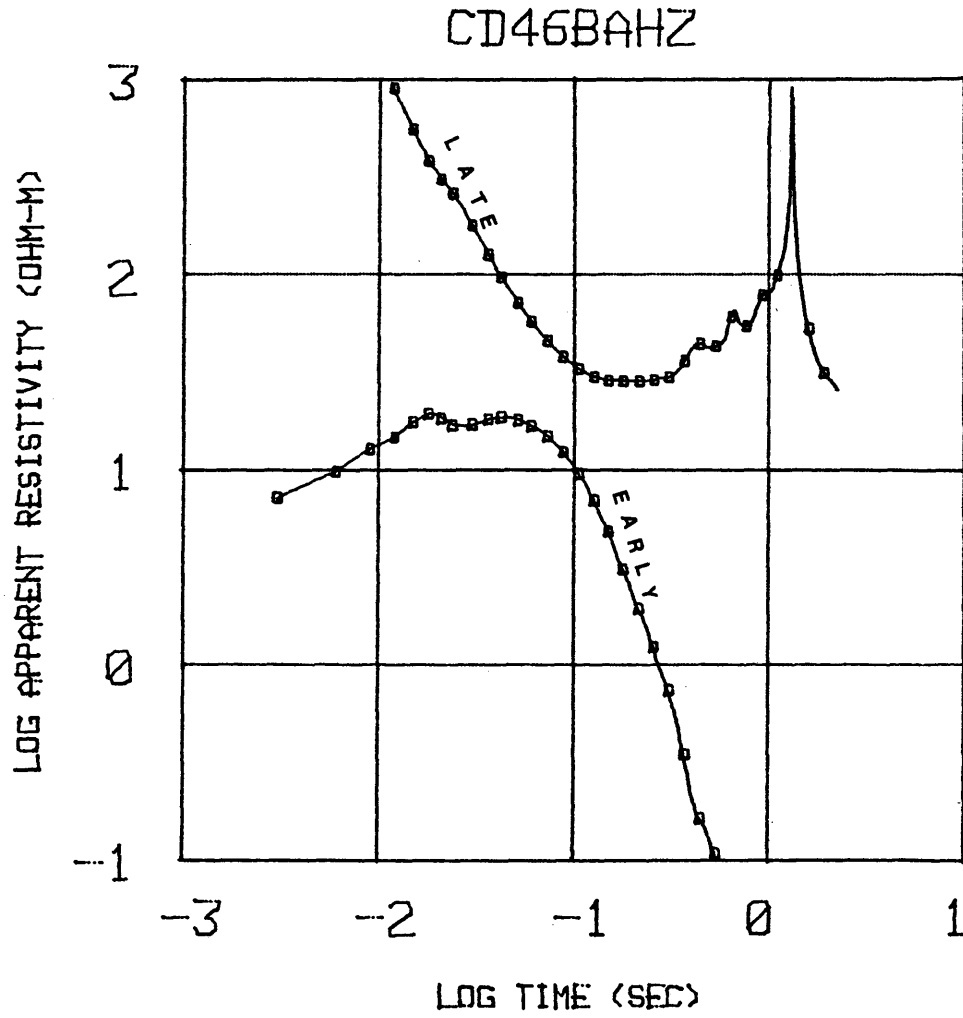


Figure 86

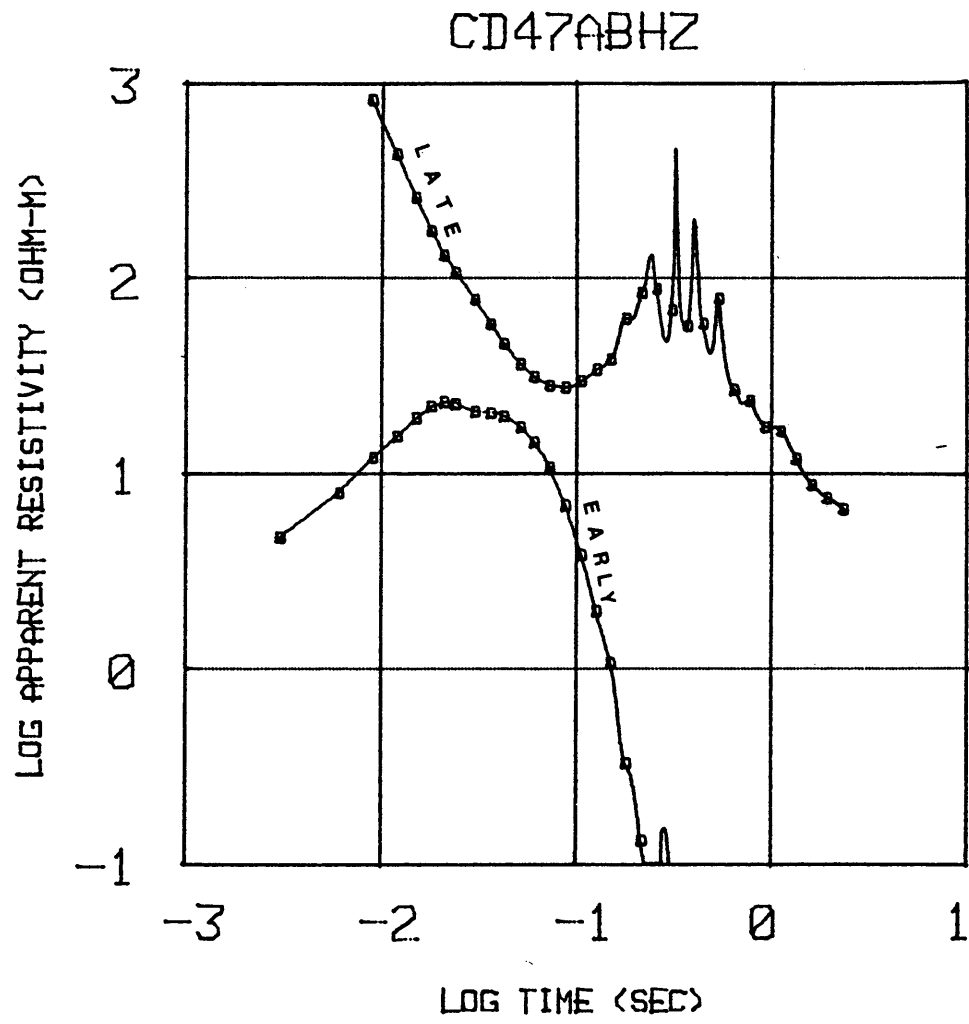


Figure 87

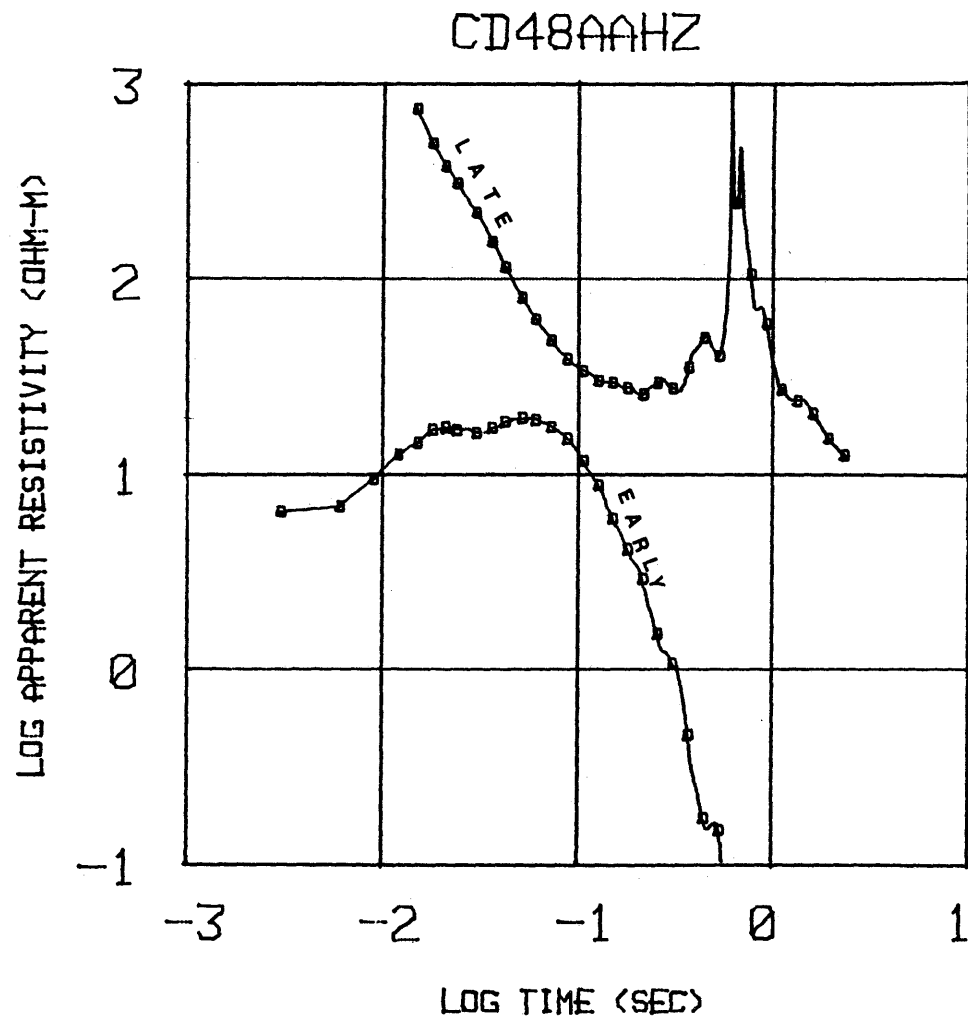


Figure 88

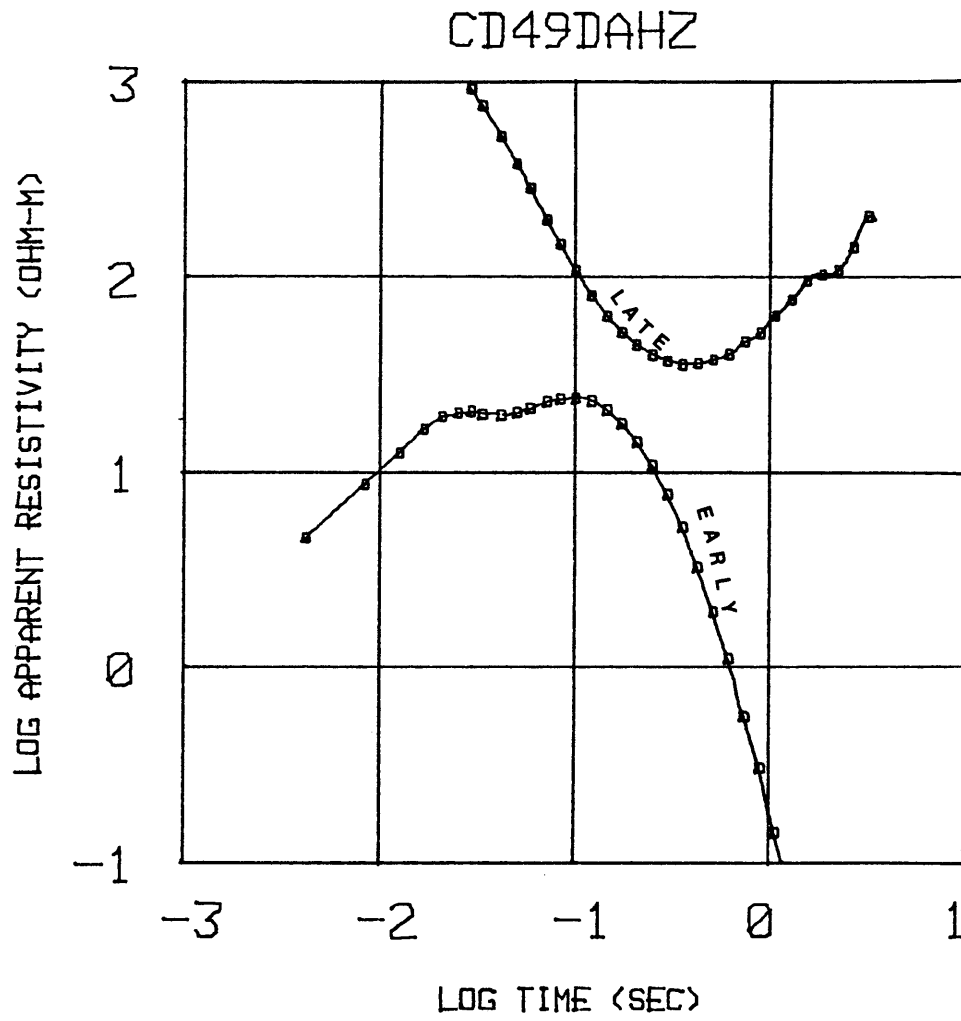


Figure 89

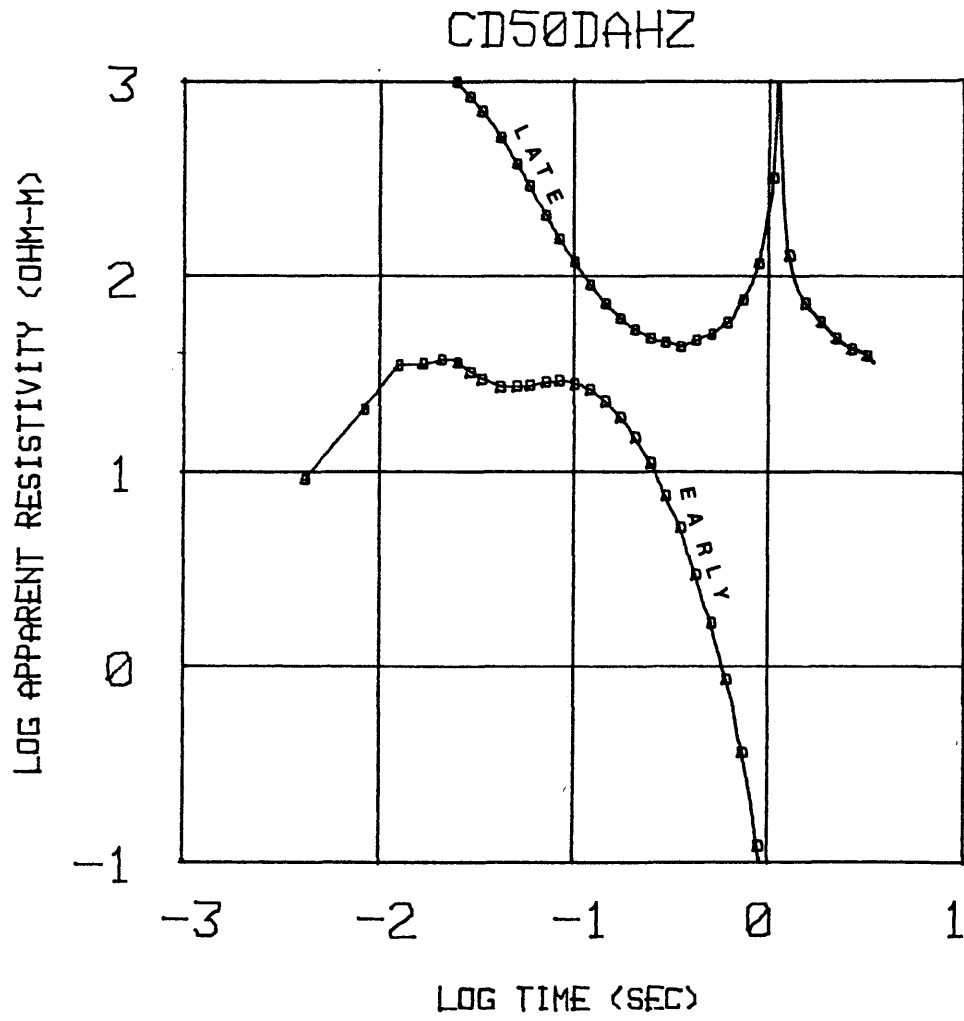


Figure 90

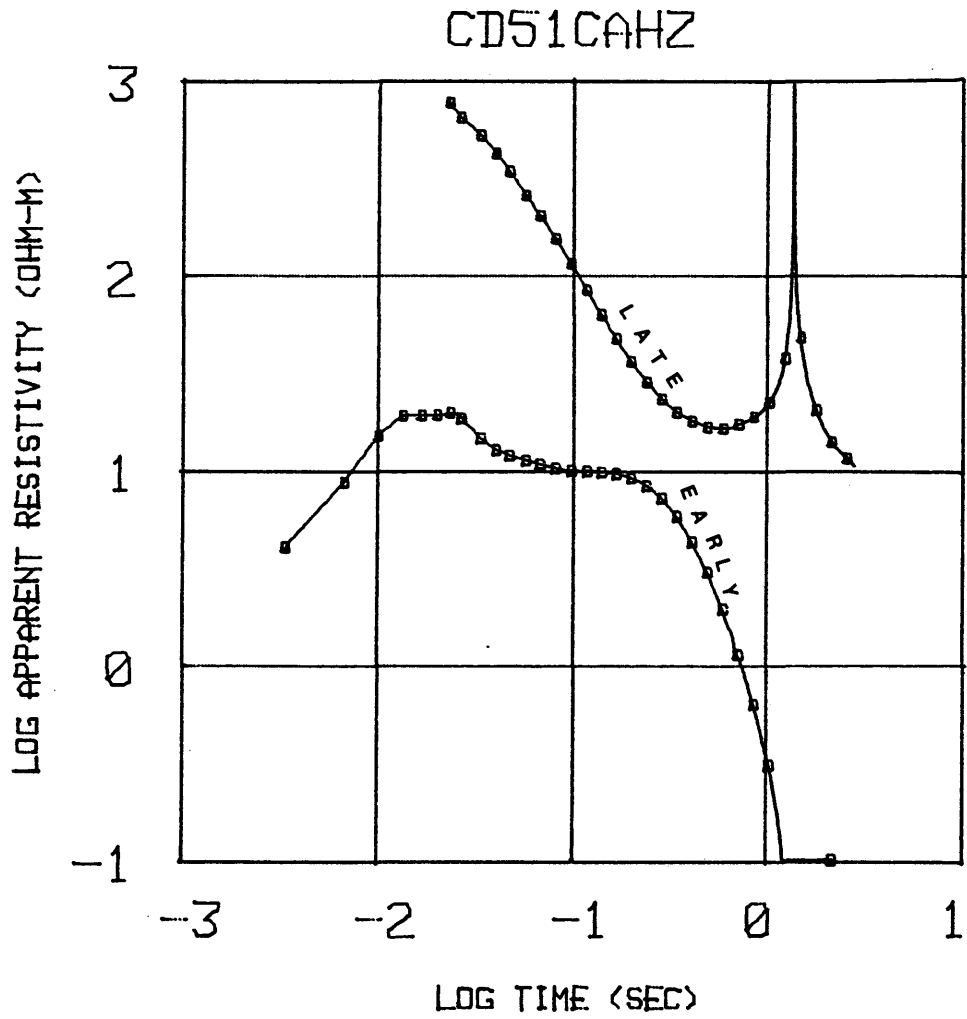


Figure 91

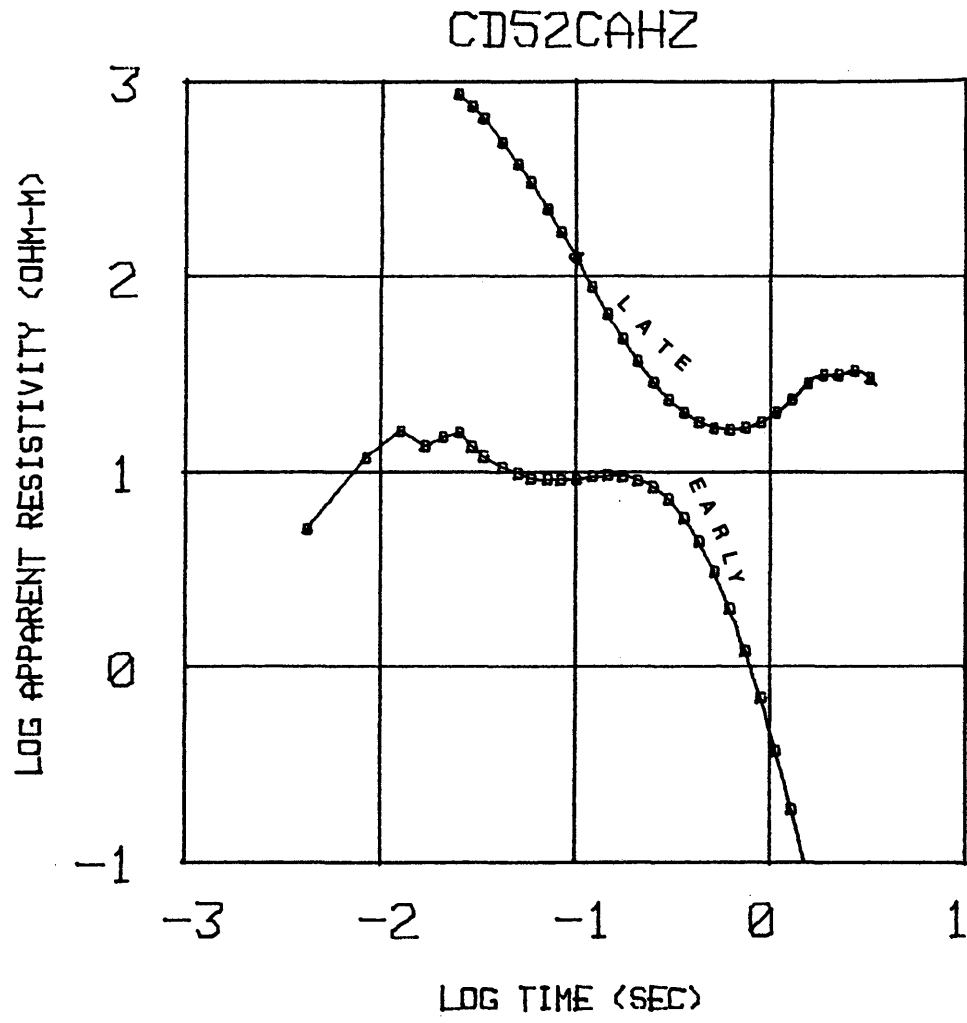


Figure 92

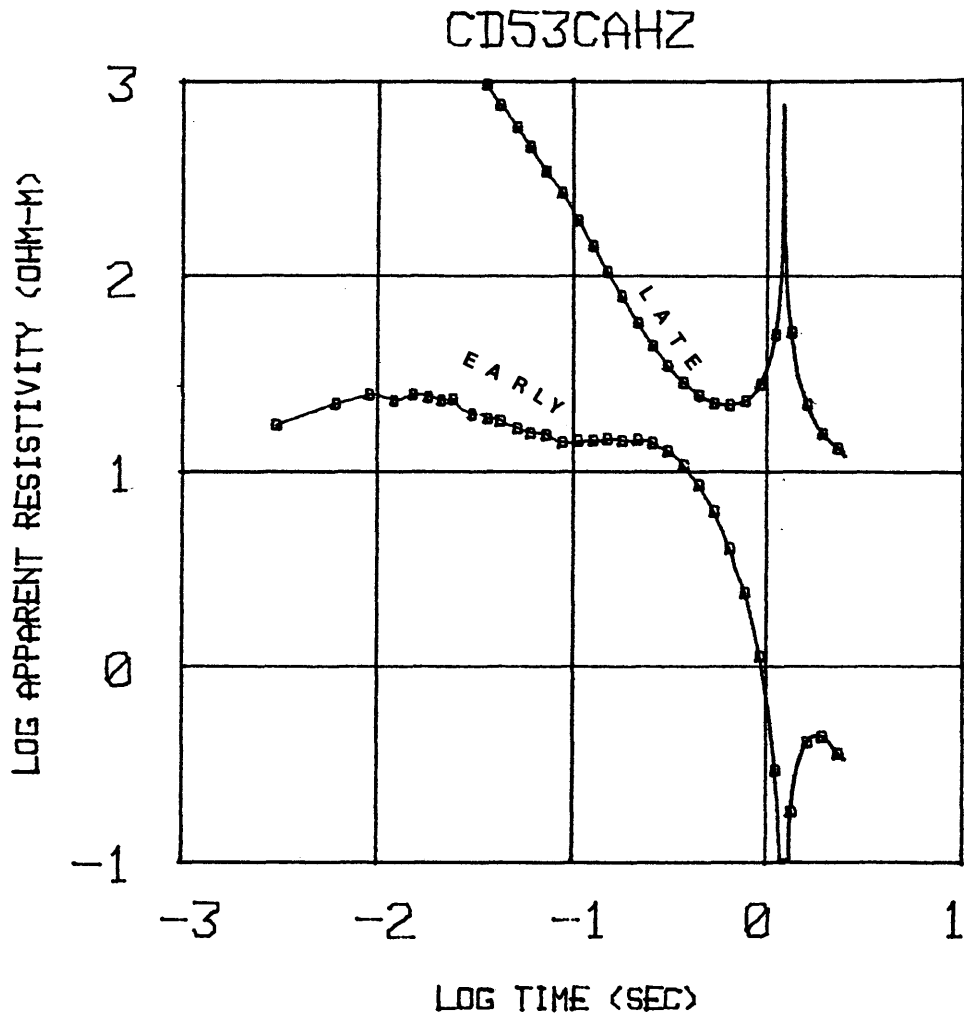


Figure 93

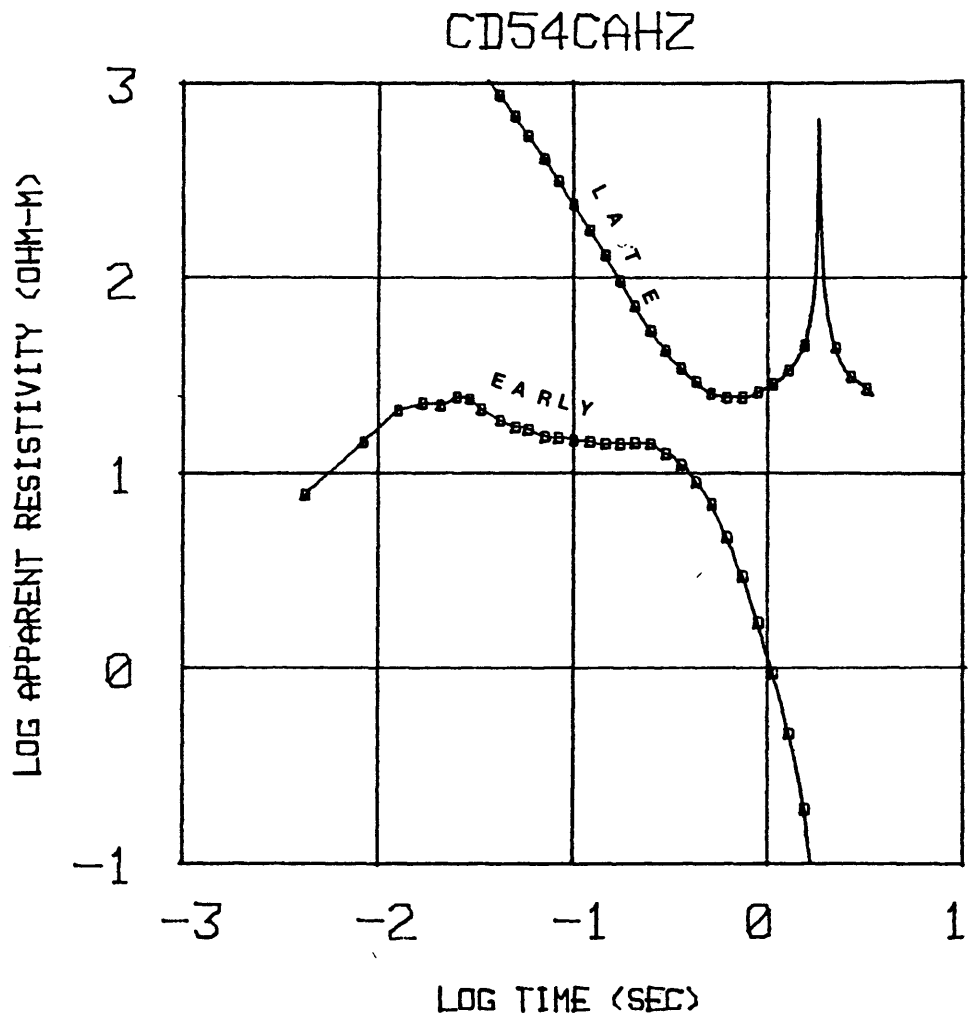


Figure 94

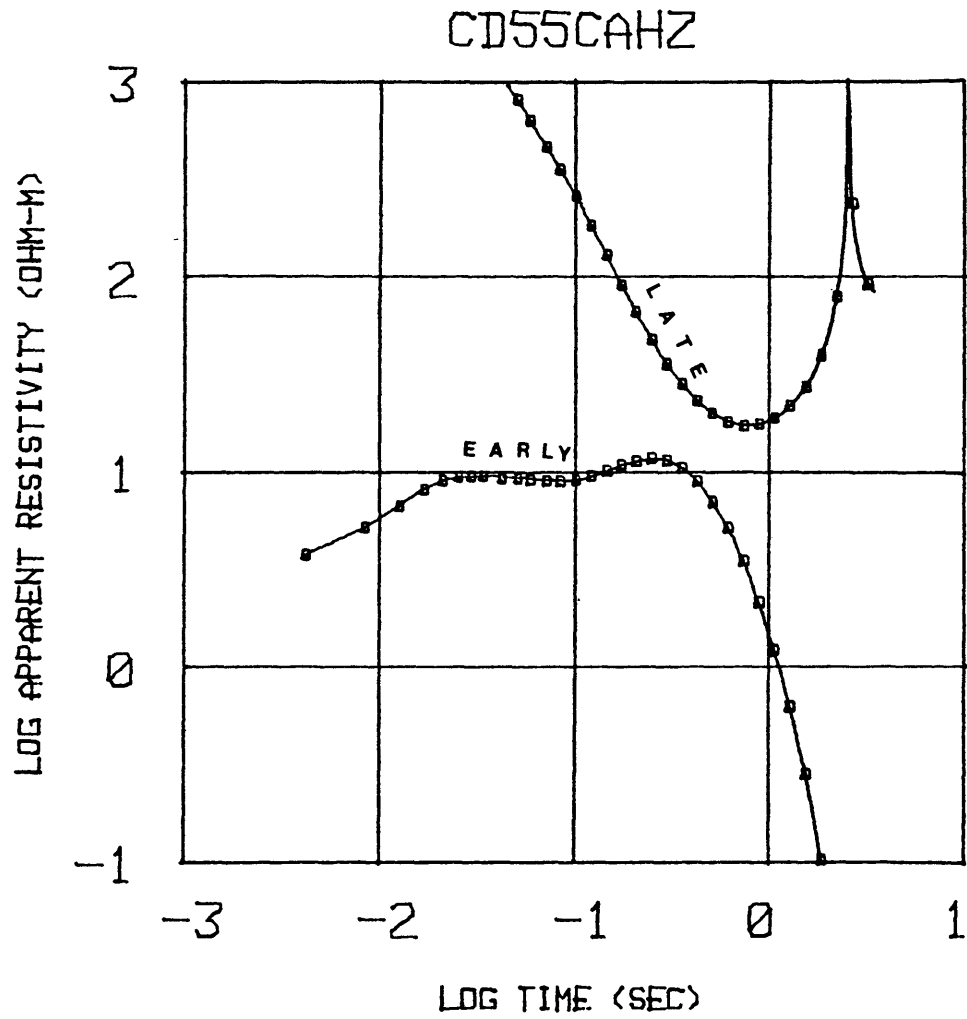


Figure 95

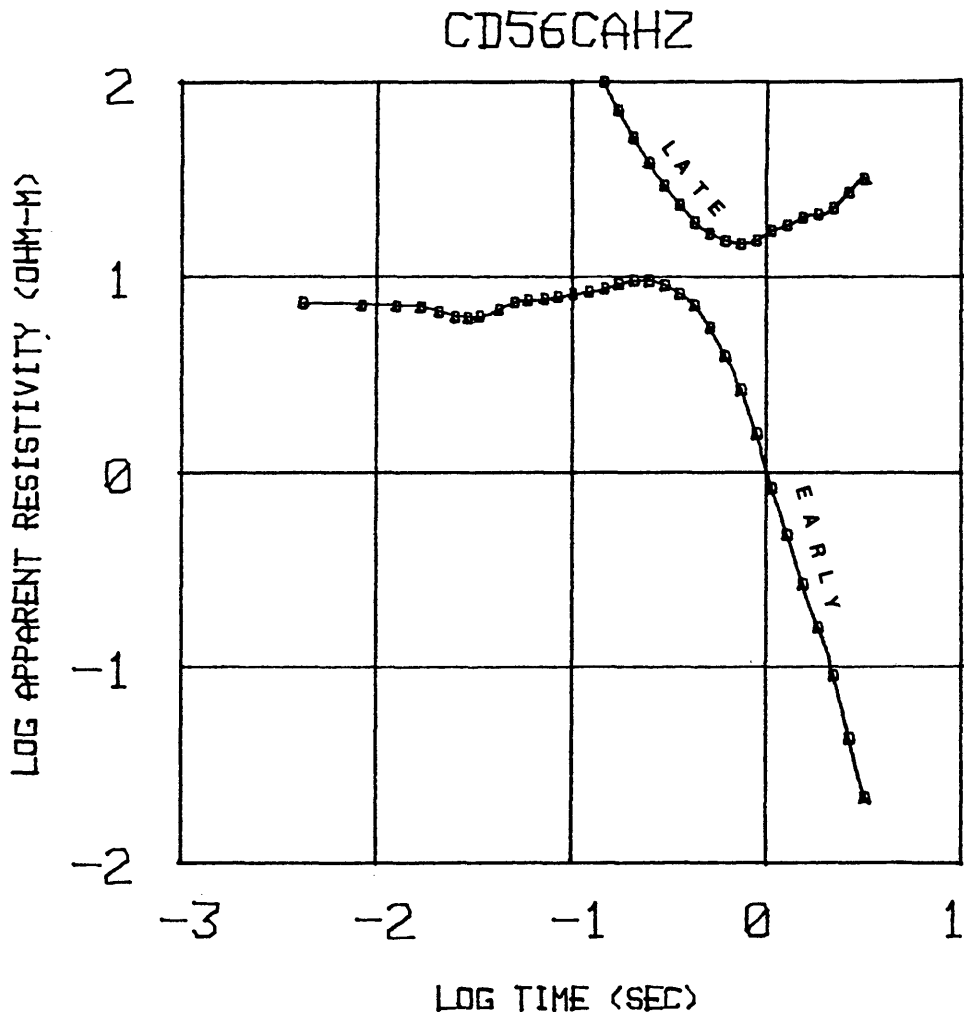


Figure 96

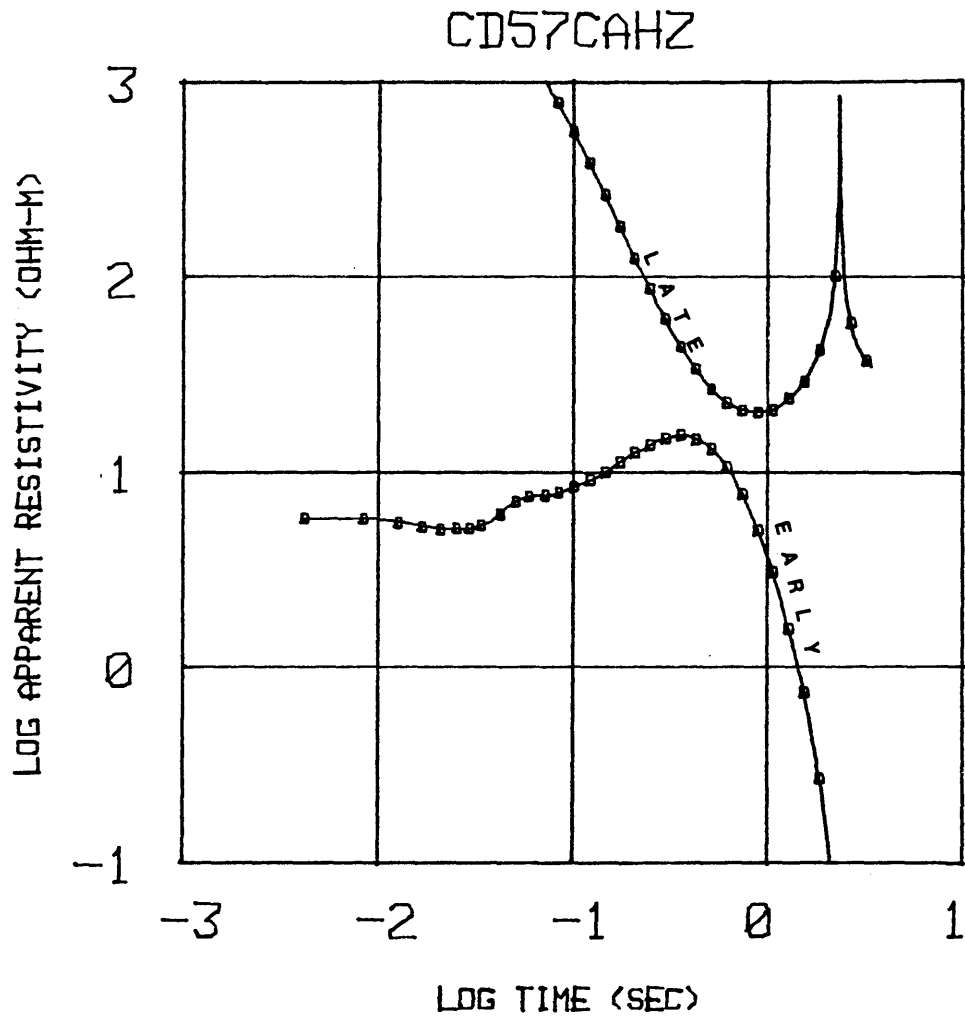


Figure 97

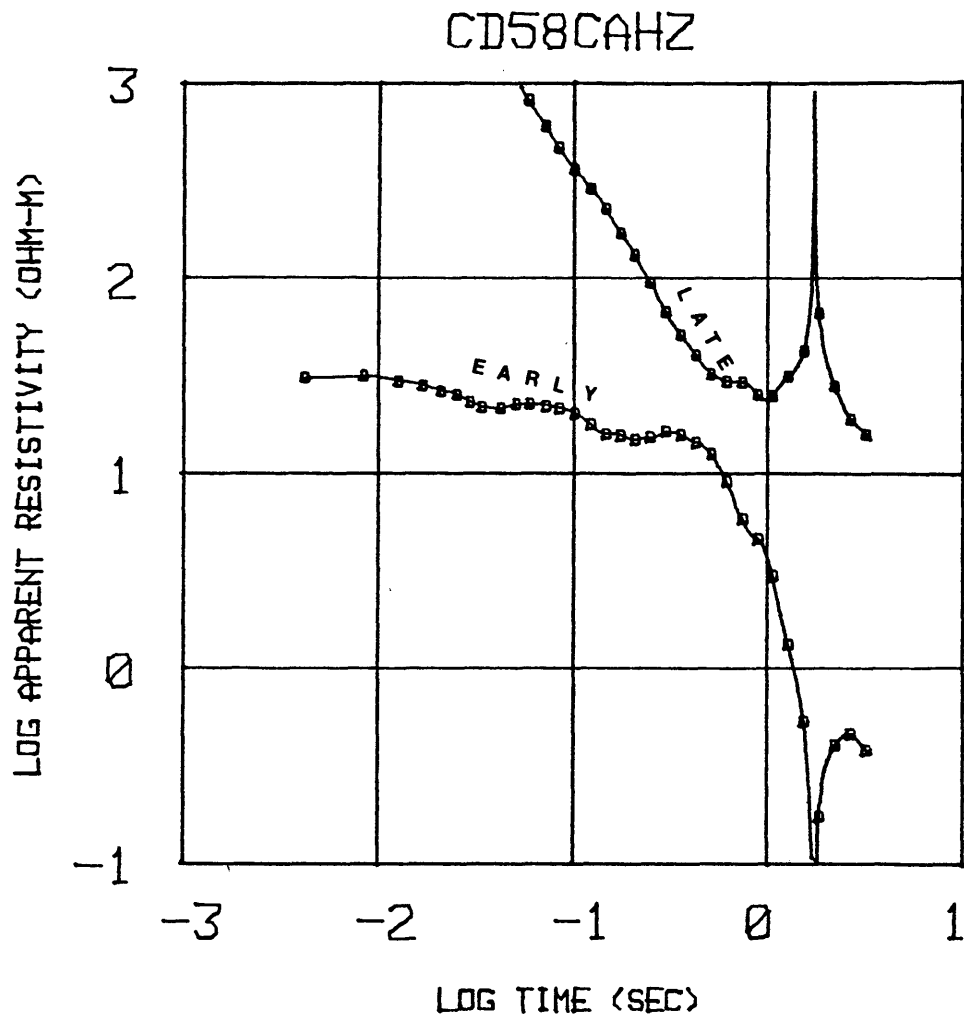


Figure 98

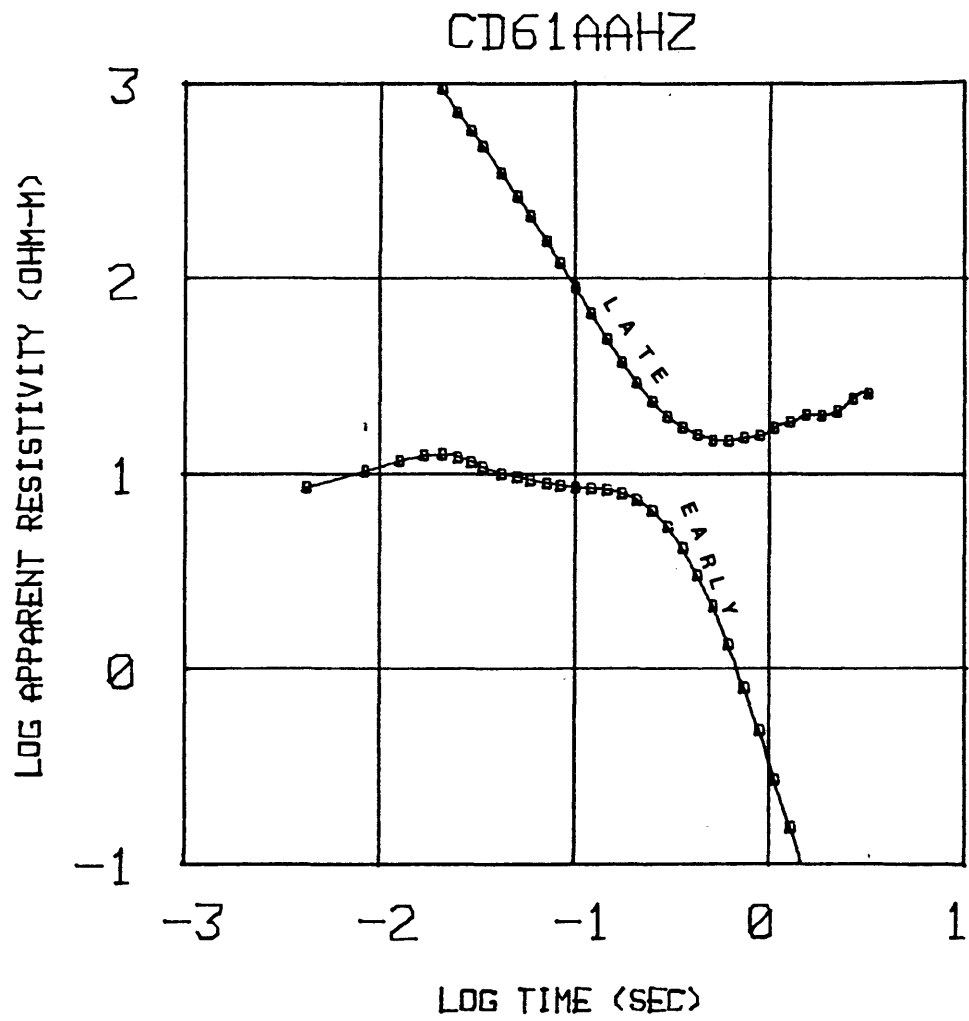


Figure 99

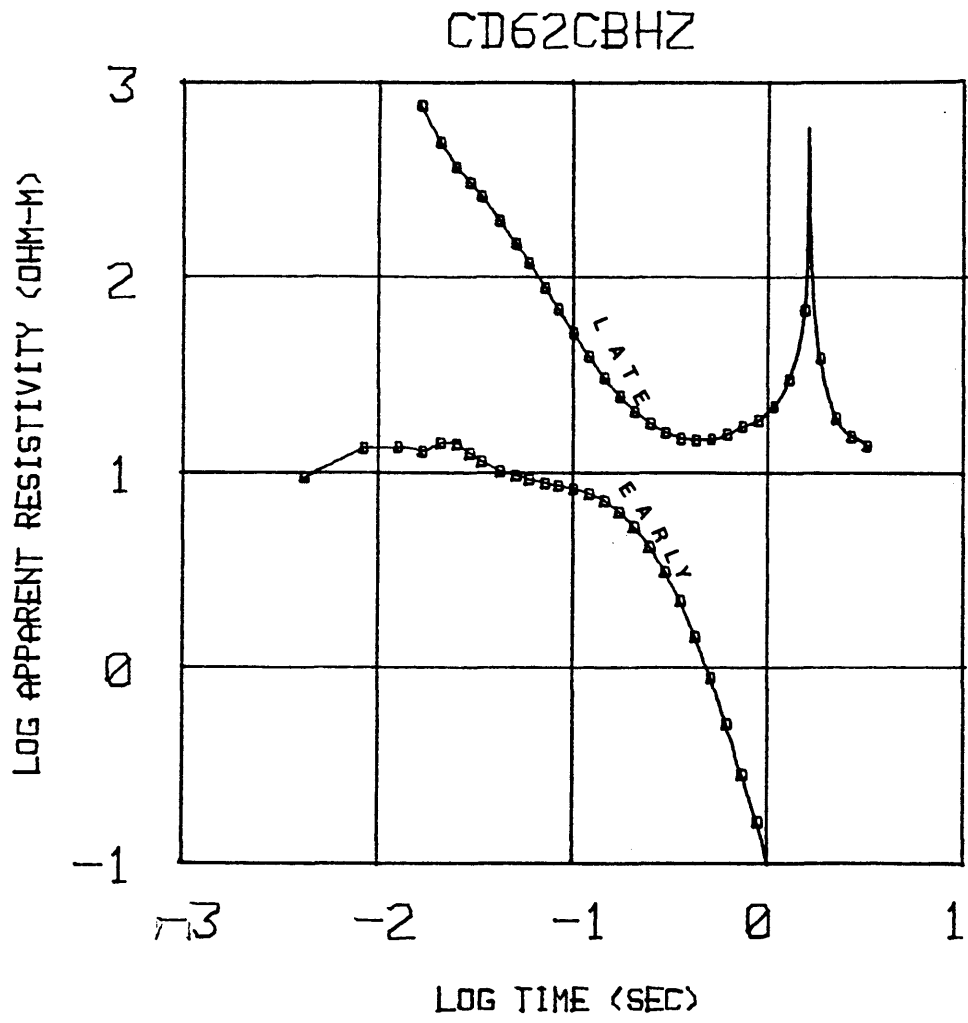


Figure 100

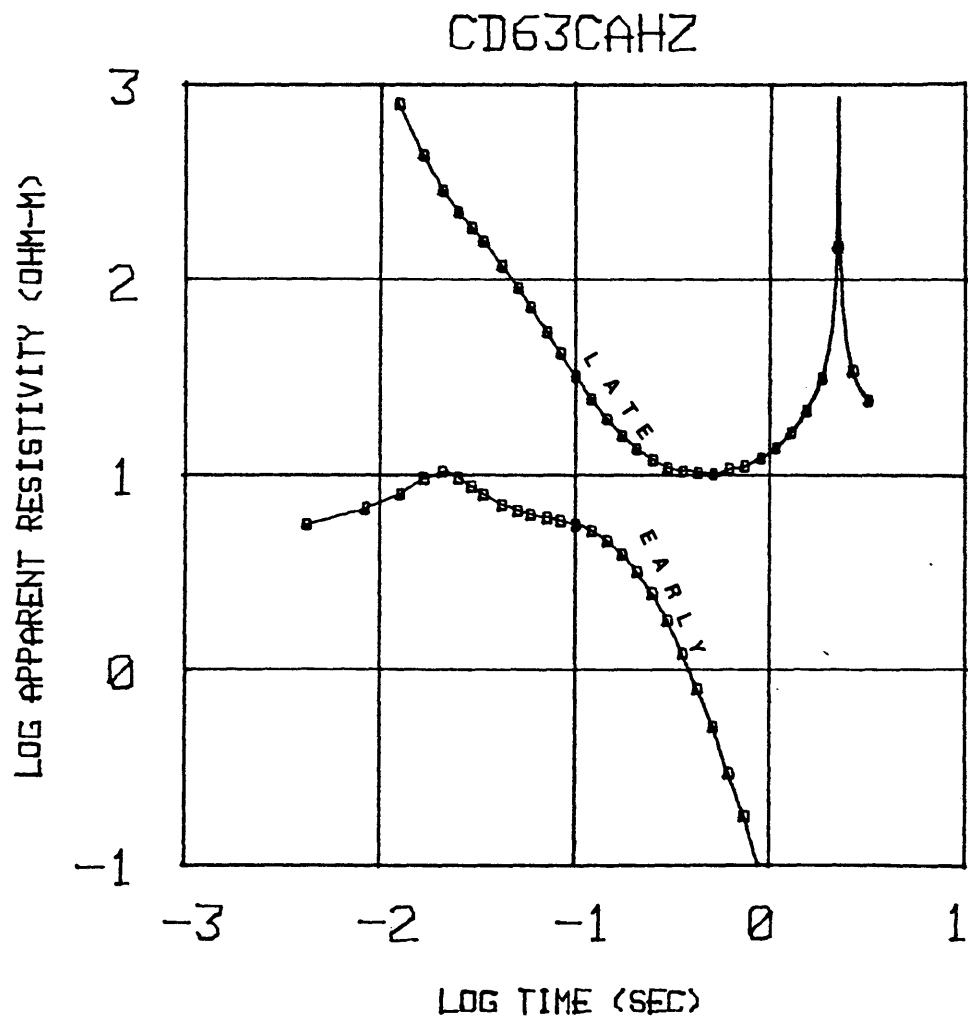


Figure 101

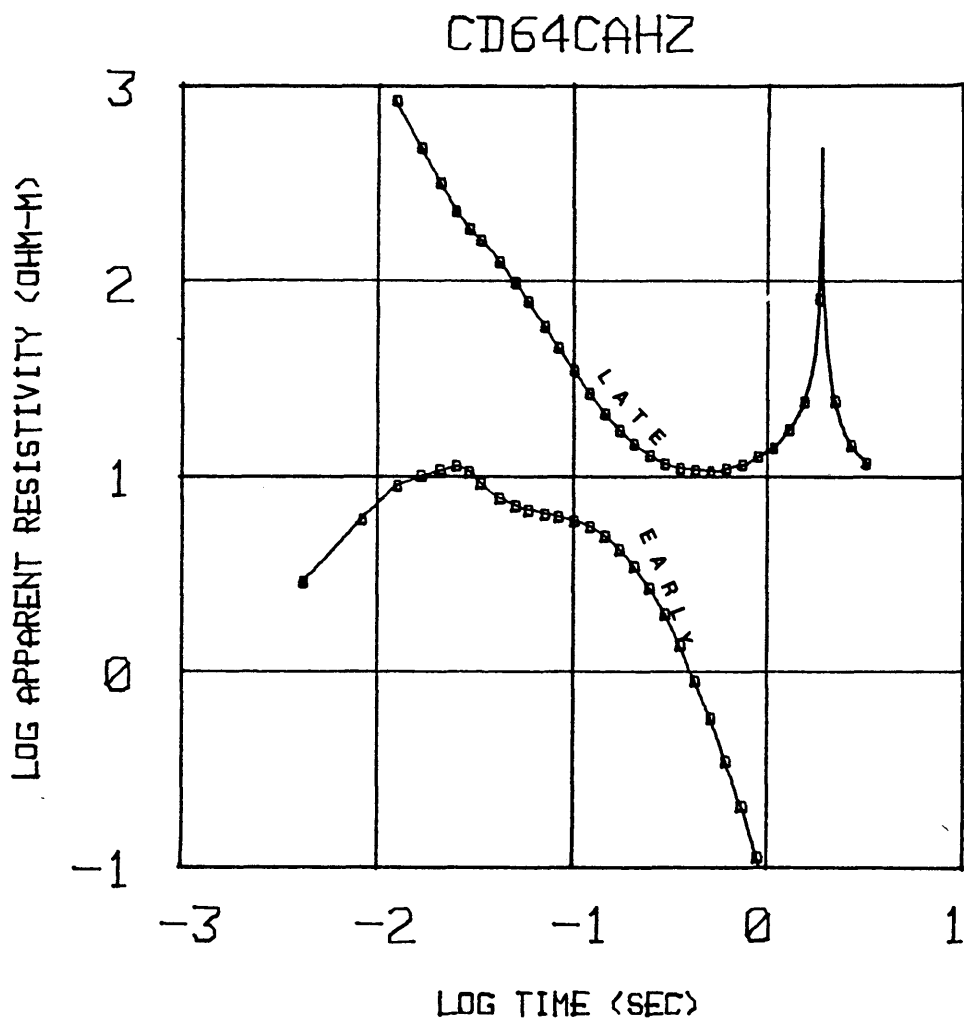


Figure 102

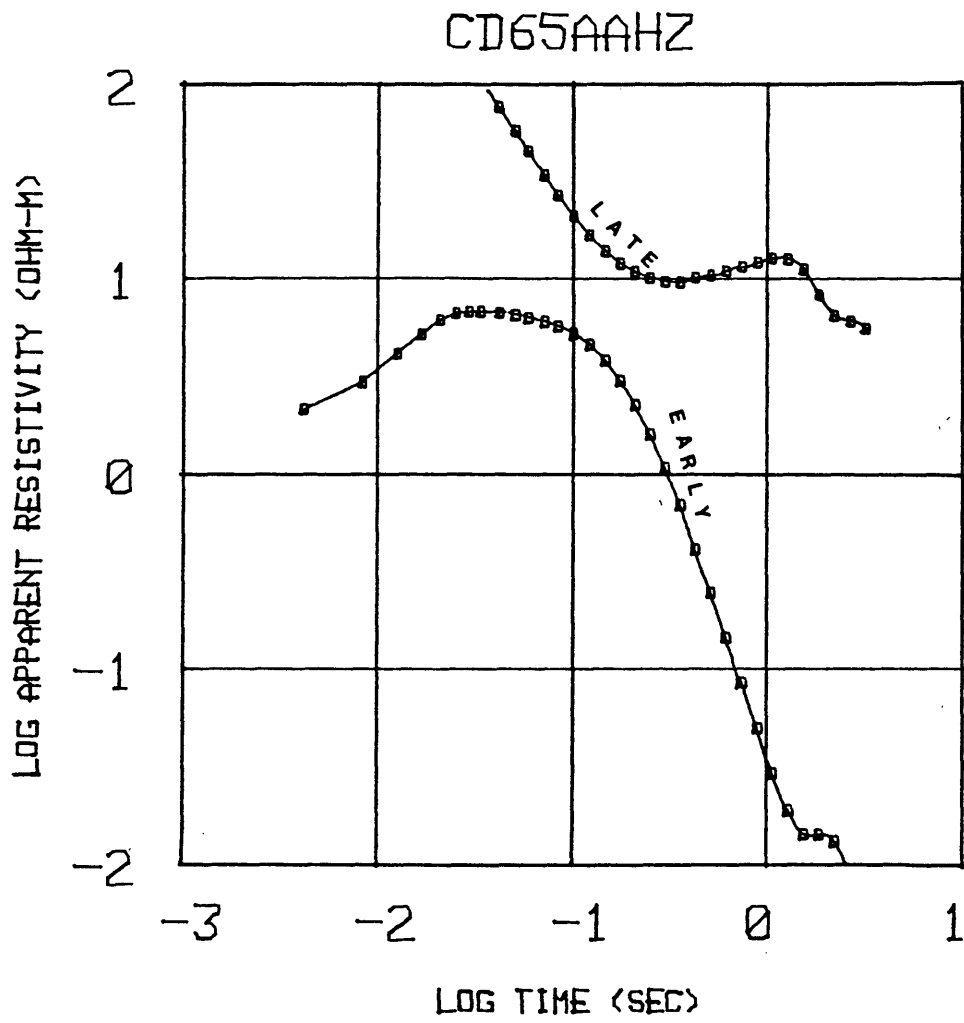


Figure 103

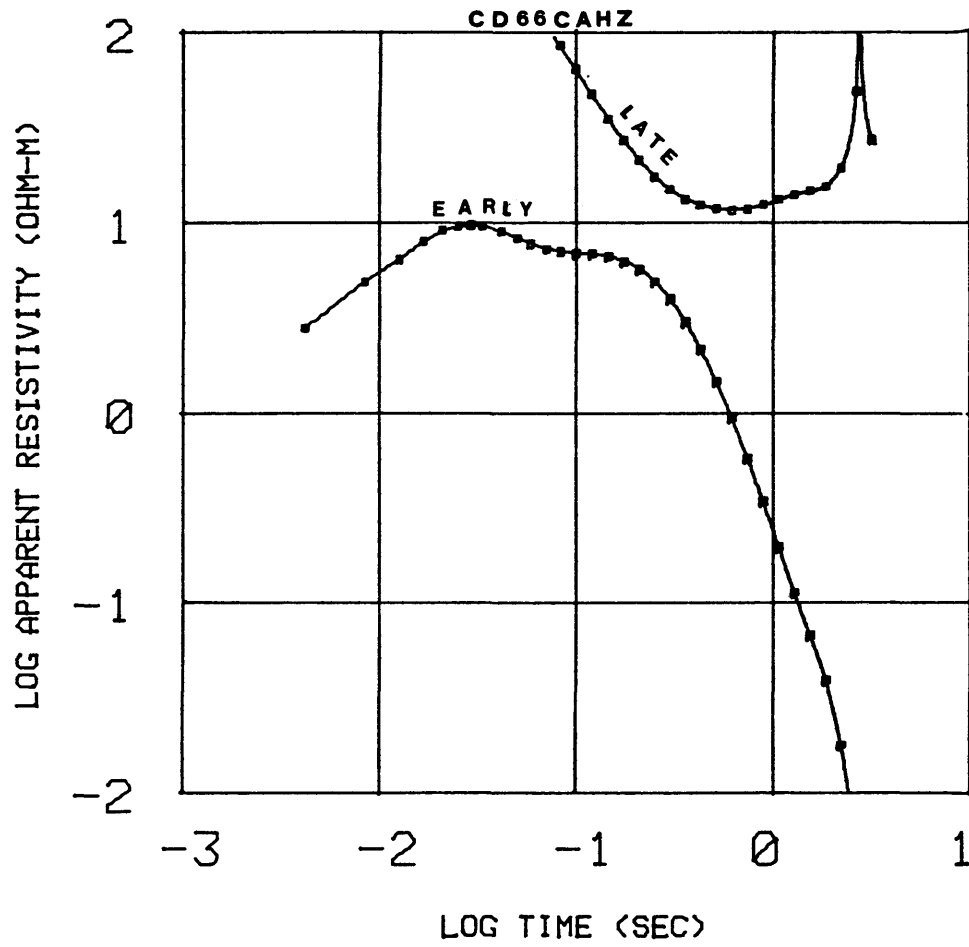


Figure 104

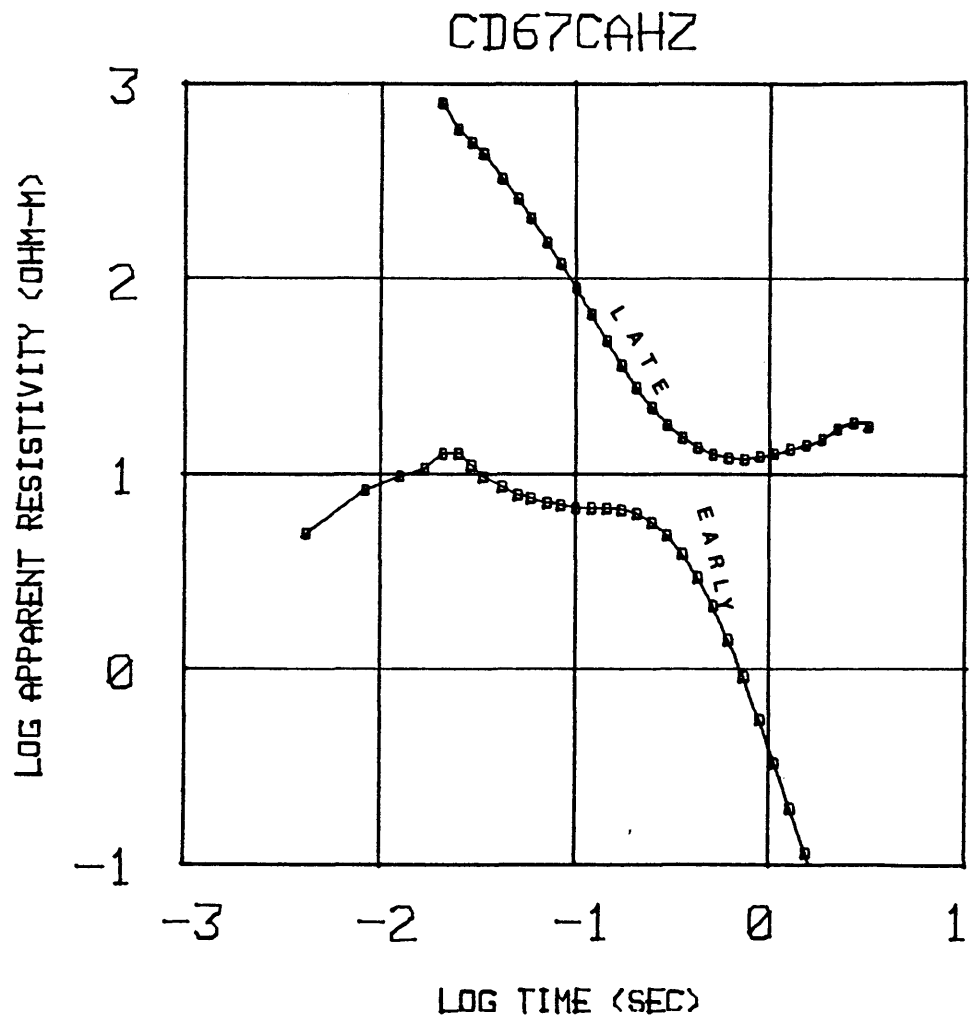


Figure 105

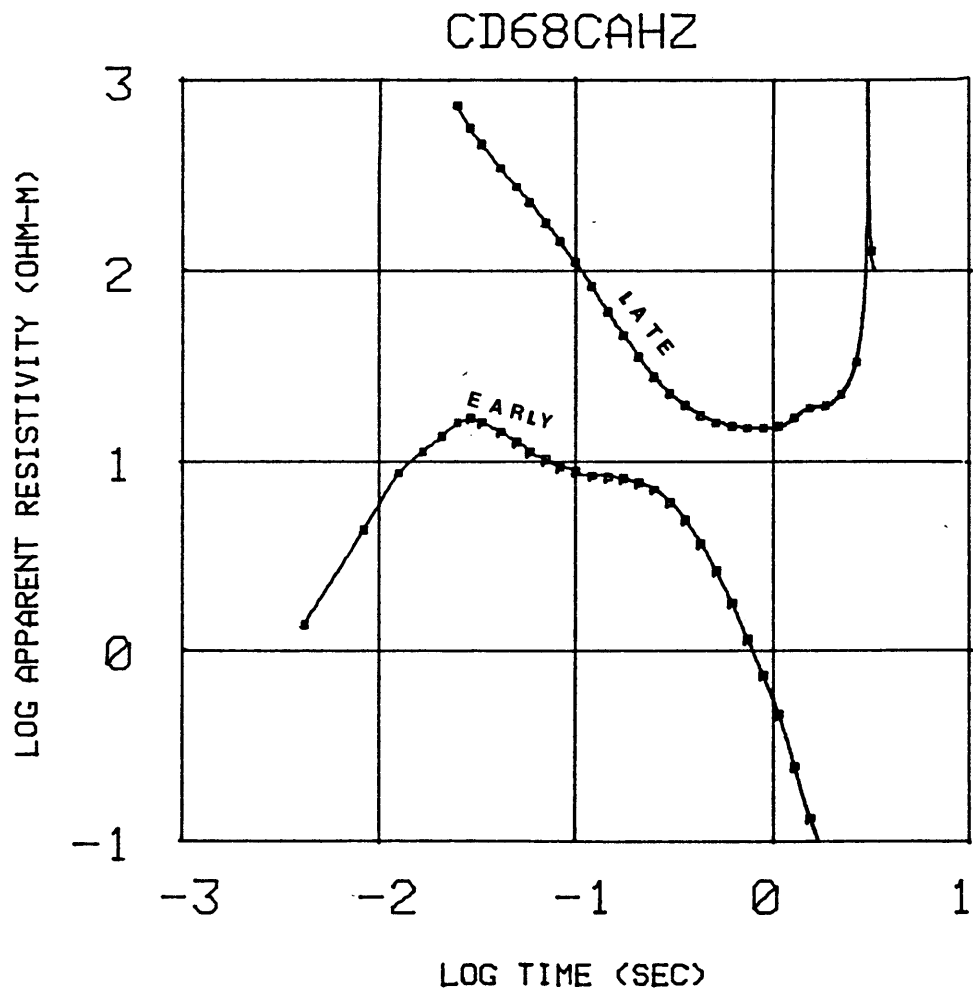


Figure 106

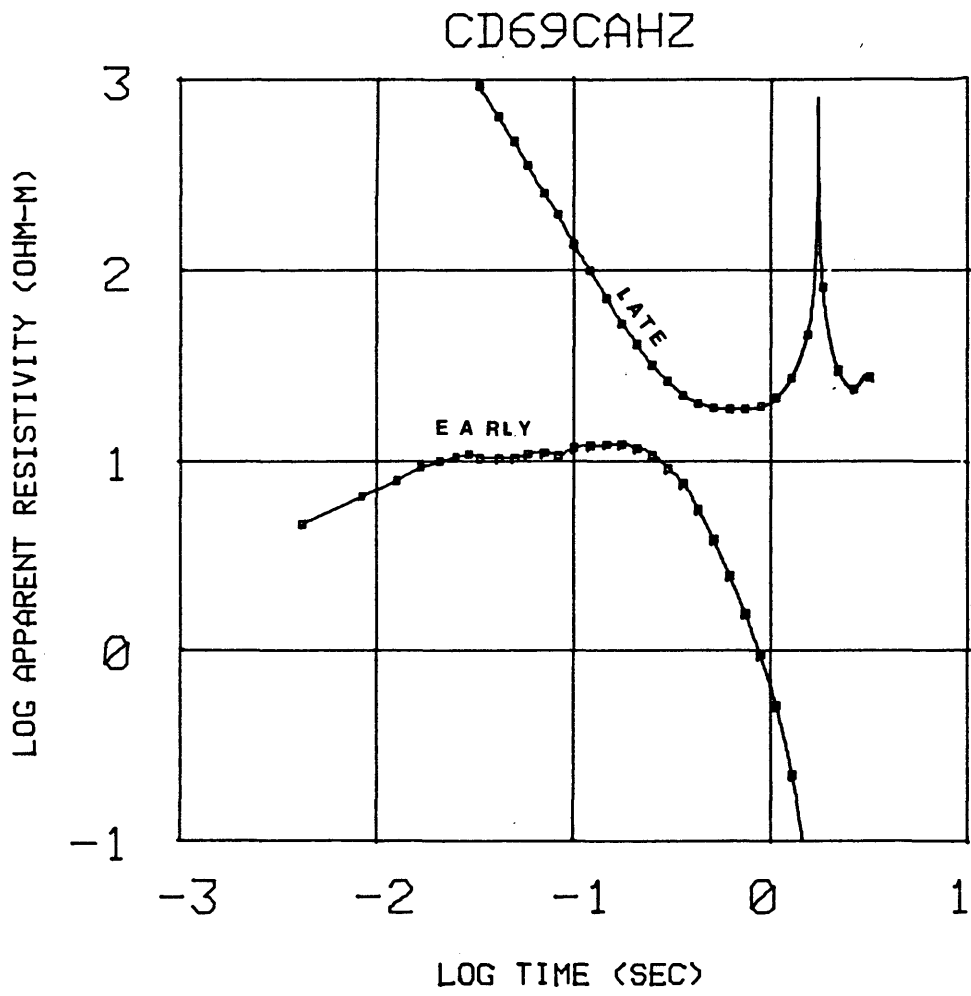


Figure 107

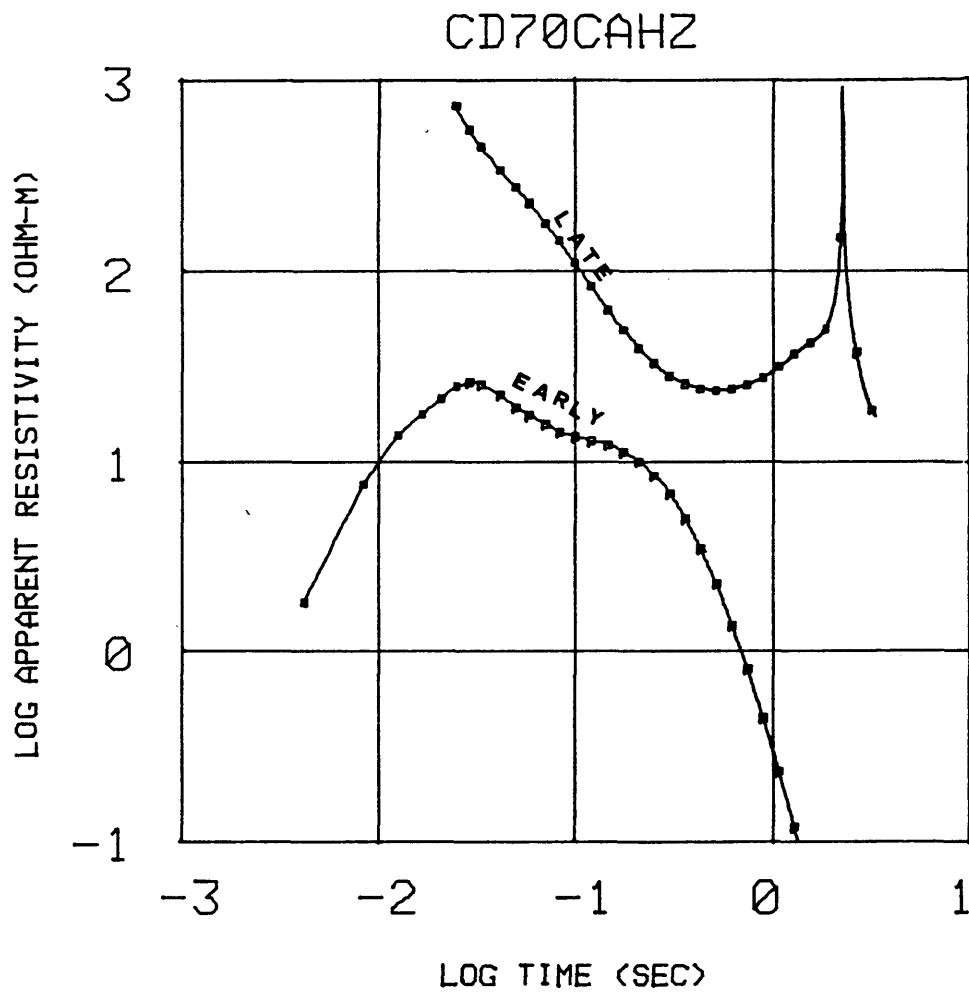


Figure 108

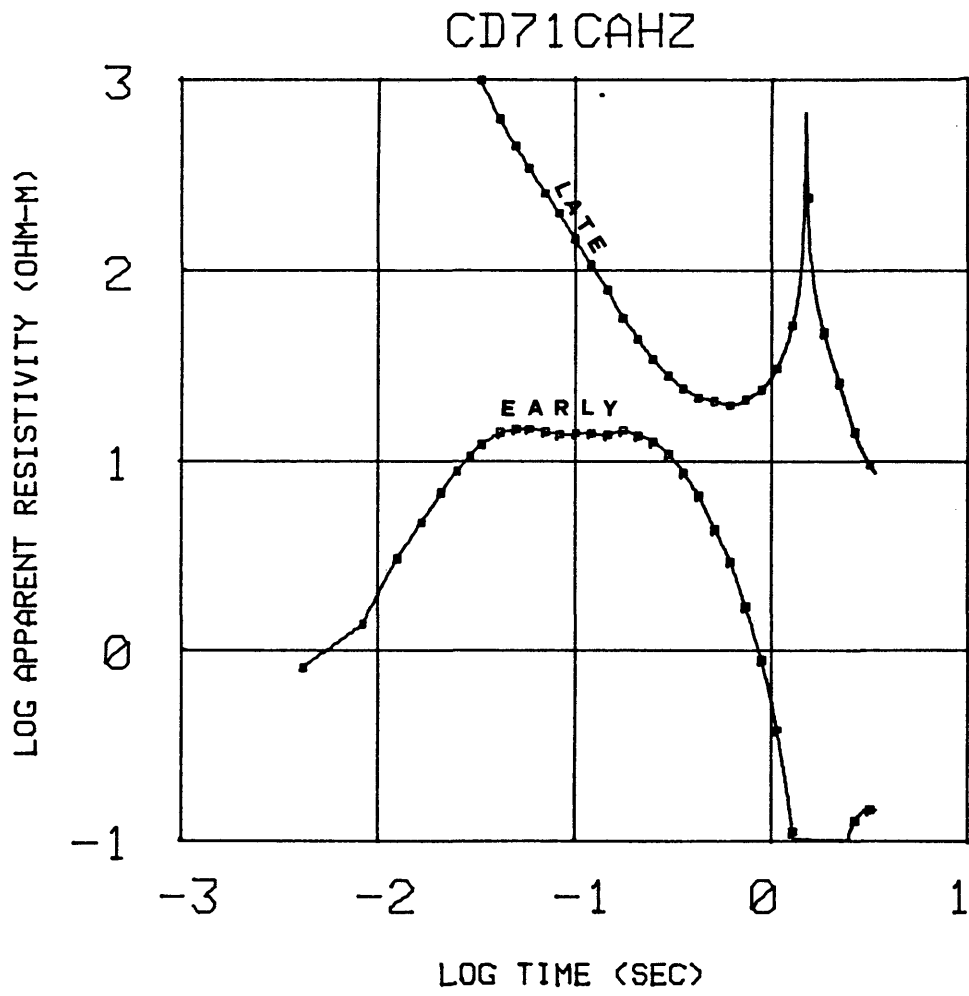


Figure 109

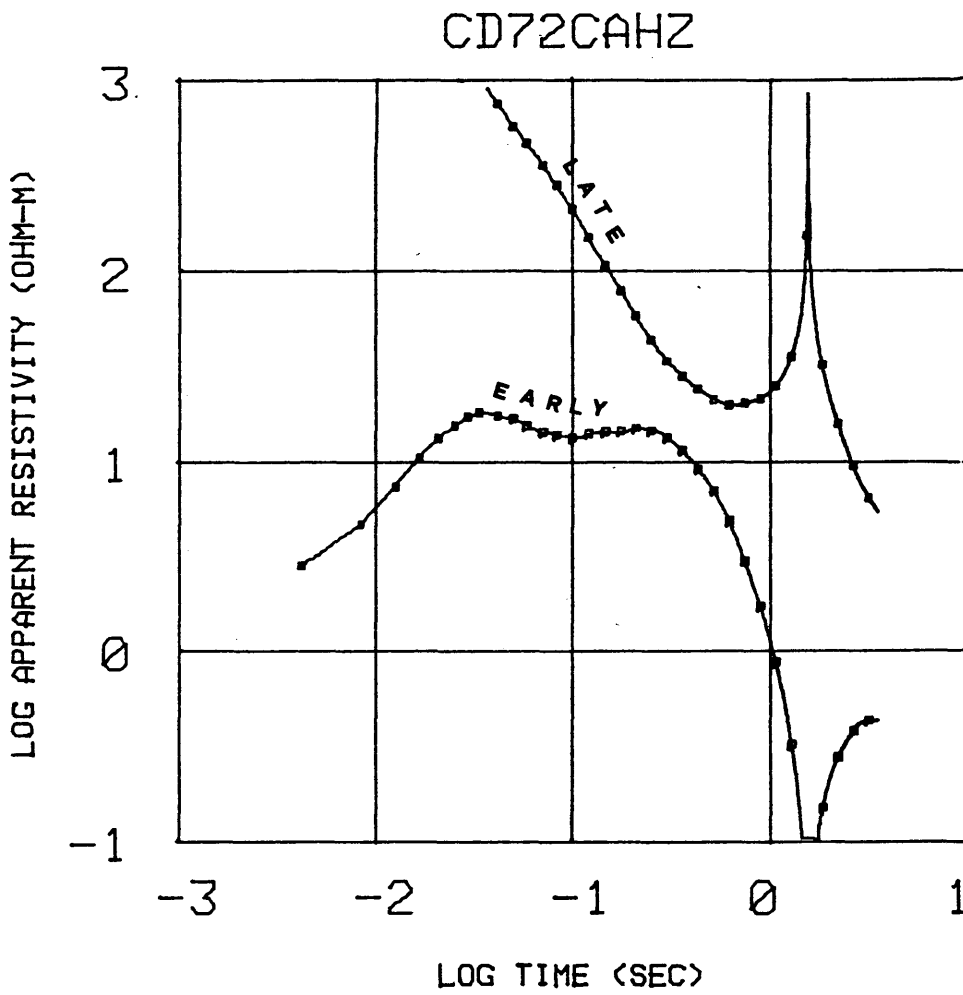


Figure 110

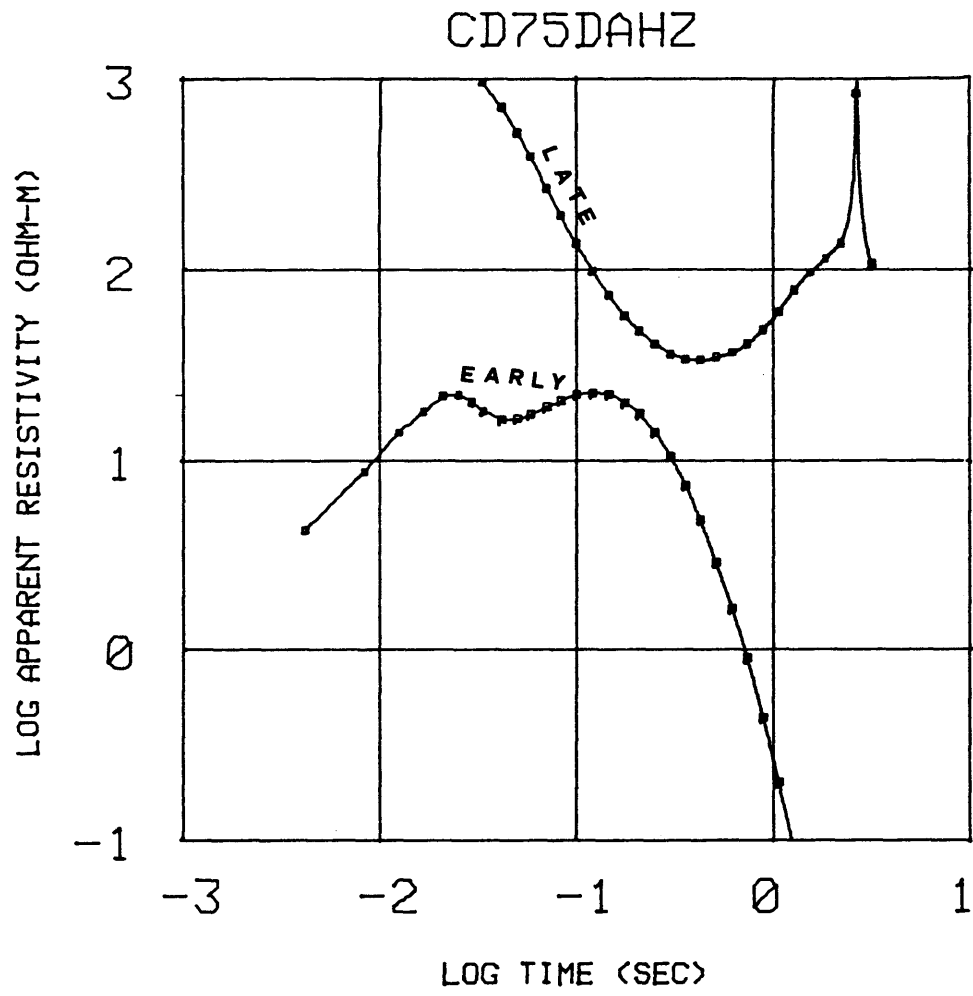


Figure 111

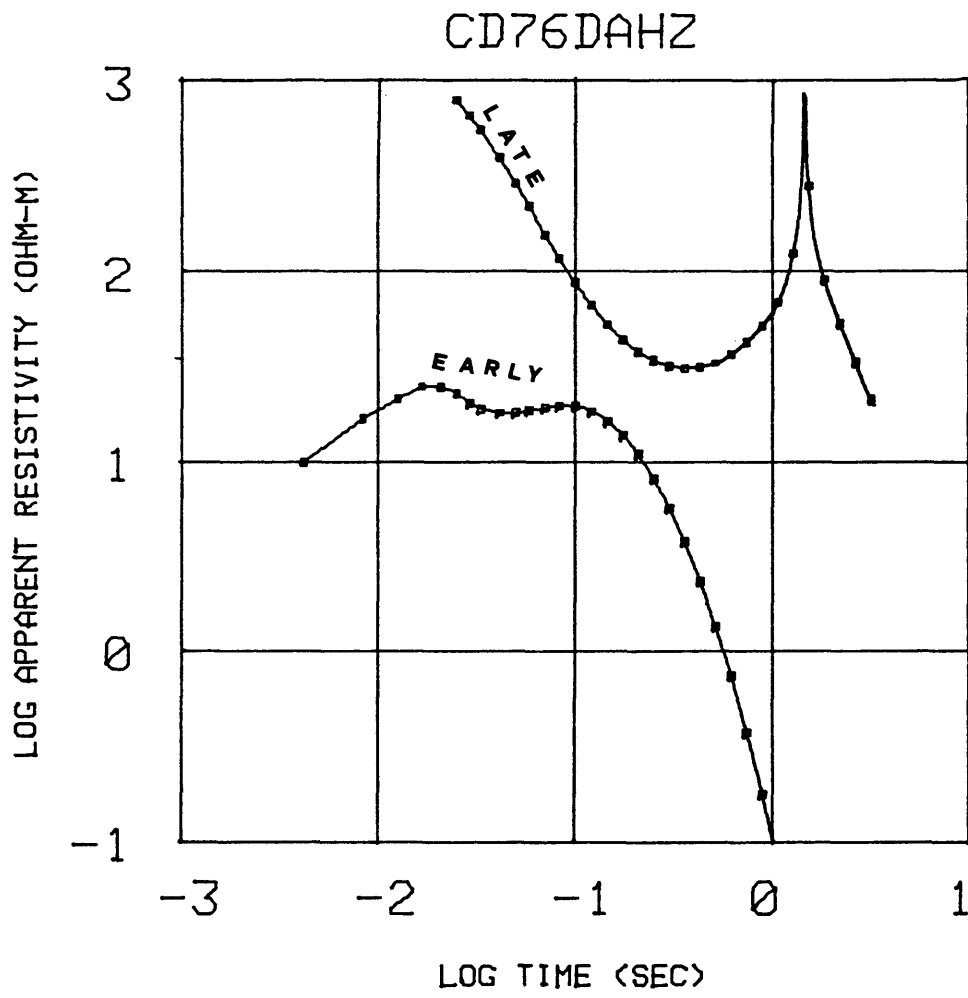


Figure 112

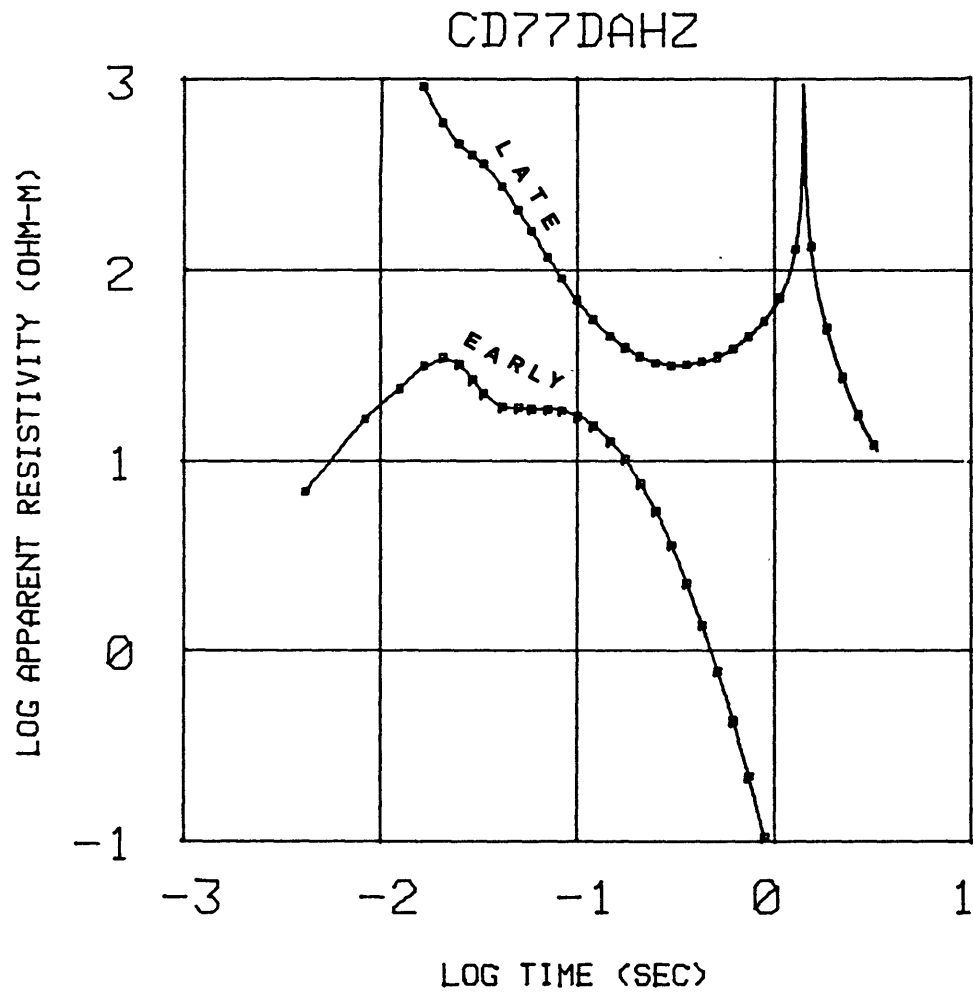


Figure 113

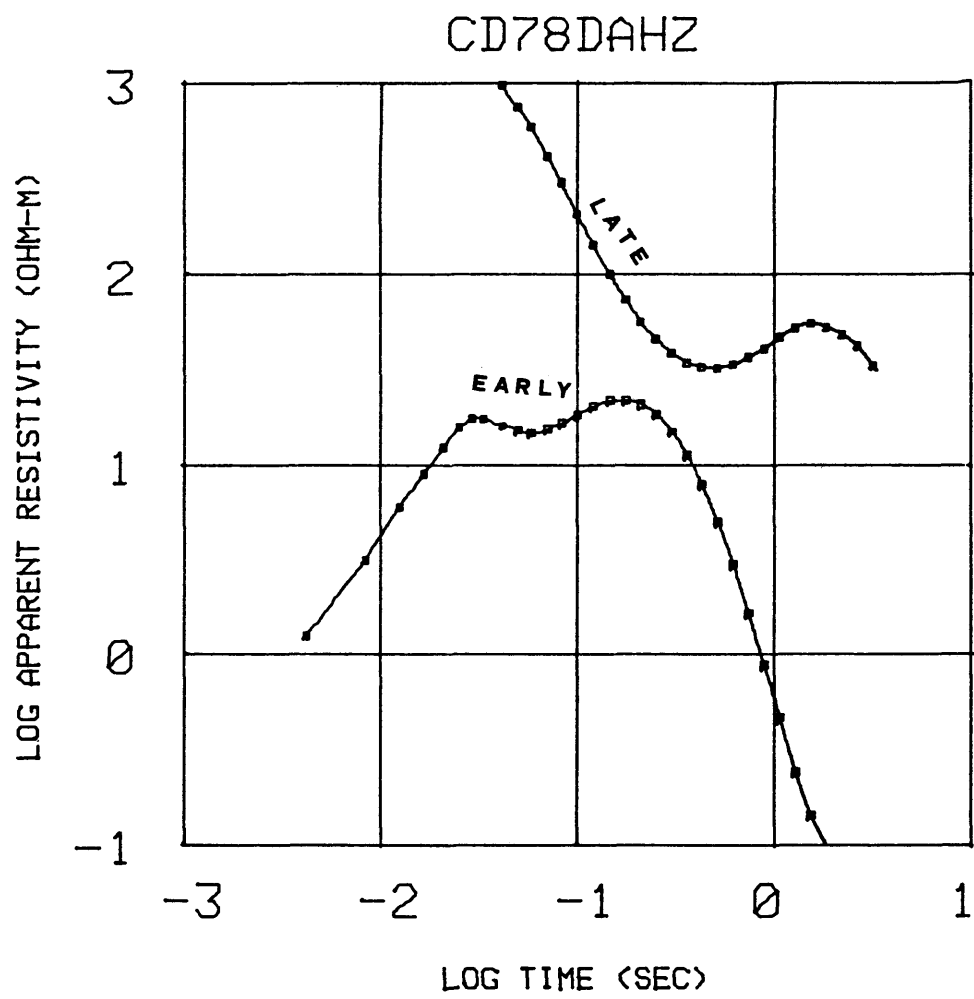


Figure 114

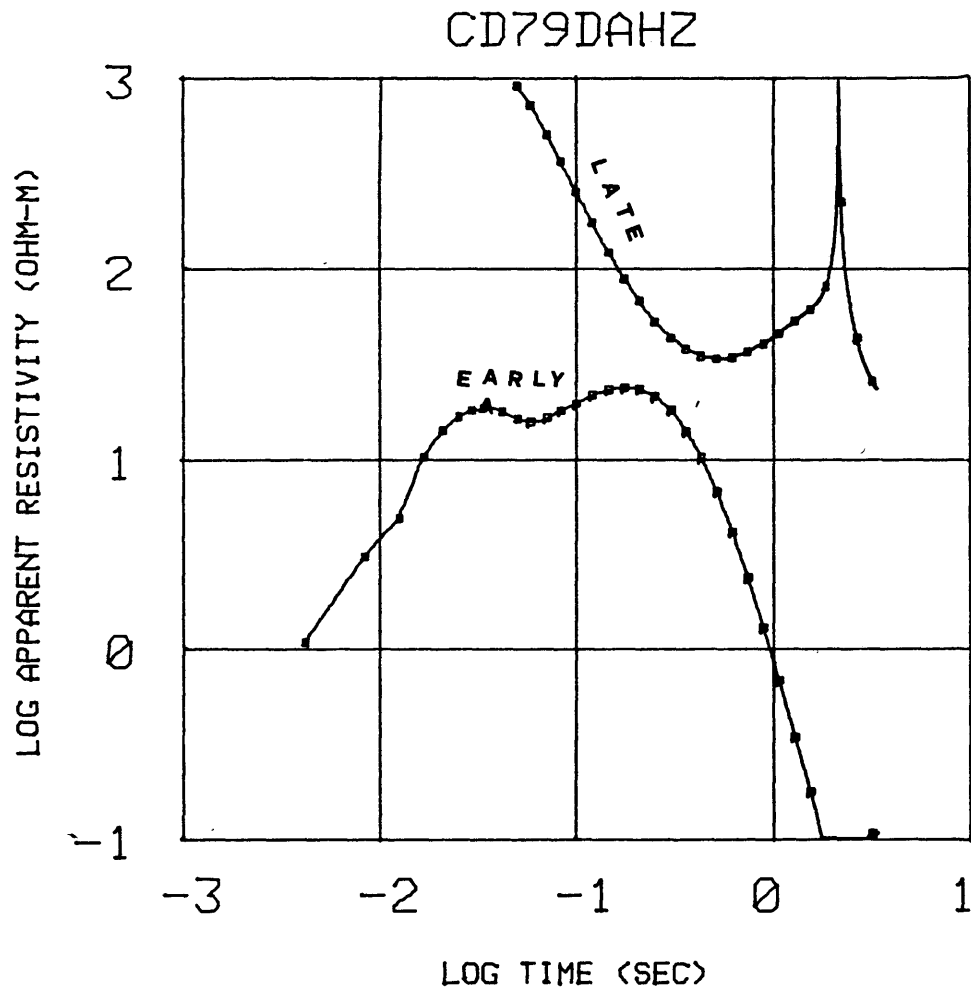


Figure 115

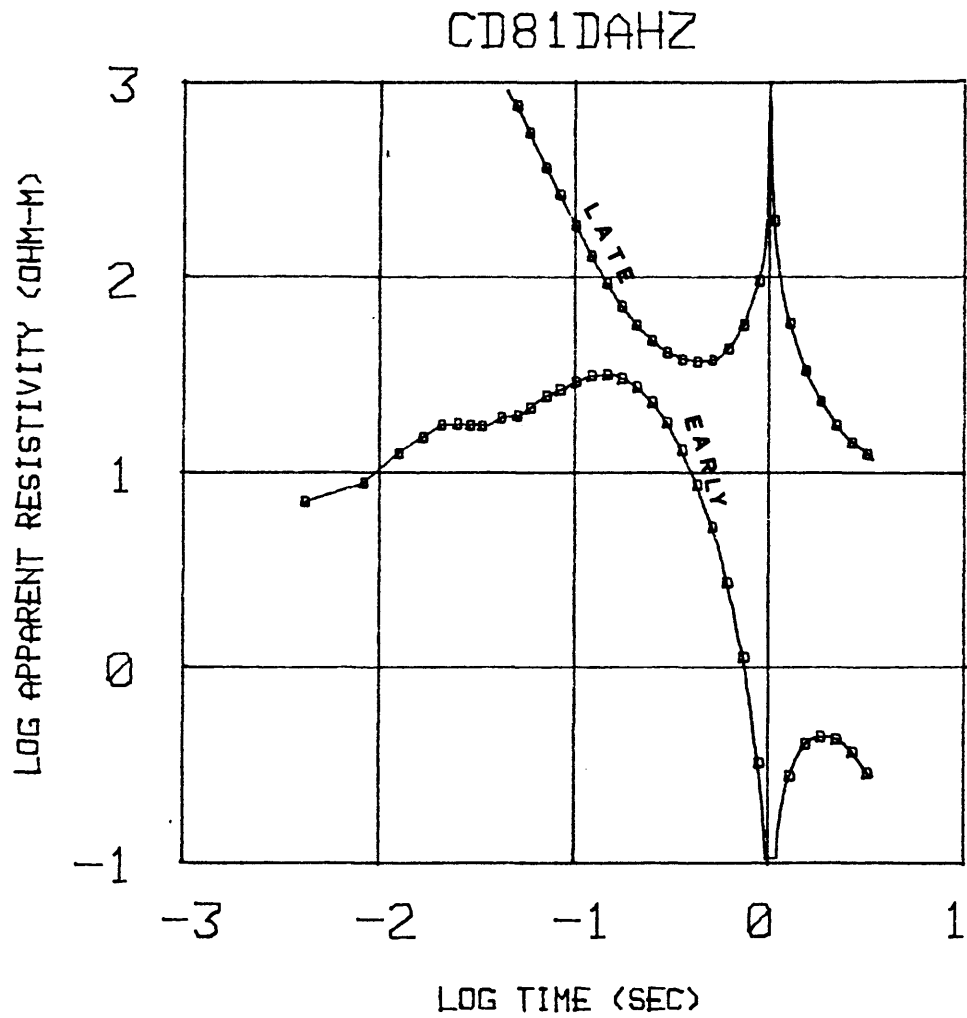


Figure 116

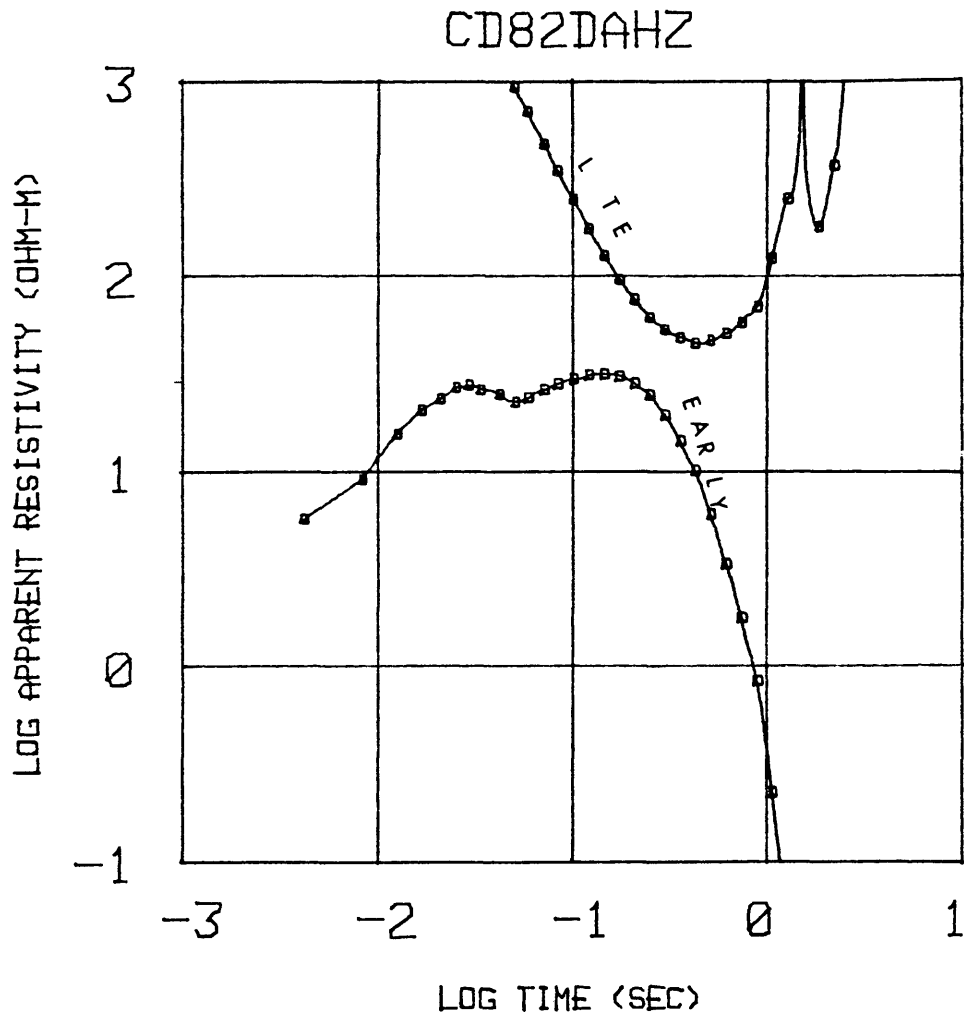


Figure 117

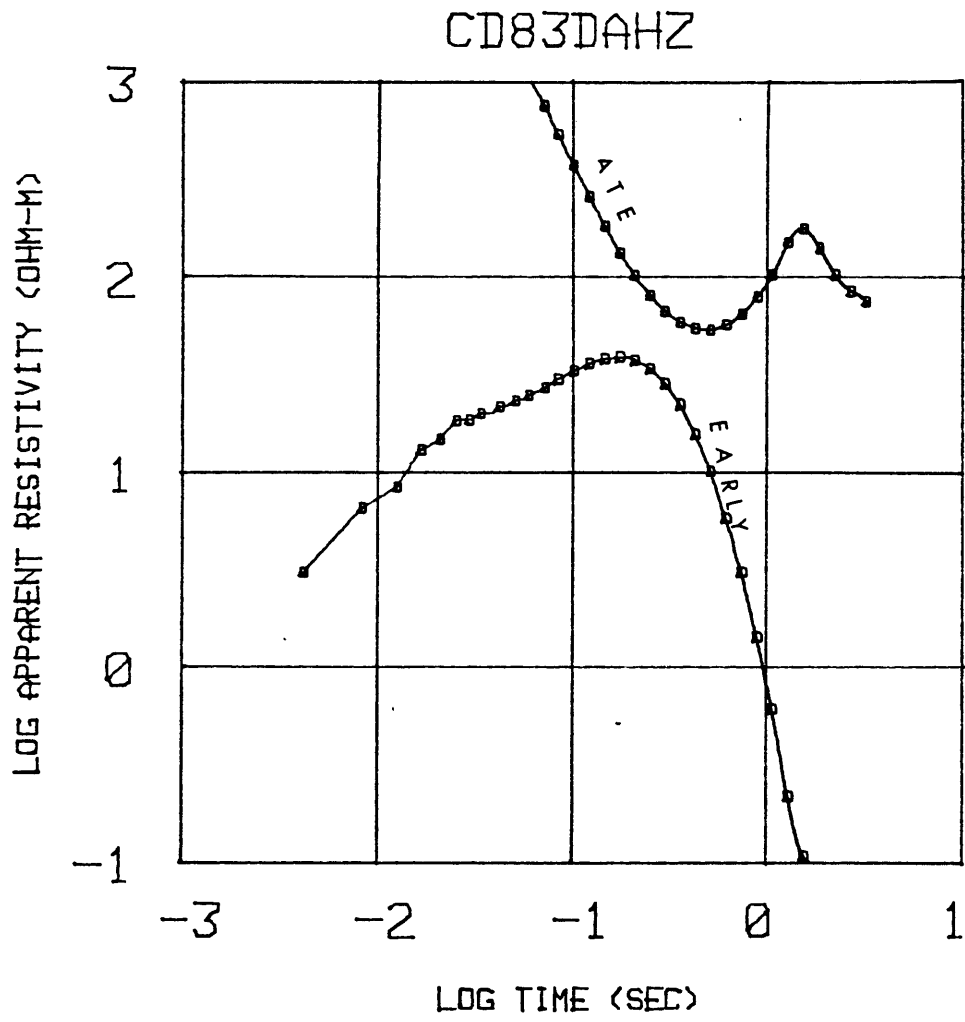


Figure 118

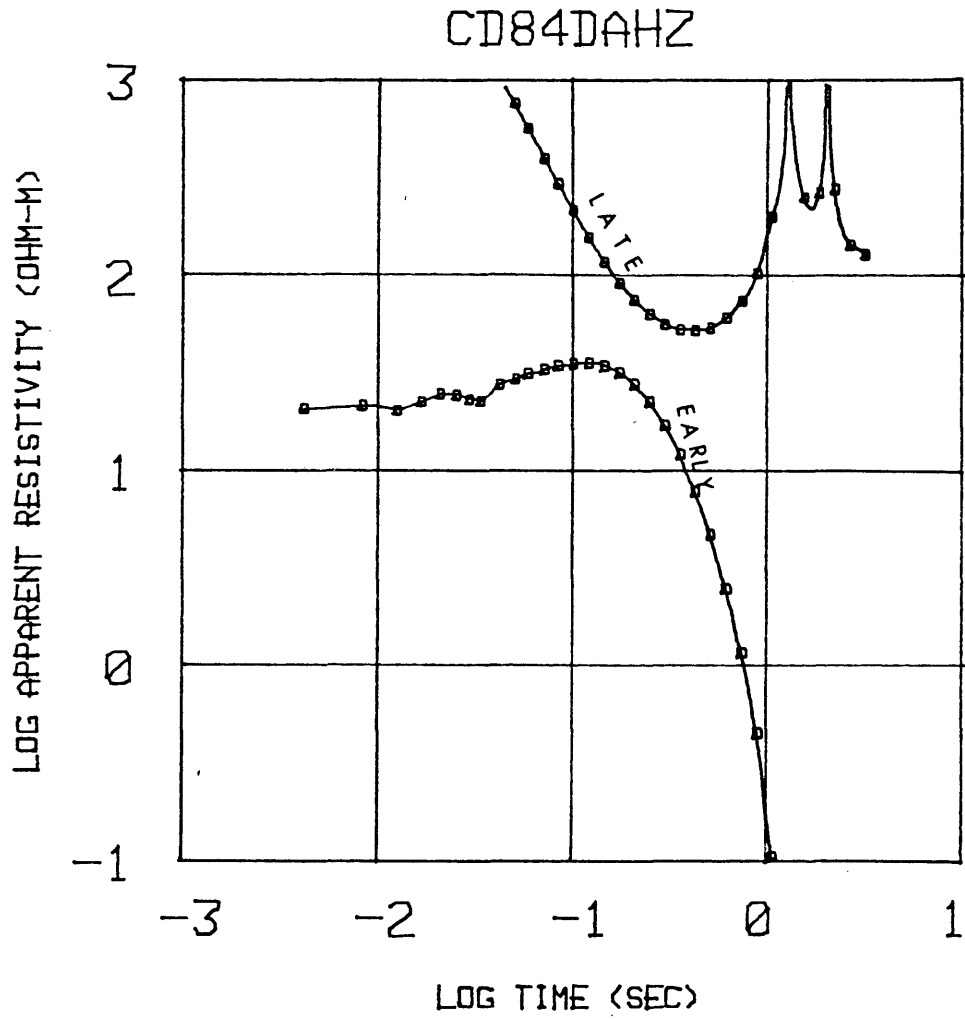


Figure 119

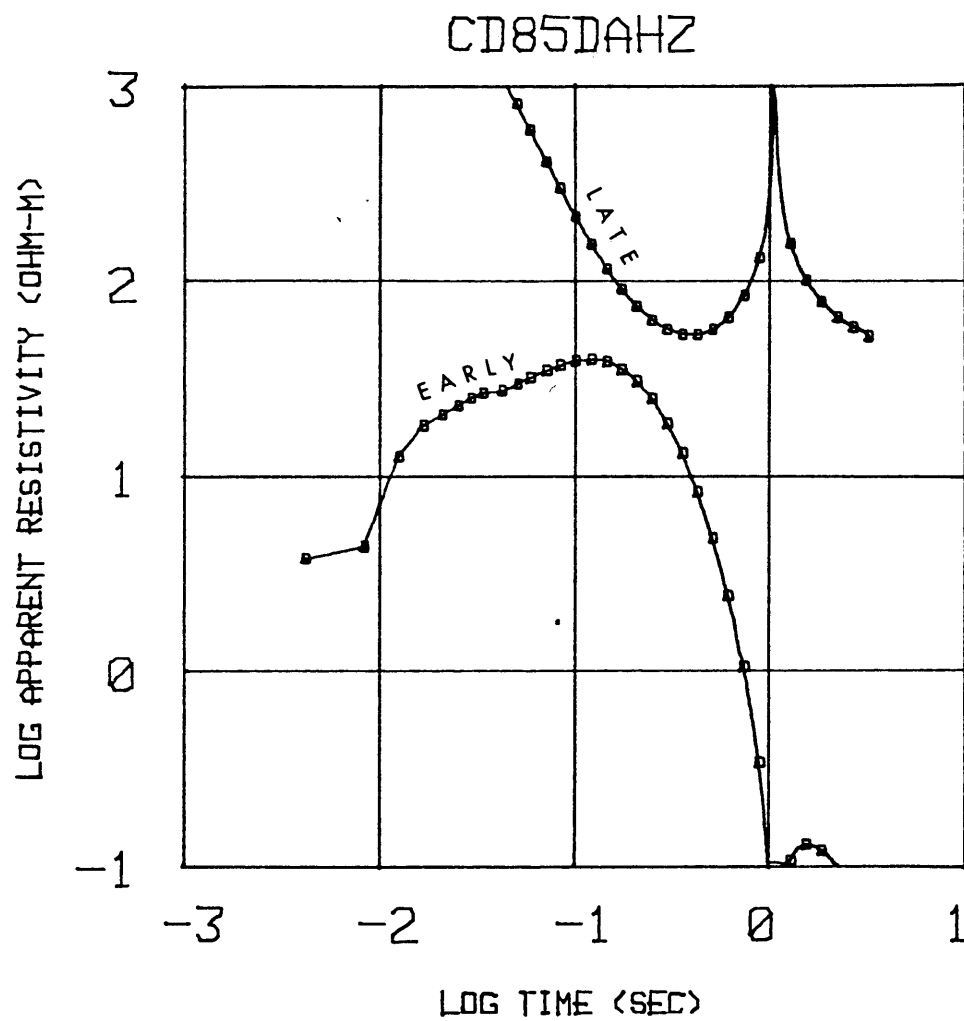


Figure 120

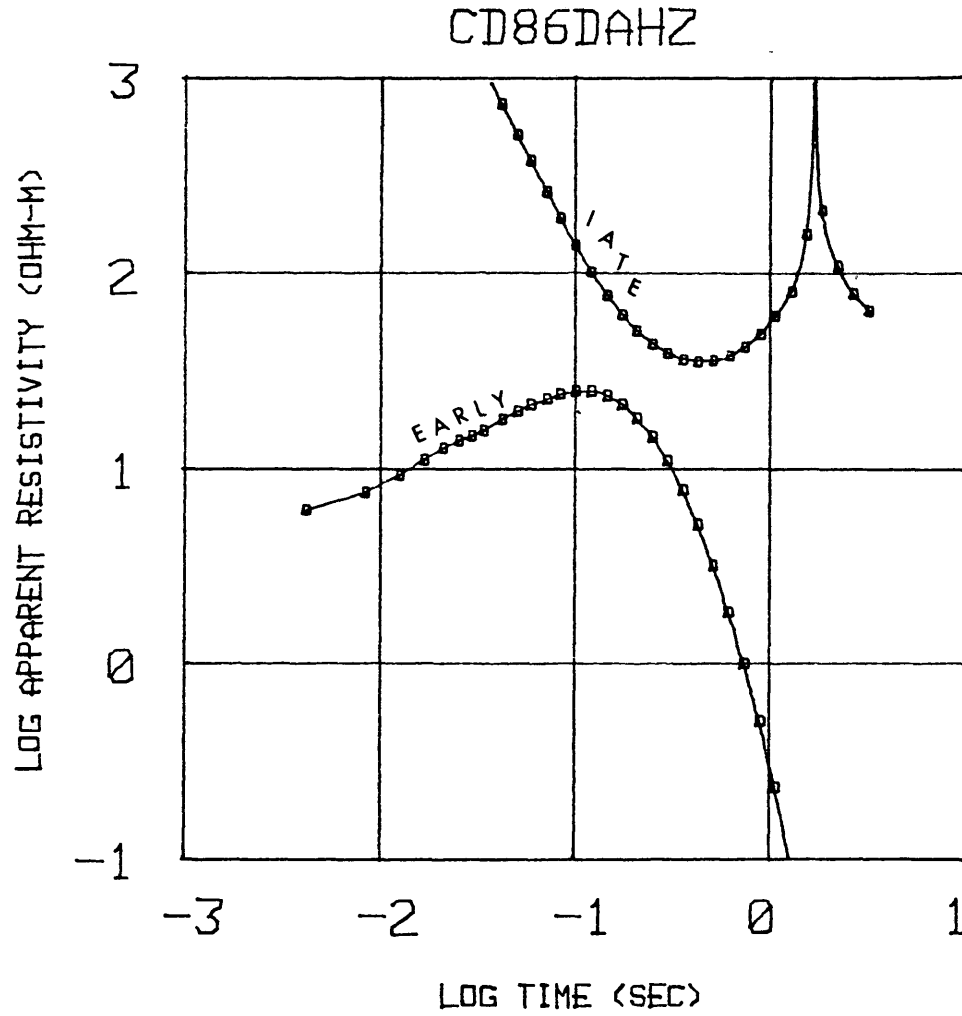


Figure 121

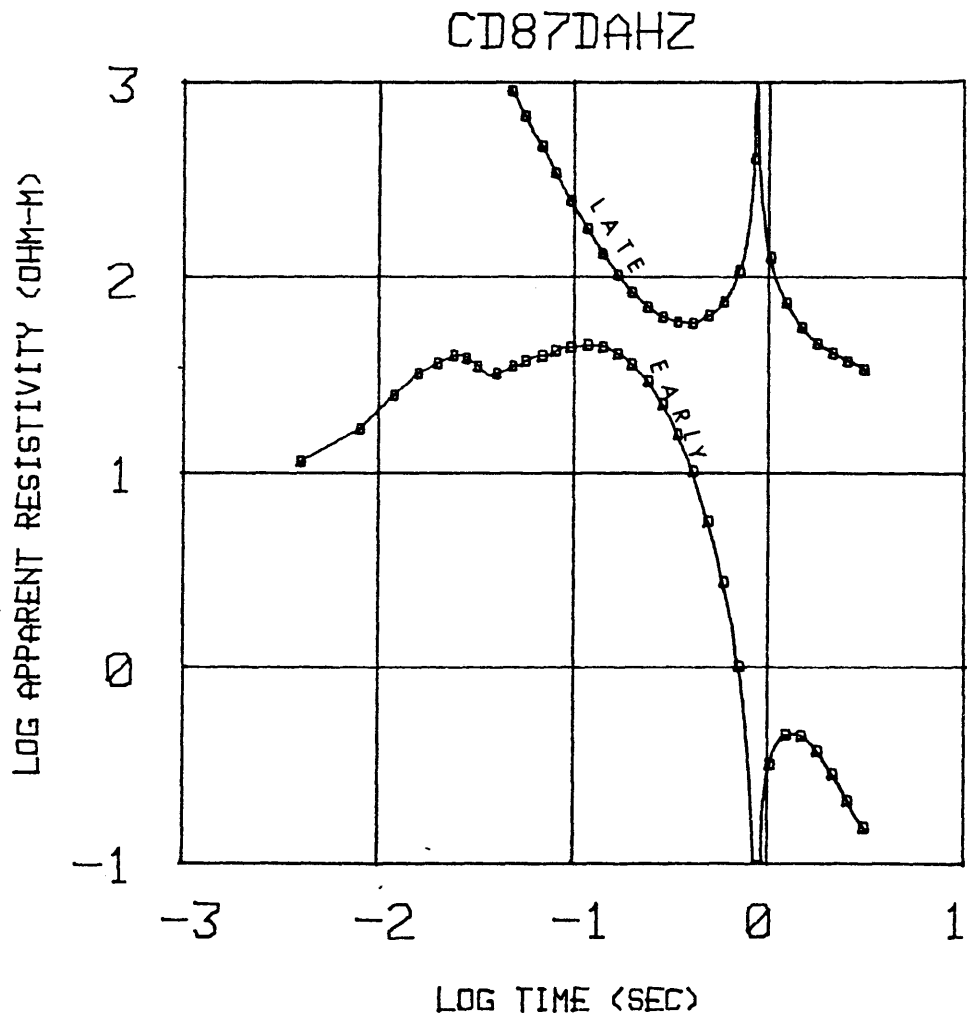


Figure 122

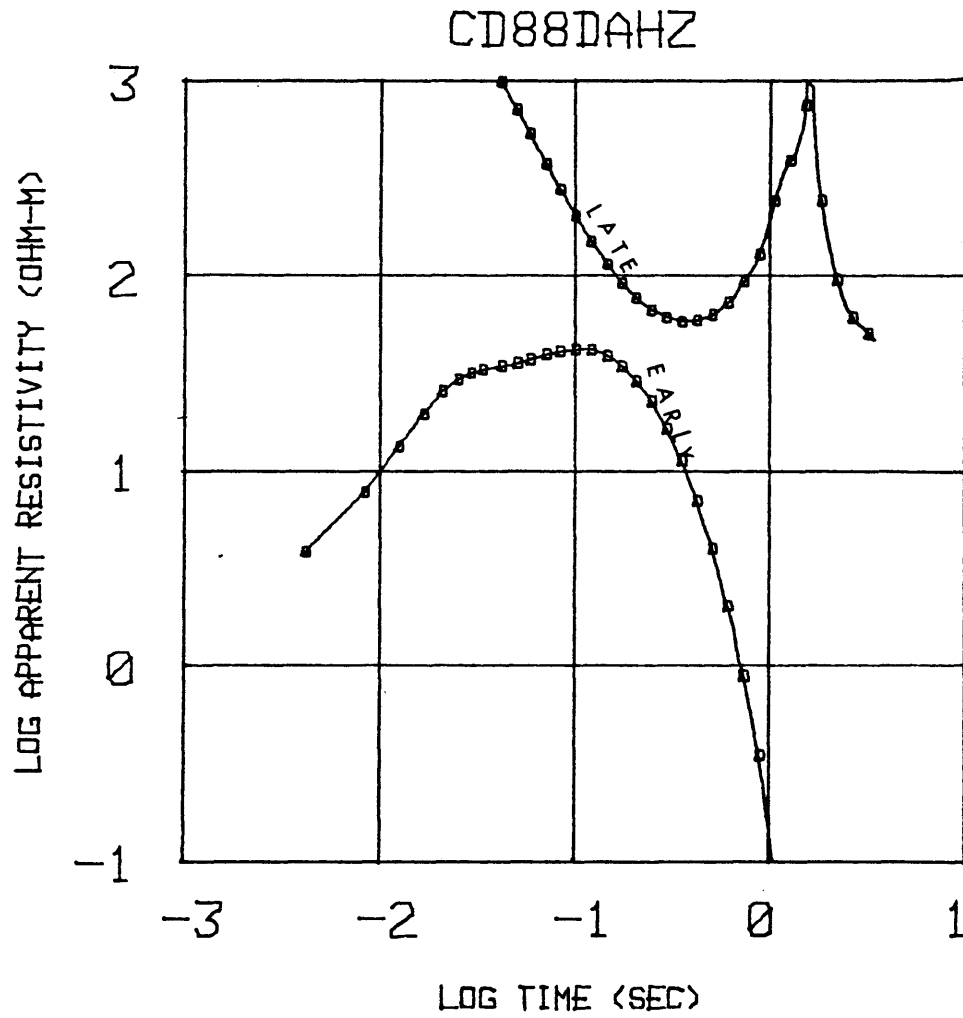


Figure 123

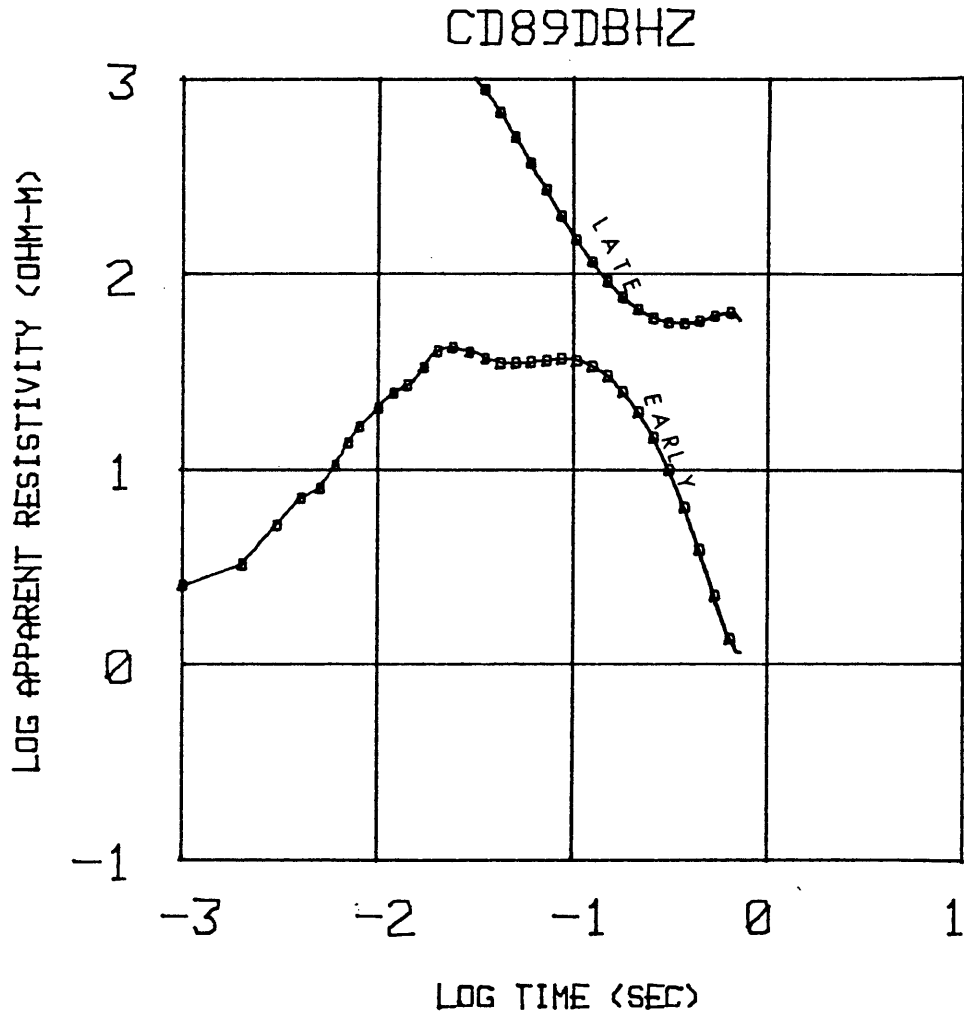


Figure 124

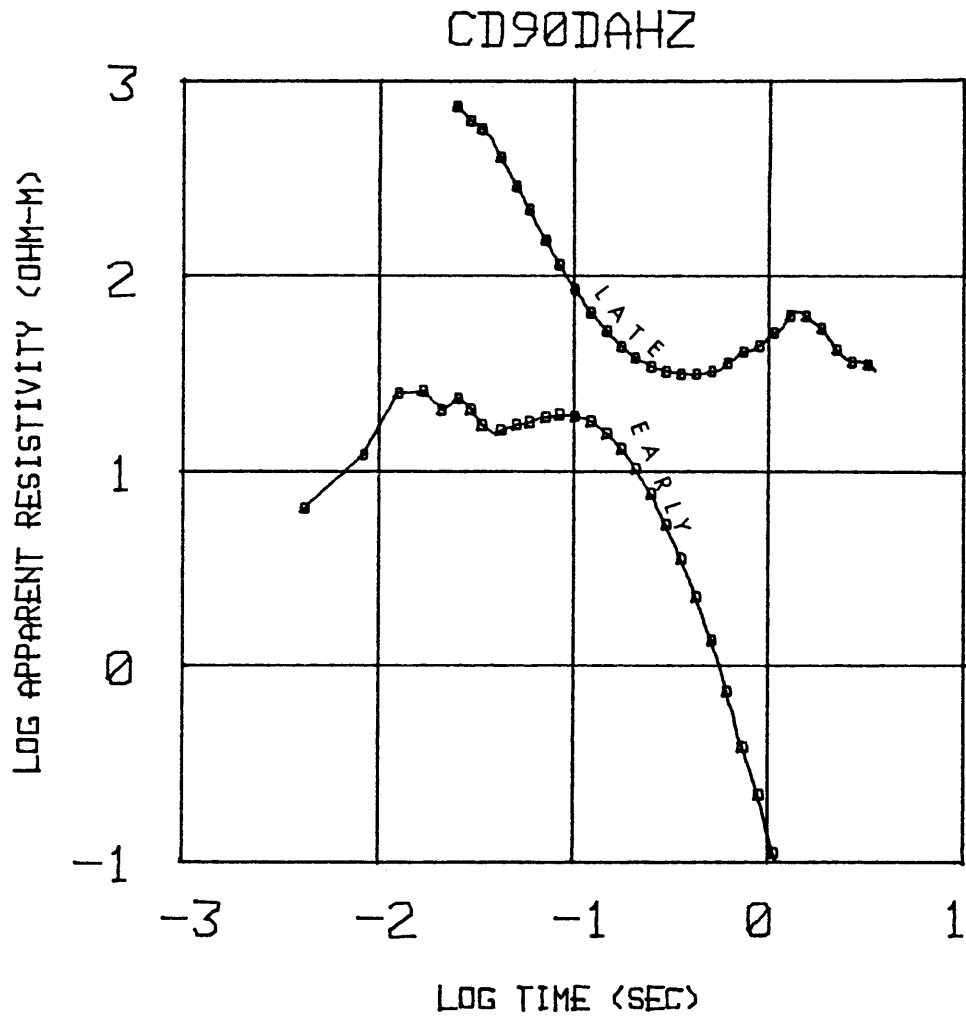


Figure 125

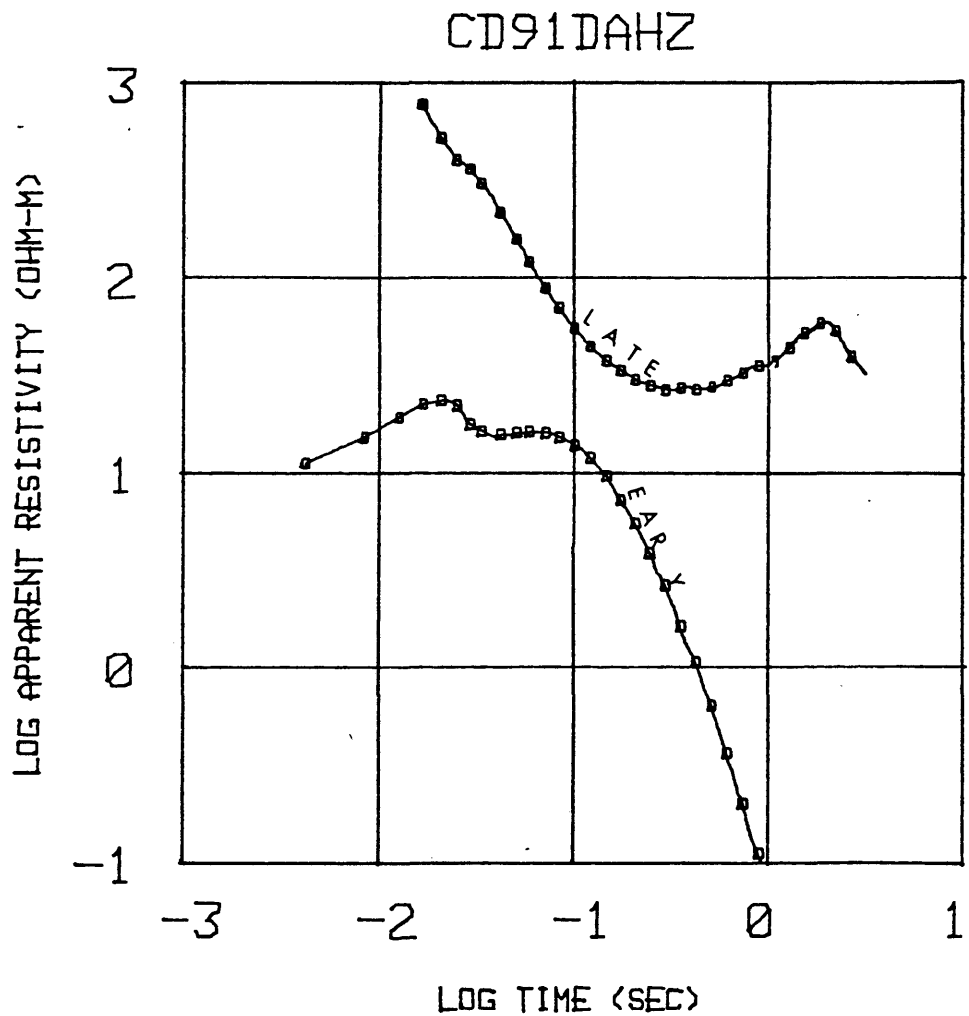


Figure 126

APPENDIX B

Appendix B consists of a table containing the calculated parameters for the earth models used in the inversion, for all receiver locations.

## Appendix B

Calculated parameters for the models at each station as obtained for inversion. Resistivities are in ohm-meters, and thicknesses are in meters.

(page 1 of 4)

Station #	$\rho_1$	$\rho_2$	$\rho_3$	$h_1$	$h_2$	Error %
01	7	3	25	615	303	2.9
06	3	7	7	120	174	3.3
07	9	7	36	486	438	10.5
09	7	11	25	135	1,250	10.7
10	8	13	7	140	395	8.6
11	33	2	62	628	313	7.0
12	2	13	8	92	247	4.4
13	12	10	14	409	724	9.7
14	5	13	15	200	586	3.9
15	4	13	9	148	638	13.1
16	7	5	7	315	355	6.6
17	4	28	7	186	286	3.8
19	6	9	43	221	926	7.8
20	11	19	8	209	233	12.4
21	6	11	8	170	517	6.0
22	34	4	23	569	243	10.7
23	6	540	340	393	933	5.2
24	5	496	23	205	2,460	8.5
25	9	53	57	80	160	9.0
26	8	89	76	129	261	6.1
27	19	77	81	377	1,050	8.3
28	10	44	248	177	2,470	4.1
29	12	56	50	158	321	11.5

Appendix B  
(page 2 of 4)

Station #	$\rho_1$	$\rho_2$	$\rho_3$	$h_1$	$h_2$	Error %
30	12	62	53	157	321	13.0
31	17	38	160	276	1,410	5.2
32	16	27	47	417	537	5.4
33	5	195	29	128	429	8.5
34	12	42	--	502	---	5.3
35	9	24	91	303	1,090	4.1
36	12	66	--	189	---	8.6
37	7	58	--	108	---	11.0
38	16	146	--	450	---	15.0
39	14	92	--	391	---	6.1
40	14	16	--	395	---	5.3
41	11	167	--	332	---	8.7
42	12	49	--	182	---	7.8
43	39	24	106	640	552	4.9
44	25	21	107	659	558	5.2
45	8	58	28	174	657	13.8
46	54	10	453	246	619	5.3
48	30	12	157	112	706	5.9
49	62	16	344	158	1,200	2.3
50	35	12	210	973	513	5.3
51	20	5	64	624	588	6.2
52	74	5	30	431	665	10.5
53	44	39	23	393	923	8.5
54	61	7	49	726	693	10.3

Appendix B  
(page 3 of 4)

Station #	$\rho_1$	$\rho_2$	$\rho_3$	$h_1$	$h_2$	Error %
55	10	7	121	363	939	4.5
56	15	6	19	37	676	5.3
57	11	3	29	76	318	6.6
58	26	12	79	660	1,720	7.5
61	14	5	298	548	632	2.99
62	18	3	134	637	302	4.9
63	20	4	159	430	515	2.7
64	20	3	158	550	375	2.5
65	6	20	--	808	---	6.1
66	14	4	882	503	543	2.7
67	30	3	151	559	552	3.1
68	42	3	86	771	504	3.0
69	9	42	--	1,230	---	4.3
70	54	5	206	988	478	4.6
71	14	8	197	793	609	3.9
72	22	6	151	664	637	4.9
73	13	6	112	854	707	6.2
74	46	9	30	865	363	15.5
75	50	15	198	129	1,210	8.2
76	41	12	162	478	823	6.9
77	40	10	199	800	646	8.4
78	28	8	300	570	560	12.0
79	19	10	132	355	612	6.4
80	26	21	78	568	978	3.5

Appendix B  
(Page 4 of 4)

Station #	$\rho_1$	$\rho_2$	$\rho_3$	$h_1$	$h_2$	Error %
81	14	54	159	896	801	3.4
82	38	26	265	107	942	12.7
83	21	18	467	162	1,100	3.7
84	18	43	91	552	1,620	5.4
85	17	60	89	616	1,100	6.4
86	7	32	39	212	274	8.2
87	33	16	197	910	503	4.2
88	22	46	202	539	2,130	3.6
89	35	16	102	1,000	435	5.2
91	42	4	225	758	236	3.6

## APPENDIX C

Appendix C explains the meaning of the symbols used in the inversion of apparent resistivity curves, using the computer program SATI.

- \* = observed data point,
- + = theoretically calculated point,
- D = match of observed and calculated value,
- R = source receiver distance in meters,
- CDXX = station number,
- TDHZ = time-domain, vertical magnetic field,
- RMS = root mean square error in the calculated fit.

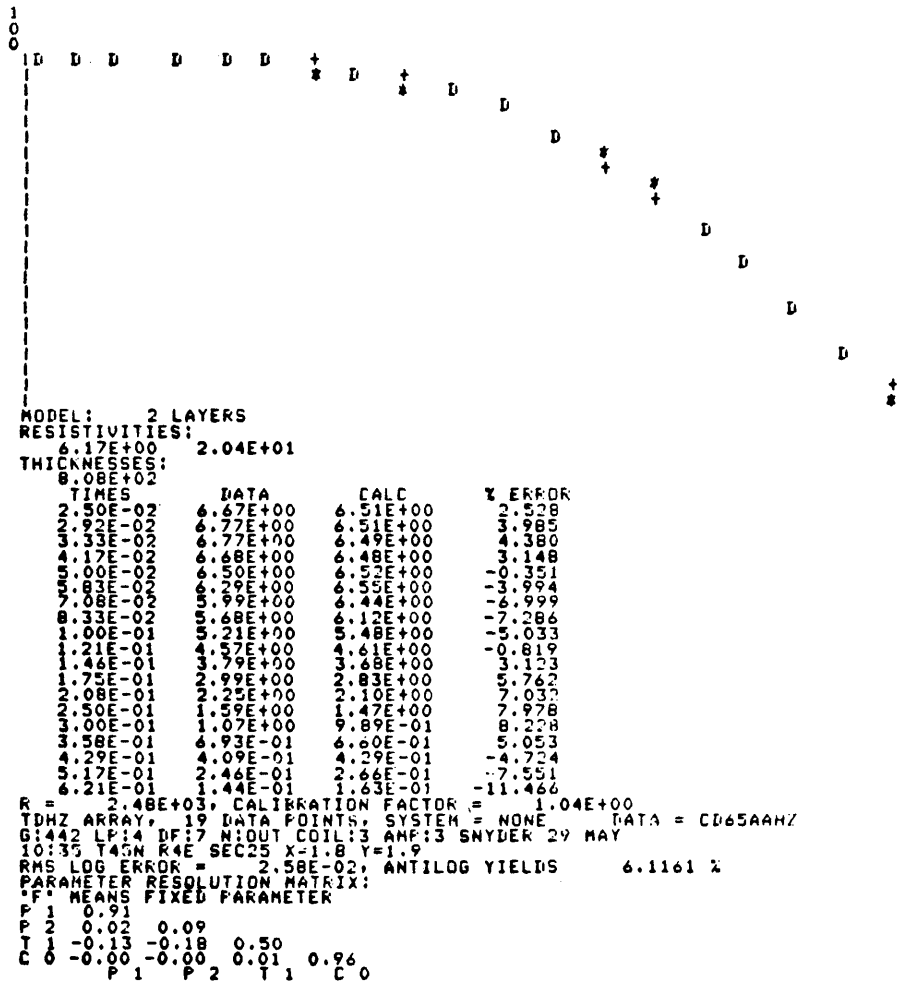


Figure 127. Example of inversion of the early and late time apparent resistivity curves, using a two-layer earth model.